UNIVERSITY OF SOUTHAMPTON

FACULTY OF PHYSICAL AND APPLIED SCIENCES

Electronics and Computer Science

The Use of Raman Microprobe Spectroscopy in the Analysis of Electrically Aged Polymeric Insulators

by

Nicola Freebody

Thesis for the degree of Doctor of Philosophy

September 2012

UNIVERSITY OF SOUTHAMPTON

ABSTRACT

FACULTY OF PHYSICAL AND APPLIED SCIENCES
Electronics and Computer Sciences

Doctor of Philosophy

The Use of Raman Microprobe Spectroscopy in the Analysis of Electrically Aged Polymeric Insulators

by Nicola Freebody

Due to its applications in high voltage insulation, a thorough understanding of the chemical reactions that occur during electrical ageing in polymers is needed. A confocal Raman microscope has a potential lateral resolution of ~1μm along both the lateral and optic axes and is able to characterise the localised chemical composition of a material; for this reason, it has been applied in the study of electrical ageing in solid dielectrics. Due to inaccurate assumptions about the optical processes involved in confocal Raman microprobe spectroscopy (CRMS), however, the exact characterisation of the processes and chemicals involved has previously proven to be difficult.

The objective of this study is to apply the technique of Raman microprobe spectroscopy in the analysis of the chemical structures of electrically aged polymers. It was found that, with the application of immersion oil and by using a refined version of a model of CRMS which is based on a photon scattering approach; CRMS is a valuable tool in the study of polymers. More accurate results can be obtained, however, by revealing the feature in question to the surface and applying non confocal Raman microprobe spectroscopy (RMS).

CRMS was applied to a variety of polymeric samples containing electrically aged voids and electrical trees. Results showed that within the electrically aged voids, chemical signatures similar to those previously found in electrical trees in PE can be found. Finally, a variety of polymeric insulators was subjected to spark ageing and corona discharge. The by-products of these ageing mechanisms were then characterized using RMS in an attempt to reproduce in bulk the chemical compounds formed in electrical treeing. The resulting Raman spectra indicated that the same by-products as those formed in voids and trees are indeed formed. Where possible all results were compared to comparative data obtained using Fourier transform infra red (FTIR) spectroscopy and scanning electron microscopy (SEM) and discussed in relation to previously published work.

Contents

List of figures

List of tables

DECLARATION OF AUTHORSHIP

I, Nicola Freebody, declare that the thesis entitled

'The Use of Raman Microprobe Spectroscopy in the Analysis of Electrically aged Polymeric Insulators'

and the work presented in the thesis are both my own, and have been generated by me as the result of my own original research. I confirm that:

- this work was done wholly or mainly while in candidature for a research degree at this University;
- where any part of this thesis has previously been submitted for a degree or any other qualification at this University or any other institution, this has been clearly stated;
- where I have consulted the published work of others, this is always clearly attributed;
- where I have quoted from the work of others, the source is always given. With the exception of such quotations, this thesis is entirely my own work;
- I have acknowledged all main sources of help;
- where the thesis is based on work done by myself jointly with others, I have made clear exactly what was done by others and what I have contributed myself;
- parts of this work have been published as:

    - N.A. Freebody, A.S. Vaughan, and P.L. Lewin, *Raman microprobe analysis and ageing in dielectrics.* Journal of Physics: Conference Series, 2009. **183**(1).
    - N.A. Freebody and A.S. Vaughan, *Surface ageing of dielectric materials in a controlled atmosphere: A Raman microprobe study.* IEEE Conference on Electrical Insulation and Dielectric Phenomena (CEIDP 2010), 2010.
    - N.A. Freebody, A.S. Vaugahn and A.M. Macdonald, *On optical depth profileing using confocal raman spectroscopy.* Analytical and Bioanalyitical Chemistry, 396 (8), 2010.
    - N.A. Freebody, I.L. Hosier and A.S. Vaughan, *Raman microprobe analyisis of electrical treeing in silicone rubber.* International Symposium on High Voltage Engineering (ISH 2011), 2011.

Signed: …….

Date:…….

Acknowledgements

I would like to acknowledge and thank a number of people without whom finishing this thesis would not have been possible. Firstly, to the EPSRC and the Supergen AMPeRES Project for providing funding for the majority of this thesis.

Secondly to all the members of the Tony Davis High Voltage Laboratory for making my time in the lab memorable and fun. In particular, to my supervisor Prof Alun Vaughan for his patience, support and guidance throughout my thesis and to Prof Paul Lewin for pushing me when I needed it the most. Special thanks also go to Mike, Brian, Ian, Dave, Celia and the CEO of Martycorp who always helped me when I needed it and provided endless amounts of technical and moral support. They never turned me away even when I repeatedly asked stupid questions.

I am also very grateful to everyone in the Southampton University Fencing Club (with special thanks to Chris A) for letting me vent and hit you with a sword whenever I needed a release. You helped more than you know.

Finally to my family including my mother, father and brother Chris, I will be forever in your debt. Thank you for being there throughout the good times and especially thank you for being there in the bad times. Your love, support and encouragement was invaluable and helped me to finally finish writing this thesis.

It took me long enough but I got there in the end.

To Terrance…

Definitions and abbreviations

CCD – Charged coupled device
CNT – Carbon nano tubes
CRMS – Confocal Raman microprobe spectroscopy
DCP – Dicumyl peroxide
FTIR – Fourier transform infra red
FWHM – Full width half maximum
HACA – Hydrogen extraction C_2H_2 addition
HDPE – High density polyethylene
HV – High voltage
IR – Infra red
LDPE – Low density polyethylene
NA – Numerical aperture
PAH – Polycyclic aromatic hydrocarbons
PD – Partial discharge
PDMS – Polydimethyl siloxane
PDMS(E)- Polydimethyl siloxane (elastomer)
PDMS(L) - Polydimethyl siloxane (liquid)
PE – Polyethylene
PEEK – Polyether ether ketone
PS – Polystyrene
RMS – Raman microprobe spectroscopy
SEM – Scanning electron microscopy
XLPE – Cross linked polyethylene
XPS – X-ray photon spectroscopy
XRD – X-ray diffraction

1 : Introduction

Due to its application in high voltage (HV) insulation, the topic of electrical ageing in polymeric materials has been widely studied and researched. Polymeric insulation is rapidly replacing the more traditional oil-paper based insulation due to its low cost and high efficiency. Over time, however, the polymer ages as it is subjected to a combination of high electrical, thermal and mechanical stresses. In some cases this ageing can result in the complete breakdown of the material. These ageing processes vary between micro and macroscopic levels depending on whether it occurs in the bulk of the material (e.g. electrical treeing) or on the surface (e.g. corona discharge). Many different techniques have been used in an attempt to characterise the chemical changes in the ageing process including FTIR [1, 2], fluorescence spectroscopy [3, 4] and, not least, confocal Raman microprobe spectroscopy (CRMS) [1, 5]. In the case of CRMS, studies can be flawed, as they do not properly take into account the optics of the system and wrongly assume that CRMS has a lateral resolution of 1μm and a vertical resolution of 2 μm [6]. In order to be able to accurately use CRMS in the analysis and characterisation of electrical ageing in polymeric insulators we must first understand polymers, electrical ageing and CRMS itself.

1.1 Polymeric Materials

The term polymer was first coined by Jöns Jacob Berzelius in 1833 from the Greek words poly and meros, meaning 'many parts', and is now used to describe a large macromolecule which is made up of repeating structural units known as monomers. There is a vast variety in polymers ranging from the natural (e.g. DNA) to the synthetic (e.g. Teflon). Modern polymers have a large influence on our daily lives; due to them being, amongst other things, light, strong, inexpensive, easily moulded to their use and reusable, they can be found in nearly everything from food to plastic packaging.

A polymer is a long (up to 1 μm in length) chain like molecule comprised of thousands of repeated molecular units linked together via covalent bonding during a process known as polymerisation. In its most basic form, polymerisation can occur via addition polymerisation. A good example of addition polymerisation is the conversion of ethylene into polyethylene, as seen in figure 1.1. Here the double bond in ethylene is opened, for example, with the aid of a catalyst [7] and hence the monomers join together to form polyethylene.

In this case, the monomers are joined in an A+A+A+A+A+A+.... → AAAAAA... form. This linear sequence of repeating units is relatively flexible due to no cross linking and the various chains in the polymer vary in length. Polymers chains containing more

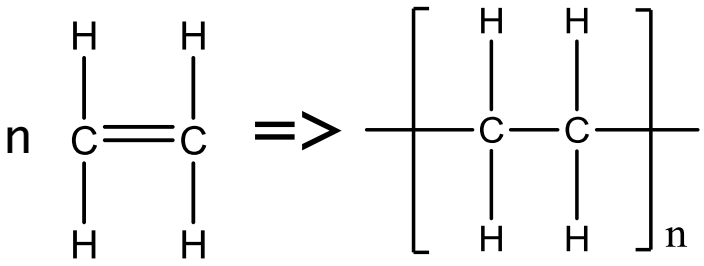

Figure 1.1: Diagram showing how the double bond in ethylene is broken to form the polyethylene chain

than one monomer are known as co-polymers due to the statistical nature of the process. The second monomers are introduced before or during polymerisation and by varying this second monomer the characteristics and properties of the final material can be altered. The possible arangements of the monomers in a copolymer include alternating, periodic, block, branched and random (see table 1.1). In the vast majority of polymers, the backbone formed by these repeating units is based on carbon, although others involving elements such as silicon and oxygen can be found.

Table 1.1: Descriptions and basic structures of co polymers (A = polymer 1, B = Polymer 2)

Type of co polymer	Description	Numerical representation	Graphical Representation
Alternating	Chains consisting of regularly alternating monomers	$[AB...]_n$	-A-B-A-B-A-B-A-B-A-B-
Periodic	Chains consitiong of a regular repeating sequence of monomers	$[A_nB_m...]$ where $n \neq m$	-A-A-B-B-B-A-A-B-B-B-
Block	Two or more polymer chains linked by a covalent bond	$[A_n]$-$[B_m]$-....	-A-A-A-A-A-B-B-B-B-B-
Branched	Polymer containing side chains of a different composition to the main backbone		-A-A-A-A-A-A-A-A-A-A | | -B-B-B-B B-B-B-B-
Random	A statistically random combination of monomers		-A-A-B-B-B-A-B-B-A-A-

Following polymerisation, the resulting material can order itself such that it has a semi crystalline structure. During this crystallisation process the long chains fold upon themselves to form stacks of flat sheets known as lamellae (figure 1.2) [8]. Polymer chains in the lamella can also extend out into the surrounding disordered amorphous region [9]. When the polymer is crystallised in the bulk, these lamellae grow out from a central nucleus, where several lamellae form together, into small spheres called spherulites which are approximately 10 – 100 μm in size [10] (see figure 1.3). The rate of growth of the lamella is linear with time [11]; the spherulites growth rate depends on factors such as the crystallisation temperature and the mobility of the polymers within the system. The degree of crystallinity of a polymer can range from zero, which is related to a completely amorphous structure and non crystalline polymer, to one which corresponds to the theoretical case where the polymer has a completely crystalline structure. Most polymers fall between the two values and contain both crystalline and amorphous regions. Many mechanical, optical and electrical properties of the polymer, such as tensile strength, flexibility, transparency and breakdown strength are related to the crystalinity of the polymer.

By manipulating the chemical structure of a polymer and introducing different monomers in the form of branches, the mechanical, electrical and optical properties of the polymer can be modified as required. Long branches can increase the overall mechanical strength (i.e. tensile) and glass transition temperature of a material whereas short branches can decrease the strength of a polymer due to an increase in crystalinity and order [8]. It is also possible to cross link polymer chains. This increases the strength of a polymer, and so it is often used in the production of rubbers [8]. A good example of introducing branches in order to manipulate the properties of a polymer is with both high density and low density

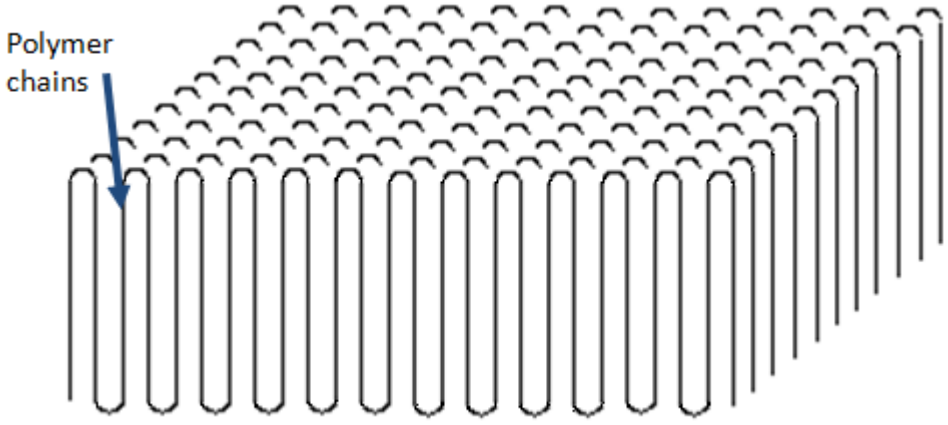

Figure 1.2: Schematic diagram showing the molecular conformations present in an idealised chainfold lamella crystal

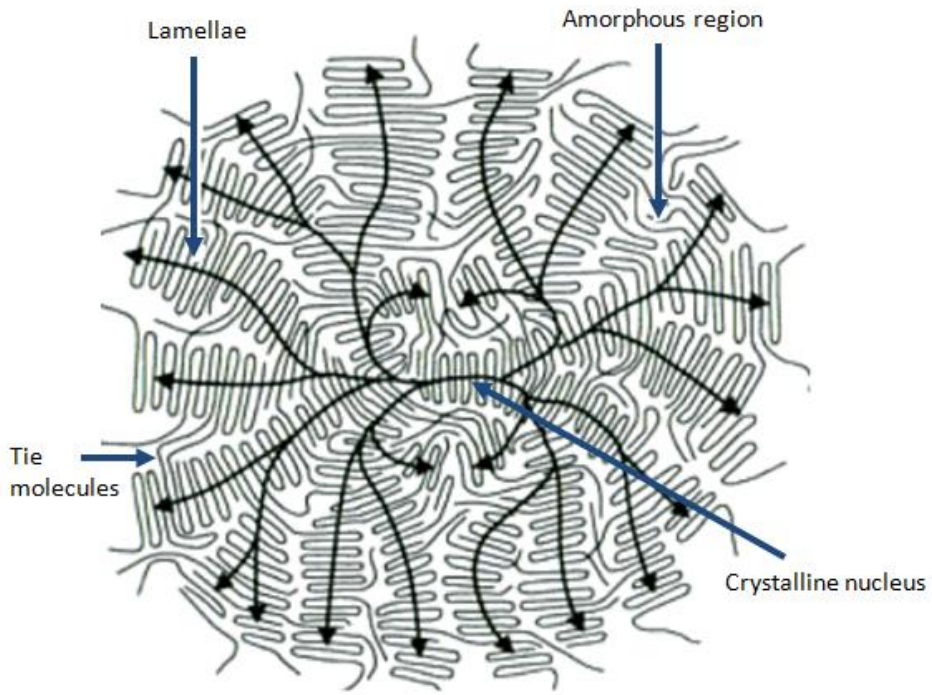

Figure 1.3: A polymer crystalline spherulite

polyethylene (HDPE and LDPE respectively). HDPE has few branches and so has a low flexibility due to its high crystalinity. LDPE on the other hand has a large amount of branches of varying length, causing it to be more amorphous in nature and relatively flexible.

1.2 Electrical ageing

Most solids fall into one of 3 categories, conductors, semi conductors and insulators. In a solid the electrons in a material occupy a number of discrete energy bands in accordance to the Pauli Exclusion Principle. A band full of electrons and which has a higher energy than all other full bands is known as the Valence band. Energy bands above this point are only partially filled and are known as conduction bands. Metals have a conduction band that overlaps in energy with the valence band, resulting in a conduction band that, regardless of temperature, is always partially filled. For this reason, metals have a high conductivity and belong to the first category; conductors. Most polymers (i.e polymers with a carbon backbone such as PE) are classed as organic solids and have a conduction band which is separated from the valence band by a band gap. This results in a low probability of electrons occupying the conduction band and hence polymers have a very low conductivity compared to that of metals. Due to this low conductivity polymers are widely used as electrical insulators. Semi conductors have a relatively small band gap in comparison to insulators and, as the excitation of electrons into the conduction band is largely a response to thermal excitation, the

conductive properties of semiconductors strongly dependant on the temperature of the material. Despite being classed as insulators, polymers aren't necessarily completely void of an electrical response (i.e. conduction) and in the 1950's polymers displaying semi conductor properties emerged [12, 13]. To date much research has been done with regards to the properties and development of conductive and semi conductive polymers [14] including studies on space charge [15, 16], polarisation [17], breakdown strength [18] and dielectric loss [19].

The electrical ageing and breakdown of polymers can be affected by many variables and occur anywhere within the bulk of the polymer. Partial discharges (PD) can be defined as electrical discharges that do not completely bridge the electrodes [20] and occur in gaseous systems, liquids and microvoids in solid dielectrics. With regards to polymers, PD activity usually occurs within macroscopic voids contained in the material, electrical treeing and floating streamers to name a few. Prolonged exposure to PD activity ages a polymer and in some cases leads to complete breakdown of the polymer and its failure as an electrical insulator.

Small cavities of gas can occur in polymeric insulators due to imperfect manufacturing techniques. If an electric field is applied to a polymer containing such voids, the low permittivity of the gas leads to an increase in the electric field [21]. If the voltage of this field is higher than the inception voltage PD activity will occur (see figure 1.4). Over a sustained period of time this activity degrades the insulator, which eventually leads to electrical breakdown.

It has been suggested that this damage is related to the dissipation of energy of electrons or ions [10], cracks caused by an increase in gas pressure within the void due to heating effects [10, 22] and chemical breakdown of the polymer [22, 23]. If the gas within the void contains oxygen then the discharges create ozone which can chemically attack the walls of the void aiding and accelerating the other ageing process present [23].

It is thought that (but not experimentally proven), over time, the degradation of the polymer due to PD activity across the void, can in turn cause some discharge channels to branch out from the void into a tree like structure [19]. These electrical trees gradually propagate through the material under an applied voltage and will grow to a point where they create a conducting path through the polymer and hence causes complete electrical breakdown [10]. Figure 1.5 shows an example of an electrical tree grown in a cube of poly(methyl methacrylate) (PMMA).

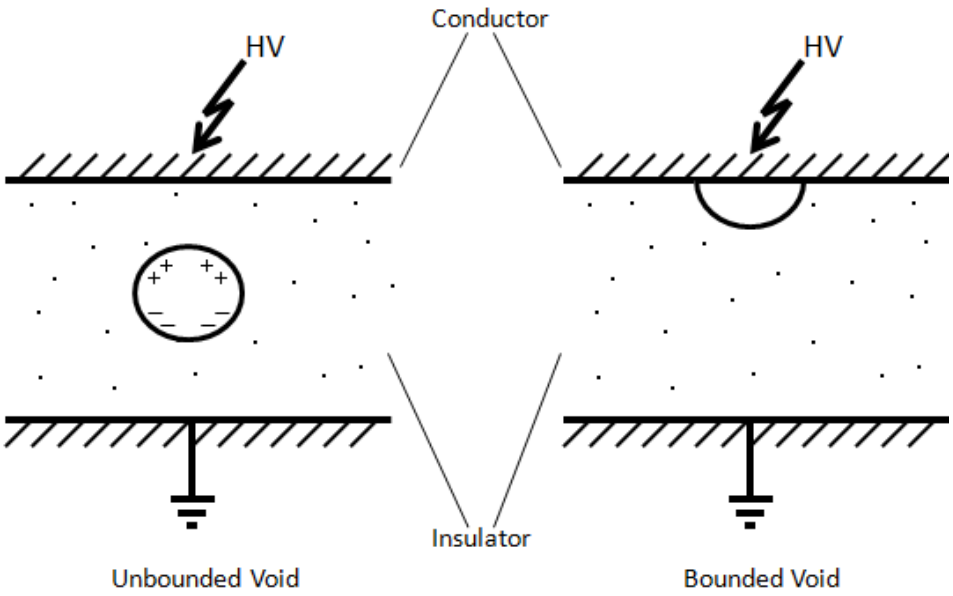

Figure 1.4: Schematic diagram showing PD activity in an unbounded void and bounded void

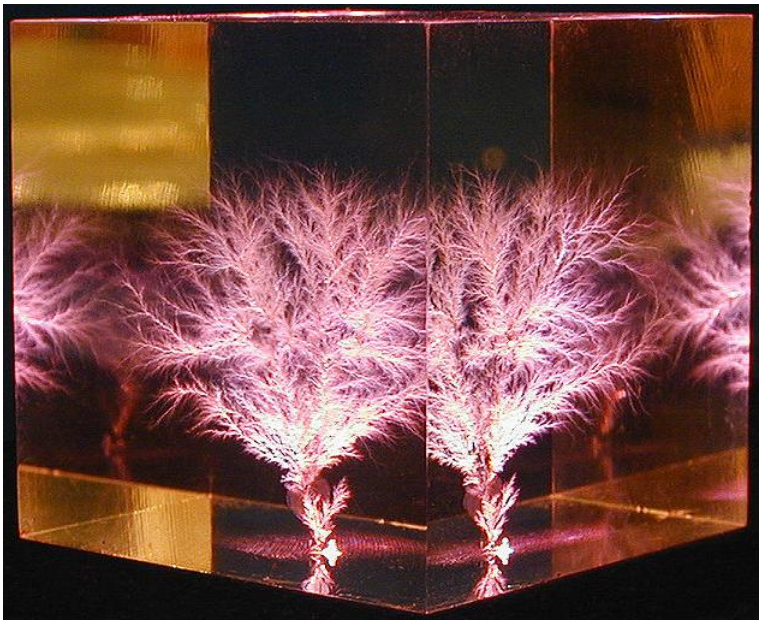

Figure 1.5: A 3D "Electrical Tree", in a cube of PMMA. Created by Berk Hickman, Stonebridge Engineering, Using a 3 MeV electron accelerator.

Electrical trees can be categorised depending on their tree pattern and basic electrical properties and include branched, bushed, stagnated, monkey puzzle and branch pine [24]. Recent work has suggested that these trees can be either conducting or non-conducting depending on the carbon content within the tree channels [25, 26].

Another type of electrical phenomenon that causes electrical ageing in polymers is termed corona discharge. According to Howatson [27], Corona discharge in air occurs when a high electric field at an electrode ionises the surrounding air. This ionisation is concentrated around the electrode and dissipates with distance from the electrode. All electrodes can create a corona but electrodes with smaller tips and sharp edges initiate at a lower voltage due to the higher electric field in these regions. The larger the radius of the curvature of the electrode the higher the voltage required to initiate and hence the corona formed will have a greater magnitude. Corona discharge occurs when an electric field excites the 'free' valence electrons (assumed to be completely detached from their ions) in the gas resulting in the electron moving in the direction of the field. These electrons may then collide with the molecules in the gas resulting in ionisation leaving a positive ion and an electron, which subsequently moves in the direction of the field and so on. After a short period of time the gas becomes filled with excited electrons and positive ions. It is this ionised gas which is the corona. If a uniform field strong enough (>33 kV cm^{-1} in air [27]), is applied between two electrodes across an air gap, the ionised gas becomes conductive and discharges between the electrodes. If an insulator is placed above one of the electrodes (such as a polymeric film) then instead of a hot localised spark there is a more defuse glow. This corona discharge (if occurring in air) produces ozone which can age a polymer if it is near the corona at the time, as is the case in electrical components such as bushings.

The exact processes involved in the electrical ageing of polymers is not clear and has attracted much research (as detailed by Tanaka in 2002 [28]) due to their importance in high voltage insulation. In order to understand the processes fully, the chemical changes involved in the ageing process must be understood. Several areas of research involve characterising the chemical changes in electrical ageing via the use of spectroscopic methods including FTIR [29], Atomic force microscopy [30], and Raman microprobe spectroscopy (RMS) [31]. RMS will be introduced below due to its excellent potential for characterising chemical changes in polymeric insulators.

Two papers in 2003 and 2006 by Liu et al and Vaughan et al respectively discuss the use of RMS in the chemical analysis of electrical trees and corona ageing in PE [31, 32]. Vaughan et al used RMS to study the differences between branched conducting trees and bush-like non conducting trees in LDPE and discovered that as well as being highly fluorescent structures the trees grown showed evidence of polyaromatic hydrocarbons in the tree channels. In 2003 Liu et al applied RMS to the analysis of corona ageing on LDPE surfaces. Despite visible damage, no chemical change was seen on the surface itself; however, analysis of deposits formed upon the HV electrode provided, evidence of carbon consistent with that found in the tree channels.

1.3 Raman Microprobe Spectroscopy

The Raman effect was discovered in the 1920's [33] yet it is only recently, with the invention and development of lasers and computation equipment, that it has been used as a spectroscopic technique. In its most basic terms, Raman spectroscopy involves using a monochromatic light source (such as a laser) to excite the molecules in a material into vibration. These vibrations are related to the molecules in question and although most of the light is scattered back elastically, a portion of it is scattered inelastically. This change in frequency/energy is indicative of each molecule, hence providing a 'fingerprint' of the molecular composition of the sample [33].

In 1928 Chandrasekhara V Raman demonstrated the Raman Effect for which he later won a Nobel Prize [33]. He realised that photons scattered inelastically from matter are characterised by a difference in energy related to the vibrational modes of the molecules in the material. This was then applied by Kohlrausch in the chemical analysis of organic compounds to produce spectra in 1931 [33]. Today Raman microscopy is a widely used technique and is readily applied to the study of polymers and dielectric materials [25].

A Raman microscope has a potential lateral resolution of ~1μm [34] and is therefore able to characterise the local chemical composition of a material. It is for this reason that it has been widely applied in the study of electrical ageing in solid dielectrics [5, 25, 31, 32]. Some studies applied the technique to electrical treeing due to its importance in polymeric HV insulation [25, 32]. However, due to inaccurate assumptions about the optical processes involved, sample damage and inadequate sample methods, the exact characterisation of the processes and chemicals involved via Raman microscopy has proved to be difficult. Raman studies of electrical trees in polymers have, however, cast doubt upon the assertions previously made about resolution [25] and, if the potential of this approach is to be realised, the true spatial origin of the detected Raman photons must be determined.

An adaptation of Raman microprobe spectroscopy is CRMS. CRMS involves placing a pinhole at the back focal plane of the objective lens such that photons originating from regions of the sample that are remote from the focal plane are strongly rejected, as demonstrated in figure 1.6. Consequently, studies of specific layers within a sample and depth profiling through a material can be achieved [34, 35]. Currently CRMS is used to study a wide variety of transparent and translucent materials including solid dielectrics and polymeric materials [36-40].

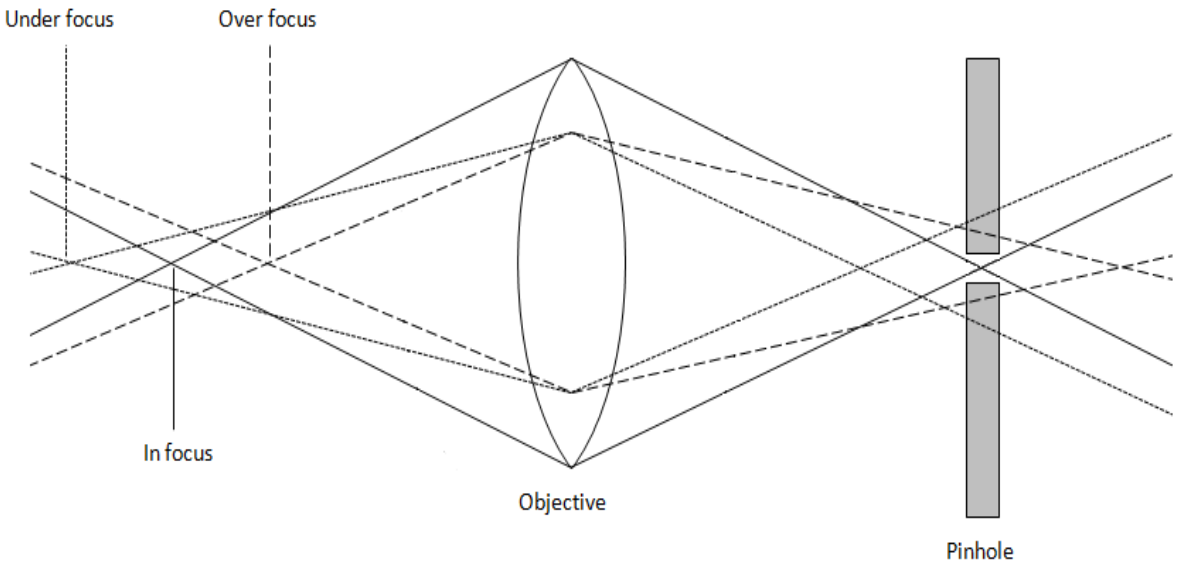

Figure 1.6: Schematic demonstrating how only in focus rays pass through a confocal pinhole

In the 2007 paper Macdonald and Vaughan, proposed a simple numerical model using a photon scattering approach [41] which attempts to predict the Raman response at various focal depths within a sample. The model was tested with samples of polyethylene and a commercial clarified propylene/ethylene copolymer Novolen 3200MC prepared in 2 different ways, and was able to account for the experimental data. Like some of the papers mentioned above, this paper, deliberately ignores refraction effects at the air sample interface and hence encounters problems. It is evident that there is a need to produce a refined model of CRMS including refraction and diffraction effects that is able to reproduce experimental depth profiles in different material systems. It is with that in mind that this study was undertaken.

1.4 Objectives

The work described in this thesis can be divided into three areas:

- To investigate the optics involved in CRMS and the effects of immersion oils on depth profiling techniques and models.
- To apply CRMS to the investigation of electrical degradation of high voltage insulation materials, specifically voids, surfaces exposed to corona discharge and electrical treeing.
- To try and replicate, in bulk, the chemical residues and by-products involved in the electrical ageing of polymeric insulators.

The initial purpose of this study is to extend the work of Macdonald and Vaughan, by eliminating refraction effects and therefore compare experiment and simulation under

more appropriate conditions. Here, in order to investigate refraction effects, the change in Raman signal at varying focal depths for samples of varying clarity and surface condition will be obtained with both air and oil immersion lenses. This will be done using an optical sectioning technique to gather depth profile data from samples of polyethylene, a clarified propylene based copolymer and polystyrene (with various surface conditions) immersed in air, silicone oil and an optical microscopy immersion oil produced by Cargille Labs. In essence, factors such as material, thickness, clarity, surface condition and the reduction of refraction by using an immersion medium will be investigated. The data collected will then be compared with the model of Macdonald and Vaughan, by matching the refractive indicies of the specimen and immersion median to test it further under conditions when the refraction effects are reduced using an oil immersion technique. As well as this, a wide selection of immersion oils will be characterised in order to determine their Raman response and their usability in the reduction of refraction effects. This work not only aims eventually to provide a model which predicts the Raman response with improved accuracy, but will also extend knowledge in the field about the effects of refraction in CRMS. It will provide the essential background knowledge in the use of CRMS as a tool for the evaluation of ageing in polymers.

The characteristics of CRMS will then be exploited such that an investigation into the processes involved in the electrical ageing of polymeric insulators is enabled. Initially, subsurface voids in polymers which have been aged by initial partial discharges will be probed with CRMS and the chemistry of the ageing explained. Voids in PE created chemically and by layering sheets of LDPE will be analysed both laterally and vertically in order to identify how the chemical composition of the polymer changes throughout the samples and voids.

Once the capability of CRMS in the analysis of surface and subsurface ageing features in polymers has been assessed, it will be applied to look at other ageing phenomena namely, electrical treeing. CRMS will be used to probe electrical treeing channels grown in polydimethyl siloxane and epoxy resin. The growth characteristics of electrical trees in these samples will be analysed using various comparative spectroscopic methods. CRMS will enable the chemical composition of the electrical tree and breakdown channels to be determined and compared to previously published work based on PE. This analysis will enable the processes involved in electrical treeing to be determined and a link with electrical ageing in voids to be made.

Finally this work will then be compared with other results obtained from samples aged via corona discharge. By analysing a wide range of materials, chemical comparisons

can be obtained and a wider understanding of electrical ageing processes obtained. This study aims to repeat and extend the work of Liu, Vaughan and Chen to include an analysis of various polymers aged via corona discharge in air and in an inert atmosphere. This study aims to provide a novel method to reproduce, in bulk, the chemical by-products that are formed during electrical ageing such that other analytical methods can be applied and the understanding of electrical ageing in polymeric insulators increased.

Throughout this study, the results obtained via CRMS of the electrically aged polymers will be reinforced by an optical and spectroscopic analysis obtained by SEM and FTIR. These methods will enable a comparison to be made to CRMS and its effectiveness in the analysis of the samples in this study assessed.

This study will follow the following format:

Chapter 1 – Introduction: A basic introduction into polymers, electrical ageing and the Raman microprobe spectroscopy. An outline of the aims and objectives of the study will be provided.

Chapter 2 - Experimental: Details on the materials and methods used in this study and information on how the samples were characterised alongside the un-aged characteristics of the samples used in this study.

Chapter 3 – Optical Depth Profiling: Theory, experimental procedure, results and discussion of the work involving investigating the use of CRMS and its application in optical depth profiling. An attempt will be made to model the predicted depth profiles obtained from polymers and the results discussed in relation to previously published work.

Chapter 4 – Void Analysis: Theory, experimental procedure, results and discussion of the application of CRMS in the analysis of electrically aged voids in PE. Results will be discussed to in the context published data and complimentary results obtained via FTIR and SEM analysis.

Chapter 5 – Electrical Treeing: Theory, experimental procedure, results and discussion of the application of CRMS in the analysis of electrical trees and breakdown channels in silicone rubber and epoxy resin. Results will be related to previously published data and results obtained via FTIR and SEM analysis.

Chapter 6 – Corona Discharge: Theory, experimental procedure, results and discussion of the application of CRMS in the analysis of the effects of corona ageing of polymeric systems under a variety of electrical ageing conditions. Following this a novel approach to replicating the chemical by-products of electrical ageing will be suggested and applied. Results will be compared to those obtained via FTIR and SEM analysis.

Chapter 7 – Conclusion and Future work: A summary of the study and the conclusions drawn as well as an indication of how this work could be developed in the future.

2 : Experimental

This chapter provides details of the materials and selection rational used throughout this study. It also discusses the experimental setups of the characterisation methods used to analyse the samples in various chapters of this study. These methods include CRMS, FTIR, SEM and optical microscopy.

2.1 Materials

A wide range of polymers have been examined during the course of this study as described below. Sample preparation procedures that relate to specific studies are given in the chapters that follow.

2.1.1 Polyethylene (PE)

Polyethylene (PE) is a thermoplastic polymer that is widely used in high voltage (HV) cable insulation. The following types of PE were used in this study:

- Low density polyethylene (LDPE)
- A blend of high density polyethylene (HDPE) and LDPE
- Cross linked polyethylene (XLPE)

LDPE and HDPE are both semi-crystalline in nature but the branches found in LDPE mean that it is more amorphous in nature than HDPE as the branches prevent the long molecular chains from forming ordered structures. XLPE contains cross-links between neighbouring PE chains, an effect that was originally achieved by cross-linking LDPE with dicumyl peroxide (DCP) in 1955 [42]. PE was chosen due to its electrical properties and wide application in HV insulation systems. Figure 2.1 shows a representation of the repeat unit of PE.

A blend of LDPE and HDPE was used in chapter 3 where the LDPE was supplied by Exxon and the HDPE was supplied by Rigidex. The LDPE and XLPE sheets used in chapter 4 were provided by the University of Bologna. The LDPE in chapter 6 was supplied by Goodfellow.

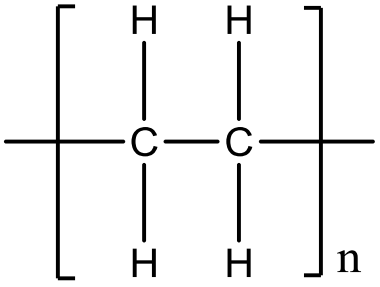

Figure 2.1: Representation of the chemical structure of PE

2.1.2 Polystyrene (PS)

Polystyrene (PS) is an amorphous glassy polymer at room temperature which is optically transparent and has good electrical properties. PS is very brittle at room temperature and was chosen due to the benzene ring in the monomer. This benzene ring leads to a higher ratio of carbon to hydrogen atoms and an increased aromatic character when compared to PE. By investigating the relationship between the amount of carbon in the polymer matrix, the production of volatiles, and carbon residue during ageing, a deeper understanding on the electrical degradation of the polymers in question will be enabled. Figure 2.2 shows a representation of the repeat unit of PS. PS is used in chapters 3, 5 and 6 of this study and was supplied by Sigma Aldrich.

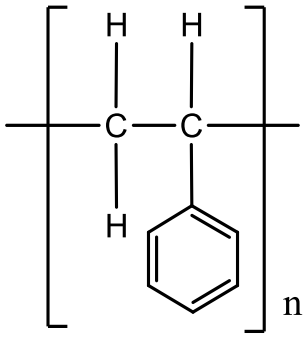

Figure 2.2: Representation of the chemical structure of PS

2.1.3 Novolen 3200MC (BASF)

Novolen is the trade name of a number of semi-crystalline propylene/ethane copolymers produced by BASF. Novolen 3200MC is one such material and it contains 0.3% dibenzylidene sorbitol derivative in order to improve optical clarity and was chosen to be used in chapter 3 as a comparison to PS and PE due to its optical properties [43]. Figure 2.3 shows the two co-monomers that form Novolen 3200MC

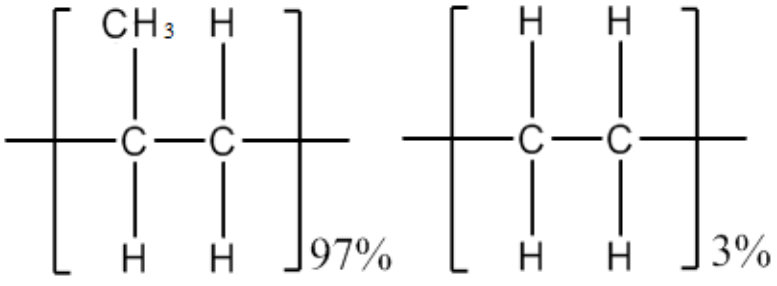

Figure 2.3: Representation of the chemical structure of Novolen formed of 97% propylene and 3% ethylene [43].

2.1.4 Polyether ether ketone (PEEK)

PEEK is a semi-crystalline polymer that has very good thermal stability and high resistance to mechanical, chemical and thermal degradation/deformation. It was selected due to its highly aromatic structure and a much higher ratio of carbon to hydrogen atoms when compared to the other polymers in this study. PEEK will not be used for any of the depth profiling investigations however, as it is opaque. The PEEK samples were supplied by Direct Plastics Online and were used in chapter 6. Figure 2.4 shows a representation of the repeat unit of PEEK.

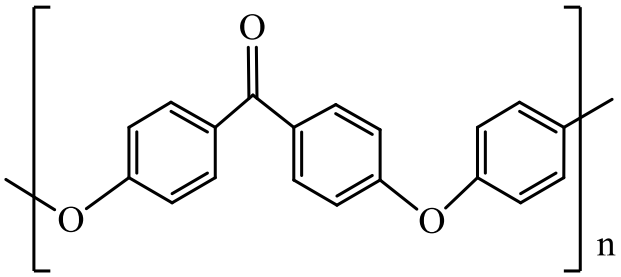

Figure 2.4: Representation of the chemical structure of PEEK

2.1.5 Epoxy Resin

The epoxy resin is used in this study employed the resin DER 332 and the polyetheramine hardener Jeffamine D230, which is a difunctional, primary amine with an average molecular weight of 230. Resin and hardener were mixed at a ratio of 1000:344 respectively and cured at 100 °C for 4 hours. It is a brittle and transparent material that was chosen due to its highly aromatic structure, insulating properties and wide use in electrical and mechanical applications. The resin and hardener were supplied by Sigma and Huntsman respectively and the cured resin was used in chapters 5 and 6. Figure 2.5 shows a representation of the repeat unit of DER 332 resin and D-230 hardener. During curing the oxirane ring at the end of the resin chain reacts with the amine in the hardener to form a link between the two molecules and allowing a chain to be formed.

2.1.6 Polydimethylsiloxane (PDMS)

Polydimethylsiloxane (PDMS(E)), where E stands for elastomer, is a silicone based non reactive, stable elastomer resistant to temperatures ranging from -55 °C to 300 °C once cured. PDMS(E) is a soft rubber-like material easily moulded into shape and often used in electrical systems due to its good electrical properties. It was chosen due to its siloxane backbone, as a comparator (chapters 5 and 6) to the aliphatic polymers in this study (i.e. PE). It was supplied by Dow Corning and is used in chapters 5 and 6. Figure 2.6 shows a representation of the repeat unit of PDMS.

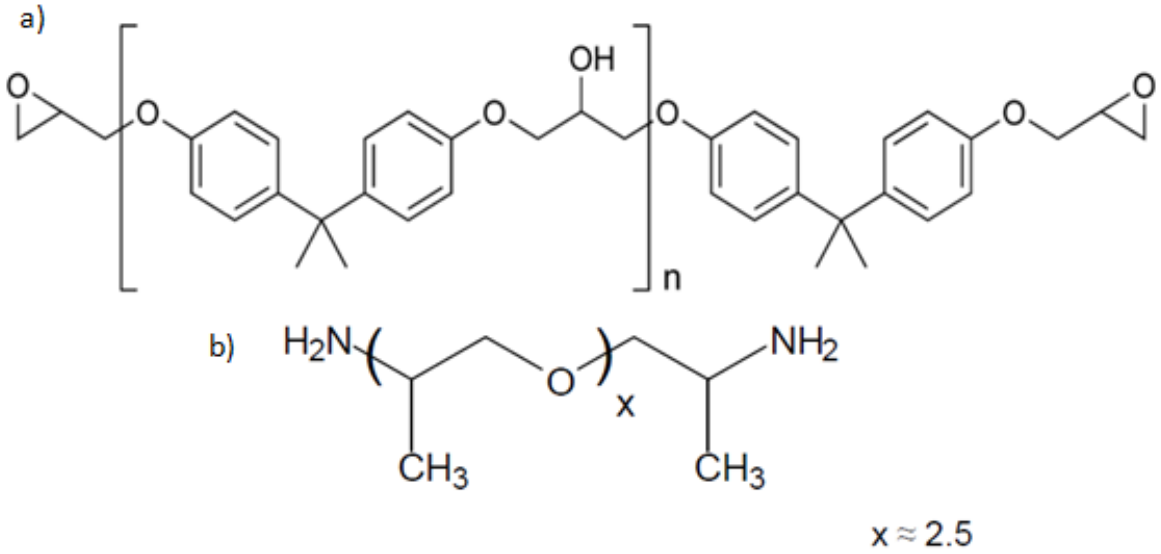

Figure 2.5: Representation of the chemical structure of a) DER 332 resin and b) D-230 Jeffamine hardener

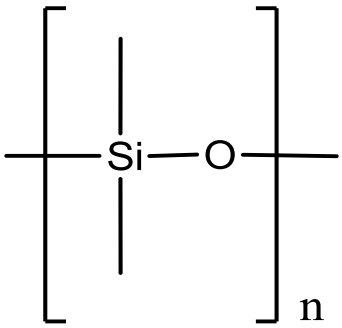

Figure 2.6: Representation of the chemical structure of PDMS

2.2 Methods

2.2.1 RMS

If monochromatic light is incident on a material, then the majority of photons [44] are scattered elastically with no change in energy or wavelength. This follows the relationship $I \propto \lambda^{-4}$ for Rayleigh scattering where I is the intensity of the light and λ is its wavelength [44]. The remaining light can then either be scattered via Brillouin or Raman scattering. Brillouin scattering occurs in transparent solids when light is scattered by lattice vibrations and it typically shifts the light by 0.1 to 1 cm^{-1}. Raman scattering, however, is a result of the scattering of light by molecular vibrations causing a shift in the wavelength of the incident light. Raman scattering is very weak and only accounts for ~10^{-7} of all the light that is scattered [45].

The Raman effect can be described both classically and using a quantum mechanical model. The quantum mechanical model shows that when light interacts with a molecule, a change in vibrational state occurs and hence, when the molecules relax into the same vibrational state there is no shift in photon energy. This is called Rayleigh scattering. When the molecule relaxes back into a lower vibrational state that differs from the excited virtual state N_v, a shift in photon energy/frequency occurs. If the molecules relax into a higher vibrational state than it originally resided prior to excitation, then the resulting photon will be shifted to a lower frequency. This is an effect termed Stokes Raman scattering. If the molecule is already in an excited state and then relaxes into a lower vibrational state the process is termed anti-Stokes Raman scattering [46]. The corresponding frequency/energy shifts are characteristic of the bonds in the molecules of a material, thus allowing the molecular composition of a sample to be determined by detecting these shifts [47]. This quantum mechanical description of the Raman effect is demonstrated schematically in figure 2.7.

Alternatively, from a classical perspective, if electromagnetic radiation incident on a material, then its electric vector ($\bar{E}$) interacts with the molecules in a sample and induces a dipole moment (μ) equal to the polarisability (α) multiplied by $\bar{E}$ of the incident radiation. If there is a change in magnitude of the induced dipole moment, then the light is Raman scattered with a magnitude determined by, α, the polarisability. Molecular vibrations occur at characteristic frequencies and hence produce changes in polarisability and induce an electric dipole which is frequency dependant.

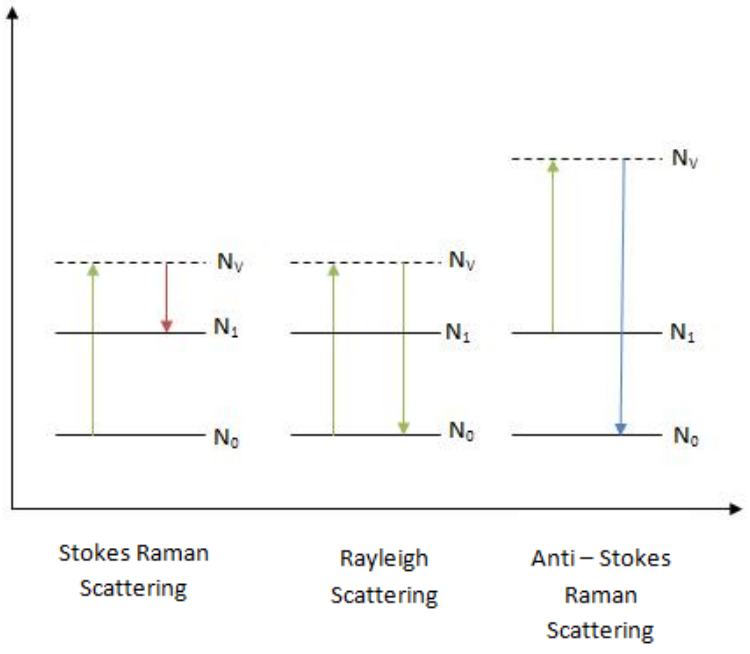

Figure 2.7: Quantum mechanical representation of photons being scattered elastically and in-elastically according to Rayleigh and stokes laws

The dipole induced can be represented by the following equation:

$$P = \alpha E_0 \cos 2\pi v_i t + \frac{1}{2}\left(\frac{\delta\alpha}{\delta q}\right)_0 q_0 E_0 [\cos\{2\pi(v_i + v_v)t\} + \cos\{2\pi(v_i - v_v)t\}] \quad (1)$$

The first term corresponds to the Rayleigh scattered light and the second term indicates how the dipole moment changes with frequency and that the change in polarisability is associated with the vibration in the molecule, $(\delta\alpha/\delta q)_0$. This means that the scattered radiation will contain 3 different frequencies; the incident frequency (ν_i), Stokes radiation ($\nu_i - \nu_v$) and anti Stokes radiation ($\nu_i + \nu_v$). An example of a spectrum showing Stokes, anti Stokes and Rayleigh scattering can be seen in figure 2.8. Due to the upper energy states having a lower equivalent population, at thermal equilibrium, the number of photons related to Stokes radiation is greater than those related to anti Stokes radiation. As the intensity of the photons is related to their initial state of the material, this results in spectral peaks with a higher intensity. For this reason it is the Stokes region of the spectrum that is conventionally used in Raman spectroscopy.

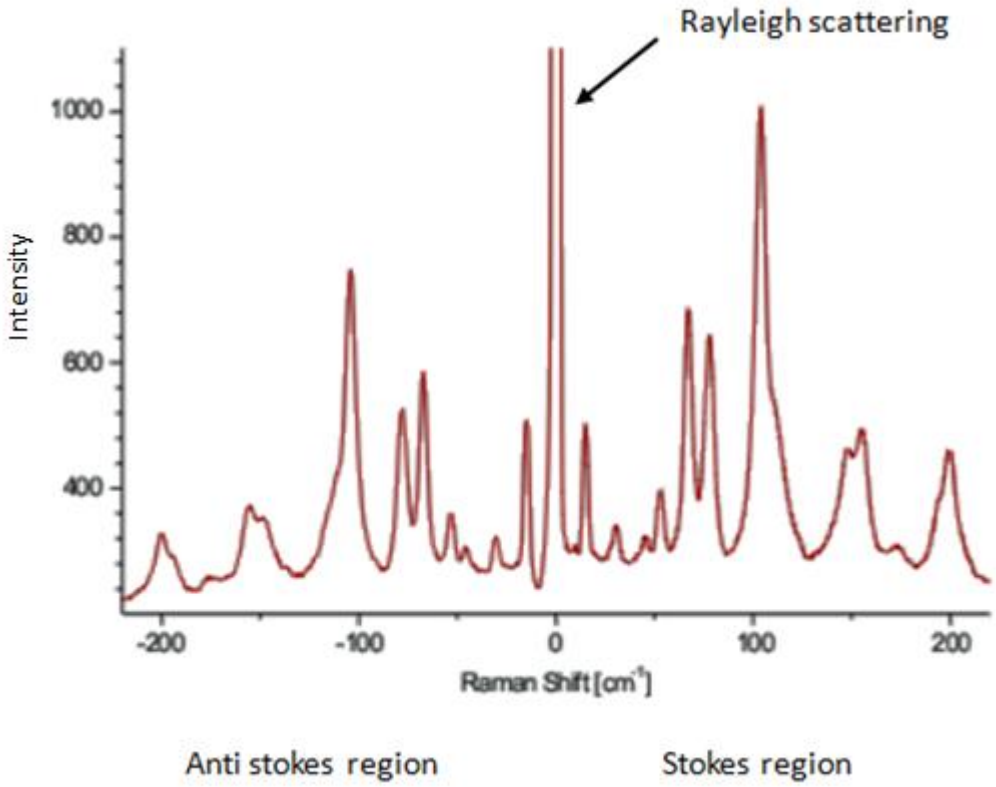

Figure 2.8: An example of the complete Raman spectrum showing anti stokes radiation, Rayleigh scattering and stokes radiation

Currently CRMS is used to study a wide variety of transparent and translucent materials including solid dielectrics and polymeric materials. A full description and literature review of CRMS can be found in Chapter 3. Raman microscopy uses visible light and as such involves relatively short wavelengths and has a low absorption when compared to other methods such as FTIR. CRMS has several advantages as follows:

- It can be used in situ
- No sample preparation is needed
- It is non destructive compared to many other analytical methods such as x-ray diffraction or electron microscopy as sample preparation is not needed.

To name a few examples, Raman spectroscopy can be used to study solids [34], liquids [48], powders [49], and gels [50]. The system is relatively portable and so can be used to study objects which cannot be moved for whatever reason (such as the prehistoric paintings from the Los Murciélagos cave (Spain) [51]). CRMS has been chosen as the main analysis method in this study for the reasons detailed above, namely the advantage of high spatial resolution that confocality provides.

One downside to using Raman spectroscopy is that the Raman spectrum may be disguised by a fluorescent background. Fluorescence, although often associated with Raman spectroscopy, is not a Raman effect as it involves the absorption of photons rather than their scattering [52]. Electromagnetic radiation of a precise wavelength is absorbed exciting the molecules from a ground electronic state into an upper electronic energy level. This excited molecule then relaxes into the ground state by emitting a photon with an energy (and frequency) corresponding to the energy difference between the ground and excited state. The difference between photons emitted by fluorescence and by Raman scattering is that in fluorescence, they occur at a resonant frequency whereas in Raman scattering they occur for all frequencies of the incident light. The emitted fluorescent photons are detected and contribute to the Raman spectrum often completely obscuring the Raman peaks as the fluorescence spectrum is much stronger and broader than the Raman spectrum. Fluorescence is common in organic and impure inorganic molecules.

Studies have investigated a number of ways of overcoming the problem of fluorescence but the two most successful ones are using a laser with a different excitation wavelength [53], and photo bleaching [54]. These two methods, however, are not always easily applied. By changing the excitation wavelength, a non resonant frequency can be used thus reducing the number of molecules excited via absorption. This method however involves using a laser of a different wavelength to the one causing fluorescence hence costing large sums of money for the laser and mount.

Photo bleaching is a much cheaper method of overcoming the problem of fluorescence but it involves leaving the laser focused on the sample for an extended period of time before a spectrum is obtained, thus allowing the excted molecules sufficient time to relax back into a ground state. With some samples however, photo bleaching can cause localised thermal damage to the sample in question.

2.2.2 Characterization of samples using RMS

All data in this thesis was collected with a Leica microscope coupled to a Renishaw Raman RM1000 system with a 785 nm CW diode laser of power 25 mW. The instrument has a Peltier cooled charged coupled device (CCD) detector. There is a holographic grating of 1800 grooves/mm to disperse the scattered radiation by wavelength and a holographic (notch) filter prevents back scattered (Rayleigh) radiation from entering the detector.

The spectrometer was set up in confocal mode, with a slit width of 15 μm and a CCD area of 4 pixels (image height) x 574 pixels (spectrometer range) which, in conjunction with the mechanical slit, acts as a virtual confocal pinhole. This configuration was used for the majority of the work described in this report. The spectrometer, when used in non confocal mode, was set to a slit width of 50 μm and CCD area of 20 x 574 pixels. These settings are in line with Renishaw's recommendations for confocal and non-confocal operation. All spectra were processed using SigmaPlot 10 and Wire 3 software. All spectra in this study were acquired using a Leica x50 (numerical aperture 0.75) air objective lens or a Leica x50 (numerical aperture 0.90) immersion objective lens.

With the exception of depth profiling, all spectra were obtained using an extended scan between 3500 cm^{-1} and 100 cm^{-1} and were built up of the accumulation of 25 scans of 10 s. For depth profiles, the main peaks were identified using extended scans, and then a static scan was used over a range of 500 cm^{-1} centred over the main peaks in the spectrum. These static scans were built up of 10 scans of 10 s and were used in order to minimise the time it takes to collect the data for depth profiles. For all spectra, the cosmic ray removal function and a laser power of 100% were used unless stated otherwise.

2.2.3 Raman spectra of materials

Figures 2.9 – 2.14 show typical Raman spectra of all the pure un-aged solid polymer samples listed in section 2.1.1. with some of the key peeks indicated. Table 2.1 identifies all of the key peaks (as identified in previous literature) in these spectra and the bonds within the samples from which they originate.

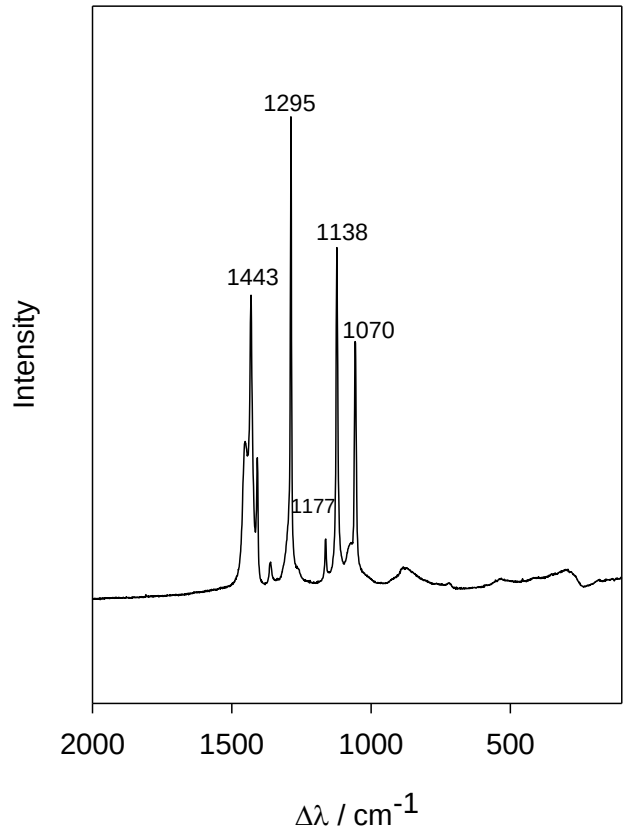

Figure 2.9: Raman spectrum of PE

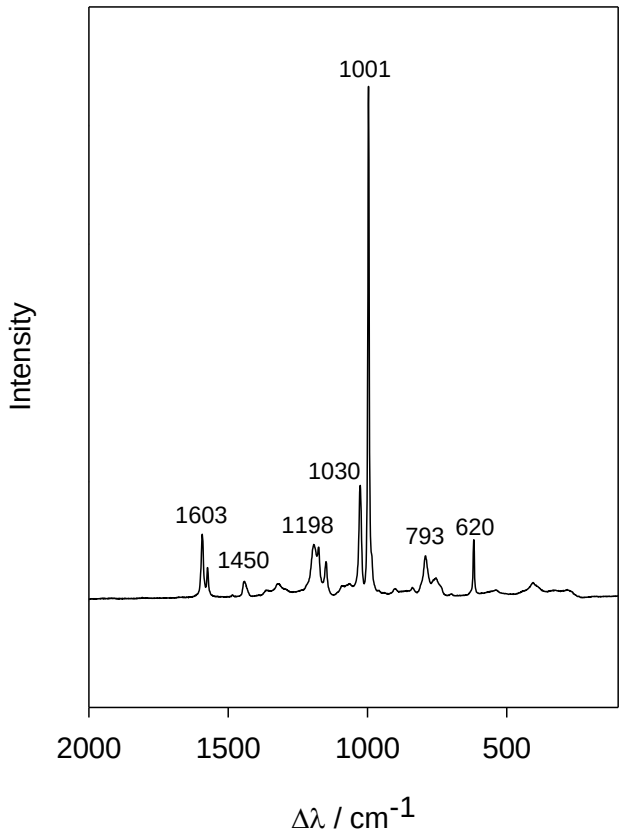

Figure 2.10: Raman spectrum of PS

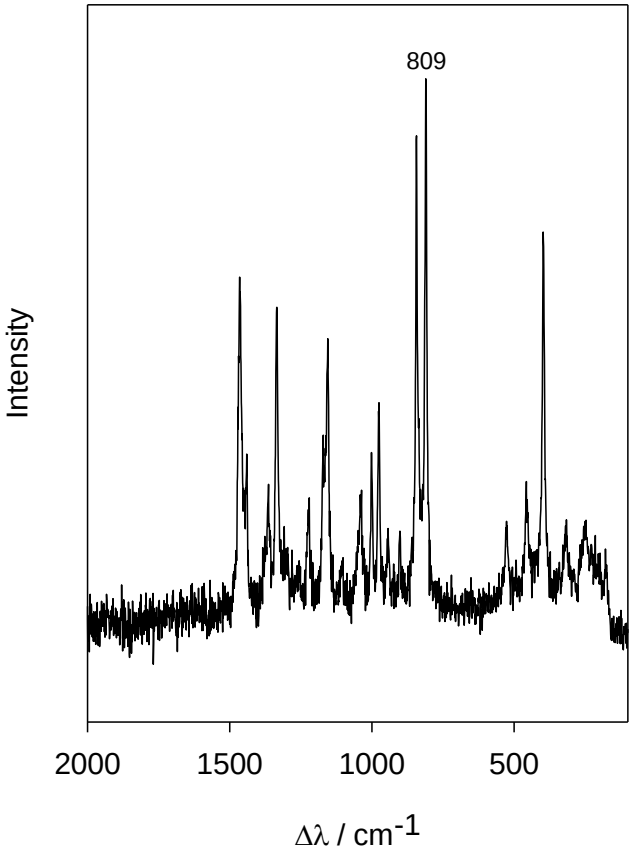

Figure 2.11: Raman spectrum of Novolen

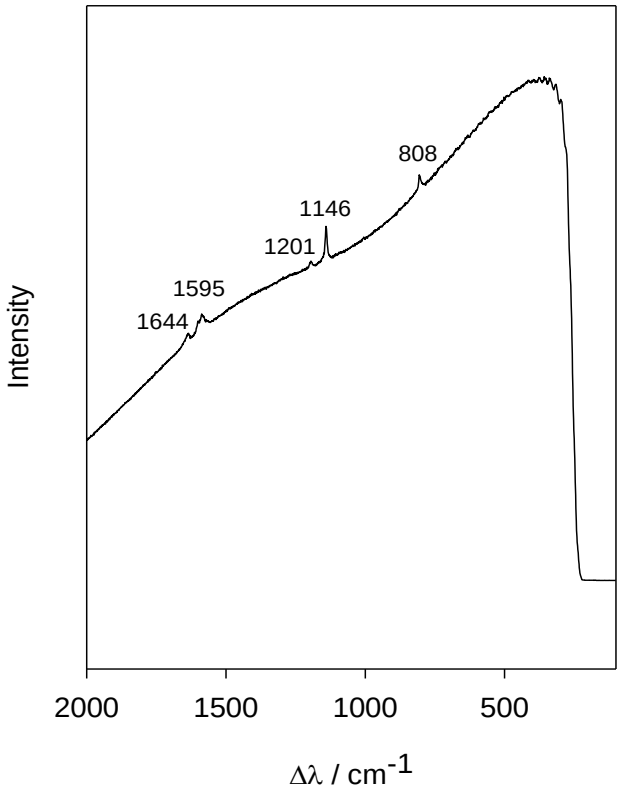

Figure 2.12: Raman spectrum of PEEK

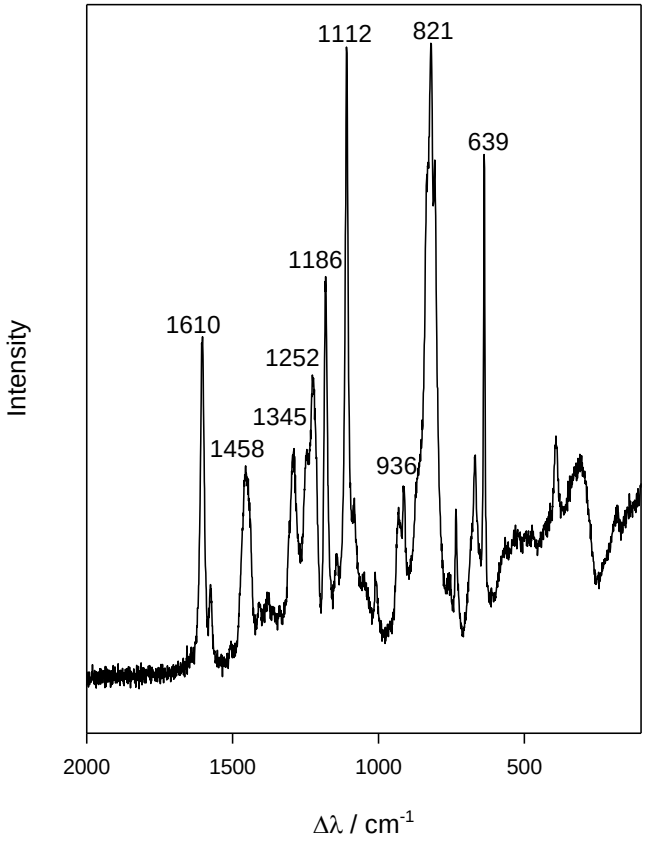

Figure 2.13: Raman spectrum of the chosen epoxy resin

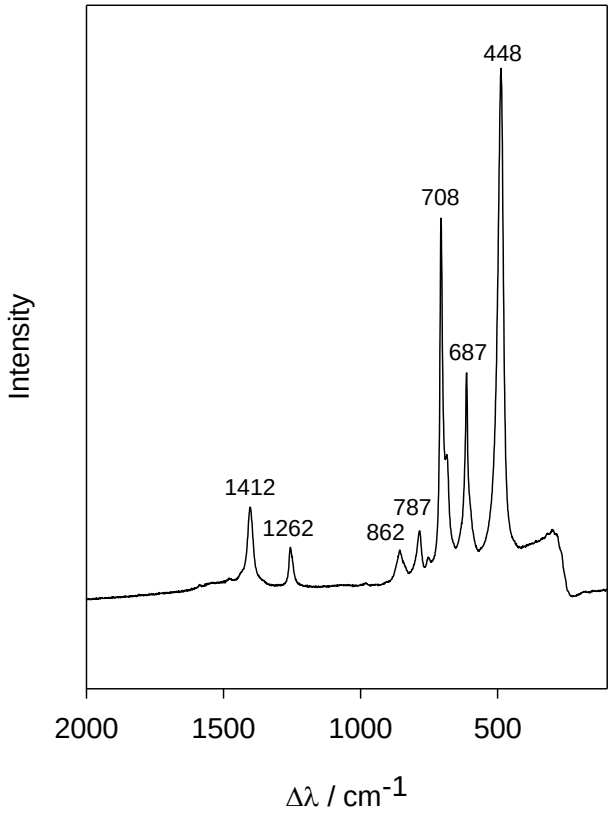

Figure 2.14: Raman spectrum of PDMS(E)

Table 2.1: Key Raman spectral peaks identified in samples used.

Polymer	*Peak/ cm^{-1}*	*Vibrational Mode**	*Reference*
PE	1070	ν C-C	[55]
	1138	ν C-C	
	1177	R CH_2	
	1295	T CH_2	
	1372	W CH_2	
	1420	β CH_2	
	1443	β CH_2	
	1464	R CH_2	
PDMS	448	ν Si-O-Si	[56]
	687	R Si-CH_3	
	708	ν Si-C	
	787	R CH_3 , ν Si-C	
	862	R CH_3	
	1262	β CH_3	
	1412	γ CH_3	
PS	537	ϕ C-C-C	[57, 58]
	620	α C-C-C	
	760	γ C-H	
	793	α C-C-C	
	905	γ C-H	
	1001	ν C-C	
	1030	β C-H	
	1070	ν C=H	
	1097	β C-H	
	1156	β C-H	
	1183	β C-H	
	1198	ν C-X	
	1330	ϕ C-H, ϕ C-C-C	
	1450	ν C-C	
	1494	ν C-C	
	1585	ν C-C	
	1603	ν C-C	

PEEK	*808*	*γ C-H*	*[59]*
	1146	δ C-CO-C	
	1201	ν (ϕ-O)	
	1595	ν C-C	
	1644	ν C=O	
Epoxy Resin	639	γ Epoxy	[60]
	736	α Epoxy	
	821	W C-H	
	916	γ Epoxy	
	936	W C-H	
	1012	ν aromatic ring	
	1031	ν C –O	
	1112	α Epoxy	
	1186	W C-H	
	1252	Epoxy ring breathing	
	1345	β CH_3	
	1458	δ CH_2	
	1580	ν aromatic ring	
	1610	ν aromatic ring	
Novolen	809	ν CH_2	[61]

$*$ ν - stretch, β – in plane bend, α - in plane ring def, γ – out of plane bend, ϕ – out of plane ring deformation, δ - deformation, X – a substitutent (vinyl or polymer), R – rocking, W – wagging and T - torsion

2.2.4 Fourier Transform Infra Red (FTIR)

Infra red (IR) spectroscopy is an absorption spectroscopy that uses electromagnetic radiation in the IR part of the spectrum ($0.78\ \mu m < \lambda < 1000\ \mu m$). If IR radiation is passed through a sample, a fraction of it is absorbed by the molecules in the sample at specific characteristic frequencies of the molecular structure. Determination of the frequencies which have been absorbed allows a spectrum to be produced of the energy (or intensity) of the absorbed radiation as a function of frequency. The frequencies absorbed by the molecules correspond to the vibrational frequencies of specific bonds or vibrational group of atoms. For a molecule to be vibrationally active in the IR spectrum there must be a fluctuation in dipole moment when it absorbs energy.

The number of vibrational modes of a molecule is dependent on the number of atoms (N) and their molecular configuration. A single atom has only 3 degrees of freedom relating to its translational motion and as such is not IR active. Simple and

symmetrical diatomic molecules (such as O_2) are not IR active as they only have one bond and thus does not create a fluctuation in dipole moment when it absorbs energy. Asymmetrical diatomic molecules such as CO, however, do absorb in the IR spectrum [62]. For molecules with N atoms, the number of vibrational modes is given by 3N-5 for linear molecules and 3N-6 for non linear molecules such as water and most organic compounds [62]. Some examples of vibrations which lead to vibrational modes (and hence IR energy absorption) include symmetrical and asymmetrical stretching, scissoring, rocking, twisting and wagging as shown in figure 2.15.

Originally, IR spectrometers were based upon a dispersive grating which separated out all the frequencies emitted by the IR source. The resulting spectrum is then a plot of the fraction of the incident energy that has passed through the sample (intensity) for each frequency [63]. This method was relatively slow and has since been replaced by the methods used in FTIR. In FTIR an IR source containing all frequencies of the IR spectrum is used in conjunction with a Michelson interferometer as shown in figure 2.16 [62]. Here the IR source is collimated and directed to a beam splitter which divides the beam such that approximately half is reflected off of a flat mirror of fixed position and the other half is reflected off of another flat mirror that is allowed to move by a few millimetres. This movement in one of the mirrors generates a mismatch in path length when the two sources are recombined resulting in an interference pattern when the recombined beam is directed towards the sample. The resulting detected signal has information about every IR frequency from the source and by

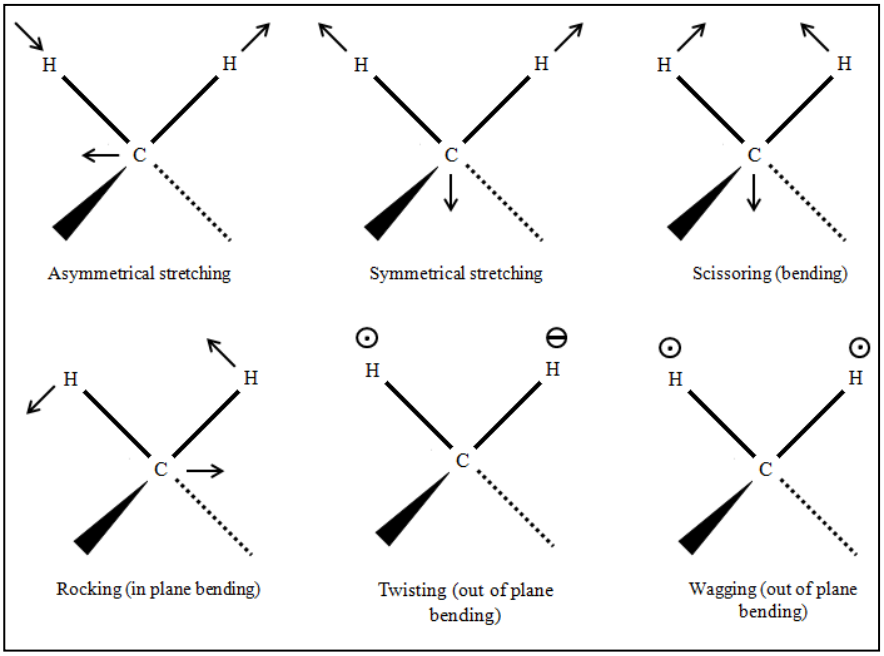

Figure 2.15: Examples of vibrational modes in a non linear molecule such as CH2 (and mean a movement out of and into the plane of the paper respectively)

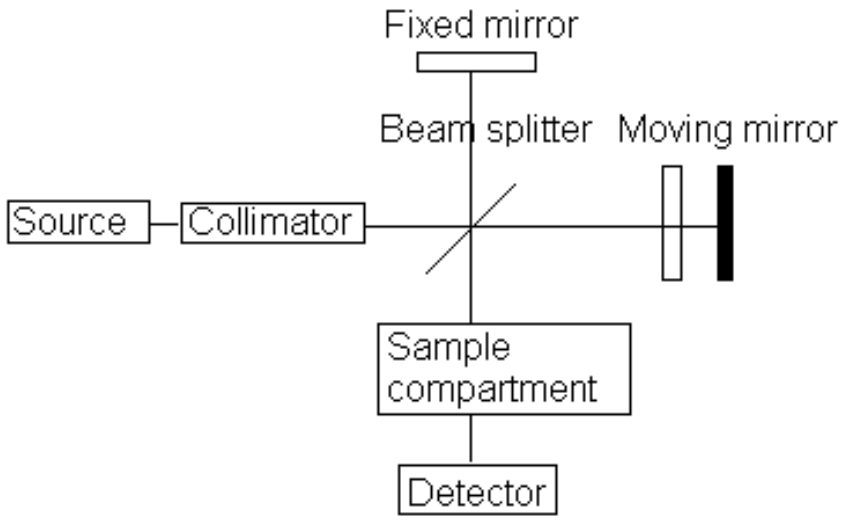

Figure 2.16: Simple schematic of a Michelson interferometer

constantly moving the mirror a plot can be made of this signal with respect to mirror position. A simple Fourier transform is then applied to this data and the spectral absorption data for every frequency and hence wavelength can be produced. By using this method, all frequencies are being measured simultaneously rather than sequentially as with the dispersive method. This enables a much faster sampling time in the order of seconds rather than minutes.

FTIR is widely used in the field of analytical chemistry and has enabled the fast and accurate identification of all types of organic as well as many inorganic compounds [64, 65]. It is a non-destructive method (in that it does not cause any damage to the sample or molecules being analysed) that can determine the molecular composition of materials and surfaces. FTIR has widely been applied to the identification of polymers [66, 67], the molecular orientation in polymer films [68] and the analysis of formulations such as copolymers [69].

FTIR is often used in conjunction with other spectroscopic techniques such as nuclear magnetic resonance spectroscopy [69, 70], mass spectrometry [71] and not least Raman spectroscopy [72]. This is because although FTIR can provide very useful molecular data about a sample, in general, minimal elemental data is provided. In addition, despite it being an inherently non-destructive technique, the samples being analysed must be relatively transparent to IR radiation and so an amount of sample preparation is usually needed. Therefore, the method cannot be used in situ in its most basic form. A modern adaptation of FTIR, however, involving a microscope allows the surfaces of samples to be analysed (providing they are not completely IR

radiation absorbing) thus allowing the method to be non-destructive and used in situ. Finally FTIR will only provide information about molecules that are active in the IR spectrum.

For these reasons FTIR is often used in conjunction with Raman spectroscopy [72] which allows a similar chemical analysis of samples to be performed in situ and allows samples that were previously inappropriate for FTIR analysis to be investigated. In addition, the two methods are complementary to each other as Raman spectroscopy can provide information about vibrational modes that are not IR active and vice versa. FTIR is also not affected by fluorescence (unlike Raman spectra) as the wavelength of the exciting source is much smaller. As well as this, FTIR interferometers are much more sensitive and can detect substances with a much lower concentration when compared to the sensitivity of RMS. One downside to FTIR is that its spatial resolution is inferior to Raman spectroscopy. Even when used in conjunction with a microscope, FTIR averages over an area of approximately 100 μm^2 instead of the 2 μm^2 that RMS can provide.

FTIR has been chosen for use in this study to provide data that are comparative and complimentary to the data obtained using Raman spectroscopy. The aim of this comparison is to hopefully obtain a deeper understanding of the samples in question and assess the ability of CRMS to analyse electrical aging in high voltage insulators.

2.2.5 Characterisation of samples using FTIR

FTIR spectra were obtained using a Perkin Elmer Spectrum GX instrument coupled with an AutoIMAGE FTIR microscope and a liquid nitrogen cooled MCT high sensitivity photo detector. Thin samples were mounted upon a gold coated slide and analysed in reflection mode such that the incident beam is transmitted through the sample and reflected off of the glass slide. Data was obtained using an accumulation of 30 scans of 1s each to reduce the signal to noise ratio and a sampling area of 100 μm^2 over a range of 500 – 4000 cm^{-1}.

2.2.6 Scanning Electron Microscopy (SEM)

SEM enables the imaging of samples on a microscopic scale via the use of a high energy electron beam. Typically, electrons are thermionically emitted from an electron gun with a tungsten filament cathode (although Lanthanum Hexaboride (LaB_6) and field emission methods are becoming increasingly more common) and are directed towards the sample. This beam then interacts with the atoms in the sample surface and generates various emissions that are incident on the detectors. Different types of signal can be produced by emissions which includes secondary electrons, back scattered emission, X-rays and light. Secondary electrons are generated as ionization

products of the electron beam (which has an energy greater than the ionization potential) exciting the atoms in the sample and, although a machine may have multiple detectors to detect more than one signal, secondary electrons are most commonly employed in SEM. The electron beam is moved across the sample in a 'raster' pattern. The secondary electrons are then detected and the signal is displayed as an image of varying brightness relating to the intensity of the signal emitted from each point. This results in images with a large depth of field where surfaces further away from the detector appear darker and the surfaces closer to the detector are brighter due to a greater number of secondary electrons being detected [73].

SEM imaging is a useful tool in the analysis of electrically aged polymeric insulators as it allows high magnification images (in far greater detail than possible with optical microscopy) of the areas of interest on the sample, such as areas of electrical degradation. The magnification can range from x10 to x500,000 [74] and the resolution between less than 1 and 20 nm depending on the specification of the SEM instrumentation. One limitation to SEM imaging is that it is surface specific and cannot be used to probe areas that are below the surface of a transparent sample. The only way to image sub surface features via SEM imaging is to expose the surface of these features using methods such as microtomy.

Another limitation with SEM is that the surface of the sample can become charged due to the incident electrons, which becomes increasingly problematic the more non-conductive a sample is. This results in image distortion. The different types of charging include general (across the whole surface), edge (on high or isolated features), area (in various areas across the sample), line by line (causing bright streaks across the image) and residual charging (from the previous scan). These effects can be minimized, and the optimum image obtained, by balancing the incoming beam electrons to the outgoing sample electrons by changing the parameters such as accelerating voltage and spot size and by performing the imaging in a vacuum with samples that are coated in a conductive layer.

Typically samples are sputter coated with gold (although other metals can be used depending on the sample) [75] in order to make the surface of the sample electrically conductive and earthed so that electrostatic charge does not accumulate. A modern adaptation of SEM is field emission gun SEM (FEG-SEM) [76] which uses an electron gun that generates a sufficient potential gradient to cause field electron emission. The resulting electron beam is smaller in diameter than conventional methods mentioned earlier, thus resulting in an improved signal to noise ration and spatial resolution. Another adaptation of SEM is environmental SEM (ESEM), which although operates in a

similar way to SEM, allows images to be obtained from 'wet' or uncoated samples due to a gaseous environment within the sample chamber to disperse the charge [77]. This is particularly beneficial for biological specimens which might be damaged by the sputter coating process. Many adaptations to SEM imaging are available and it is often used in conjunction with another analytical methods (such as x-ray microanalysis) [73, 78]. However, in this study only the imaging capabilities have been applied and a description of alternative methods has therefore not been included here.

2.2.7 Characterisation of samples using SEM

SEM images were obtained using a JEOL JSM 5910 SEM instrument on a number of samples throughout the study. Once the samples were prepared and fixed onto SEM stubs and sputter coated with gold they were inserted into the imaging chamber and placed under a vacuum of 2×10^{-5} mbar. An accelerating voltage of 15 kV and a spot size of 5.0 nm were used to capture the images in this study. These parameters were chosen such that clear images could be obtained efficiently and without over charging the sample.

2.2.8 Optical Microscopy

Optical microscopy uses light in the visible range to image samples. The use of optical microscopes does not allow the identification of chemical composition as with CRMS and FTIR. It can however, be a useful tool in the identification of surface features related to the basic morphology of polymers if the magnification is high enough [79]. As well as this, although it cannot image samples at the same magnifications as SEM, it does enable the changes in colour and contrast of the areas in question to be determined which aids the understanding of the changes in chemical composition. In this study, optical microscopy was used to image the samples to identify any key features of potential interest thus providing a guideline for a more focused approach to the Raman analysis. The images provided in this study also aid the descriptions of the samples and methods used throughout.

2.2.9 Characterisation of samples using Optical Microscopy

A Leitz Aristomet optical microscope with Leitzlar objectives (of values x50, x100, x200 and x500) was used to obtain the optical micrographs of the samples used in this study. The optical microscope was coupled to a Delta Pix DP3 300 CCD camera (along with the related software). In all cases where such an image is used the value of the objective lens will be stated and the appropriate scale bar used.

3 : Optical Depth Profiling

In order to use CRMS effectively in the analysis of electrical ageing in polymers, we must first understand the processes involved and the various issues that occur when using CRMS. This chapter discusses the challenges and investigates a model of CRMS proposed by Macdonald and Vaughan in 2007 [41], which is designed to eliminate some of the potential pitfalls. The model will be compared to depth profiles of polymers using both air and oil immersion objectives and a range of sample surface conditions obtained.

3.1 Background

3.1.1 Confocal Raman Microprobe Spectroscopy

Confocal optical microscopy was patented by Minsky in 1957 [35] and seeks to exclude out of focus light when focusing on a transparent/translucent material, thus enabling an image from a specific location within the sample to be obtained. To achieve this, a small aperture or 'pin hole' is placed in the back focal plane of the objective lens. Light from the plane of focus then passes through the aperture, whereas light from the out of focus planes is defocused and only the central portion passes through, contributing little to the final signal.

Since Minsky, many applications for confocal microscopy have been developed, including CRMS. Non confocal RMS is a useful tool in the chemical analysis of samples as it has a lateral resolution of approximately 1 μm. RMS cannot be used for the analysis of layered samples however, as it has no resolution along the optic axis due to light being collected from all planes. The addition of a confocal pinhole adds a resolution, initially thought to be approximately 2 μm, in the vertical direction so that thin layers of a sample can be analysed. Based on this resolution, CRMS was then applied to a number of different polymer laminates [80-86].

3.1.2 Geometric Optical Approach

In 1992 Tabaksblat, *et al,* developed the technique of CRMS into what it is today [34]. They presented a model for CRMS based on geometrical optics and applied it such that the depth resolution of a CRMS system with a range of objectives and pinhole sizes could be determined. According to the model, factors such as diffraction at the pinhole and the influence of refraction, scattering and absorbance at the sample surface are disregarded and the theoretical performance of CRMS is determined by the optical properties of the system, including the size of the confocal pinhole, the numerical aperture (NA) of the objective lens, etc.

In the model, the depth resolution for confocal optical systems was defined using the full width half maximum (FWHM) criterion of a silicon wafer (used for its simple spectra and well defined peak at 520 cm^{-1}). The FWHM is measured using a silicon wafer depth profile, as determined using the main silicon peak at 520 cm^{-1}. The width of this depth profile is measured at half of its maximum intensity in order to give the FWHM. Theoretical values for depth with different objective lenses and pinhole sizes were hence calculated using this method by Tabaksblat *et al*. These values were compared to the actual resolution of the system measured using a PE film separated by a thin layer of air (the thickness of which can be measured optically) from a PP block. By probing through the sample, the contribution of the PP signal to the spectrum can be measured. If, when focused on the bottom layer of PE, there is no interference from PP in the observed spectrum, then it can be concluded that the actual optical resolution of the system is smaller than the size of the air gap. It was found that when measured experimentally, the resolution of the microscope was actually less than the resolution calculated by the FWHM for both objective lenses. Tabaksblat, *et al,* noted that these results vary depending on the sample and it is important to take into account the effects of refraction, absorbance and surface condition of the sample, due to the resulting distortion of the exciting laser spot making its exact position difficult to determine.

3.1.3 Virtual Pinholes

Williams, *et al,* [87] further improved CRMS in 1994 by using a CCD detector to provide a virtual pinhole instead of using a physical one at the focal plane of the objective. Here, the entrance slit of the spectrometer acts as one dimension of the pinhole whilst 'pixel binning' of the CCD is used to form the other. Combined with Tabaksblat's work this has led to numerous studies of transparent polymers and the ability to 'depth profile' a sample has been developed. Subsequent studies of transparent polymers using CRMS [3-9] have, however, led to the realisation that CRMS is not as simple as previously thought. In order to gain accurate data, refraction and other optical effects need to be taken into account, as concluded by Tabaksblat *et al*.

3.1.4 Ray Tracing Approach

Although the problem of refraction effects in CRMS was discussed by Hell, *et al*, [88] and Hajatdoost, *et al*, [89, 90], it was not properly addressed until 2000, when Everall published the first of many papers on the subject [6, 91-95]. In the first of these [91], a simple ray tracing approach is used to predict the effects of refraction at the air/sample interface and its effect on the depth resolution of the system. The effects of diffraction are deliberately ignored here as, compared to refraction, their effects are thought to be insignificant.

Figure 3.1 shows a simple diagram used by Everall to explain his model and show how the path of the light is affected by refraction. A ray of light from the objective is refracted at the surface of the sample such that it is focused at P_2 at a depth Z below the surface. If the refractive indices n_1 and n_2 of the sample and surrounding air respectively are equal then no refraction effects would be present and the ray would hence end at P_1 at a depth Δ below the surface. Δ is equal to the focal length of the objective focus (f) minus the height of the objective above the surface of the sample and is often referred to as the apparent focus. Also marked on the diagram are the relative angles of the rays of light to the normal.

By applying Snell's law to the model presented, Everall concluded that the point of focus (z_m) is given by:

$$z_m = \Delta\left[m^2\frac{NA^2(n^2-1)}{(1-NA^2)}+n^2\right]^{1/2} \tag{3.1}$$

And the depth of focus is given by:

$$d.o.f = \Delta\left[\left[\frac{NA^2(n^2-1)}{(1-NA^2)}+n^2\right]^{1/2}-n\right] \tag{3.2}$$

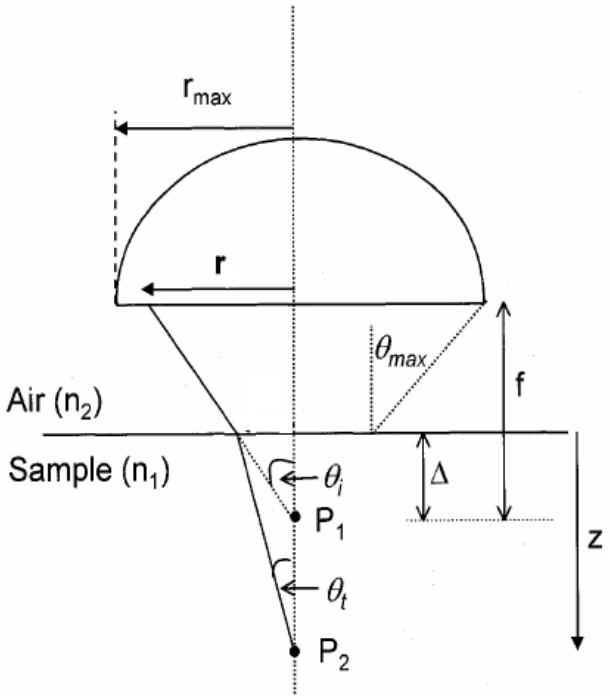

Figure 3.1: Diagram used by Everall in [46] to explain his ray tracing model for the refraction effects in CRMS.

where Δ is the apparent focal position, m is the normalised radius (r/r_{max}), NA is the numerical aperture of the objective lens and n, the refractive index of the sample (= n_1/n_2). Everall's equations show that not only does the point of focus change with Δ, but the depth of focus increases linearly with Δ; for an objective with NA= 0.95, the depth of focus is 2.2Δ. Therefore, Everall calculated that if n=1 and the laser is focused at an apparent 5 μm below the surface, the depth of focus actually extends from 7.5 to 18.5 μm, dramatically contradicting Tabaksblat's estimate of an axial resolution of approximately 3 μm. Everall concluded that once focused a few micrometers below the surface of the sample, obtaining a pure spectrum from a layered sample becomes 'impossible'.

Everall suggested that, in order to overcome the errors caused by refraction, physically cross sectioning the sample and then laterally scanning across the layers, is the most accurate method due to the lateral resolution remaining constant. Using an oil immersion objective and oil which matches the refractive index of the sample thus reducing (and possibly eliminating) refraction effects at the air sample interface is another alternative suggested by Everall, but this method is not tested until his next paper in 2000 [6] and discussed in greater detail in 2007 [94].

Everall's second paper and modifications to the model initially proposed [6] was based on the work of Baldwin and Batchelder [96] in 2001, which was still in preparation when Everall published his first two papers on the subject. Baldwin and Batchelder's paper is also based on refraction at the air sample interface, whilst ignoring diffraction. As well as this, it agrees with Everall's conclusion that the focal position is deeper than expected and that the depth of focus increases with position. Baldwin and Batchelder then extend Everall's model to account for the effect of spherical aberration on the size of the sample volume. Spherical aberration significantly degrades the performance of the microscope and increases the depth of focus due to the distortion of the scattering volume defined by the confocal pinhole, thus resulting in a significant reduction in the intensity of collected light with respect to an increased focal depth.

Baia *et al's* study in 2002 [97] took into account both refraction and diffraction and characterised the dimensions of the focal volume at different depths inside a coated sample. The key problem in CRMS is that obtaining the optimum spatial resolution perpendicular to the optic axis is 'ultimately limited by diffraction'. Baia et al then provided a model that takes into account the refraction based models of Everall, Baldwin and Batchelder, and the previously omitted diffraction effects. The models proposed by to Everall, Baldwin and Batchelder, are in good agreement with the experimental data obtained from thin films, for thicker samples, diffraction effects

reduce the length of focus with Δ. The resulting model was found to be in good agreement with experimental results.

3.1.5 Spherical Aberration

Another paper which was published by Michielsen in 2001 [98] provides an alternative model for the limitations of CRMS. Michielsen noted that spherical aberrations, due to a mismatch of refractive indices, are introduced into the illumination and collection of light, thus leading to an error in the measured intensity and axial resolution. A model based on geometrical optics was presented approximating the distortion of the beam resulting from this mismatch of indices. The model was then applied such that the errors apparent in the analyisis of subsurface features when using CRMS are accounted for and minimized.

It was also noted that, as previously mentioned by Everall, the focal point is displaced and 'smeared' to form a focal volume as the focus of the laser is moved deeper into the sample. The position and shape of the focal volume is affected by the refraction of light according to Snell's law. If the refractive indices at the air/sample interface do not match, the focal position is given by:

$$f = d_s \frac{n_2}{n_1} \frac{\cos\left[\sin^{-1}\left(\frac{n_1}{n_2}\sin\theta_0\right)\right]}{\cos\theta_0} \tag{3.3}$$

Which simplifies to:

$$f \cong \frac{n_2}{n_1} d_s \tag{3.4}$$

for small values of θ. Here, f is the focal position, d_s is the apparent focal position (in Everall's paper equal to Δ), n_1 the refractive index of the medium between the microscope objective and the sample, n_2, the refractive index of the sample and θ_0 is the angle of incidence.

This leads to a smearing of the focal point as the paraxial and marginal rays in the system are focused in different planes. Michielsen equated this smearing of the focal point, s, using the following equation:

$$s = d_s \frac{n_2}{n_1} \left| 1 - \frac{\cos\left[\sin^{-1}\left(\frac{NA}{n_2}\right)\right]}{\cos\left[\sin^{-1}\left(\frac{NA}{n_1}\right)\right]} \right| \quad (3.5)$$

Thus s is greater when NA and the difference between n_1 and n_2 increases. Michielsen suggested the use of an oil immersion lens and appropriate immersion oil to reduce this effect. Finally, the paper compares the model presented to experimental data and good agreement was found. Michielsen then concludes that the drop in Raman intensity during a depth profile is indeed due to spherical aberration as well as the scattering and absorption suggested by Everall.

3.1.6 Electromagnetic Approach

Much work has been done to improve the models discussed above [99, 100] and introduce new ones. To date, the most rigorous and complete descriptions of the problem were provided by Torok *et al* in 1995 [101] and Sourisseau *et al* in 2003 [102]. In these papers, the contributions from all the optical parameters previously proposed were taken into account. A rigorous electromagnetic treatment was applied to the problem including diffraction, which has otherwise been oversimplified or ignored. These descriptions, however, despite being the most complete, are highly complex and beyond the scope of this study.

3.1.7 Predicting the Raman Depth Profile Response

The objectives of the models described above are to provide an accurate description of the confocal Raman response obtained at various depths throughout a transparent sample and the resulting shape of the depth profiles obtained experimentally from these samples. These models are based on geometrical optics and incorporate a number of optical factors such as NA, refractive index, diffraction, off axis contributions and the nature of the confocal pinhole. A complete understanding of the Raman response was not achieved, however, due to material properties such as scattering and absorption not being accounted for. The resulting models were therefore unable to fully account for the shape of a depth profile and intensity of the Raman signal.

3.1.8 Oil Immersion

One way to improve the axial resolution of CRMS is to use an oil immersion objective to reduce the mismatch in refractive index, as proposed by both Everall and Michielsen [6, 94, 98]. Froud *et al* applied the use of an oil immersion objective and an appropriate immersion oil to a multi layered polymer laminate [103]. These results were then compared to those obtained using a 'dry' non immersion objective in air.

The studies concluded that oil objectives do improve the resolution of CRMS, as predicted, and they allow for the determination of various polymer layers. They also noted, however, that this could only be done if a suitable immersion oil, which matches the refractive index of the sample, can be found. Michielsen pointed out that [98] this is not always a straight forward process and an exact match in refractive index cannot always be found. If the refractive index of the oil is a perfect match to the refractive index of the sample, however, refraction effects are reduced to zero allowing more accurate results to be obtained.

3.1.9 Photon Scattering Approach

In 2007 Macdonald and Vaughan took a novel approach and proposed a numerical simulation based on a photon scattering approach [41]. The purpose of the simulation was to predict the CRMS response of a material with respect to depth of focus by adjusting 3 main parameters within the simulation. These parameters are as follows:

- Position of the surface layer (relative to the plane of focus).
- Coefficient of Raman scattering efficiency.
- Attenuation coefficient ('the rate of change of intensity of the exciting laser photons and Raman scattered photons within the material').

A key concept of the model is that Raman photons can be generated at any point within the region of the sample that is illuminated by the laser. It is also possible for these photons to be scattered in such a way that they pass through the confocal pinhole and contribute to the detected spectrum. CRMS is based on the idea that only Raman photons generated close to the focal point of the system's laser are important since it is these that will pass through the confocal pinhole. In 2004, however, Everall proposed that when the focal point is below the surface of the sample in question, photons produced at any point along the optical axis can contribute to the spectrum, as the photons travel back along this axis. Macdonald and Vaughan's paper in 2007 added to this, hypothesizing that photons from any part of the illuminated area can contribute to the detected signal, not just the ones originating from the focal point or from along the optic axis. It stands to reason that there is a non-zero probability that the photons produced throughout the illuminated region could be scattered in such a way as to pass through the pinhole. It was also noted that the illuminated region also extends beyond the focal point making it possible for photons to be detected when the focal point is above the sample surface. Figure 3.2 shows (a) a simple schematic of the illuminated region and (b) how it can contribute to the spectrum.

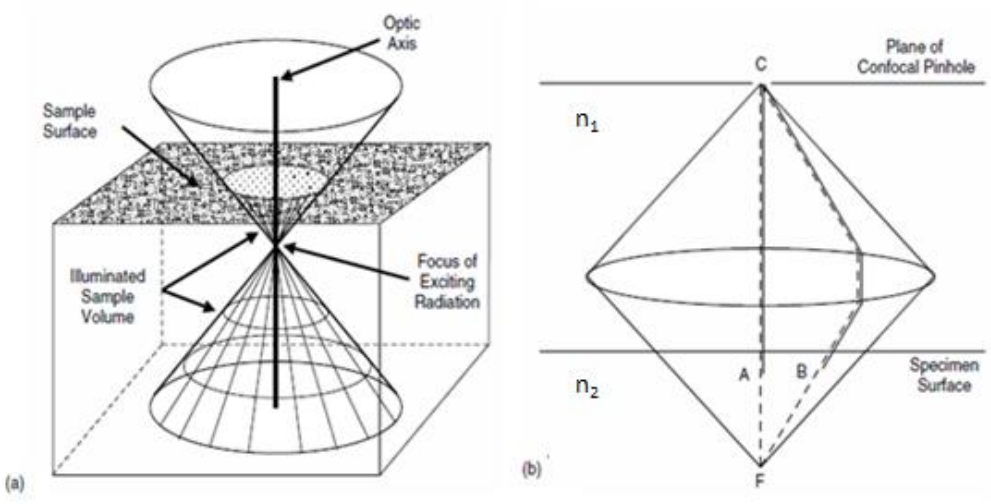

Figure 3.2: Schematics showing (a) area of material illuminated by a laser where Raman photons may be produced, (b) Raman photons produced at points A and B may follow paths allowing them to pass through the confocal pinhole C whilst the laser is focused at F (where $n_1=n_2$) [29]

Another concept, on which Macdonald and Vaughan's model is based, is that both the photons from the exciting laser and the consequent Raman photons within the system can be attenuated via scattering and absorption within the sample. The intensity of the laser and probability of Raman scattered photons returning through the pinhole therefore decreases with depth. In Macdonald and Vaughan's paper it is assumed that both these factors decrease exponentially with depth.

If these concepts are correct, then the model proposed calculates the probability of the Raman photons generated within the illuminated region being scattered in a way such that they pass through the confocal pinhole and add to the spectrum. This is done by modelling the illuminated region as a 2 dimensional set of discrete cells and calculating the probability that the photons produced in each cell given by position (n_x, n_y) away from the focal cell (1, 1) as shown in figure 3.3, follow the path needed to contribute to the spectrum. The efficiency of the material at producing the Raman photons, the attenuation factor of the material and the depth of focus with relation to the surface are also taken into account. This is easily converted into a 3 dimensional cylindrical polar co-ordinate system. Using this co-ordinate system, the probability of a Raman photon produced in a particular cell of position z and radius r (labelled as cell (n_r, n_z)) passing through the confocal aperture and contributing to the spectrum is given by:

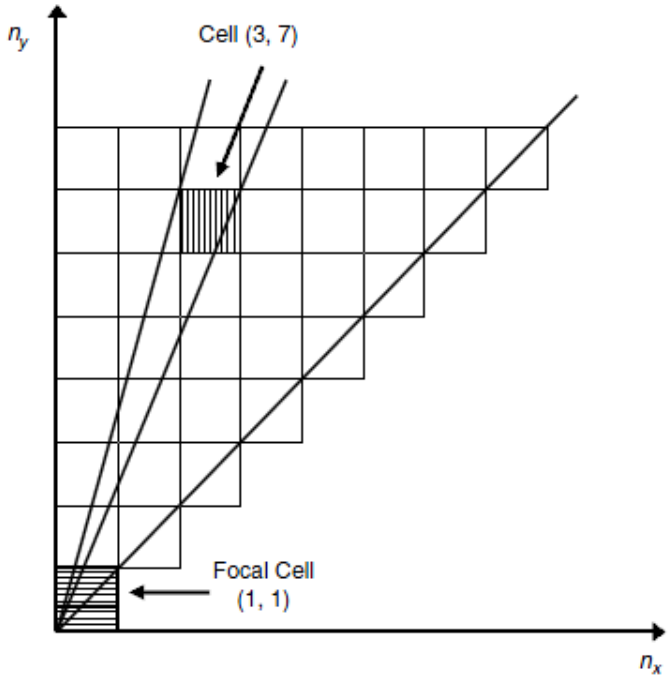

Figure 3.3: Diagram as illustrated in [29] showing a 2 dimensional array of cells used to define the contribution of each cell to the signal.

$$P_{r,z} = \frac{1}{2}\left|\cos\left[\tan^{-1}\left(\frac{n_r}{n_z}\right)\right] - \cos\left[\tan^{-1}\left(\frac{n_r - 1}{n_z}\right)\right]\right| \times \left\{K_e \frac{\Phi_p}{{n_z}^2}\text{exp-}k_e\Delta_z\right\} . \text{exp-}k_R\Delta_z \qquad (3.6)$$

where Δ_z is the depth of cell (n_r, n_z) with reference to the surface, Φ_p is the total exciting photon flux, and k_e and k_R are assumed to be equal and relate to the attenuating factors of the exciting beam and Raman photons respectively. The first term in this equation calculates the position of the cell in question, the second term calculates the number of photons arriving from the laser source to the cell in question and the final term calculates the number of photons emitted from the cell following excitation. Note that this model assumes an equal contribution from the cells both above and below the focal point.

In summary, the confocal approach should not be applied without caution to RMS due to a poorly defined 'focal point'. The volume from which the spectra can be obtained is displaced and blurred due to many factors, not just the optical effects occurring at the sample surface. An effective method of increasing the resolution of CRMS along the optic axis is to use an oil immersion objective. The photon scattering approach suggested by Macdonald and Vaughan [41] successfully explained the form of the

Raman depth profiles of polymers which is surprising due to its deliberate omission of the optical effects discussed by the likes of Everall [6, 91, 93-95]. The resulting numerical model based on this approach accounts for some of the effects seen in the collection of Raman data in terms of contributions from the illuminated volume where previous models have failed.

3.1.10 Aims and Objectives

This study aims to apply the model proposed by Macdonald and Vaughan to depth profile data obtained from a selection of different polymer systems ranging in refractive indices and optical clarity. The model will be compared to data obtained using both an objective in air and an oil immersion lens in a selection of immersion media. As well as this, the effect of surface abrasion on the depth profiles will be assessed. This will enable an evaluation of the model's ability to predict the Raman response and depth profile in various polymeric systems. Evidence will also be provided to support the value of using the photon scattering approach to model CRMS and all its associated phenomena.

3.2 Experimental

3.2.1 Materials

Ten oils were investigated in this study. The first of these is the liquid form of poly(dimethylsiloxane) PDMS(L), which has a chemical backbone composed of alternating silicon and oxygen atoms (see figure 3.4) [104].

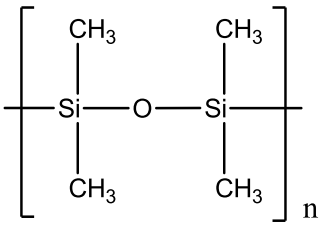

Figure 3.4: representation of the chemical structure of PDMS(L)

The PDMS(L) used in this study was the 200/20cs grade obtained from Dow Corning® which, at room temperature, has a similar viscosity to water, and a refractive index of approximately 1.41 [105]. As well as PDMS(L), a variety of microscope immersion oils supplied by Cargille Laboratories were investigated and compared to the results given by the PDMS(L). Cargille immersion oils are specifically designed for use with optical microscopes. They are non-drying and vary in properties such as viscosity and refractive index.

Polymeric samples of PE, PS and Novolen were examined in this study. A polyethylene blend of 20% linear high density polyethylene (HDPE) (Rigidex 160-25 obtained from BP) and 80% branched low density polyethylene (LDPE) (LD100BW obtained from Exxon) was produced. Due to its semicrystalline structure and sperulitic morphology it is significantly scattering and has a refractive index of approximately 1.54. Block PS and Novolen 3200MC samples were made using the same method as the PE and were hot compression moulded against an optically flat glass surface and quenched from the melt before cutting to size. Two of the samples of Novolen were abraded using 1200 grit wet and dry paper, in order to study surface scattering effects. One sample was finely abraded whilst the other, severely abraded. The PS samples have a refractive index of 1.59 and the Novolen samples have a refractive index close to 1.51.

3.2.2 Sample Characterisation

Initially, spectra from all of the immersion oils were obtained using an extended spectrum, as detailed in chapter 2, to find the position of the main peaks in the spectrum of each oil. Following this, depth profiles were obtained from each oil, using the 'optical sectioning' [6] approach described by Everall. For this a x50 air objective was used and the position of the sample was moved incrementally both above and below the nominal focal point of the exciting radiation and the intensity of an appropriate peak recorded.

The same approach was used to obtain depth profiles of the Novolen, polyethylene, and polystyrene in air. In order to obtain the depth profiles for these samples, the intensity of the following peaks (chosen due to their high intensity) was recorded: the 1295 cm^{-1} C-H twisting band of polyethylene [55], the 1001 cm^{-1} C-C stretching mode of polystyrene [57] and the 809cm^{-1} $\rho(CH_2)$ vibrational mode [61] of Novolen. The depth profiles were then repeated with the x50 oil immersion lens and with the samples immersed in either PDMS(L) or the selected Cargille immersion oil. In all cases a x20 objective was used to find the surface before using the x50 (or x50 oil immersion objective after applying the oil to the sample) to obtain the spectra.

3.3 Results and Discussion

3.3.1 Immersion Oils

Figures 3.5 and 3.6 respectively show the Raman spectrum and depth profile data obtained from PDMS(L). PDMS(L) was chosen because of its simple spectrum whose spectral peaks should not overly overlap with those of the polymers investigated here in this study. As well as this, it has a different refractive index to the Cargille oils and therefore enables the effect of refractive index mismatches to be explored. Note that in figure 3.6 and all following depth profiles, the surface of the oil/sample is indicated by

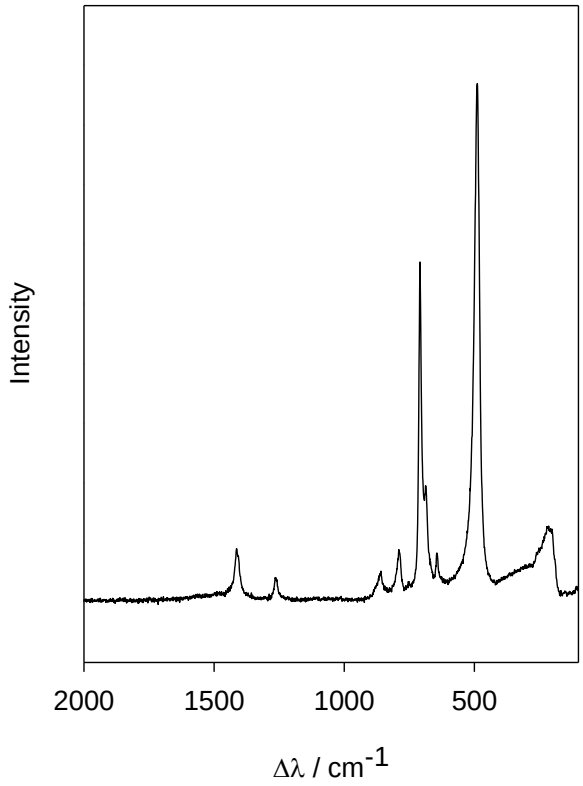

Figure 3.5: Full Raman spectra of PDMS(L)

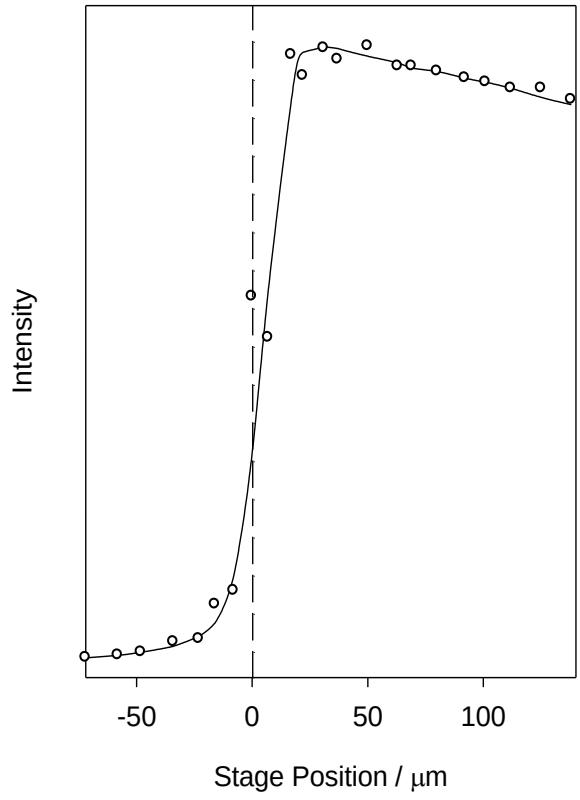

Figure 3.6: Depth profile of PDMS(L) obtained from the intensity of the peak at 500 cm^{1} in the full spectrum; raw data indicated by open circles and the overall shape indicated by solid line

a dashed line at a stage position of 0 μm. It can be seen in figure 3.6 that, whilst depth profiling PDMS(L), the maximum intensity of the peak used to generate the depth profile does not occur when the laser is focused on the surface of the oil but rather, when the stage has been shifted such that the apparent focal point is approximately 10 μm below the surface of the oil.

Figures 3.7 and 3.8 show the Raman spectra and depth profiles obtained from all the Cargille immersion oils used in this study. All these spectra differ slightly, as they were designed for different purposes, but most nevertheless contain a number of similar features. Table 3.1 lists some of the properties of the oils tested, which may aid understanding of the spectra. Cargille oil types A and B were designed to be interchangeable, with type B having a slightly higher viscosity. The spectra for oil types A and B are therefore expected to be very similar with only minor differences in features contributing to the difference in viscosity and, as can be seen from figure 3.7, this is indeed the case. If fluorescence is ignored, then the spectra for Cargille oil types DF and 37DF are similar. This similarity is likely to be due to oil type 37DF being designed to have the same properties as DF but with a slightly higher viscosity and working temperature. Oil types NVH, OVH and 37 exhibit similar spectral features (again ignoring fluorescence in oil type NVH) and, as before, these similarities in the Raman spectra are to be expected as they were designed for the same purpose and have similar optical properties. Oil types HF and FF exhibit few features in common with the other oils. Oil type HF shares only one main feature with the other oils and exhibits a relatively simple spectrum, perhaps due to Cargille oil type HF not containing any halogens thus having a simpler chemical makeup and hence fewer spectral peaks. Oil type FF does not contain the feature at 1000 cm^{-1} that is present in all the other spectra and, with the addition of fluorescence in the spectrum, it is notably different from the other oils.

Peaks that are present in the majority of the oil spectra can be found at 1293 cm^{-1}, 1446 cm^{-1} (related to the vibrational modes of CH_3 [55]), 1599 cm^{-1} and 1003 cm^{-1} (which are both associated with the C-C stretch in benzene [106]). With the exception of oil type FF, all spectra contained a peak at 1003 cm^{-1}, and so it was the intensity of this that was used to obtain the depth profiles shown in figure 3.8. For oil type FF the intensity of the peak located at 1446 cm^{-1} was used. As with PDMS(L) in figure 3.6, the resulting depth profiles all exhibit a similar shape and peak at a focal position close to 10 μm below the surface of the oil (indicated by a vertical solid line). Although the intensity and exact data points may vary slightly the average shapes of these depth profiles is repeatable and little difference can be seen between the different oils. Cargille oil type OVH was chosen to be the immersion oil used to compare with

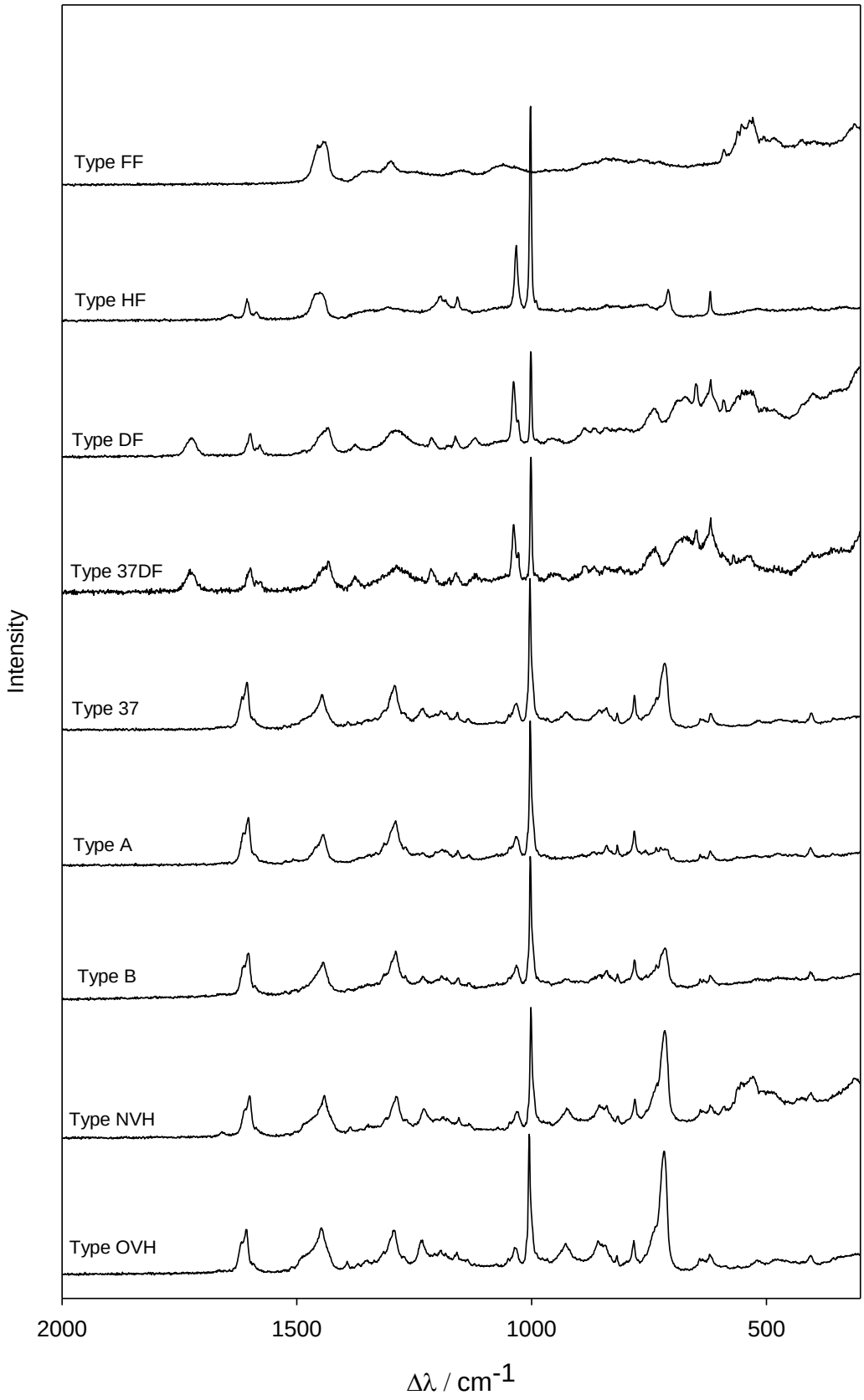

Figure 3.7: Raman spectra for full range of immersion oils provided by Cargille Laboratories.

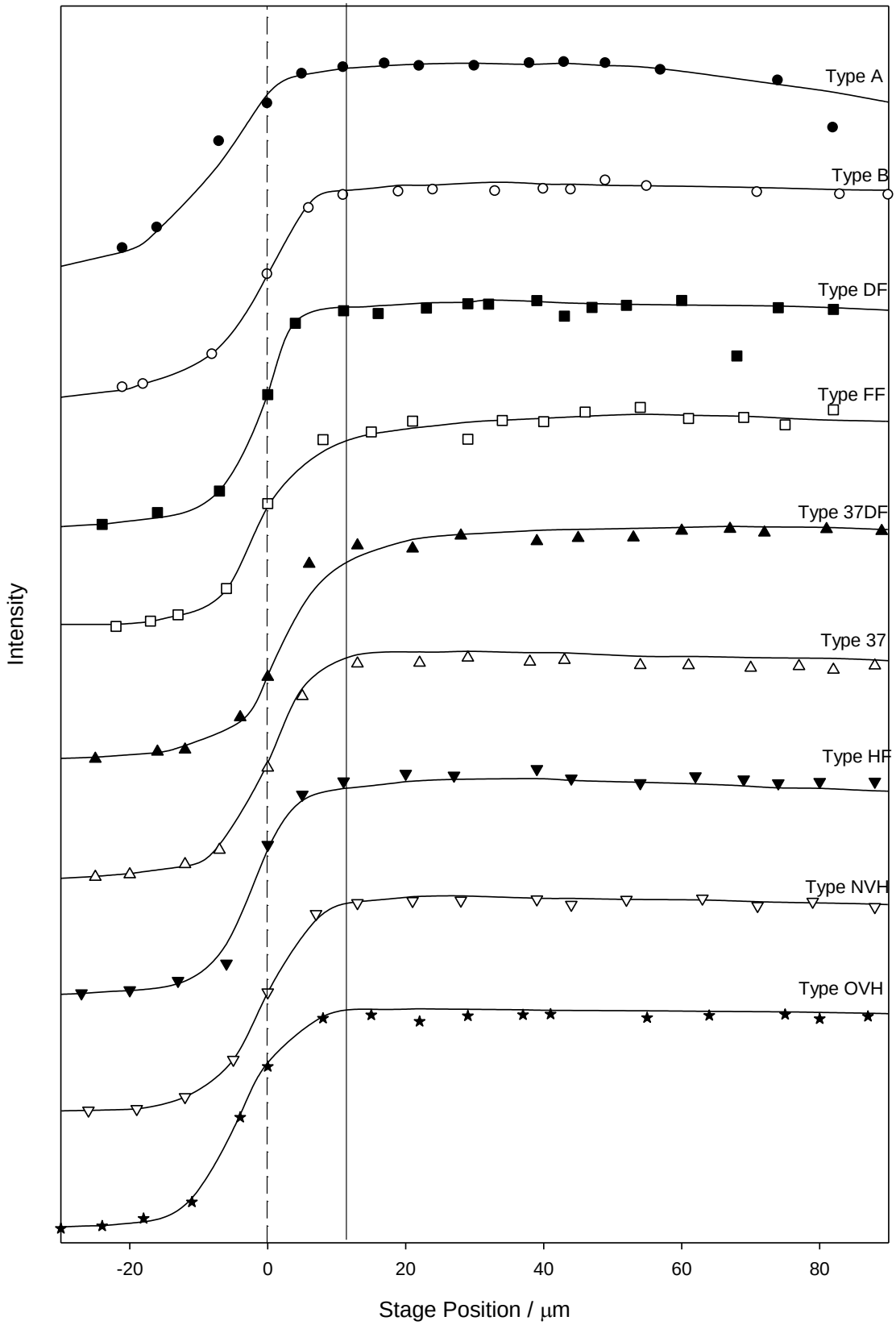

Figure 3.8: Depth profiles of all Immersion oils provided by Cargille Laboratories (obtained using intensity of peak seen at 1003 cm-1 in full spectra).

Table 3.1: Cargille immersion oils and their properties

Oil type	*Approx refractive index at 23° c*	*Fluorescence*	*Viscosity*	*Comments*
A	1.52	Low	Low	Designed for light microscopy, interchangeable
B	1.52	Low	High	Designed for light microscopy, interchangeable
DF	1.52	Very low	Medium	Designed for low fluorescence
FF	1.48	Very low	Low	Designed for low fluorescence
HF	1.52	Very low	Medium	Halogen free
37	1.52	Low	High	Designed for elevated temperature
37 DF	1.52	Low	Very high	Designed to be combination of DF and 37 with a high viscosity
NVH	1.52	Low	Very high	Designed for long focus instruments
OVH	1.52	Low	Very high	Designed for long focus instruments

PDMS(L), as its spectrum contains no fluorescence and enables the easy identification of the key peaks in the polymer spectra. As well as this, its refractive index closely matches that of the samples, hence enabling refraction effects at the system surface to be minimised. Oil type OVH has a refractive index of 1.52, is clear and has a very high viscosity [75]. The high viscosity of oil type OVH however makes it hard to work with and so, in hindsight, a better choice might have been Cargille oil type B.

3.3.2 Polymeric Spectra

Figure 3.9 shows typical full spectra for all materials and oil systems used in the remainder of this chapter. The main peaks for each polymer in this figure were identified to be located at 1001 cm^{-1}, which is associated with the in-plane breathing mode of the phenyl ring of PS [57], 1295 cm^{-1}, associated to the γ_1 CH_2 twisting mode of PE [55] at and the peak located at 890 cm^{-1}, related to the C-H stretch for Novolen [61]. The relative intensities of these peaks were then used to calculate the depth profiles shown in the rest of this chapter. The data presented are the initial raw data and, as

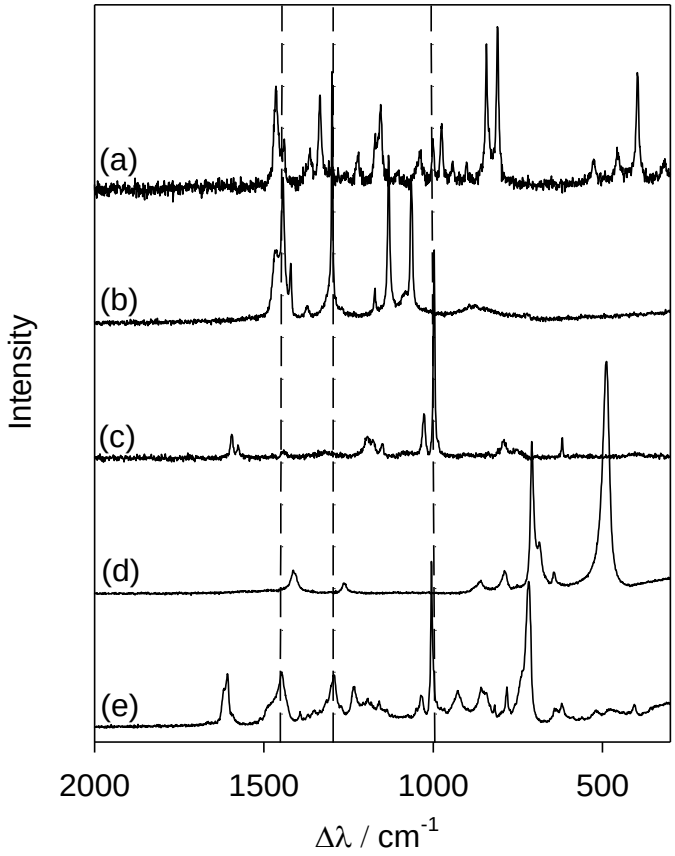

Figure 3.9: Full Raman spectra obtained in air for (a) Novolen, (b) PE and (c) PS with (d) PDMS(L) and (e) Cargille immersion oil type OVH for comparison

such, data were collected over a period of several weeks. Due to unavoidable variations of the system, the vertical scale of the depth profile (but not the overall shape) was found to vary from day to day. For this reason, the intensities of all spectra and depth profiles have been rescaled and normalized such that the maximum intensity of the depth profiles is comparable.

When immersed in oil, the acquired Raman data from the samples is a combination of the signal from the sample and the signal from the oil. As the focus of the microscope objective is moved throughout the oil and the sample, their relative contributions to the overall combined spectra change accordingly. If the oil has a simple spectrum where the spectral peaks do not overlap with those belonging to the sample spectrum, such as the PDMS(L) when compared to the polymers in this study, determining the contributions of both the oil and sample to the final spectra is relatively straight forward. Immersion oils such as Cargille oil type OVH, however, do not have a simple spectrum and, often, peaks from the oil overlap with the signal from the sample. The peaks located in the spectrum for oil type OVH at 998, 1298 and 1450 cm^{-1} all overlap with spectral features characteristic of the polymers, as indicated by the vertical

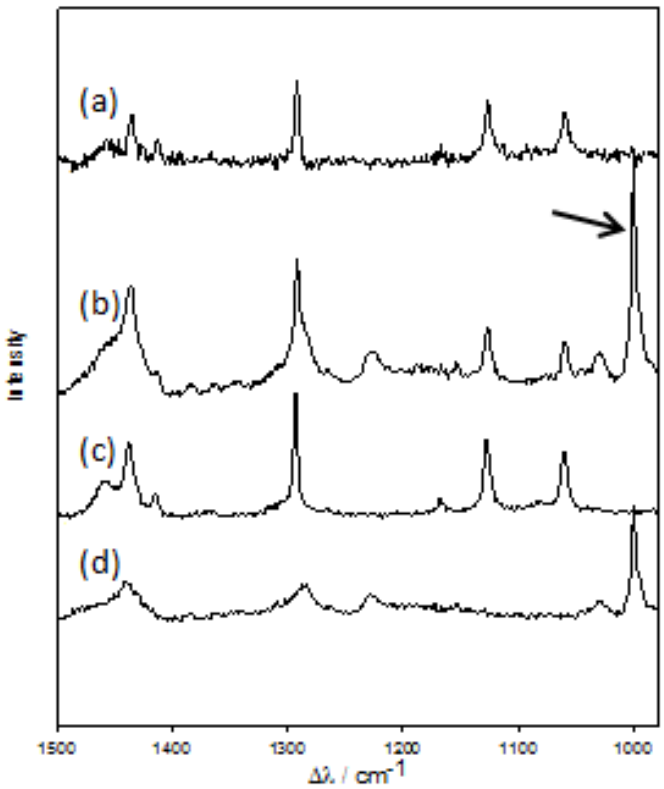

Figure 3.10: Spectra demonstrating the process of data recovery (a) recovered PE spectrum following data subtraction, (b) spectrum from a sample of PE immersed in Cargille oil type OVH, (c) spectrum from pure PE (d) spectrum from pure Cargill oil type OVH and the peak used to perform process as indicated by an arrow.

dashed lines in figure 3.9. This overlap of signals leads to difficulties in determining the polymer depth profiles, due to both the oil and sample contributing to the intensity of the peaks used. It is therefore necessary to remove the contribution from the immersion oil. This process is demonstrated in figure 3.10 and described below.

In order to obtain the recovered spectrum of the sample (a) the following method was applied:

- A peak was identified in the combined spectrum (b) which correlated to the immersion oil but not the sample as identified by comparison with the pure spectra of the sample (c) and the immersion oil (d). For this example the peak at 998 cm^{-1} was used as it is located well away from any spectral featured associated with PE as shown in figure 3.9. This peak is indicated in figure 3.10
- A factor of the immersion oil spectrum (d) was then subtracted from the combined spectrum (b) such that the identified peak was no longer visible and thus, the oil was no longer contributing to the final spectrum.

Following this subtraction the contribution of the sample to the spectrum can be obtained and true depth profiles can be determined as before. The peak used in this explanation, however, overlaps with features found in Novolen and PS and so the peak located at 1620 cm^{-1} in the spectrum for OVH was instead used throughout the rest of this study to recover the polymer spectra from the raw oil immersed data.

Figure 3.11 shows the raw, unprocessed depth profile data obtained from PS. It can be seen that the form of the data obtained using OVH and silicone immersion is similar when the apparent focal position is below the surface of the sample. Above the sample surface, however, the contributions of the oil in the spectra dominate and a higher intensity can be seen originating from the contribution of the OVH. Figure 3.12 shows a comparison between the depth profiles of PS obtained in PDMS(L) and OVH oil using the raw spectral data, and the depth profile of PS obtained in OVH once the data have been processed using the method described above (filled circles). The curves drawn on these profiles are visually estimated indications of the overall shape of the depth profiles obtained using an oil immersion lens. This figure shows, as expected, that when focused above the sample, the immersion oil gives a Raman response greater than that of the sample and so dominates the overall spectrum. As the apparent focus is shifted deeper into the sample, the contribution of the oil becomes insignificant as the majority of the signal then originates from the sample. There is good agreement, within experimental error, between the processed OVH data and the PDMS(L) data. Consequently, it can be concluded that the method of data processing described above is adequate for removing the influence of the immersion oil from the composite spectrum, where the immersion oil peaks overlap with those from the polymer. Throughout the remainder of this chapter, filled squares represent the processed OVH data, the open squares represent the raw silicone data and the triangles represent data points obtained in air.

3.3.3 Polymeric Depth Profiles

Figures 3.13 to 3.15 show the variation in peak intensity with stage position for all the samples with optically flat, glass-like surfaces immersed in the chosen media. It can be seen that, when focused above the sample, a signal from the sample can still be seen and that this diminishes rapidly as the sample surface drops below the focal point of the exciting radiation. This confirms MacDonald and Vaughan's conclusions about Raman active photons being generated throughout the illuminated volume, rather than from just the focal point. As the focus of the laser is moved into the surface, the observed intensity of the signal increases dramatically, peaking between 20 and 50 μm below the surface, depending on the sample, before steadily decreasing (with the exception of some oil immersions) in intensity as the focus is displaced even deeper

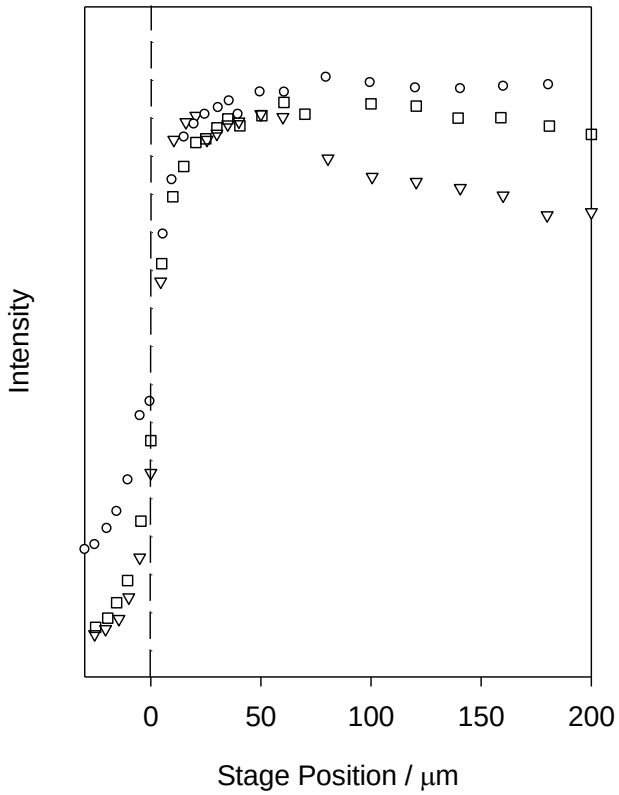

Figure 3.11: Raw depth profile data of PS, data obtained in air are shown by open triangles, PDMS(L) by open squares and OVH oil by open circles.

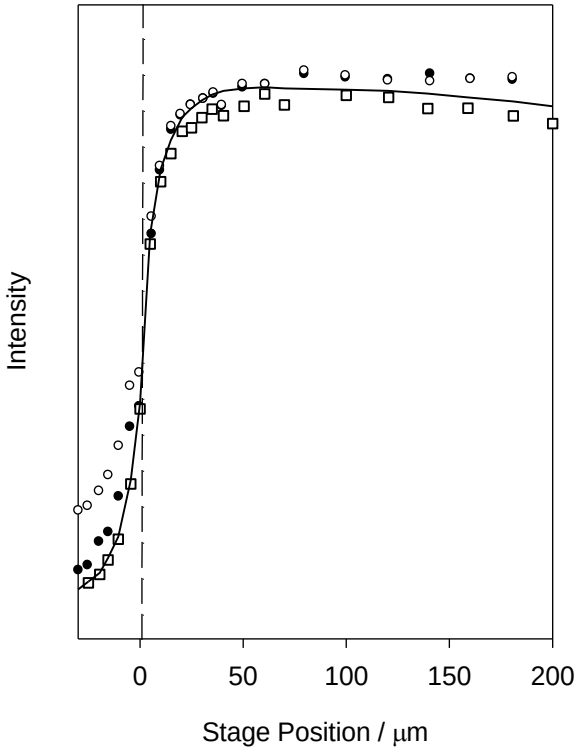

Figure 3.12: PS depth profile comparison between raw OVH data (open circles), recovered OVH data (closed circles), PDMS(L) (open squares) and a solid line providing a visual guide to the overall shape of the depth profiles

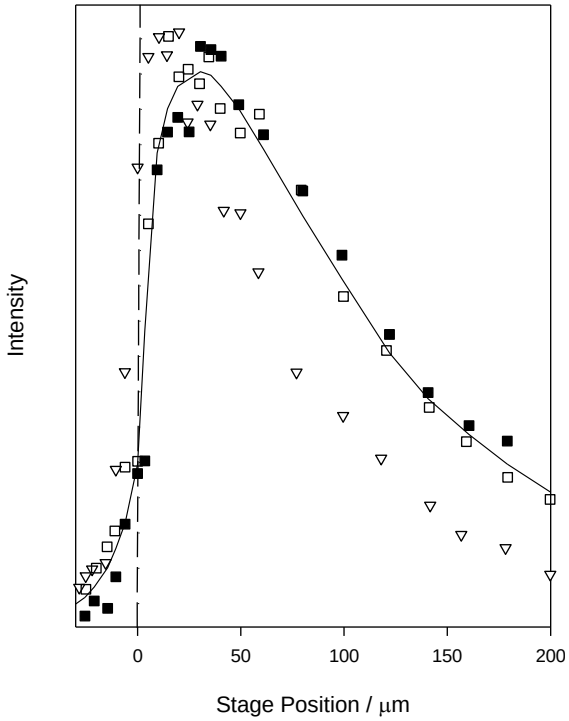

Figure 3.13: Depth profile data for PE showing data obtained in air (open triangles), PDMS(L) (open squares), processed OVH data (closed squares) and a solid line providing a visual guide to the overall shape of the depth profiles

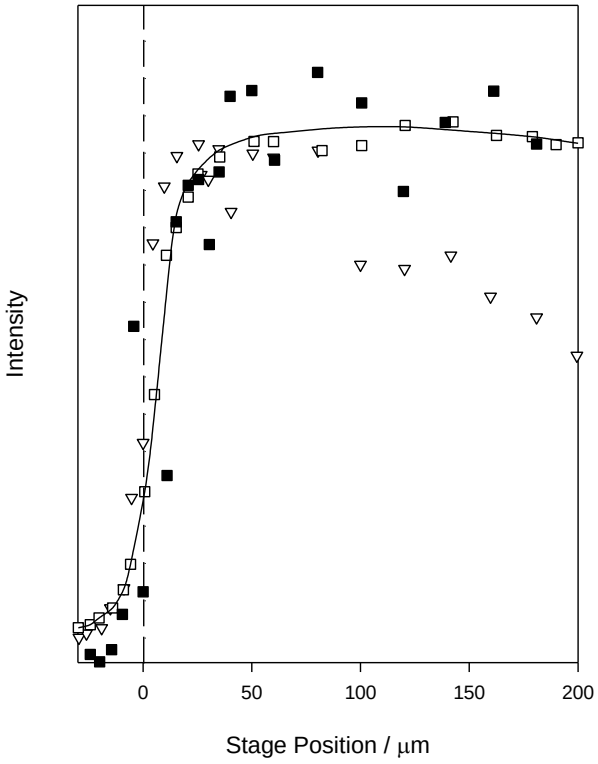

Figure 3.14: Depth profile data for Novolen showing data obtained in air (open triangles), PDMS(L) (open squares), processed OVH data (closed squares) and a solid line providing a visual guide to the overall shape of the depth profiles

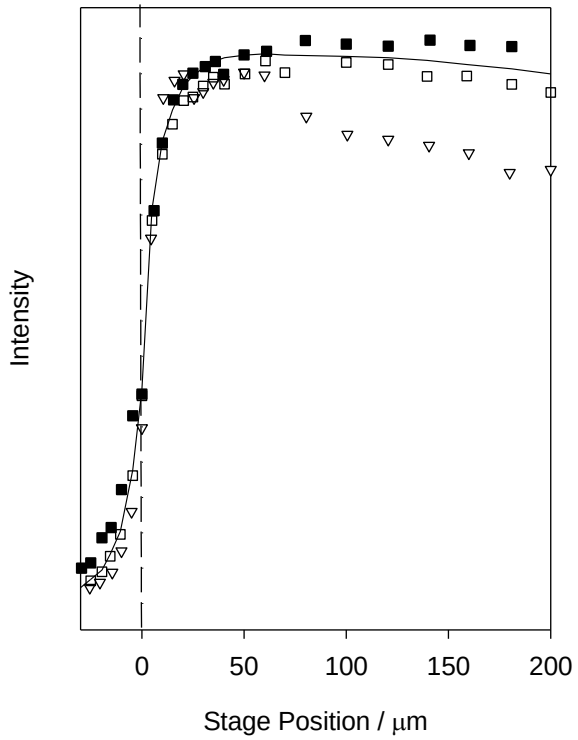

Figure 3.15: Depth profile data for PS showing data obtained in air (open triangles), PDMS(L) (open squares), processed OVH data (closed squares) and a solid line providing a visual guide to the overall shape of the depth profiles

into the sample. This is again consistent with the data collected by MacDonald and Vaughan in 2007.

In the model presented in [41] attenuation is assumed to be partially due to (a) the scattering of the Raman photons within the sample and (b) refraction at the sample surface. The signal attenuation seen in figures 3.13-3.15 fits well with these assumptions. The PE sample is relatively opaque and highly scattering compared to the other samples thus resulting in a rapid attenuation of signal past the optimal focal position as can be seen in figure 3.13. PS and Novolen, in comparison, are optically clear. This clarity leads to fewer photons being scattered within the sample compared to PE and, hence, little or no signal attenuation is seen within the depth profiles.

In all the samples, with the addition of immersion oil, the rate of decline is also reduced compared to the case in air, indicating that as well as reducing the refraction effects as predicted by Everall [6, 94], Michielsen [107] and Froud [108], the decline in signal is also due to scattering effects at the sample surface. All samples are homogeneous block samples with a glass like surface and in depth profiles from all the samples (figures 3.13. to 3.15), there is little difference between the PDMS(L) and the Cargille oil type OHV, despite their refractive indices differing by 0.1. This suggests

that for samples with an optically flat surface an exact match in refractive index is not critical when the samples have an optically flat, uniform, surface.

3.3.4 Surface Abrasion

The same techniques as previously mentioned were adopted to study the importance of surface scattering and refractive index matching for samples with an irregular surface. Samples of Novolen with surfaces that were finely and severely abraded were compared to data obtained from the 'ideal' glass-like surface. Figures 3.16 and 3.17 show that the results from the Novolen samples with abraded surfaces differ greatly from those given by the sample with a glass-like surface (figure 3.14). In these figures it can be seen that the signal attenuation for the non immersed samples is rapid, as with the PE sample. This observation supports the theory that the rate of decline of signal is affected by optical clarity of, and the degree of light transmission through, the sample. The surface condition is also extremely important when it comes to oil immersion. Ignoring vertical scaling factors, when the finely abraded sample is immersed in PDMS(L) there is only a very slight change in the decline in signal, indicating that refraction and scattering effects are still important, as the refractive index of the PDMS(L) does not match well with the Novolen. When immersed in Cargille oil OVH however, the depth profiles for the sample do not decline within the tested range. This suggests that the OVH oil provides a closer match in refractive index to the sample than the PDMS(L). This match not only affects gross refraction phenomena but also helps to eliminate any surface scattering.

Results for the Novolen with a severely abraded surface are shown in figure 3.17. Although similar to figure 3.16, these data are more variable and the stage position corresponding to maximum signal appears shifted. With the non-immersed sample, this shift occurs before the surface of the sample. This is likely to be due to the inaccuracies of finding the real surface due to the severe abrasion. Also, when the sample is immersed in OVH the signal decreases, unlike in figure 3.14, but this attenuation is not as severe as with PDMS(L). This indicates that with an increase in surface abrasion, the effects of scattering dominate and the importance of finding an exact match in refractive index between the immersion oil and sample also increases. OVH oil provides a closer match in refractive index to the Novolen sample than PDMS(L), this match however, only minimizes the attenuation caused by surface scattering and does not remove it completely when the surface is badly abraded.

3.3.5 Thin Film Samples

The benefits of using an immersion oil to reduce refraction effects can also be seen when analysing thin film samples as shown by Everall in 2000 [6]. Single layer thin

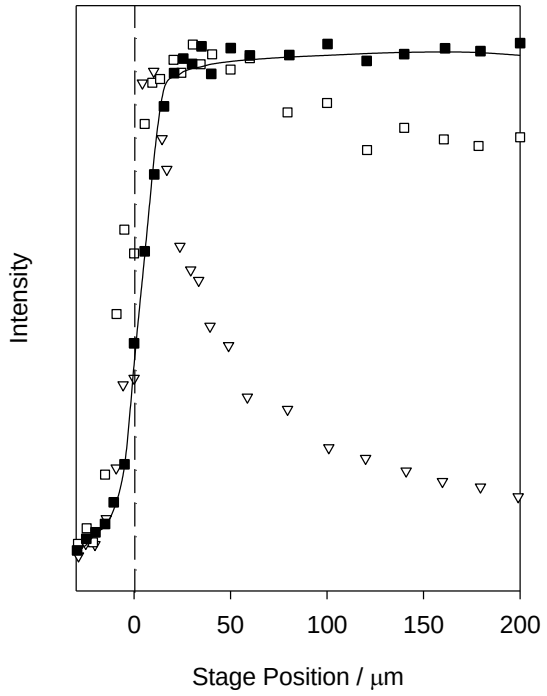

Figure 3.16: Depth profile of Novolen with a finely abraded surface, data obtained in air (open triangles), PDMS(L) (open squares), the processed from OVH data (closed squares) and a solid line providing a visual guide to the overall shape of the depth profiles

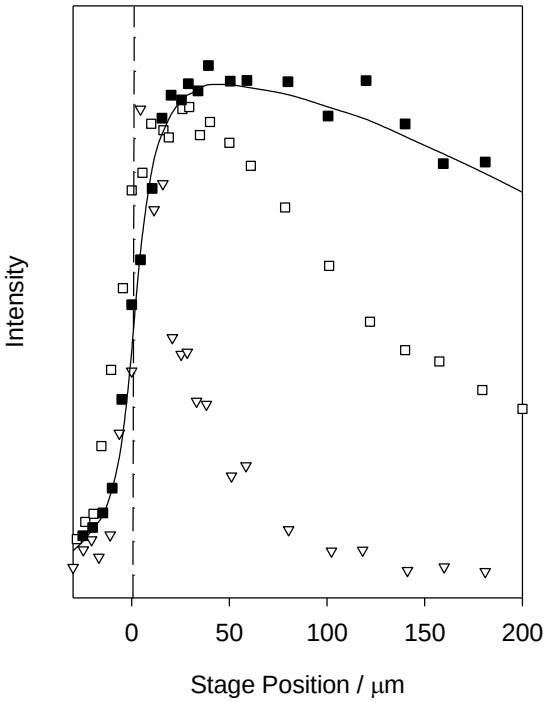

Figure 3.17: Depth profile of Novolen with a severely abraded surface, data obtained in air (open triangles), PDMS(L) (open squares), the processed from OVH data (closed squares) and a solid line providing a visual guide to the overall shape of the depth profiles

films allow the depth resolution of the polymer system to be obtained experimentally. Being able accurately to obtain the depth resolution of a single polymer system would enable the exact location of subsurface features to be determined. Figure 3.18 shows a depth profile of a thin film sample of PS. This depth profile signal initially increases rapidly, as with the block samples, but declines just as rapidly as the focal region emerges from the bottom surface of the sample. The sample thickness as measured using a micrometer was found to be approximately 70 μm, whereas with the depth profile obtained in air, the sample thickness appears to be close to 35 μm. With the addition of PDMS(L), this is increased to 60 μm, which is in much closer agreement to the actual thickness of the film, indicating as expected, a reduction in refraction effects. If the depth profile were repeated with Cargille oil OVH, the width of the depth profile would be expected to increase again and be even closer to the measured thickness of the sample. This was not achieved, however due to the viscosity of the oil causing sample movement, thus making the definition of the sample surface inaccurate.

These results fit well with the theory and results published by Everall [6] and show that when the depth profile is obtained in air the focal volume is indeed displaced and extended. As a result, the film appears much thinner than measured. This leads to the inference that subsurface features would also appear to be much thinner and closer to the sample surface than they actually are. For the case of PS, a NA of 0.75 and a refractive index of 1.59 (presented in figure 3.18), the experimental depth of focus is approximately twice the apparent depth. When using PDMS(L), this extension of depth of focus (and hence a reduction in sample thickness) is reduced again, as predicted by Everall [6]. PDMS(L) is not a perfect match in refractive index to PS however and hence the focal volume is still displaced and extended leading to an inaccuracy in determining the exact thickness and position of subsurface features It can be concluded therefore that even for samples with a uniform surface, an exact match in refractive index between the sample and immersion media is more important than discussed in previous sections.

3.3.6 Numerical simulation

As indicated earlier, Macdonald and Vaughan's numerical model, based on a photon scattering approach, fitted well with experimental data obtained using an air objective despite omitting, for simplicity, optical parameters such as refraction and the surface scattering of photons. This model will now be applied to the data obtained using an oil immersion objective to see if an accurate prediction of the depth profiles can be

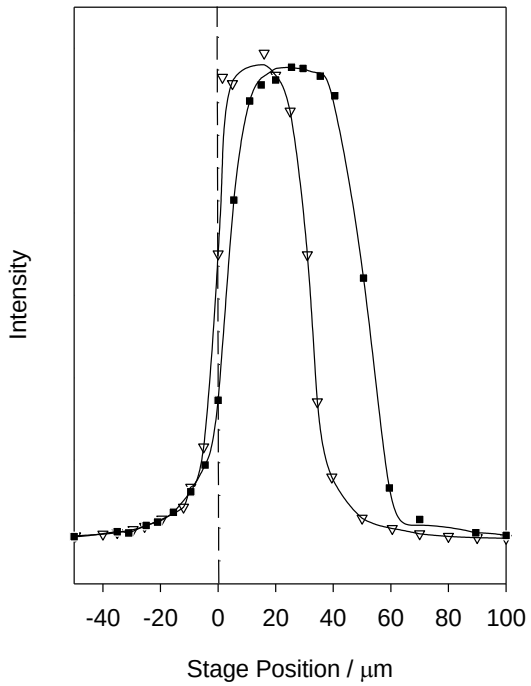

Figure 3.18: Depth profile of PS film in air (open triangles), the processed data from PDMS(L) (closed squares), and a solid line providing a visual guide to the overall shape of the depth profiles

obtained when refraction is minimal at the sample surface and if it is affected by surface scattering in abraded surfaces.

The various coefficients and scale factors used to fit the raw data to the numerical simulation can be seen in table 3.2. The aim of this section was not to create a new model but to see how the one presented compares with the data from samples immersed in oil, and so, for this reason, full details of the model have been omitted. Full details of the model can be found in [41]. It is interesting to note that for samples with a glass like surface the attenuation coefficients for both oil immersion method as are the same and much smaller than those obtained from air. This shows that a large portion of the attenuation in the model is related to surface scattering. This is also evident with the abraded surfaces when the lowest attenuation coefficients are needed for Cargille oil type OVH which has a much closer refractive index to the samples thus reducing surface scattering effects.

Using these coefficients and scale factors it was possible to fit the model to all of the data from the block samples in the previous section. Figures 3.19 to 3.23 show the comparison between the above numerical fits produced by applying the model to the

Table 3.2: Coefficients used to obtain fits with numerical model

Material	Surface Quality	Immersion	Attenuation Coefficient	Scale Factor
Polyethylene	Glass	Air	0.06	8.5
		PDMS(L)	0.04	11
		Cargille Type OVH	0.04	16
Novolen	Glass	Air	0.01	10
		PDMS(L)	0.000001	8.5
		Cargille type OVH	0.000001	9.5
	Finely	Air	0.07	17
	Abraded	PDMS(L)	0.01	15
		Cargille type OVH	0.0005	14
	Badly	Air	0.09	14
	Abraded	PDMS(L)	0.03	14
		Cargille Type OVH	0.005	12.5
Polystyrene	Glass Block	Air	0.00005	72
		PDMS(L)	0.005	80
		Cargille Type OVH	0.005	90

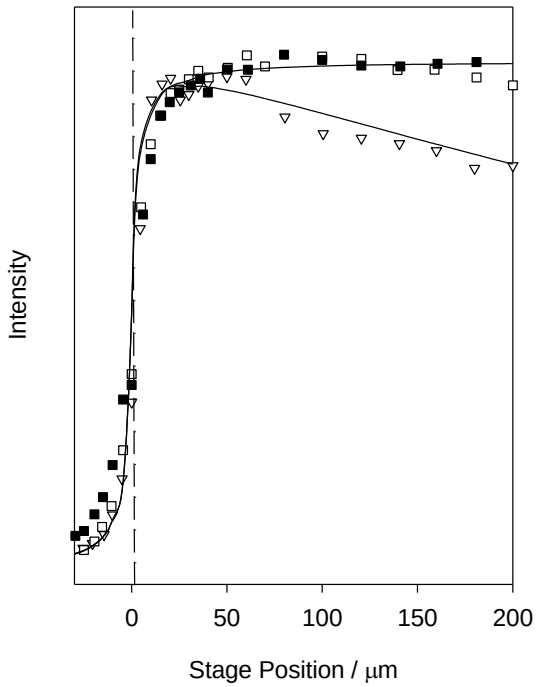

Figure 3.19: Comparison between the numerical simulation (solid lines), and immersion data of PS using an objective in air (open triangles), using an oil immersion objective in PDMS(L) (open squares) and processed data obtained using an oil immersion objective in OVH oil (closed squares)

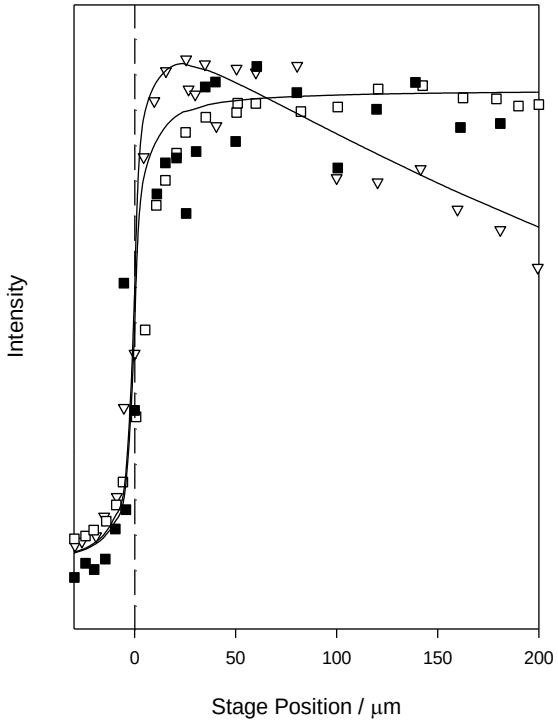

Figure 3.20: Comparison between numerical simulation (solid lines) and experimental data of Novolen in air (open triangles), PDMS(L) (open squares) and processed data from OVH oil (closed squares)

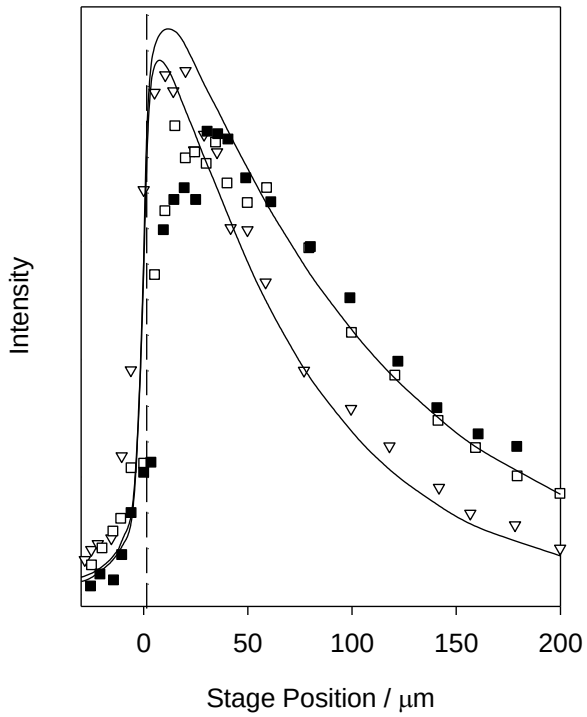

Figure 3.21: Comparison between numerical simulation (solid lines) and experimental data of PE in air (open triangles), PDMS(L) (open squares) and processed data from OVH oil (closed squares)

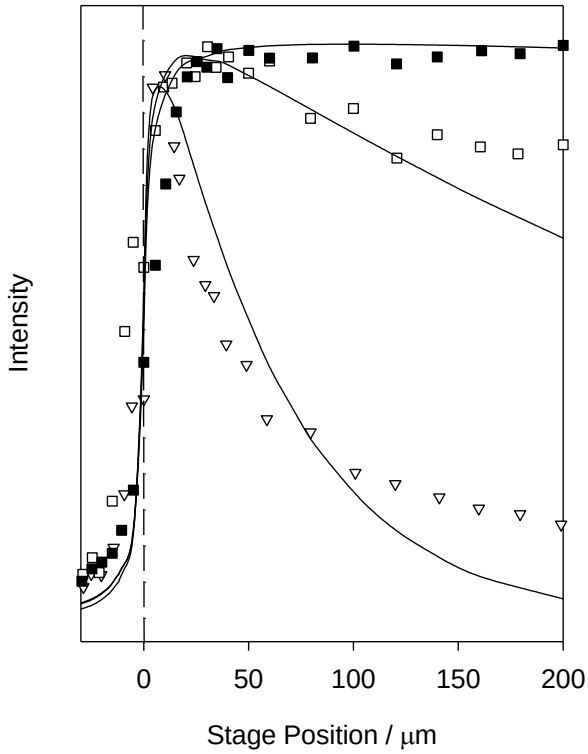

Figure 3.22: Comparison between numerical simulation (solid lines) and experimental data of Novolen with a finely abraded surface in air (open triangles), PDMS(L) (open squares) and processed data from OVH oil (closed squares)

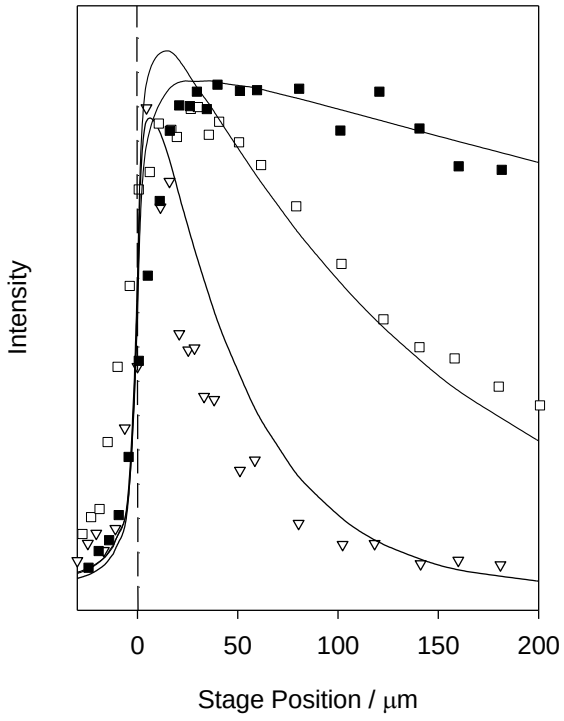

Figure 3.23: Comparison between numerical simulation (solid lines) and experimental data of Novolen with a badly abraded surface in air (open triangles), PDMS(L) (open squares) and processed data from OVH oil (closed squares)

raw data. When the samples have a high clarity and glass-like surface, such as with PS and Novolen (shown in figures 3.19 and 3.20), good agreement can be seen between the model and the data from the oil immersion objective with both immersion oils, just as when the data were obtained in air. In these figures the solid line now represents the predicted depth profile from the model. When the model is applied to the data obtained from PE (figure 3.21), which is of a lower optical clarity than Novolen and PS, there is good agreement between the model and the data obtained in air.

Comparing the predictions of the model and the experimental data obtained with oil immersion, it is evident that the former involves a more rapid initial rise in intensity than is seen in the experimental data, although the following decline and rate of attenuation is similar in both cases. Figures 3.22 and 3.23 show how the model compares to samples with abraded surfaces. Here, in both cases, the model fits poorly with the data obtained due to the scattering effects at the sample surface. With the application of immersion oil, however, the model begins to resemble the experimental data more closely and the agreement between the simulation and experiment is best when the sample is immersed in OVH. This leads to the conclusion that although the model is unable to accurately predict the depth profiles of samples with a highly scattering surface, with the application of appropriate immersion oil, agreement between the experimental and simulated data can be found. It can also be concluded that with a closer match in refractive index between the sample and immersion oil the closer the simulated data fits with the experimental data as predicted in the previous section.

Although agreement was found with the experimental data, the model provides the most accurate fits when the samples are in air and, with the exception of the abraded samples, least accurate when the refractive index of the sample is matched with Cargille oil type OVH. As well as this, significant discrepancies exist when the focus lies above the sample surface. In this case, the response predicted of the model increases more rapidly than the signal measured experimentally. More important, however, is that in some cases a near 0 attenuation coefficient had to be used in order to fit the model to the data. A revised version of the simulation is needed in order to take account of previously ignored phenomena, such as oil immersion and surface condition. From the data it is clear that refractive index and sample thickness are an important factor and the ability to simulate the Raman photons both above and below the sample needs to be improved. In an attempt to address some of these issues the model was revised.

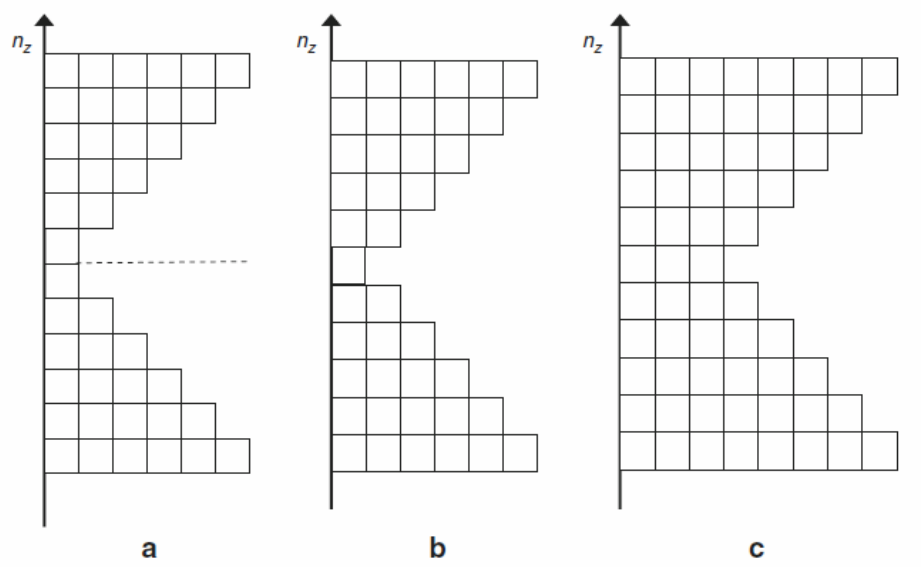

Figure 3.24: Schematic diagram of model, (a) shows the original model, (b) shows revision 1 and (c) shows revision 2

Two revisions were added to the model such that symmetry at the focal point and lateral focal blurring were taken into account. Figure 3.24 shows schematic diagrams of the original model and the model after each revision. In this figure, each cell can be thought of as an annular volume surrounding the rotation axis, *Z*, in which the probability of photons generated in this volume is calculated. The original model shown in figure 3.24(a) assumes symmetry at the focal point (cell (1,1)) such that the illuminated volume is reflected in the mirror plane shown by the dashed line. This mirror plane increases the focal point to cells (1,1) and (-1,-1), which is similar to the ideas of Everall as mentioned earlier. The first revision to the model involves moving the mirror plane such that it intersects cell (1,1), reducing the focal point in the model to a single cell, as shown in figure 3.24(b). The second revision takes into account lateral focal blurring; the extent of the focal point has been increased laterally from one to three cells, as shown in figure 3.24(c). This revision simulates forward scattering of the exciting beam, which serves to change the photon trajectories thus meaning there is no precise focus within an appreciably scattering material.

Figures 3.25 to 3.27 show the comparison between the experimental data obtained from the glass-like samples with immersion oil and the revised model. It is worth noting that in order to obtain suitable fits the degree of lateral 'blurring' due to scattering needs to be adjusted depending on the clarity of the material. The optically clear PS required the least amount of blurring (a focal point of 3 cells was used) and the Novolen required a focal point of 5 cells. PE, however, is considerably more opaque than the other samples and hence the effects of scattering are increased; a

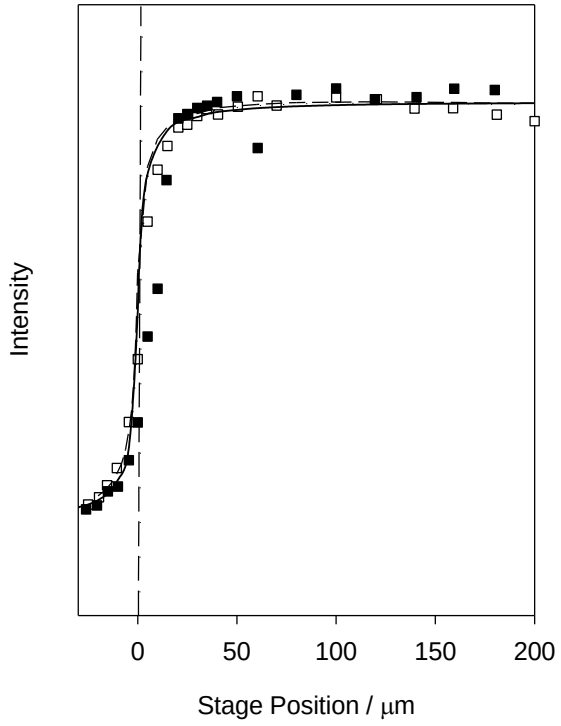

Figure 3.25: Comparison between revised model (solid curve), original model (dashed curve), experimental data from PS in PDMS(L) (open squares) and processed data from OVH oil (closed squares)

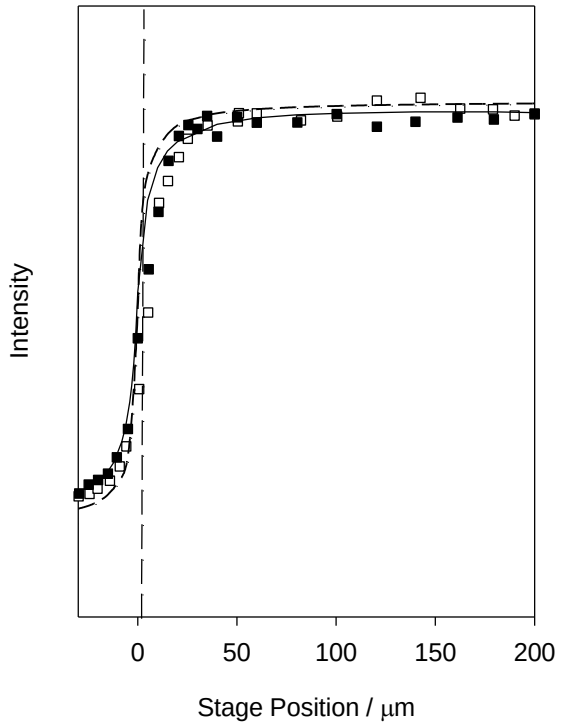

Figure 3.26: Comparison between revised model (solid curve), orginal model (dashed curve), experimental data from Novolen in PDMS(L) (open squares) and processed data from OVH oil (closed squares)

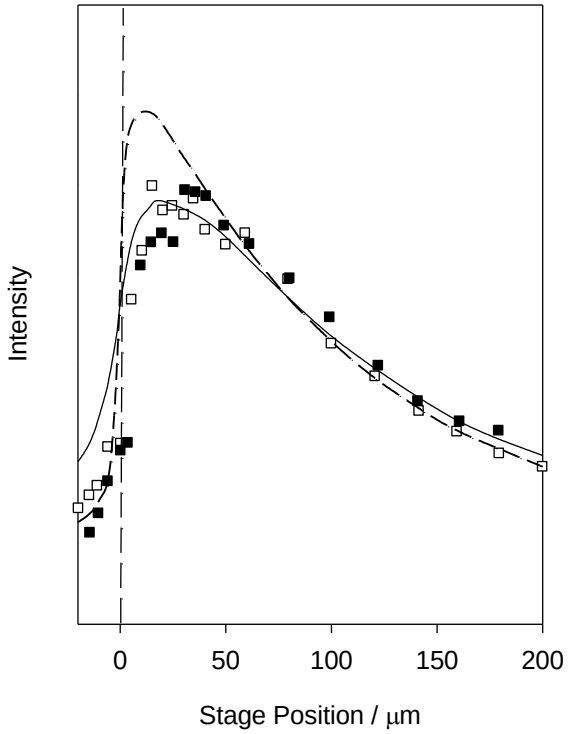

Figure 3.27: Comparison between revised model (solid curve), original model (dashed curve), experimental data from PE in PDMS(L) (open squares) and processed data from OVH oil (closed squares)

much bigger focal point is therefore needed in order accurately to simulate the experimental data. In the data shown, a focal point of 15 cells was used for PE.

As with the initial model, there remains good agreement between the model and experimental data. As with the previous version of the model however, the increase in intensity of the depth profile for stage positions between 0 and 20 μm below the sample surface is greater than that of the experimental data. Despite this the depth profiles predicted are in closer agreement than previous attempts, especially for the optically clear samples. The prediction of the depth profile of PE, however, shows a large increase in intensity when focused above the sample despite excellent agreement after the focus has been shifted below the sample surface. This suggests that the effect of lateral blurring is not constant and in order to provide an optimum fit of the model to the data, focal blurring should be treated as a function of depth. Ideally no lateral blurring of the focal area is required when focused above the sample but when focused below the surface of the sample, significant blurring is needed, the value of which is dependent on the scattering properties and clarity of the sample.

3.4 Conclusions

The application and effectiveness of CRMS in the analysis of transparent polymers has been studied. Depth profile data were obtained from a variety of different polymers and immersion media and the results compared to a numerical model proposed by Macdonald and Vaughan. This comparison enabled both the effectiveness of the model and experimental procedure to be evaluated and refined. Factors such as sample thickness and surface condition were also taken into account.

From the work described above 3 key conclusions can be drawn:

- Previous work on CRMS suggests that the focal point within a sample is well defined even when certain optical effects such as refraction are taken into account. This work, however, has shown that a Raman signal can be found up to 50 μm above the sample surface as well as below, regardless of whether an immersion oil is used or not. This suggests that the Raman photons come from a large extended illuminated volume instead of a small, well defined focal point.

- With the application of an oil immersion lens and an oil of suitable refractive index to a sample with a non-perfect surface, the attenuation seen in the depth profiles below the sample surface is reduced. This is due to a reduction in the scattering of photons at the sample surface and hence leads to an increase in Raman signal. When the sample surface is optically flat, however, an exact match in refractive index between sample and oil becomes less important. In either case, care must be taken in the selection of the immersion oil so that the Raman peaks of the oil do not interfere with those of the sample. If this overlap does occur, then a simple numerical correction can be applied to the raw data to eliminate the contribution of the peaks from the oil in the final spectrum.

- Finally, the form of the depth profiles obtained via CRMS can be predicted with some accuracy with a revised version of the numerical model proposed by Macdonald and Vaughan, which was based on the photon scattering approach. These revisions provided close predictions to the experimental data of the samples analysed with immersion oil and takes into account the optical clarity of the system. The model, however, still needs further revisions.

In summary, careful consideration of the optics involved in CRMS and the application of immersion oils to reduce refraction and surface scattering, combined with modelling

the system on a basic photon scattering approach, it is possible to use CRMS more accurately than previously assumed to depth profile transparent polymeric materials. The model and experimental method are still not perfect and further revisions are required but in its current form it is possible to use this approach with some confidence to study the chemical compositions of transparent polymers both above and below the sample surface.

4 : Void Analysis

Electrical ageing in polymeric insulators is generally believed to originate in small gas filled voids within the bulk of the material [10]. Understanding the ageing process that occurs within these voids is essential as conventional wisdom indicates that it is a precursor to electrical treeing and complete electrical failure [109]. The process of ageing originating in voids was investigated using CRMS on subsurface voids found in samples of electrically stressed LDPE. This also enabled the investigation of the application of CRMS in the analysis of electrically aged polymers. An optical depth profiling technique was used to probe an electrically aged void along the optic axis whilst a void subjected to complete breakdown was analysed at various lateral positions. These results were compared to voids of known dimensions in samples formed by layering sheets of PE and subjected to PD activity provided by the University of Bologna.

4.1 Background

4.1.1 Void production

During the manufacturing process of polymers, small gas filled voids ranging in diameter from a millimetre down to a few tens of nanometres are formed within the bulk of the polymer [10]. In polymers used as high voltage cable and machine insulators, such as PE and epoxy resin, voids may additionally develop in between the polymer insulation and the electrode. These voids have been reported to arise from non-uniform mechanical stresses on the polymer or from chemical reactions during processing [109]. Great care is taken to minimise the presence of voids in polymeric insulators during manufacture and processing but it is difficult to rid the polymer of them completely. High voltage machine insulation is, in particular, prone to the formation of voids within the insulation. Voids can be caused in insulation systems based on layered mica or glass fibre embedded within a resin, by delaminations, cracks and wrinkled or damaged mica layers [109-112]. If a polymer is subjected to a high electric field, as in the case of high voltage insulators, PD occurs across the voids within the polymer, thus resulting in degradation of the insulation.

4.1.2 Partial discharge mechanisms within gaseous voids

Gas has a lower permittivity (ε_g) than polymeric insulators (ε') [9]. By definition, a vacuum has a relative permittivity of 1. Under the same conditions air has a relative permittivity of approximately 1 and polyethylene 2.25. When there is a gas filled void within a polymer under the influence of an electric field (*E)*, the lower permittivity in the void leads to an increase in the local electric field E_v [10]. The degree to which the field is increased across the void depends on factors such as the nature of the

insulation, the type of gas present in the void, the size and shape of the void, the pressure of the gas and the temperature of the system [9]. For a disk like void:

$$E_v = E\frac{\varepsilon\prime}{\varepsilon_g} \tag{4.1}$$

If the electric field within the void is of a sufficient strength and the voltage across the void is greater than the breakdown voltage (V_b) (defined as the voltage below which breakdown will not occur across a gas filled void under certain conditions [10]), then breakdown of the gas and hence PD activity can occur. If ε_g = 1 then the breakdown voltage is given by [9]:

$$V_b = E_g d'[1 + (d/d' - 1)/\varepsilon'] \tag{4.2}$$

Where E_g the dielectric strength of the enclosed gas, d the thickness of the specimen, and d' the thickness of the cavity.

PD activity occurs when a 'free' electron within the void is accelerated by the applied electrical field. The first free electron within a void appears when a molecule either in the gas in the void or the surrounding bulk material receives enough energy from surrounding field to overcome its binding energy. As the electron is accelerated it interacts with the gas molecules within the void and, if it has sufficient energy, ionizes them. This ionization results in another 'free' electron, a positive ion, and heat (amongst other by-products). These bi products propagate throughout the void due to the electric field thus resulting in further collisions with gas molecules and hence more free electrons/ionisation products. This process of gas ionisation is known as Townsend electron avalanche [113]. It has also been shown that conductive channels and streamers can form across the void in the direction of the field enabling a PD to occur [114].

4.1.3 Paschen's law

Its is assumed that the discharges within the void obey Paschen's law which states that the breakdown voltage (V_b) across a uniformly stressed gap (between two copper electrodes) depends on the product between the length of the gap (d) and the pressure of the gas (p) as given by [10]:

$$V_b = \frac{apd}{\ln(pd)+b} \tag{4.3}$$

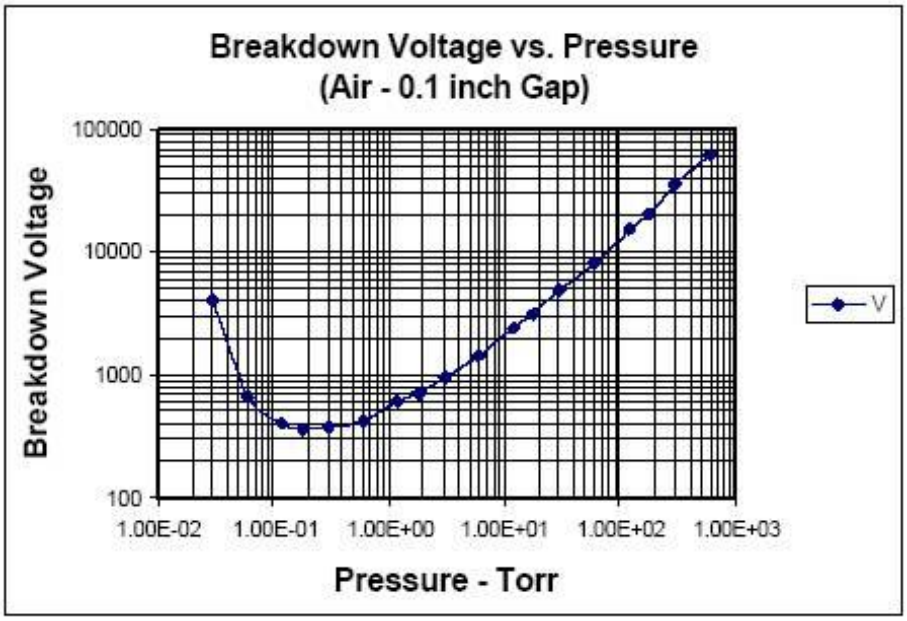

Figure 4.1: typical Paschen curve for air across a gap [35]

Where *a* and *b* are constants related to the composition of the gas in question. Figure 4.1 [47] shows a typical Paschen's curve for air and from this we can conclude that there is a minimum breakdown voltage regardless of the size of gap or density of gas (for air this is 327 V at a standard atmospheric pressure and a gap of 7.5 μm [10]). With constant gap spacing, however, below a minimum value of voltage, the voltage required to break down the gas increases rapidly with a decrease in pressure. This increase is due to a reduction in the number of molecules within the gas and hence increasing the mean free path of the free electrons prior to collision [47]. After the minimum voltage is reached, the breakdown voltage increases with pressure. This increase is due to the 'free' space between molecules in which electrons can move, decreasing and hence reducing the mean free path of the electrons prior to collision [47]. It should be noted that the shape of the curve for all gasses is similar but with slightly varying values for the minimum breakdown voltage and rate at which the V_b increases with pressure.

4.1.4 Polymer degradation via PD activity

Despite the fact that the polymer itself does not break down when $V>V_b$, the PD activity across the void is damaging to the polymer and over time may cause complete breakdown of the insulator [115]. The initial degradation processes that occur within a polymeric insulator can be categorised into one of two categories: ion/electron bombardment and chemical reactions [10]. PD activity within a gas filled void causes high energy ions and electrons to be produced. These high energy particles are accelerated by the electric field to the walls or edges of the void, and impact with the

walls of the void. Although the individual energies of these particles may not be sufficient to cause damage, combined they may cause localised damage [116].

Serra, Montanari, Mazzanti and Dissado have suggested that this ion bombardment combined with the resulting increase in localised temperature causes small micropits to form on the void walls [117-120]. In these studies it was reported that these micropits do not by themselves cause a large amount of damage to the polymer but when combined with damage caused by chemical reactions they can help accelerate damage by deepening cracks. These cracks are reported to be the precursor to electrical treeing and complete breakdown as hypothesised by Serra et al [117], Liu et al [31] and Dissado et al [22] to name a few.

The PD activity can also cause chemical reactions within the gas. If the gas within the void contains oxygen (such as air), then the high energies of the PD activity can lead to the formation of atomic oxygen, ozone and nitrogen oxide [23]. These highly reactive molecules can then in turn, react with the void surface causing damage [22]. As well as this the pressure of the gas within the void can increase as the temperature rises which decreases the rate of PD activity (due to a higher inception voltage needed). The rise in pressure however can accelerate the degradation by widening cracks in the void surface [10].

4.1.5 Void degradation and electrical treeing

Dissado et al have reported that electrical ageing of voids is a precursor to electrical treeing [115] and thus, complete electrical breakdown of a polymer. Characterising the chemical processes that occur during degradation of polymeric insulators due to PD activity within voids is of great importance as it enables us to understand how electrical insulators age. In recent studies by Vaughan et al [25, 32] CRMS has begun to reveal the chemical processes involved in electrical treeing and ageing in dielectric materials.

As described in previous chapters, this technique is thought to have the potential to provide spectroscopic data with a spatial resolution of the order of 1 μm along both the lateral and optic axes [34] and, since excitation involves visible photons, the technique is also thought to be capable of interrogating the interior of transparent dielectrics, such as polyethylene and polystyrene. As discussed in chapter 3, CRMS is however, more complicated than previously thought. Due to various factors including diffraction, refraction, scattering and absorption, the focal region in CRMS becomes displaced and blurred leading to an inaccuracy in calculating the spatial location and

resolution of the system. If the full potential of this approach is to be realised, the true spatial origin of the detected Raman photons must be determined.

This chapter describes an alternative and novel approach to this problem and combines the optical depth profiling technique used in the previous chapter with a chemical analysis of voids that have experienced PD activity within a polymeric insulator.

4.1.6 Aims and objectives

Specifically, the aim of this chapter is to apply the methods described in chapter 3 to analyse the chemical changes that occur within electrically aged voids in PE. This will not only facilitate an evaluation of the effectiveness of CRMS in the analysis of polymeric insulators but will provide an initial investigation into the electrical ageing of polymers which will be compared to other types of ageing in following chapters. Following CRMS analysis, the voids will also be analysed via FTIR, SEM and optical imaging. The results will be discussed with respect to electrical ageing in voids and electrical treeing in PE.

4.2 Experimental

4.2.1 Materials

Plaque samples of low density polyethylene (approximately 700 μm thick) were prepared by hot compression of a blend of LDPE and azodicarbonamide in a mould. Heating the samples for a second time causes the azodicarbonamide to decompose into a gaseous state (containing mainly CO_2), so generating voids within the bulk of the sample. By regulating the amount of azodicarbonamide, the number of voids in the samples could be controlled to result in singular voids approximately 1mm in diameter. PD was then initiated across samples containing voids. In the account that follows, sample 1 is aged yet intact whereas the partial discharge across sample 2 resulted in complete breakdown and caused the void to burst.

As well as this, for comparison, samples containing voids, supplied by Wang Le and Prof G. C. Montanari (University of Bologna), were also analysed. These samples were made by hot pressing 2 sheets of cross linked polyethylene (XLPE) on either side of a layer of LDPE in which a micro cavity was embedded. The structure and dimensions of the samples is shown in figure 4.2. An AC voltage of 10 kV (RMS), which corresponds to an average electric field in the cavity of 43.5 kV/mm was applied across the sample using planar electrodes. These samples were then aged under this voltage for 16, 54, 75, 110, 123, 140 and 157 hours. Unfortunately no additional information was

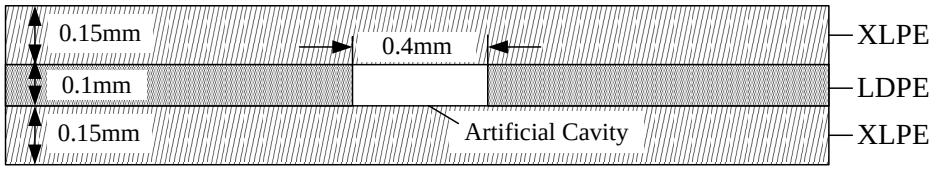

Figure 4.2: structure and dimensions of layered void sample

available concerning the exact nature and manufacture of the materials used for these samples

4.2.2 Method

The samples containing voids were analyzed via CRMS using the method for depth profiling detailed in the previous chapter but with the laser set to 25% power to minimize sample damage. Sample 1 was probed at various positions along the z axis through a void and sample 2 was analyzed at several lateral positions across the burst void. The layered samples were also probed using CRMS at various intervals along the z-axis in air, and using an oil immersion lens before being split via microtomy and the exposed void surfaces analysed using CRMS, FTIR, SEM and optical microscopy.

4.3 Results and discussion

4.3.1 Blown samples

Various stage positions ranging from the focal point being at the sample surface to it being deep inside the void in sample 1(as shown in figure 4.3) were analysed using CRMS. Thereafter, various lateral positions (figure 4.4) along the surface of the failed void in sample 2 were analysed using the same technique. The resulting spectra can be seen in figures 4.5 and 4.6.

It can be seen from the spectra in figure 4.5 that when focused on the surface of the sample, the typical spectrum of PE results, (as shown in previous chapters) with the addition of a small extra feature located at approximately 500 cm^{-1}. As the focus is moved into the sample, this PE signal initially increases (as predicted in chapter 3). When at a stage position of approximately 100 μm below the surface, no PE is present in the spectrum, indicating the presence of a void. Beneath the surface of the sample there is a rise in each spectral background at the lower wave numbers. This rise is associated with fluorescence effects and, although no chemical data can be extracted from these Raman spectra, it is taken to indicate ageing as shown by Sayers et al [5]. There are also additional spectral features present in all of the spectra between 600 and 300 cm^{-1}. These peaks are located at approximately, 318, 409, 508, 542 and 587 cm^{-1}. These features are not present in scans of pure PE in previous chapters but are

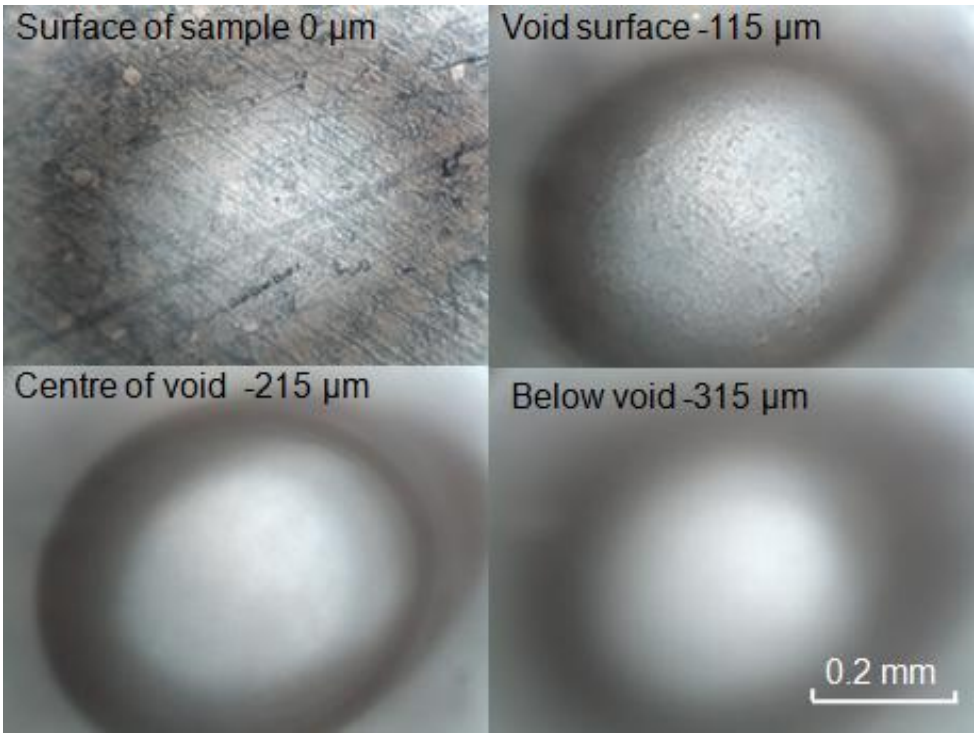

Figure 4.3: Optical micrographs of the void in sample 1 at various positions along the optical axis

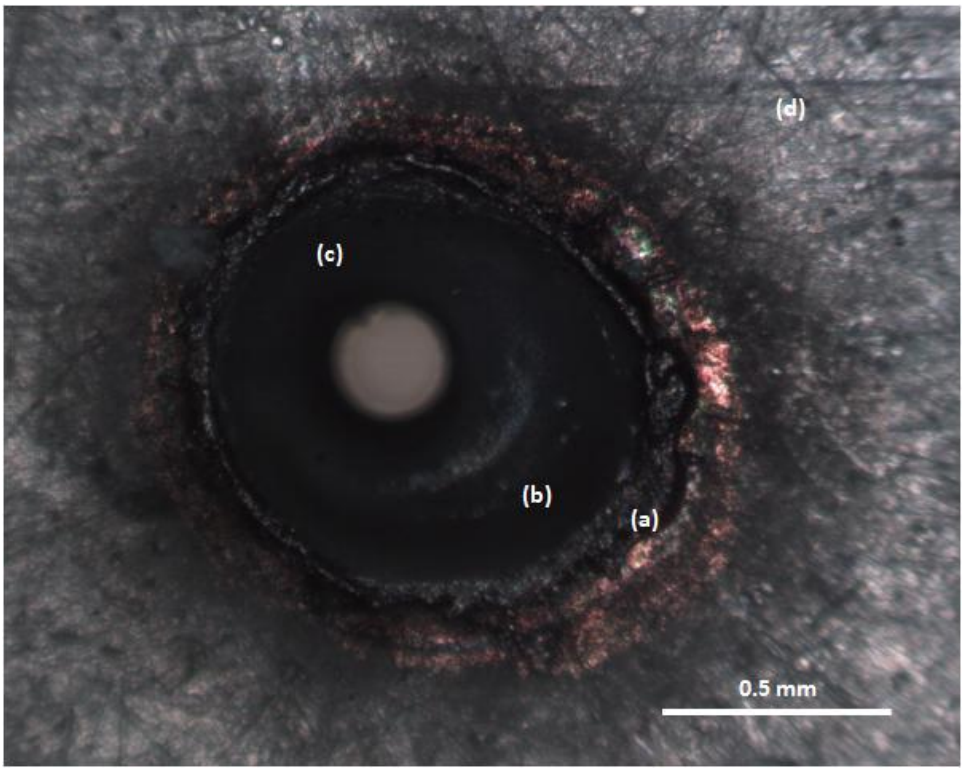

Figure 4.4: Optical micrograph showing lateral positions analysed in sample 2

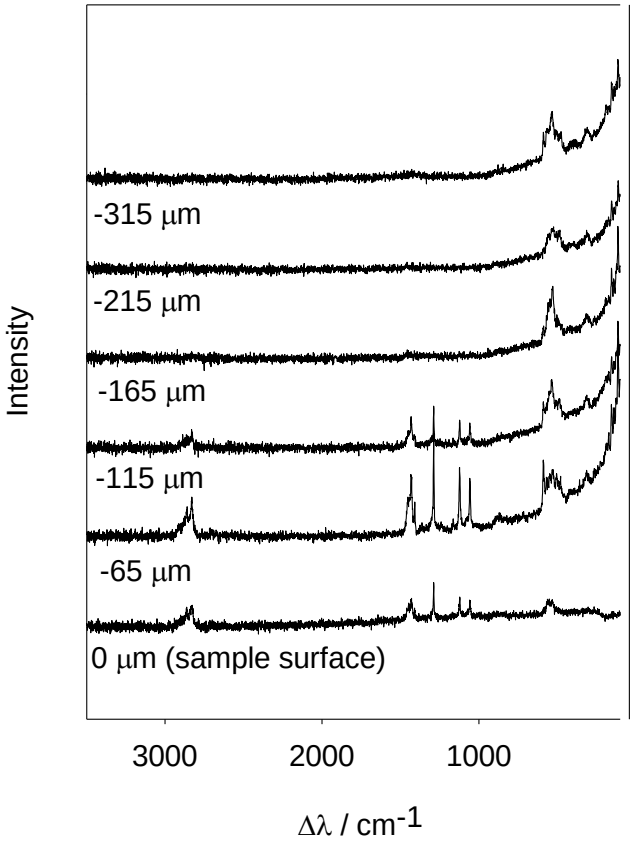

Figure 4.5: Raman spectra for various depths in void in Sample 1

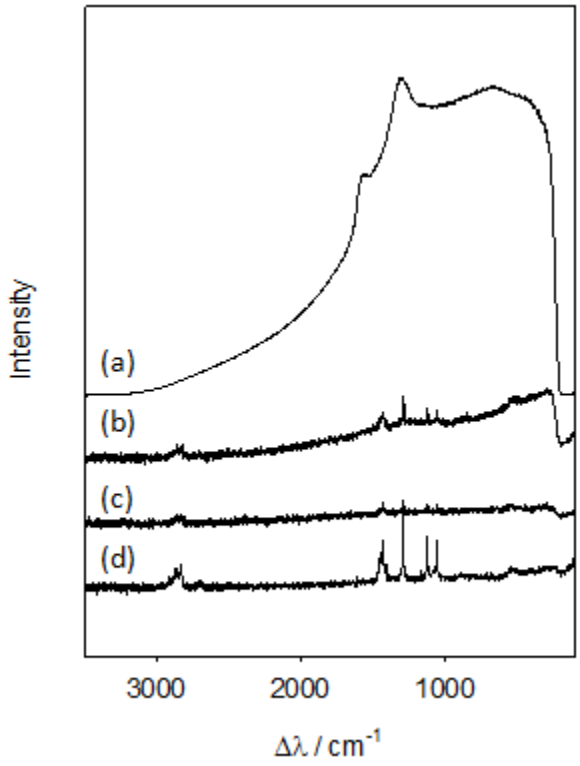

Figure 4.6: Raman spectra for lateral positions of sample 2

located on the surface of the sample and are present throughout the sample and void. This indicates that the origin of these peaks could be either from the polymer bulk or the void itself. In the later case, the photons originating from the void surface must be of a sufficient number to enable detection from up to 100 μm below the focal plane of the laser.

In figure 4.6, the laser is focused in a region of undamaged PE and so the spectrum from region (d) is typical of PE with an extra feature at around 500 cm^{-1}. Region (c) is in the centre of the burst void and so the spectrum gained from this region shows nothing other than vestigial PE peaks associated with material remote from the focal point. At low wave numbers, in the spectrum gained from the edge of the void (region b), a PE signal is recognisable but with an increase in background signal as with the spectra in figure 4.5. We take this to indicate fluorescence and hence ageing. Finally, in region (a), which corresponds to the discoloured region at the edge of the burst void, a large amount of fluorescence is present as well as two wide bands at approximately 1320 and 1580 cm^{-1}. These two bands are the D and G bands of graphitic carbon and they indicate the presence of sp^2 hybridised carbon in the form of polycyclic aromatic hydrocarbons (PAHs) [25, 121].

The presence of carbon in these samples is not unexpected and it indicates that the energies involved with the PD activity that occurred within the void during ageing were sufficient to initiate scission of the polymer chain to form smaller polymer fragments. In 2002 Frenklach studied polymer fragments from PE and small aliphatic compounds which then under subsequent reactions to produce ring structures via the following reactions [122]:

$$C_3H_3+C_3H_3 \rightarrow C_6H_6 \text{ (benzene)or } C_6H_5+ H \text{ (phenyl)}$$

$$nC_4H_3 + C_2H_2 \text{ (acetylene)} \rightarrow C_6H_5$$

$$nC_4H_5 + C_2H_2 \rightarrow C_6H_6+H$$

Additional phenyl rings are then added to form PAHs of various sizes. There are 3 main proposed mechanisms involved in the addition of these rings as described below:

1. Acetylene additions and ring closure reactions following the loss of a hydrogen atom. Sometimes referred to as H abstraction C_2H_2 addition (HACA). Proposed by Frenklach et al [122-124].

2. Two acetylene molecules combine and then react with the existing ring to form an additional one, termed the Bittner-Howard mechanism [125].
3. A reaction between two C_5H_5 rings followed by a rearrangement to form two fused C_6 rings [126].

While the reacting molecules are rather different from the likely decomposition products of PE, and it is entirely possible that the composition of the gas within the voids could affect the chemistry, the above reactions do illustrate how PAHs can be formed under appropriate circumstances from simple precursors.

It is the carbon bonds within these PAHs which give rise to the D and G bands identified in Raman spectra in figure 4.6. The G band, located at 1580 cm^{-1}, is related to the C-C stretching mode in the layers of graphitic carbon whereas the D band, located at 1320 cm^{-1}, has been reported to be related to scattering from defects and disorder which break the symmetry of the graphene sheet [127]. The ratio between the intensity of the D and G bands provides an indicator to the level of disorder within the system and is often used to distinguish between different types of carbon nano tubes (CNT) [36, 128].

The spectral signature for region (a) of the spectrum is characteristic of certain electrical trees grown in PE. Previous Raman studies of electrical trees in PE have [25, 31, 32] yielded the 3 following signatures; pure PE in the regions between tree branches, fluorescence in the regions close to the tree channels and the D and G bands of disordered sp^2 carbon in the centre of conducting tree channels. As can be seen from the results presented above, the same three spectral signatures as those found in electrical trees were obtained by a lateral examination of voided samples that have experienced partial discharge activity.

Whilst gathering the data for figure 4.6, it was possible to focus on the surface of the void. The apparent focal position of the void surface however, appeared much closer to the surface of the sample compared to its actual position. CRMS enables transparent samples to be probed and subsurface features revealed but, due to the factors described in the previous chapter, it is difficult to quantify the exact positions within the sample from which data are obtained. CRMS was much more effective in analysing the lateral positions in sample 2 and chemical signatures matching those in other work on electrical ageing in PE was found [5, 31, 32, 116]. In order further to understand the use of CRMS in depth profiling voids, the same process was repeated on layered samples where the exact location of the void is known.

4.3.2 Layered samples

The layered samples containing voids were probed using the same depth profileing method as used on sample 1. Spectra were obtained from the surface of each sample and at regions beneath the sample surface obtained by moving the stage in increments of 50 μm such that the focal volume is moved through the sample and into the void. In most of the samples the observed void surface lay at a stage position of 80 μm below the surface (an observations predicted in chapter 3).

Figures 4.7 to 4.12 show the spectra obtained for all the layered samples. With the exception of figure 4.9, all of the samples contain similar spectral features. At the surface of the samples, the spectral peaks of PE are visible between 1000 and 1500 cm^{-1}. As the focus is shifted into the bulk of the sample towards the surface of the void, these PE peaks are still present but at a reduced intensity. All spectra also appear to exhibit fluorescence with the intensity of this flourescence increasing with ageing time.

As soon as the focus is no longer at the surface of a sample, the same series of peaks between 600 and 300 cm^{-1} appear as identified in the previous section. These peaks are not present in the spectra of PE as shown in chapter 2, so it can concluded that their origin is not from the PE matrix. It can also be concluded that they are not related to the cross linking by-products of XLPE, as, there has been no previous evidence of them in the Raman spectra of un-aged XLPE [129]. Although they are present in an un-aged layered sample, they are also present in samples made from LDPE instead of an LDPE/XLPE 'sandwich'. This further reinforces the suggestion that the features in question do not originate from the residues that remain from the cross linking process of PE. It is possible that these peaks originate from some antioxidant additive in the PE [130], or contamination during the manufacturing process of the samples.

Another possibility is that these peaks are related to oxidisation by-products that occur when the oxygenated species react with the void surfaces during ageing. As the voids are filled with air it is logical to assume that there is a significant volume of oxygen within each void. If ageing does indeed cause the bonds between the various atoms in the polymer to be broken, it can also be assumed that there is an amount of carbon and hydrogen in this gas following ageing. It is therefore possible that these molecules can then react with each other to form bi- products such as CO_2 and OH. Raman studies of these substances have revealed that some peaks for these

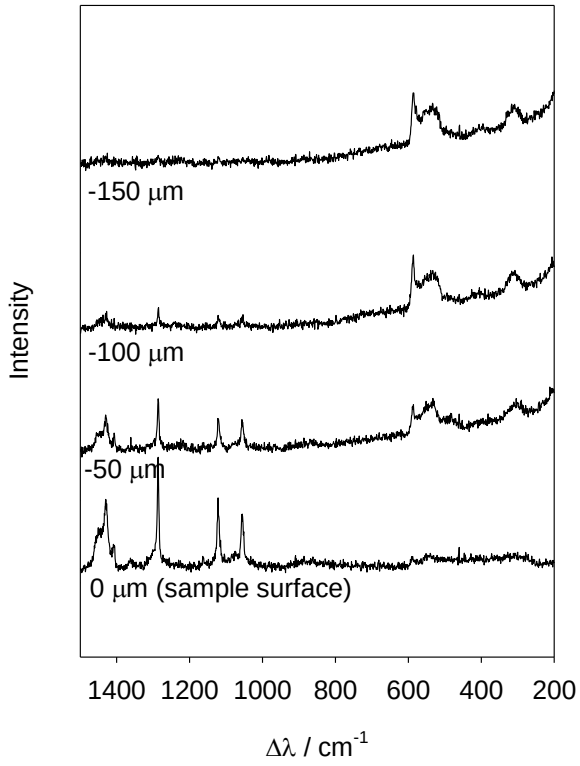

Figure 4.7: Raman spectra taken at various optical depths for layered sample aged for 54 hours

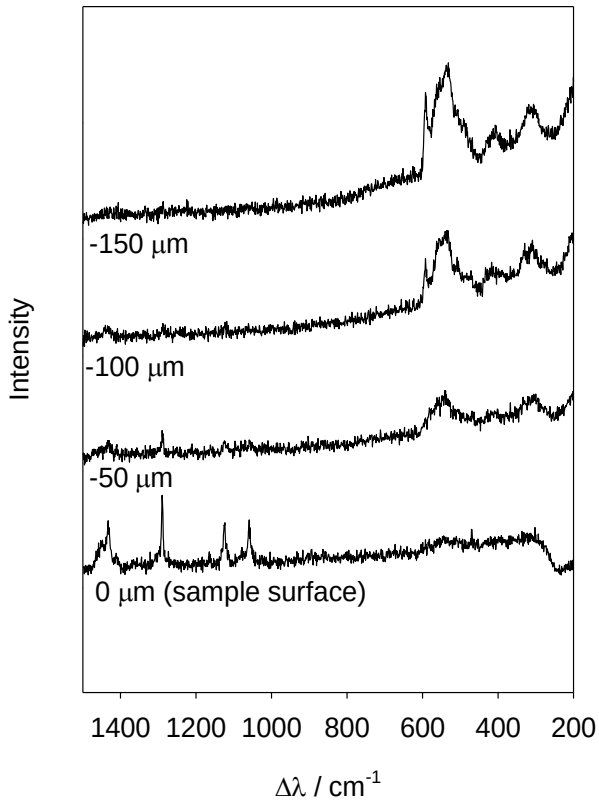

Figure 4.8: Raman spectra taken at various optical depths for layered sample aged for 75 hours

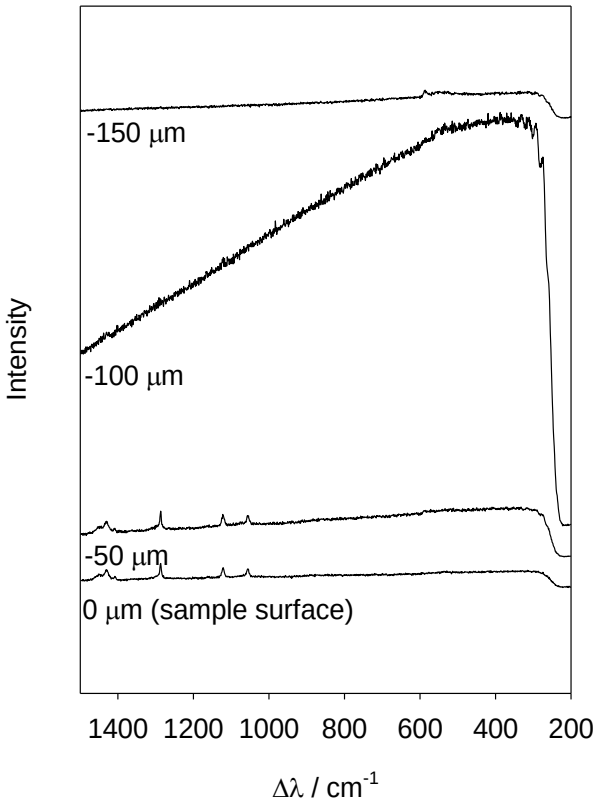

Figure 4.9: Raman spectra taken at various optical depths for layered sample aged for 110 hours

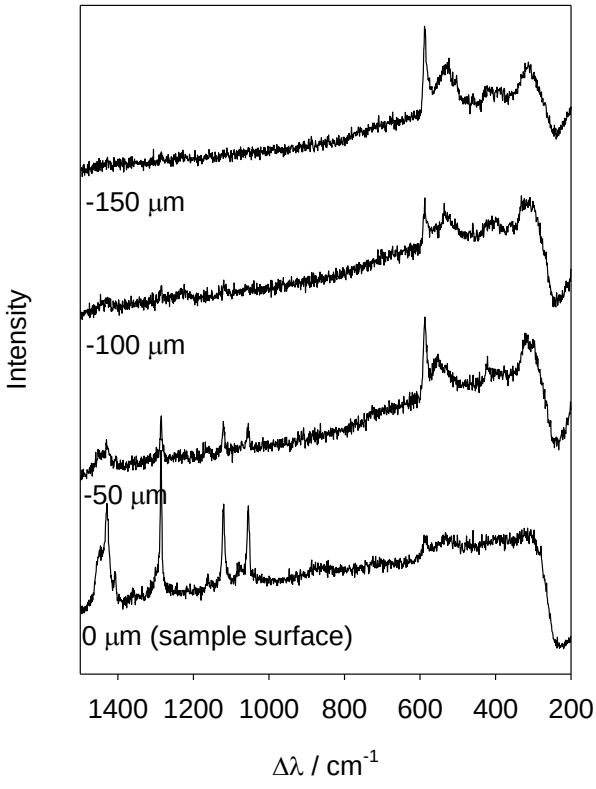

Figure 4.10: Raman spectra taken at various optical depths for layered sample aged for 123 hours

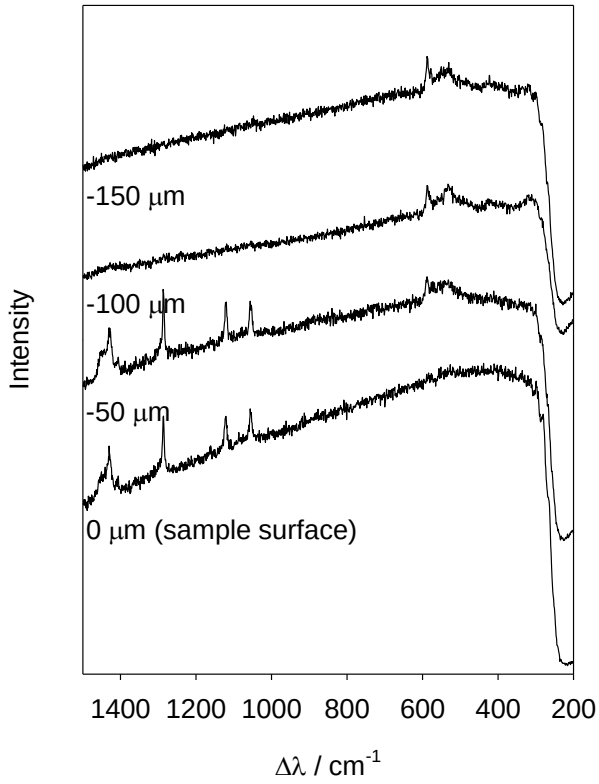

Figure 4.11: Raman spectra taken at various optical depths for layered sample aged for 140 hours

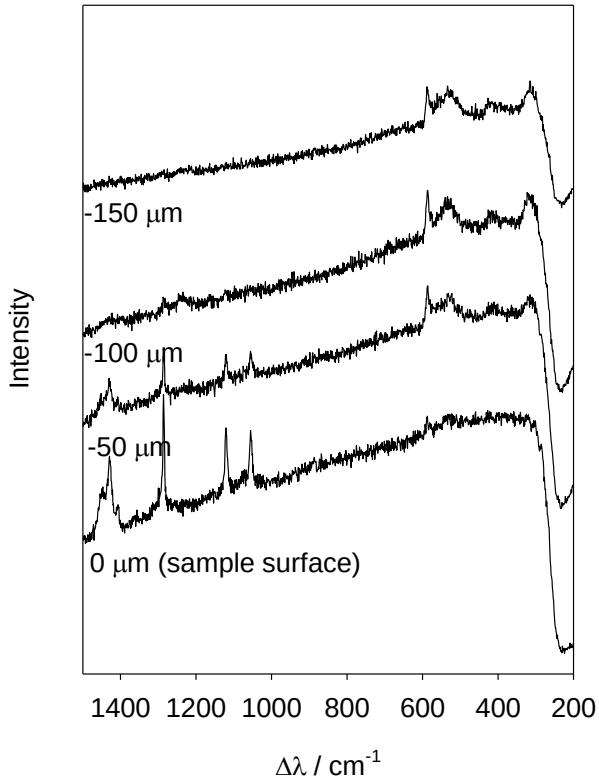

Figure 4.12: Raman spectra taken at various optical depths for layered sample aged for 157 hours

Table 4.1: Raman spectral peaks of electrically aged PE between 600 and 300 cm-1 and their possible vibrational modes

Approximate spectral peak value ($\Delta\lambda$ / cm^{-1})	*Possible vibrational mode*	*Reference*
318	-	-
409	-	-
508	δ CO2	[131]
542	T O-H	[131]
587	T O-H	[132]

δ – deformation, T – torsion

substances overlap those peaks belonging to the void samples in this chapter [131, 132]. A list of the identified peaks in the region between 300 and 600 cm^{-1} for the void samples in this chapter and their possible related vibrational modes can be seen in table 4.1. Not all the peaks found in this region could be identified and so further chemical analysis is needed.

Figure 4.9 is the exception to the trends discussed above. At 0 and 50 μm the presence of PE can be seen, as with the other samples, but the peaks at lower wave numbers can no longer be seen due to a large amount of fluorescence at 100 μm. The cause of such a large presence of fluorescence is unknown but is constrained to this focal region and when the focus is moved deeper into the void it is no longer visible. One reason for this could be that for this particular sample the ageing process left a highly fluorescent residue on the void walls. This residue did not occur, or at least not to the same extent, in the other samples. The presence of fluorescence in the spectra is similar to the results obtained when Vaughan et al performed a similar study on a conducting electrical tree in PE [25]. As well as this the noise levels seen in the spectra appear to be lowere. This is merely due to the different scales used to present the data due to the large amounts of fluorescence in the spectrum at -100 microns.

Following this analysis, comparative depth profiles were performed on 2 layered samples. One of the samples contained an un-aged void and the other was an aged sample containing no void (see figures 4.13 and 4.14). The depth profile was performed at regular intervals up to and including a stage position of 200 μm below the sample surface.

Figure 4.13 shows the un-aged void and, as expected (and discussed in the previous chapter), the peaks belonging to PE initially increase in intensity before dropping off and disappearing at a stage position of approximately 80 μm below the sample

surface. Although the position of the void is known to be approximately 150 μm below the sample surface, refraction effects explain the apparent shift in the position of the void when the data was collected. Also the peaks of unknown origin at around 600 cm^{-1} are present in all the spectra even when focused within the void.

This leads to one of two possibility; either the entire sample (including the air within the sample) contains this chemical trace or, the walls of the void contain large amounts of this species and the Raman shift caused by it is strong enough that it can be seen when focused a large distance above the area in question. As these peaks are present in the un-aged sample spectrum, it could be possible that they belong to a bulk effect in the material and perhaps a by-product of the manufacturing process. The exact nature of the mechanisms involved in the production of these chemical species which cause these peaks remain unclear. This may not be related to the ageing process as previously discussed and in order to determine their origins, further chemical analysis is needed.

Figure 4.14 shows a layered sample that has been aged for 157 hours but does not contain a void. This sample yielded the expected results and the spectral peaks of PE could be seen throughout the sample at relatively uniform intensity with the addition of the same unknown peaks at 600 cm^{-1}. These results reinforce the idea that detected Raman photons do not come from a focal point but from an extended focal volume which, due to refraction, is shifted deeper into the sample in question, thus making the exact spatial resolution of subsurface features difficult to determine. Despite these limitations with respect to spatial resolution, depth profiling nevertheless can provide data that demonstrates variations in chemical composition with position in a subsurface void in the form of varing intensity of fluorescence and the presence of the D and G bands of carbon. Once the spatial resolution of CRMS can be properly determined, the full potential of its application in the study of subsurface features in dielectrics can be realised.

4.3.3 Oil immersion

One method for improving the spatial resolution of CRMS as discussed previously is to profile samples using an oil immersion lens and immersion oil with a refractive index close to that of the sample. Refraction and scattering effects at the sample surface are hence minimised and the spatial precision associated with the analysis of sub-surface features is improved. Oil immersion using silicone oil was applied to a number of the layered void samples. It was shown in the previous chapter that an exact refractive index match between the sample and immersion oil is not essential and silicone oil is sufficient when depth profiling a polymer with a non abraided surface.

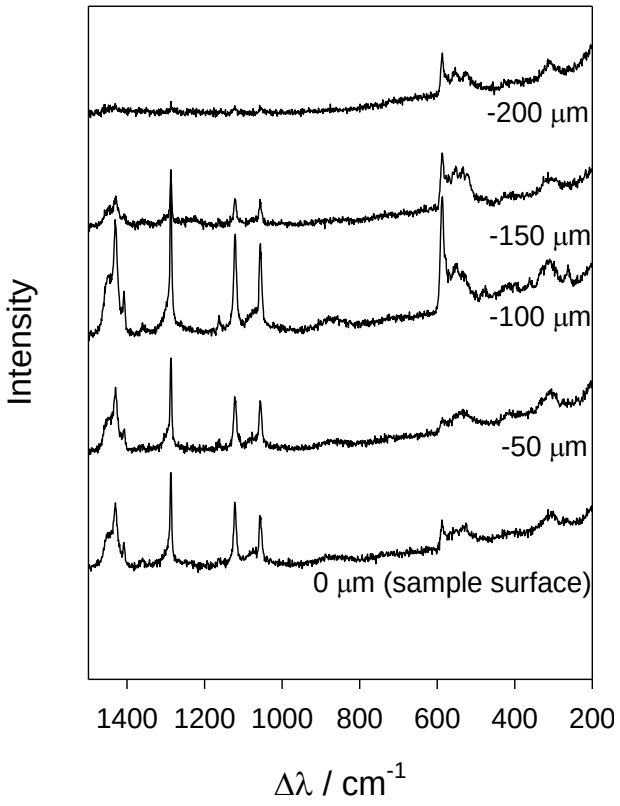

Figure 4.13: Raman spectra taken at various optical depths for layered an un-aged void

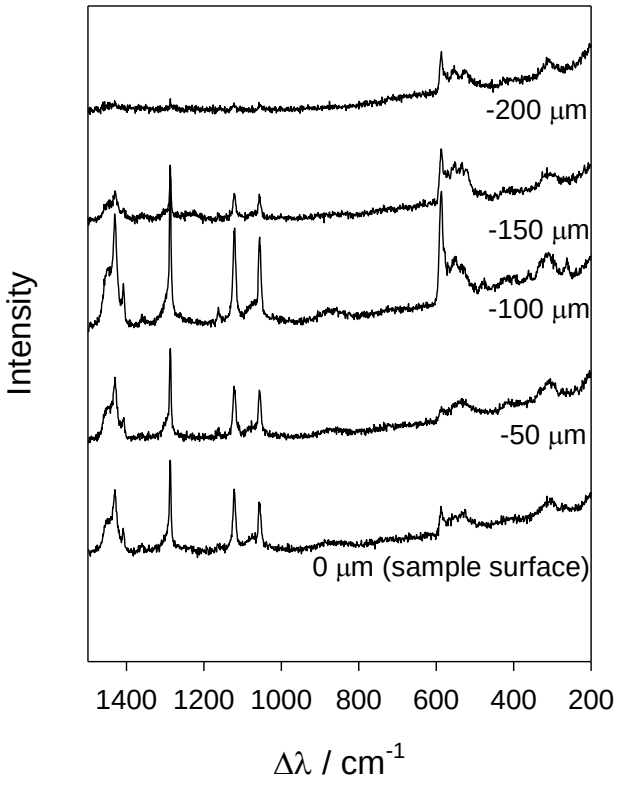

Figure 4.14: Raman spectra taken at various optical depths of sample bulk for layered sample aged for 157 hours

Figures 4.15 and 4.16 show depth profiles obtained in oil and air respectively for a void aged for 157 hours. In order to make the figures comparable both figures are formed of spectra obtained from the same X and Y co-ordinates relative to the void and same stage positions relative to the surface of the sample. In both figures the same spectral features described above can be found, more specifically, PE up until the void surface, fluorescence and the same series of peaks at around 500 cm^{-1}.

As before when the depth profiles are obtained in air, the peaks correlating to PE can be seen up to approximately 100 μm below the sample surface with fluorescence steadily increasing with depth until a maximum is obtained after which it decreases. It can be assumed that beyond this point the majority of Raman photons are originating from inside the void. It is difficult to locate the exact position of the void surface when the spectral data is obtained in air, due to the focal volume becoming elongated due to refraction effects as discussed in the previous chapter. As a result, Raman photons originating from the void surface can be seen in spectra a number of microns above the void surface. This can be seen in figure 4.16 where there is more than one spectrum with large amounts of fluorescence. The position of the focal area is also displaced and so the void surface appears much closer to the surface of the sample

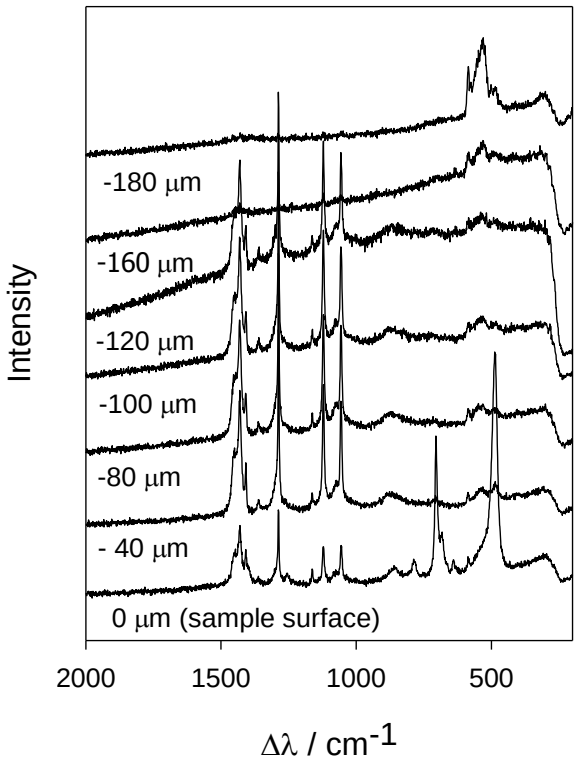

Figure 4.15: Raman spectra taken using an oil immersion objective at various optical depths for layered sample aged for 157 hours

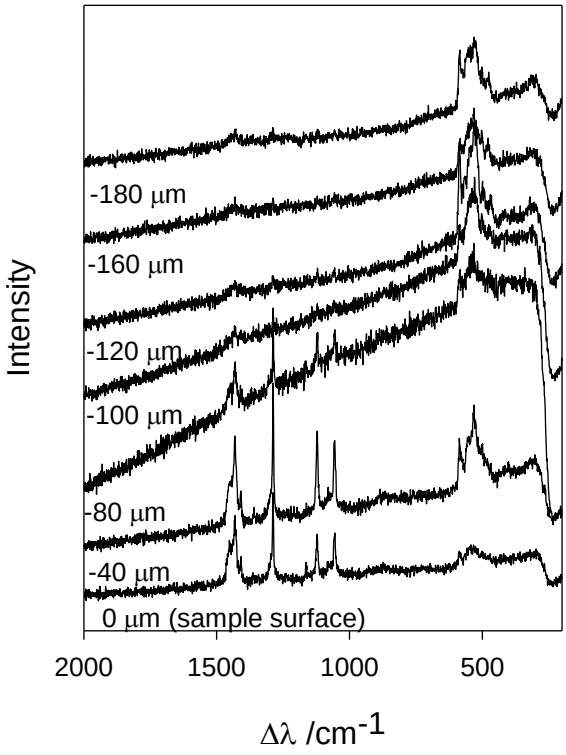

Figure 4.16: Raman spectra acquired in air at various optical depths for layered sample aged for 157 hours in air

than it actually is.

When compared to figure 4.15, where the spectra were obtained using silicone oil as an immersion media, the peaks corresponding to PE can be seen in all but 2 of the spectra where the laser was focused below the void surface (now located at approximately 120 μm). The fluorescence increases slightly with depth until a large increase can be seen indicating the void surface. Figures 4.15 and 4.16 provide evidence that by using an immersion lens and appropriate oil, focal spreading and displacement is reduced allowing greater accuracy in locating features at various depths within the sample. Finally in the spectra relating to a focal position of 0 μm, the spectral peaks relating to silicone oil can be seen but once focused below the sample surface they no longer interfere with the spectra of the sample.

Using the oil immersion method, due to the reduction in refraction effects, it was possible visually to focus on the internal surface of the void and apply CRMS to specific features. Figures 4.17 and 4.18 show, for two aged samples, a number of spectra obtained from the internal surfaces of the voids. In these figures there is a large amount of fluorescence, to the extent that most of the other spectral features are

difficult to discern. In figure 4.17, however, there are some small traces of PE from the material above the surface of the void.

In addition, as shown in figure 4.18, there is evidence of a broad band in the same region we would expect to see the D and G bands of carbon. This possibly indicates the presence of PAHs, all be it that the constitutional D and G bands are broadened to such a degree to be indiscriminate. It is also clear from these figures, especially in the case of figure 4.17, that the surface of the void is not homogeneous since the spectra vary greatly depending on location. Finally, there is no evidence of the peaks previously found around 500 cm^{-1} most likely due to the intensity of the fluorescence in this region.

4.3.4 Split voids

Following Raman analysis via oil immersion, the remaining voids were split to expose the void surfaces. This was achieved by embedding the samples in Kraton (using

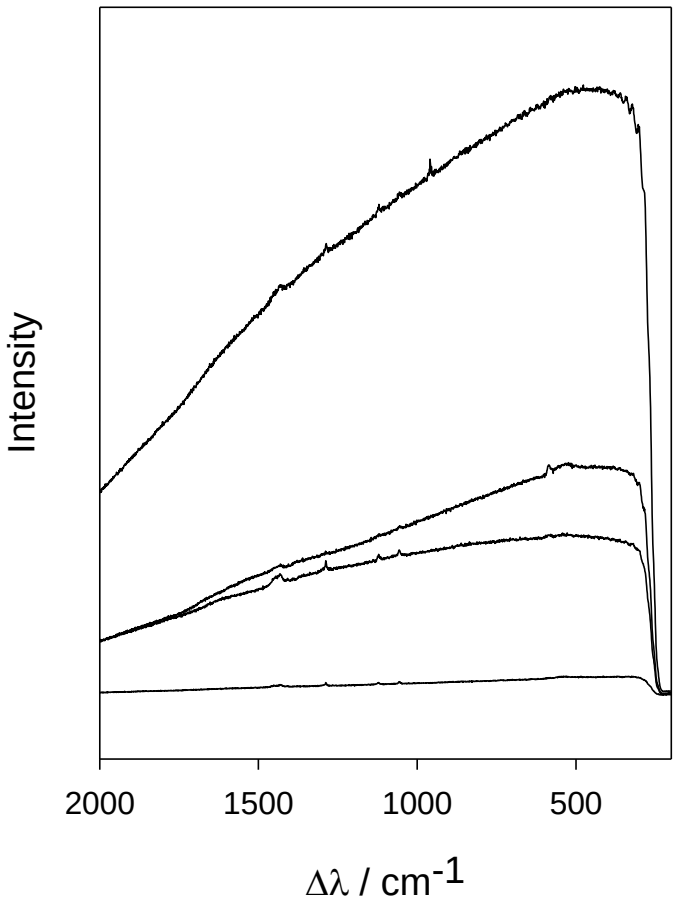

Figure 4.17: Raman spectra taken from various positions on the void surface for layered sample aged for 140 hours using oil immersion objective

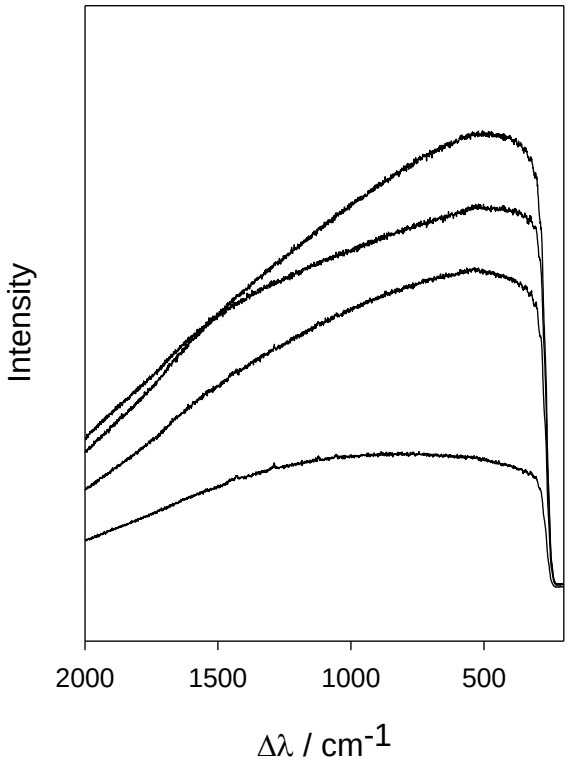

Figure 4.18: Raman spectra taken from various positions on the void surface for layered sample aged for 157 hours using oil immersion objective

toluene to ensure good adhesion) before microtoming at a temperature of -70 °C. This method was used due to the thinness of the samples along the desired axis and thethis way allowed CRMS to be applied to the void surfaces directly. Surface features of the void, which before were indistinguishable, could now be analysed and compared with previous results. Three samples of varying ageing times were split and CRMS was applied to the surface of the void. Figures 4.19 to 4.21 show the typical spectra obtained. Contrary to figure 4.13 and 4.14, where depth profiles were obtained in air and little evidence of fluorescent by-products, in figures 4.19 and 4.20, fluorescence is present. With few exceptions from figure 4.21, this fluorescence is of a sufficient intensity to mask the peaks originating from the original polyethylene matrix as seen previously. The fact that with these voided samples fluorescence can be seen in the aged samples but not the un-aged voids, however, leads to the hypothesis that there is a link between fluorescence and the chemical processes involved in electrical ageing as suggested in previous papers [25, 31]. This fits well with the theory that ageing conditions such as ageing time also affect the presence of fluorescence as the intensity of the fluorescence in figure 4.21, where the sample was only aged for 74 hours is much less than its intensity for the other samples to the extent it is still possible to identify the original PE peaks.

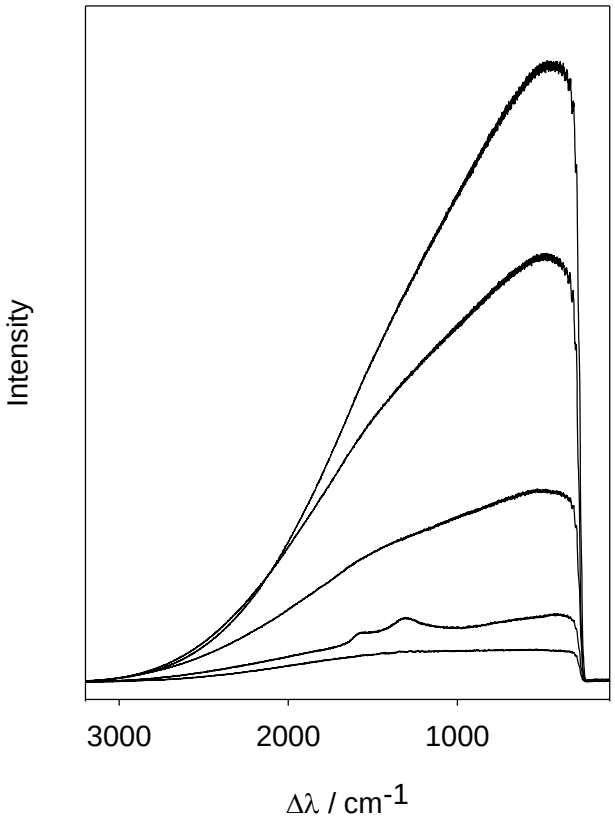

Figure 4.19: Raman spectra taken at various positions on the surface of split void aged for 140 hours

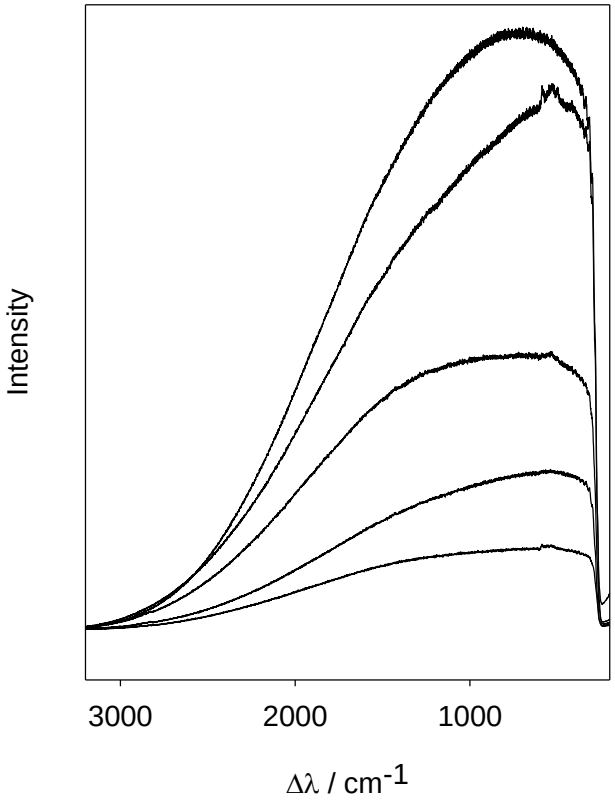

Figure 4.20: Raman spectra taken at various positions of split void aged for 120 hours

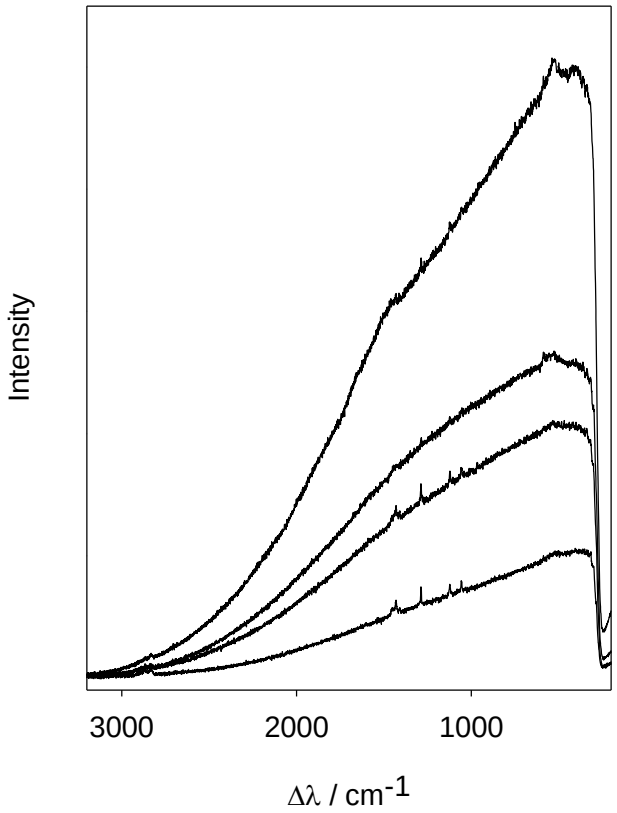

Figure 4.21: Raman spectra taken at various positions of split void aged for 75 hours

Other features that can be seen in figures 4.19 to 4.21 include, for spectra with a relatively low amount of fluorescence, various spectral features between 600 and 300 cm^{-1} (as was initially noted and identified in figure 4.5). Now that these features have been located on the void surface instead of within the bulk of the void, we can also attribute it to the ageing processes that occur within the void. Finally the voids aged for 140 and 75 hours show in some spectra the presence of the D and G bands of sp_2 hybridised carbon. These features were found on the debris located at the edges of the voids or from features that arise from the middle of the void surface.

4.3.5 FTIR

Following Raman analysis, the split voids were analyzed using FTIR, to provide complimentary data to the Raman spectra. By comparing the two methods it is hoped that not only will the same chemical by products as identified by RMS will be found, new features previously unidentified by RMS, may be identified using FTIR. These features could lead to a deeper understanding into the origins of fluorescence and possibly enable a clear link between fluorescence and the production of PAHs (and hence the D and G bands identified in the RMS spectra) during ageing.

Figures 4.22 to 4.25 show typical FTIR spectra for the split voids over a range of 1400 to 2500 cm^{-1}. Each figure shows an average of spectra taken from the bulk of the material, the centre of the void and the edge of the void. In addition, figure 4.25 also shows the average spectra from the area just outside the void where the polymer had split during ageing. In these figures, peaks at 2325 cm^{-1}, 2200 cm^{-1}, 1900 cm^{-1} and 1500-1700 cm^{-1} are visible which relate to carbonyl groups [133]. The broad band located between 1500 and 1700 cm^{-1} appears to be related to, and indicate the quantity of, the carbon present in the system [133] as the reflectance is greatest at the edges of the samples and weakest when sampled away from the voids. This is in good agreement with the data obtained via CRMS and the production of small amounts of carbon within the voids during ageing seems evident. In these spectra however, it was not possible to identify any 'new features which could be possibly attributed to the fluorescence seen in Raman spectra.

4.3.6 Imaging voids

During Raman analysis of the layered voids using the oil immersion method, it was noticed that due to the minimisation of refraction effects it was possible to image the inner surface of the void without destructively damaging the sample. Figure 4.25 shows just such an image obtained from the surface of a void aged for 157 hours. Despite poor image quality, it is possible to identify features of approximately 2 μm in

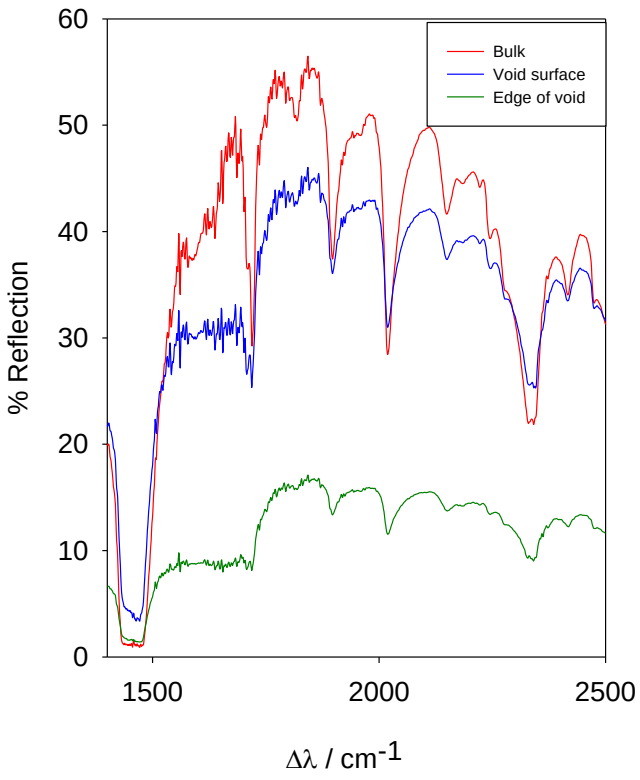

Figure 4.22: Average FTIR spectra of various areas of void aged for 140 hours

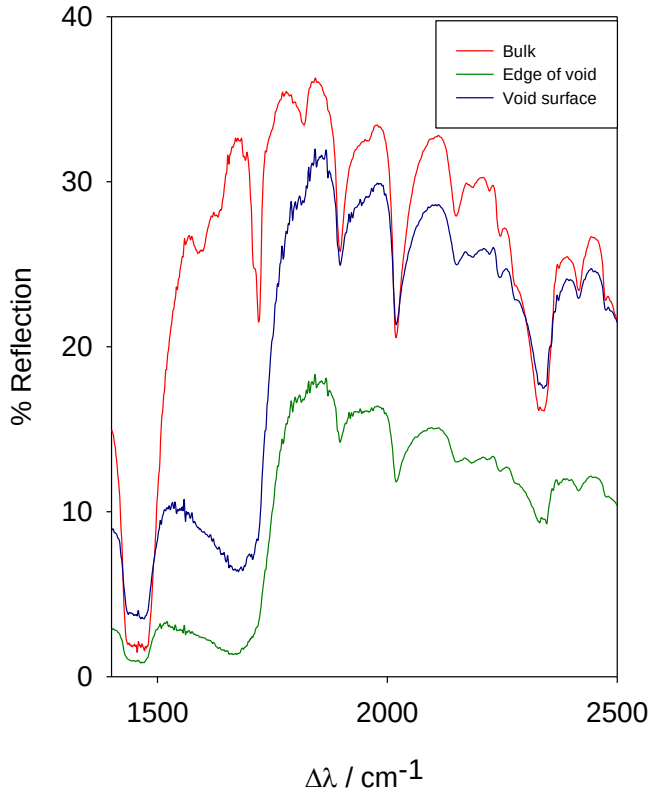

Figure 4.23: Average FTIR spectra of various areas of void aged for 120 hours

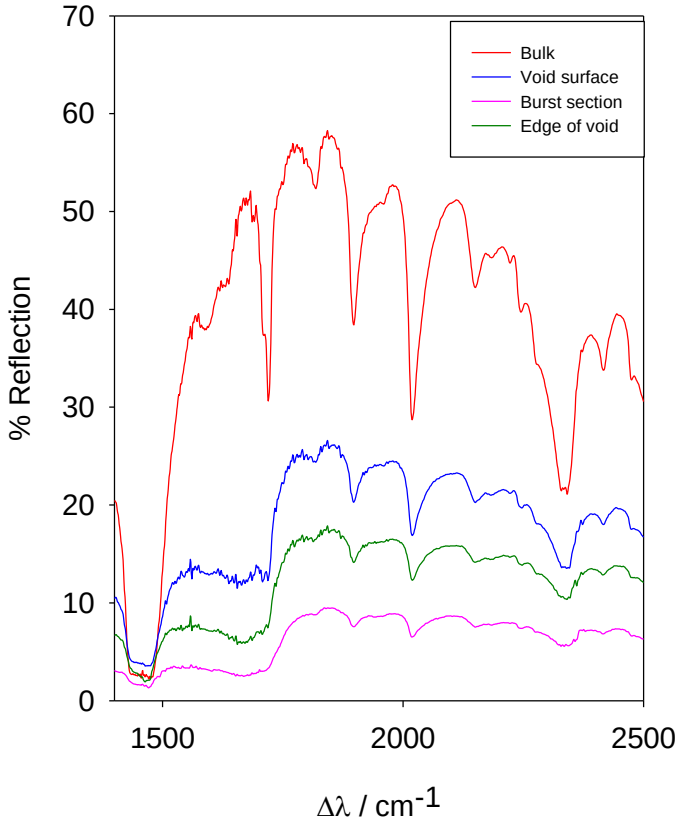

Figure 4.24: Average FTIR spectra of various areas of void aged for 75 hours

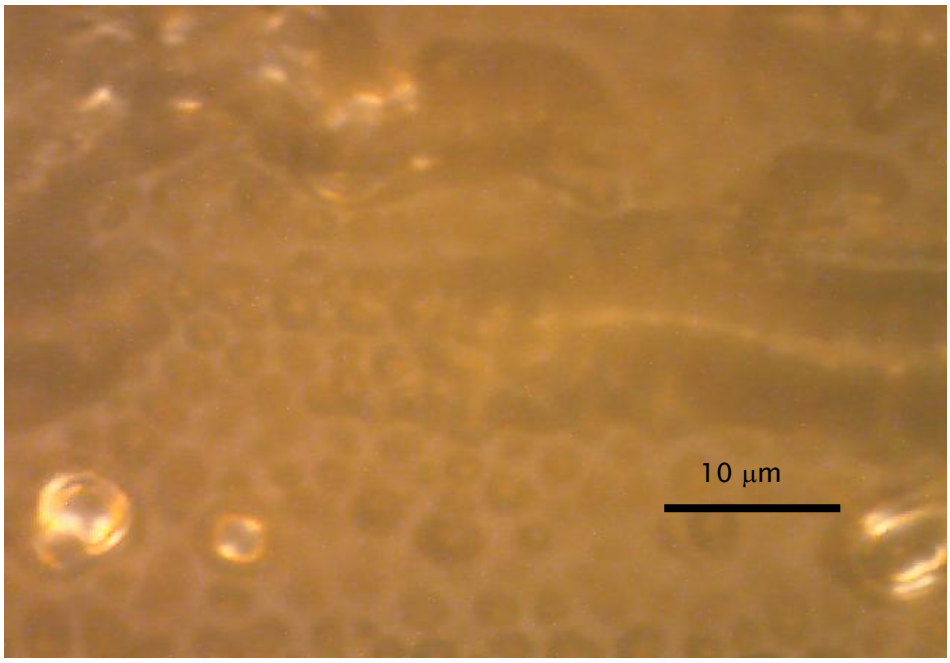

Figure 4.25: Optical micrograph of void surface (140 hours) as seen by Oil immersion

diameter in the surface of the void. If this is the case then these features would fit well with theories of micropitting and the degradation of the polymer via electron bombardment suggested by Dissado, Montanari, Sayers, *et al* [10, 117, 119]. Another suggestion by Morshuis is that these features are actually protrusions from the surface and are possibly droplets of hydrated oxalic acid or crystals of dehydrated oxalic acid formed during the ageing process [134]. Due to the poor image quality, however, it is difficult to confirm whether these features are pits or debris from such images alone.

Splitting the voids using microtomy facilitated direct imaging of the internal void surfaces in order to probe further the origins of the features seen in figure 4.25. Cross sections of the voids were taken such that the voids could be viewed 'edge on' and the depth of the features could be determined. Samples were then sputter coated and imaged prior to examination in the SEM. Figure 4.26, parts a) and b), shows a split un-aged void and one of its edges. From figure 4.26 it can be seen that although the process of sample production can lead to a slightly misshapen void, there is little or no damage to the void surfaces themselves.

When we compare these images to those found in figure 4.26 c) and d), some significant differences can be seen. Figures 4.26 c and d each shows a cross-section of a void, but this time the original void had been aged for 157 hours. In these images features up to 8 μm in size can be seen protruding from the surface of the void edges.

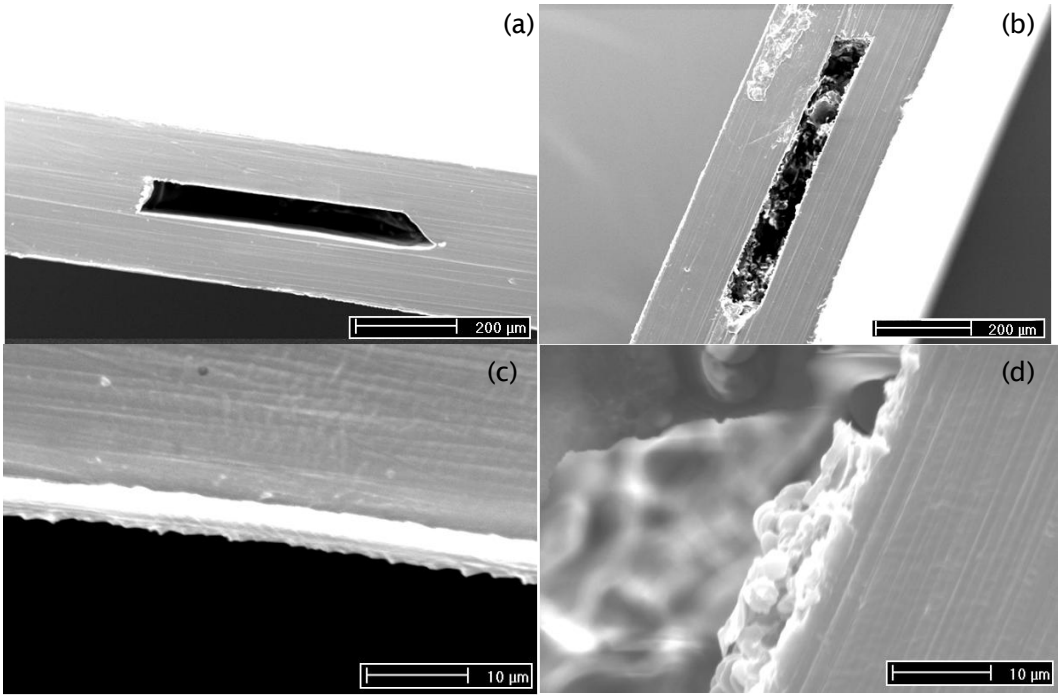

Figure 4.26: SEM images of edge of exposed voids, (a) and (c) are of the void and edge (respectively) of an un-aged void, (b) and (d) are of the void and edge (respectively) of a void aged for 157 hours

Contrary to the theory of micropitting and figure 4.25, these features appear to be protruding out from the surface instead of into the surface of the void.

A number of other voids were also split, such that the internal void surface was exposed. Prior to SEM analysis, possible areas of interest on the void surfaces were identified using optical imaging. Figure 4.27 shows optical images of the void surfaces prior to coating and SEM analysis. From these images we can see a number of different features depending on the void. The voids aged for 120 and 75 hours show some large protrusions from the surfaces of the voids and a generally uneven surface. The sample in figure 4.27 (b) appears to have burst along the boundaries of the layers during ageing, presumably due to the high gas pressures generated by the electrical ageing process. The sample aged for 140 hours has no large protrusions but its surface appears to be covered in lots of very small pits (as inferred from figure 4.25). All of the voids appear to have features around the edges of the voids of a similar size and shape to those in figure 4.24 showing that they are consistent across all the samples. The origins of these features is unclear however it is possible that due to the higher field at corners and edges of the void (compared to the uniform field in the central portions of the void) more damage occurs in these reigions. In addition, the protrusions around the edges appear to be discoloured compared to the original

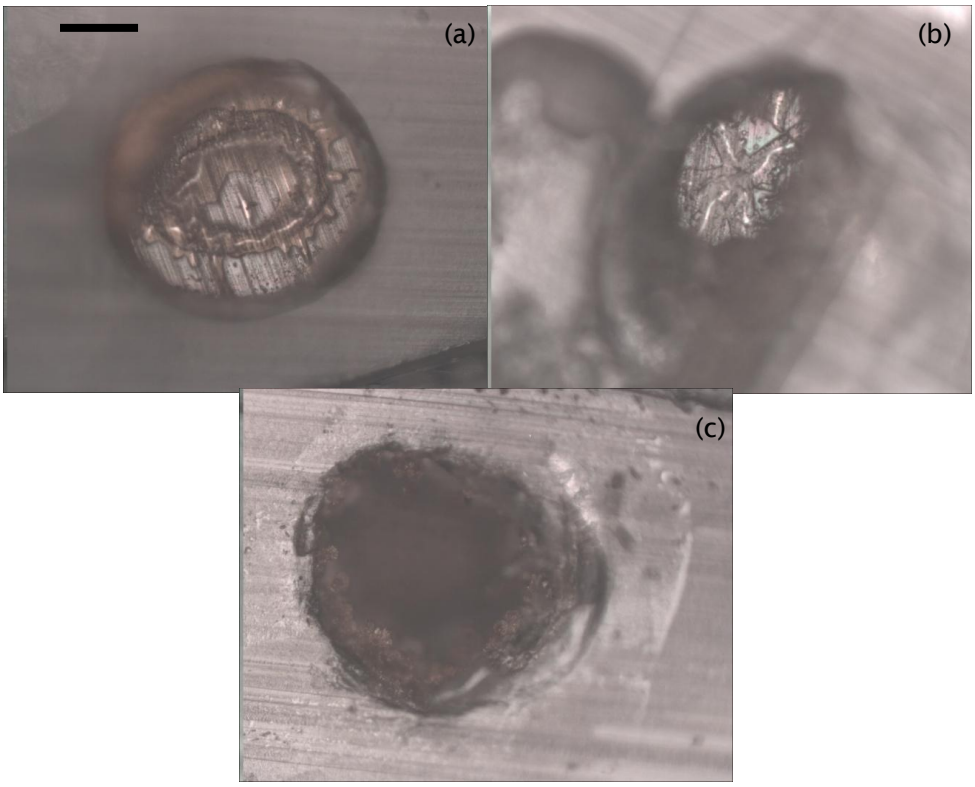

Figure 4.27: Optical micrographs of the surfaces of split voids aged for (a) 120, (b) 75 and (c) 140 hours, the scale bare is equivalent to approximately 200 μm

polymer, in a similar way to the discolouration found on the blown voids. This implies that they are the debris formed in the blown and layered voids are chemically similar.

These voids were then sputter coated and examined using SEM. Figures 4.28 to 4.30 show a selecton of SEM Images for the split voids. In each figure (a) is of the whole void, (b) is a detail of the void surface and (c) is an image of the void edges. From these images, similar features to those in figure 4.27 can be seen.

Figure 4.28 shows the SEM images obtained from a void aged for 120 hours. In the image of the whole void it can be seen that it has a uneven surface with a number of cracks across the central portion of the void. These cracks are possibly a response to the gas pressure during ageing. When the surface of the void is viewed with a higher magnification, bubble like features ranging in size from 1 – 10 μm can be found. A number of the features have small cracks on their surfaces indicating the possibility that they are not solid and are also affected by the gas within the sample during ageing. The edge of the void (figure 4.28 c) shows that following ageing, the edges of the void are not smooth and have protrusions approximately 20 μm in size. This

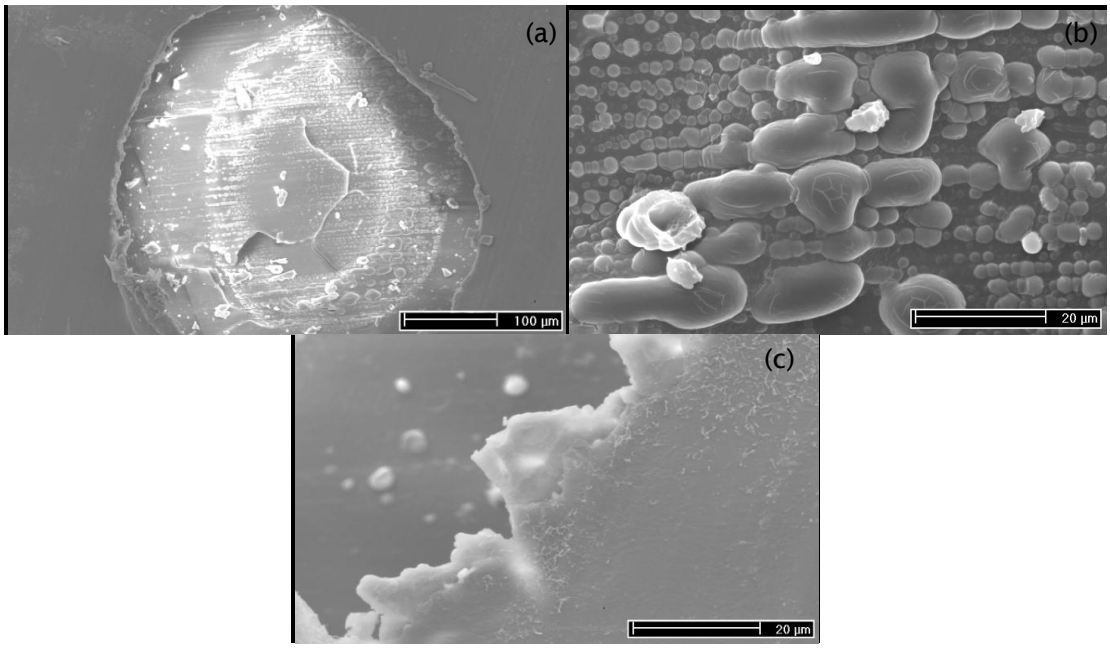

Figure 4.28: SEM images of (a) whole void, (b) void surface and (c) void edge of void aged for 120 hours

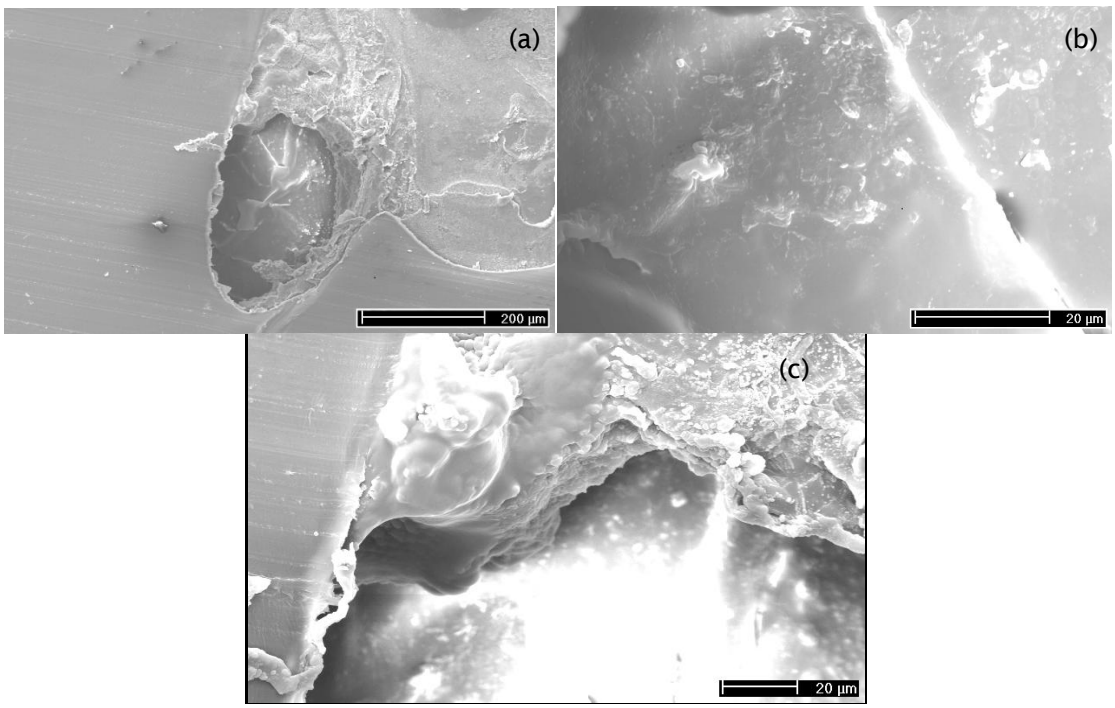

Figure 4.29: SEM images of (a) whole void, (b) void surface and (c) void edge of void aged for 75 hours

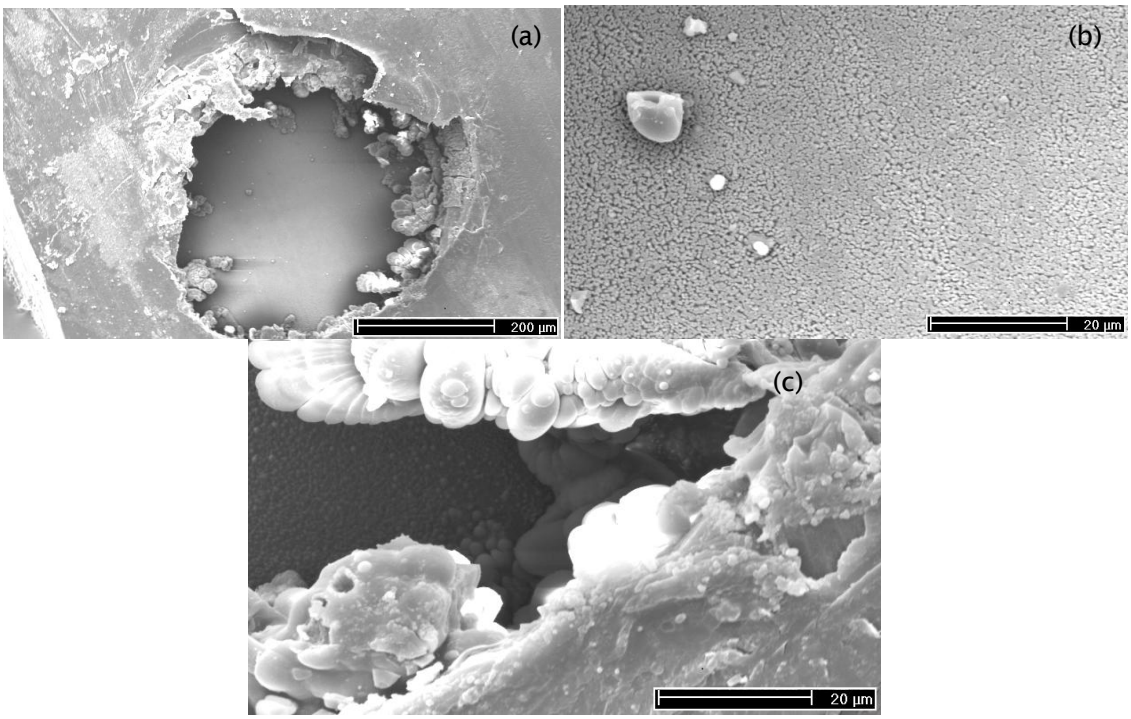

Figure 4.30: SEM images of (a) whole void, (b) void surface and (c) void edge of void aged for 140 hours

degredation at the edges suggests that when ageing occurs it is not localised to the void surfaces and debris is also eroded from the edges.

The void aged for 75 hours, as shown in figure 4.29, has some similarities to the void shown in figure 4.28. In part a) we can see that the void surface is again not uniform and has large cracks accross the surface. When focused at a higher magnification on the void surface, there are some very small (<1 μm) features. At this magnification, however, it is difficult to determine the nature and origin of these features. One possibility is that they are merely the same type of features as seen in 4.28 b. These features have not, however, had a sufficient amount of time during ageing to grow to the same sizes as for the void aged for 120 hours. As with the previous sample the edges of this void are not smooth but rather exhibit many recesses and a nodular structure.

Contrary to figures 4.28 and 4.29, the void in figure 4.30 has an apprently smooth surface and no pressure induced cracks. The close up of the surface of this void, which was aged for 140 hours (figure 4.30 b), shows, however, that the surface is not uniformley smooth and small pits of >1 μm as can be seen as predicted in figures 4.25 and 4.27. As can be seen in figure 4.30 c, however, large protrusions have formed around the edges of the void. These protrusions are fairly large in comparison to the other samples and as with the void aged for 75 hours, are nodular in

appearance. These protrusions fit with the evidence given by the cross sections of the voids and appear to vary from sample to sample (and possbly ageing time).

4.4 Conclusions

Samples of polyethylene containing sub surface voids have been examined using CRMS with a depth profiling technique. Samples containing voids created using a blowing agent and by layering LDPE were analysed. Following lateral and depth profile analysis, the layered samples were split open such that the void surfaces could be analysed with CRMS and compared to FTIR and imaging data. From the results it is possible to draw the following conclusions:

- CRMS has provided data which demonstrates variations in chemical composition within voids and revealed that, for a void which has experienced PD and broken down, the same signatures as those found in electrical trees can be seen. For samples that have experienced PD but not broken down, the spectral peaks of PE can be seen, as well as another set of peaks between 300 and 600 cm^{-1} who's origin is possibly related to the oxygenated by-products of ageing. Further analysis is needed however in order to confirm this theory and determine the exact spatial and chemical origin of these peaks.

- As predicted in chapter 3, it was found that the concept of CRMS is not as simple as generally thought and is subject to inaccuracies in spatial resolution as the Raman photons which contribute to the detected signal emanate from both above and below the focal surface. The limitations of CRMS are minimised, however, with the use of an oil immersion lens and appropriate immersion oil thus enabling it to be a useful tool in the analysis of subsurface ageing (such as voids) in dielectric materials. Where possible, obtaining spectra from exposed surfaces is preferable depth profiling using CRMS.

- The results showed that voids created in thin films by using a blowing agent and then aged via PD are chemically comparable to voids that are created by the layering of polymers containing the void which is then also aged via PD. Therefore, creating voids of known dimensions within layered LDPE can be used as a comparison to voids in insulation systems and enable cylindrical models of these voids to be made which can in turn be compared to models of PD in spherical voids.

- FTIR analysis of the void surfaces revealed few chemical changes between the sample bulk and the void surface with the exception of a change in intensity of

a peak related to the presence of carbonyl compounds. This reinforced the Raman data and the conclusion that carbonyl compounds and PAHs, are present within the sample and the chemical traces on the walls of the void do indeed resemble those of electrical trees in PE. However, no indication of any substances possibly linked to fluorescence could be found.

- By imaging the voids it was possible to see that, as predicted, a degree of micropitting occurs within the void during ageing. SEM images also revealed the production of nodular debris, particularly around the edges of the void, that appears to increase in quantity with ageing time. Other damage to the voids during ageing include cracks to the void surfaces possibly caused by the pressure of the gas within the void as the PD activity during ageing increases the temperature and, as PV=nRT, the pressure of the gas also increases during ageing. It is also possible however that the gas within the voids slowly defuses away through the polymer bulk.

In summary, it is possible to apply CRMS in the investigation of the chemical composition of electrically aged subsurface voids and it has shown that blown voids and layered voids are chemically comparable. By applying this method to the voids that have broken down due to the ageing process, and comparing to FTIR spectroscopy, chemical signatures similar to those found in electrical treeing can be seen. When applying CRMS to voids that have not broken down however, the spectra show the typical spectrum of PE but with some additional peaks at lower wave numbers. Further analysis is needed to determine the exact nature of these peaks in the layered samples. Optical analysis showed the formation of debris, cracks and micropitting, all of which have previously been associated with the growth of electrical trees from subsurface voids in dielectric materials. Finally, it is also recommended that in future work, if it is possible to analyse the sample on the surface rather than depth profiling, either non confocal Raman microprobe spectroscopy or CRMS with an oil immersion lens and oil, should be used in order to minimise the limitations and increase the spatial accuracy of the analysis.

5 : Electrical Treeing

This chapter applies the method of CRMS discussed in previous chapters to the study of electrical treeing. The preliminary work in Vaughan *et al's* papers (in 2004 and 2006) on electrical treeing phenomena in PE will be discussed and extended to include studies of treeing in other polymeric systems. Following this, alternative methods of analysis such as FTIR and SEM will be applied such that, the chemical changes involved in electrical treeing can be identified and a deeper understanding of the processes involved obtained.

5.1 Background

5.1.1 Tree initiation and Dimension

Electrical treeing in polymeric materials is a technologically important phenomenon due to its relevance to high voltage insulation materials, as it can lead to catastrophic electrical breakdown. The process of electrical treeing occurs in three stages [10]. First, inception, namely the formation of a micro void at a region of high electrical stress. Second, propagation, the micro void develops into a fractal structure composed of fine channels, which develop through partial discharge activity; this is the growth stage of the electrical tree. Finally, when the tree channels create a continuous conducting path between two electrodes, breakdown is said to occur. As discussed by Fothergill *et al*, the shape of the resulting tree can be described as either branched or bushed depending on its fractal dimension, $D_{f.\,[135]}$. Branched trees have fewer channels and grow rapidly (and at lower inception voltages) through the polymer bulk and correspond to the situation where $1<D_f<2$. Conversely, bushed trees tend to grow slowly from high inception voltages and correspond to the case where $2<D_f<3$ [135, 136]. Studies based on measurements of PD activity and optical observations have shown that as well as the internal structure and optical appearance differing between bushed and branched trees, the electrical activity that produced them also varies [137-139]. It has been reported that branched trees are more conducting in nature and that the walls of the tree channels in branched trees are sufficiently conducting to prevent discharges within the tree, thus confining electrical activity to the growth tips. Bushed trees however are thought of as non-conducting and electrical activity occurs throughout the entirety of the tree [26, 139, 140].

In order to understand electrical tree formation, the production of low density regions/voids in solids through the application of an electric field also needs to be understood. The development and growth of electrical trees involves the chemical conversion of polymers into volatile fragments due to the transfer of energy from the electric field [141]. The final form of the tree structure that develops is determined by

the PD activity within the trees, which is influenced by many factors, including morphology [142], chemical composition [143], mechanical stress [26], and so on.

Due to its implications for high voltage engineering, much research on polymer insulation has been focused on electrical treeing. Many studies are concerned with the electrical [136] and propagation characteristics of electrical trees [144] and the various factors that cause tree initiation [145]. The vast majority of treeing studies have been performed on variations of PE and epoxy resin with much recent research being dedicated to how the presence of nano filler affect the treeing processes [146-149]. Other treeing studies have included PDMS [145, 150-152], poly(methyl methacrylate) [153, 154], ethylene-vinyl acetate [147, 149] and polypropylene [142, 155].

5.1.2 Tree Modelling

Many models have been proposed to describe the processes involved in electrical treeing. Some rely on random and unknown spatial and temporal variations in physical properties [156-158], whereas others model the PD activity physically by representing inhomogeneous material properties/temporal fluctuations in space charge within the tree structure with random elements [22, 115, 157, 159]. These latter models assume that the electrostatic energy dissipated as a result of the partial discharges within the tree structure is the cause of localised material damage. Early models of electrical treeing suggested that the discharges within tree channels results in a concentrated electric field at the channel tips exceeding the breakdown strength of the material [160-162]. Other models attribute tree propagation to the chemical damage caused by molecular excitation/ionisation at the tree tips triggered by partial discharges [22, 115, 136, 157, 159]. Essentially, these models all suggest that issues such as PD activity, space charge and the physical properties and form of trees are all closely interrelated. It is therefore essential that an understanding of the exact processes involved in the formation of electrical trees, and whether they are conducting or non-conducting, is obtained.

5.1.3 Chemical analysis of Electrical Trees

Despite its potential to aid further understanding of fundamental factors that lead to electrical treeing, relatively few studies have performed a chemical analysis of electrical treeing. Early studies used FTIR to study trees grown in epoxy resin [144, 163]. More recently, two papers by Vaughan *et al* (2004 and 2006) [25, 32] reported on the structure and chemical changes involved in electrical treeing in PE through the application of CRMS. In the first of these papers by Vaughan *et al* [25, 32], a 'conducting' tree grown in PE was analysed with CRMS in order to characterise the chemical structure of the tree and to explore the effectiveness of CRMS as a practical

tool for the study of electrical treeing and breakdown phenomena. Results showed that, due to its spatial resolution, CRMS appears to be an ideal approach to the analysis of electrical trees. The technique can be rather invasive however and with closer inspection, the spatial resolution is not as well defined as previously thought. Despite these limitations, Vaughan *et al* concluded that, CRMS can still be applied to the study of electrical trees provided that it is done, and the data are interpreted, with caution. Raman spectra obtained in this study showed that an electrical tree structure can be interpreted to contain 3 separate elements that vary at different spatial locations within the tree. First, throughout the tree, both in the tips of the tree channels themselves and, in the surrounding bulk material, the spectrum of PE was reported. Second, in the main body of the tree, the presence of fluorescence was identified, which has been linked to the degradation of a material. Finally, when analysing mature tree channels, the D and G bands of sp^2 hybridised carbon could be seen. This suggests that the tree channels can be thought to be surrounded by a conducting carbonaceous shell, with non conducting PE tips. Figure 5.1 shows the data Raman spectra published in this paper, showing the 3 different features found in the Raman spectra of the tree that was analysed.

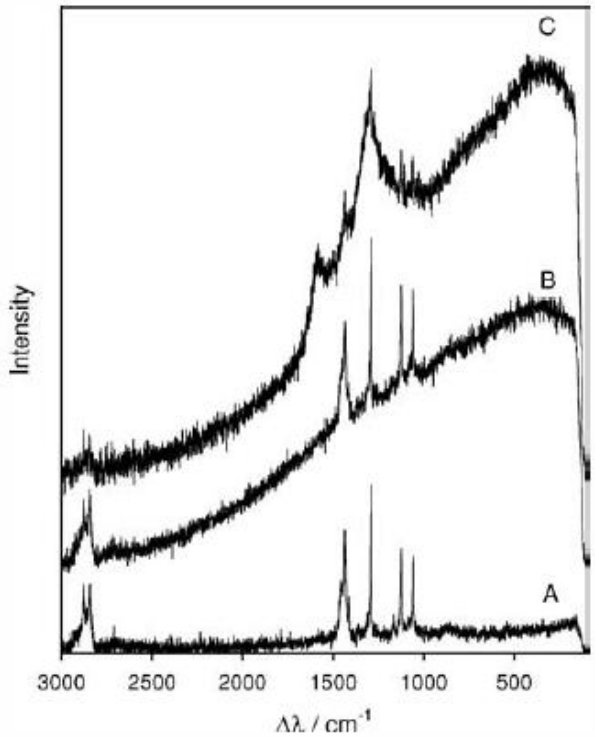

Figure 5.1: Raman spectra published by Vaughan et al showing the Raman spectra acquired from a conducting electrical tree grown in PE (a) relates to a position away from a tree channel, (b) at the edge of a tree channel and (c) the centre of a tree channel. [20]

The second paper by Vaughan *et al* [32] set out to extend the work reported in the first paper, by applying a more thorough analysis of both conducting and non conducting trees. The paper also related the compositions to the physical properties of the tree and the related mechanism of formation. Two trees grown in LDPE at 20°C and 30 °C, which exhibited different structures despite being grown under similar conditions, were analysed using CRMS. Both trees were initiated by applying a 50 Hz AC voltage at 20 kV until a small (~ 50 μm) tree was formed. The trees were then allowed to propagate between the electrodes at 13.5 kV. Tree A (conducting and grown at 30 °C) was the same tree as used in the 2004 paper and the intensity of the graphitic carbon found within the tree channels led to the estimation that the tree channels have a resistance of 1 – 10 Ω μm^{-1}. Tree A is therefore, as predicated, sufficiently conducting to prevent localized discharge activity. Tree B (non conducting and grown at 20 °C) showed evidence of PE and fluorescence in the spectra obtained, but no evidence of carbon was found. Both trees were highly fluorescent structures, with the fluorescence rapidly decreasing towards the edge of the tree boundary. The magnitude of the fluorescence in tree B however, was much higher than that of tree A, despite it not leading to the conductivity of the overall structure. It was suggested that it is the decomposition products in tree A, acting as a precursor to the graphitic conducting tree channels, that give rise to the fluorescence, possibly due to the continuous discharge and the presence of an organically rich atmosphere. The authors concluded that, in order fully to understand and determine the electrical properties of electrical trees, it is necessary to understand the transition process between the non-conducting fluorescent structures and the conducting graphitic carbon found in conducting trees.

5.1.4 SEM Analysis of Electrical Trees

Vaughn *et al's* paper also examined the tree channels using SEM. These results showed that the bulk of the material in both trees showed the spherulitic structure commonly seen in LDPE. When examining tree A, however, there was a thin layer (≈1 μm in thickness) surrounding the tree channels which did not show this spherulitic morphology which was suggested to be related to the localised heating effects of the PD activity creating the trees. Upon examining the interior walls of the tree channels in tree A, there appeared to be a nodular coating on the walls of the tree channels that did not appear within tree B, which was resistant to etching. It was later suggested that this material is carbon based. Figure 5.2 contains images obtained by Vaughan *et al,* and shows the spherulitic structure of LDPE, the nodular surface of the conductive tree channel and area of modified material surrounding the tree channel in conducting trees.

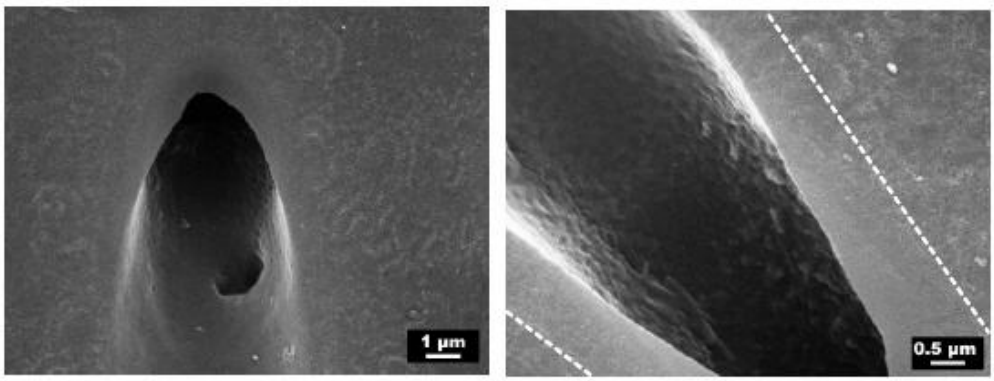

Figure 5.2: SEM images of conducting electrical tree channels in PE as published by Vaughan et al [24]

5.1.5 Aims and Objectives

The study described in this chapter aims to extend the work of Vaugan *et al* further by performing a similar analysis on trees grown in PDMS(E) and an epoxy resin. These materials were chosen for their siloxane backbone and high carbon content respectively allowing chemical comparisons to be made. This will enable the identification of possible trends in the spectra when the chemical structure of the polymer is markedly different to PE. In this study, samples of breakdown channels and tree branches grown are examined using CRMS, FTIR and SEM in order to compare the results to those obtained by Vaughan *et al,* such that an improved understanding of the chemical processes involved in electrical treeing can be found.

5.2 Experimental

5.2.1 Materials

The PDMS(E) samples in this study were all made from the Dow Corning Sylgard 184 silicone elastomer kit. This kit contains the base compound and a curing agent. In order to make the samples the 2 compounds were mixed at a ratio of 10:1, degassed and cured in a mould at 100 °C as per the kits instructions. Samples were then cut to size (6x10x15 mm) and a needle was slowly inserted in order to grow electrical trees.

The epoxy resin samples were made of resin (DER 332) and hardener (Jeffamine D230) mixed at a ratio of 1000:344 respectively, degassed and cured in a mould, at 100 °C for 4 hours. The needles were preinserted and, after curing, each sample was cut to the required size.

5.2.2 Method

Electrical trees were grown in the samples by inserting a needle electrode attached to a variable voltage 50 Hz AC high voltage supply; a minimum gap of 2 mm between the

needle tip and a planar earthed electrode was used for these experiments. The sample was then immersed into a silicone oil bath, to prevent flashover. A schematic of the set up used to grow the trees can be seen in figure 5.3. A voltage between 1 and 25 kV rms (AC 50 Hz) was applied until a tree formed at the needle tip or complete breakdown occurred. Although the experimental setup employed here is capable of providing an output of the PD activity in the trees during their growth, when the applied voltage is greater than 18 kV discharges from the high voltage transformer interfere with the PD signal from the sample. As such, the PD data from the trees, are not provided here. Following the initiation and growth of the trees, images were obtained of the evolving trees using a Leica sterio microscope fitted with a GXCam 1.3 at x3.2 magnification.

Samples containing an electrical tree / breakdown channel were cut open using an RMC MT-7 ultra microtome equipped with a CR-21 cryo-system set at -120 °C for PDMS(E) and 0 °C for Epoxy resin in order to provide a surface containing open segments of the tree/ breakdown channel. Samples were then characterised at various

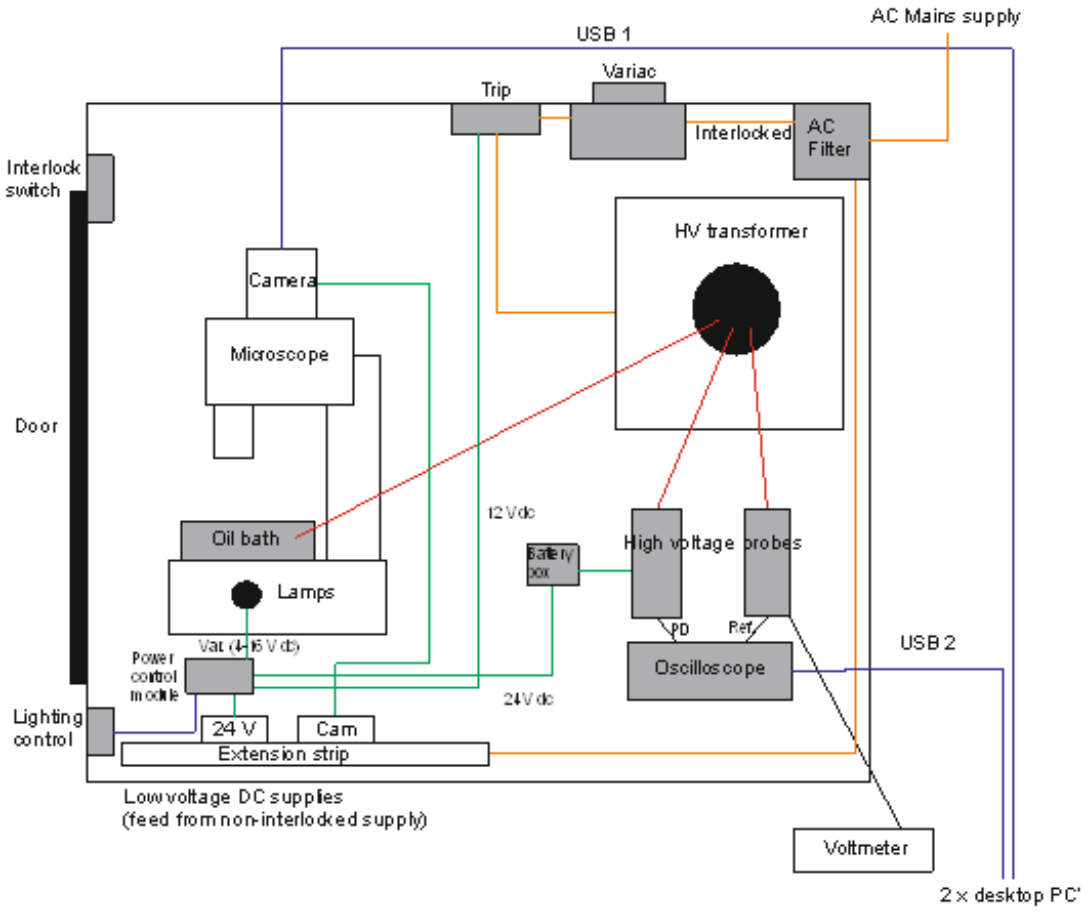

Figure 5.3: System diagram of experimental set up for the growth of electrical trees

positions around the tree/breakdown channels using CRMS with a laser power of 25% to minimise sample damage. Following Raman characterisation, the microtomed surfaces were subjected to FTIR analysis and sputter coated with gold such that the tree structures could be examined by scanning electron microscopy (SEM).

5.3 Results and discussion

5.3.1 Tree structures

Figure 5.4 shows a series of images of trees grown in PDMS(E) at voltages between 8 and 15 kV. Figure 5.4 a) shows a tree grown at 8 kV and each subsequent figure shows a tree grown at a voltage that has been increased by 1 kV. The tree in figure 5.4 a) grew to approximately 500 μm in length before it appeared to stagnate and cease to grow. Tree stagnation in PE has previously been linked to the non-uniform crystallisation, spherulitic structure and charge dynamics of the dielectric [164, 165]. Silicone rubber is amorphous, however, and this stagnation is more than likely due to the electric field not being sufficient to sustain detectible tree growth away from the needle tip (also visible in the image) hence causing a reduction in is growth rate. Tree a) comprises of two main branches with a number of short, fine branches along the lengths of the main branches.

Tree b) was grown at 9 kV and consists of 3 main branches connected to some smaller side channels. As with tree a), tree b) stagnated after a period of time, although it grew to approximately double the size of tree a) before this occurred. Trees c) to h) were grown at voltages between 10 and 15 kV and increase in complexity with voltage. None of these trees became stagnated and were therefore allowed to propagate through the material until a sufficient tree had formed before the voltage was switched off to prevent break down. In all cases the structure of the trees is based on a number of main branches with smaller side branches leading off. Increasing voltage does not appear significantly to affect the number of main branches but rather the number and size of the side branches. When tree f) (13 kV) was grown, one of the main branches became a leader and the propagation of the tree was focused along this branch. When leader branches form, the growth rate of the tree rapidly increases. In terms of fractal dimension all of the trees grown here are classed as branched trees as even for the more complex trees grown at 15 kV, $D_f < 2$.

The increasing voltage not only increased the fractal dimension of the trees grown but also increased the growth rate of the trees and decreased the time to initiation of the trees. In comparison to the trees grown in PE by Vaughan *et al* [25], the growth rate of trees grown in PDMS(E) ranged from minutes at 8 kV to seconds at 15 kV (as shown in figure 5.5). If a higher voltage is required to grow a 'bushed' tree in PDMS(E), as

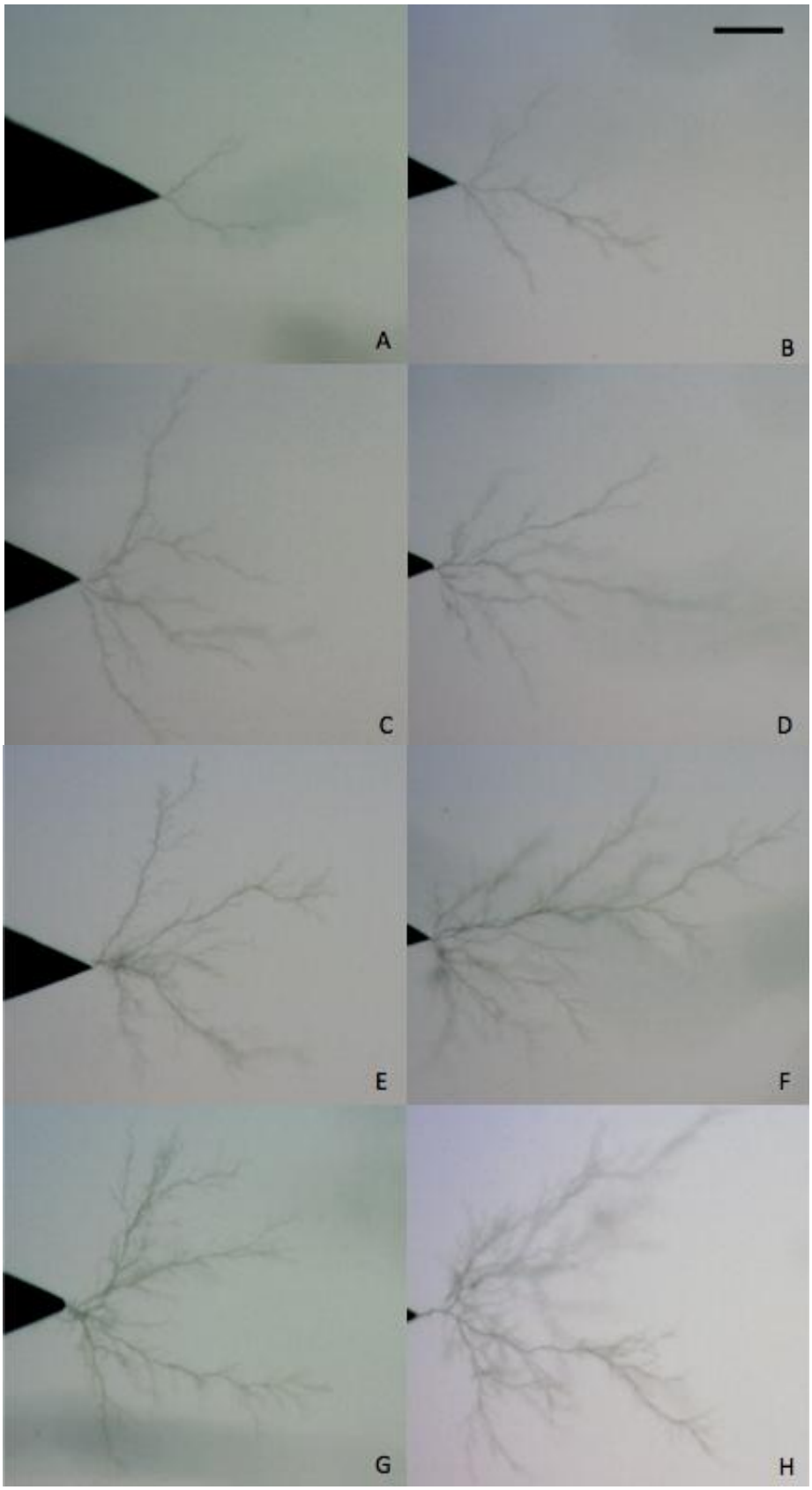

Figure 5.4: Micrographs taken in situ of electrical trees grown in silicone rubber at a) 8 kV, b) 9 kV, c) 10 kV, d) 11 kV, e) 12 kV, f) 13 kV, g) 14 kV and h) 15 kV (note: scale bar applies to all images and is equivalent to 250 μm

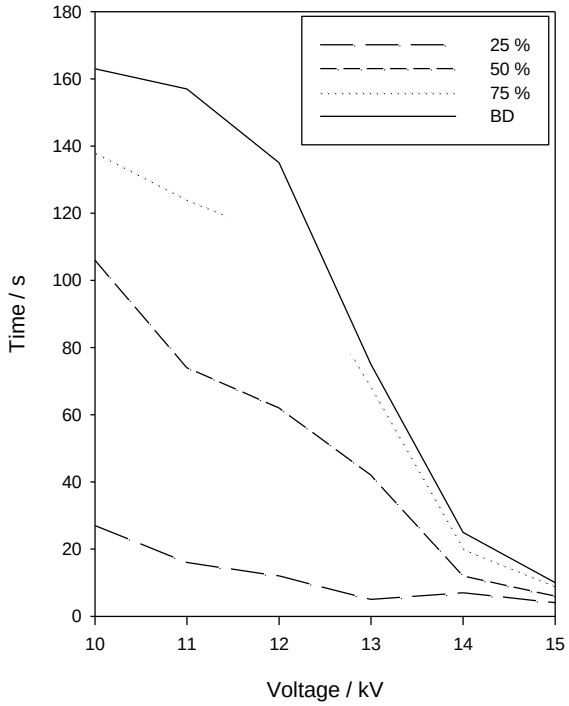

Figure 5.5: The time for an electrical tree to propagate across 25, 50 and 75% of the bulk material after tree initiation at various voltages and the time to breakdown

predicted by [113], the electrode separation needs to be increased such that the time to breakdown is also increased. In an attempt to grow a 'bushed' tree in silicone rubber the electrode separation and applied voltage was increased to up to 5mm and 23 kV respectively. The resulting trees grown although highly branched were not bushed trees as defined by Fothergill and Dissado [135, 136], indicating that other factors such as temperature are also important.

In 2011 Du et al published a paper discussing the growth characteristics of electrical trees grown in silicone rubber [150]. They reported that the occurrence of different tree structures in PDMS(E) is related to the temperature of the system. It was shown that the probability of growing a branched tree at an ambient temperature of approximately 30 °C is 90 % and bushed trees 10 %. This probability decreases with an increase in temperature and at 60 °C branched trees occur only 20 % of the time whereas bushed trees have a probability of forming of 65 % and the remaining 15 % are branch pine trees. This supports the findings in this chapter as all the trees were grown at room temperature and hence, according to Du *et al*, have a high probability of being branched structures. Due to the capabilities of the experimental set up used in this chapter, the effects of ambient temperature on electrical treeing were not investigated here.

5.3.2 A Breakdown channel in PDMS(E)

Figure 5.6 shows a breakdown channel in PDMS(E) grown at 15 kV and exposed via microtomy. The approximate positions, both in and around the breakdown channel, that were analysed via CRMS are marked in figure 5.6 and the resulting spectra are shown in figure 5.7. From these spectra we can see that as with the results obtained by Vaughan *et al* [25, 32] there are 3 components to the breakdown channel. Firstly, in all the spectra, the typical peaks relating to PDMS can be seen between 450 and 1500cm^{-1} (as identified in chapter 2). In all cases these peaks are superimposed on varying degrees of fluorescence. This suggests that, as with the PE, there is material degradation in the areas surrounding the breakdown channel. Finally when analysing the interior of the breakdown channel the presence of the D and G bands of sp^2 hybridised carbon can be seen located at approximately 1320 and 1580 cm^{-1} respectively. These bands have varying intensity and prominence compared to the presence of PDMS thus suggesting that although the walls of the breakdown channel are lined with PAHs there are some regions where there is a low density of carbon, such that, the peaks relating to PDMS dominate.

To reinforce this, Raman spectra acquired at different distances from the central axis (indicated by the dashed line in figure 5.6) of the breakdown channel can be seen in figure 5.8. In these spectra the D and G bands of graphitic carbon appear to be the dominant spectral feature inside the breakdown channel (up to 70 μm from the central axis) only reducing in its contribution to the spectra when located in the bulk of the

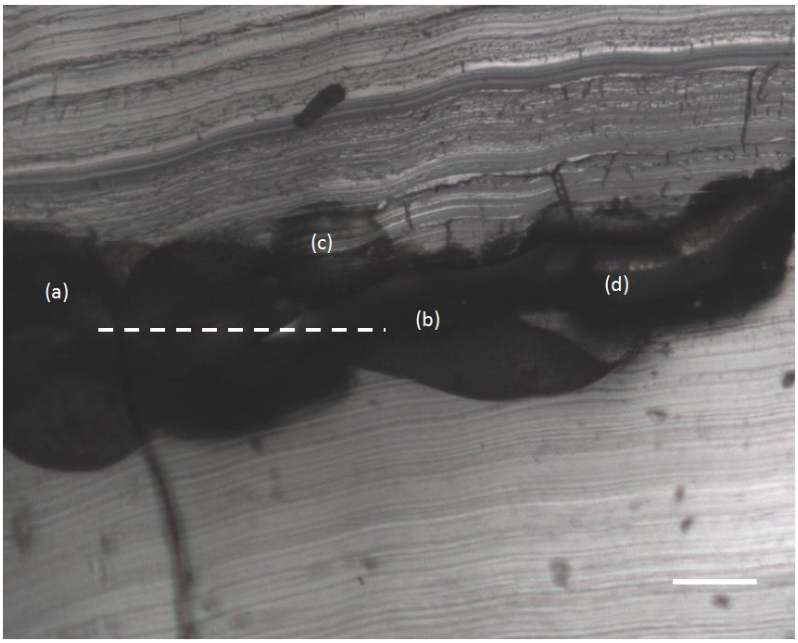

Figure 5.6: Optical micrograph showing the relative positions analysed on an electrical breakdown channel in PDMS(E) (scale bar equivalent to 250 μm)

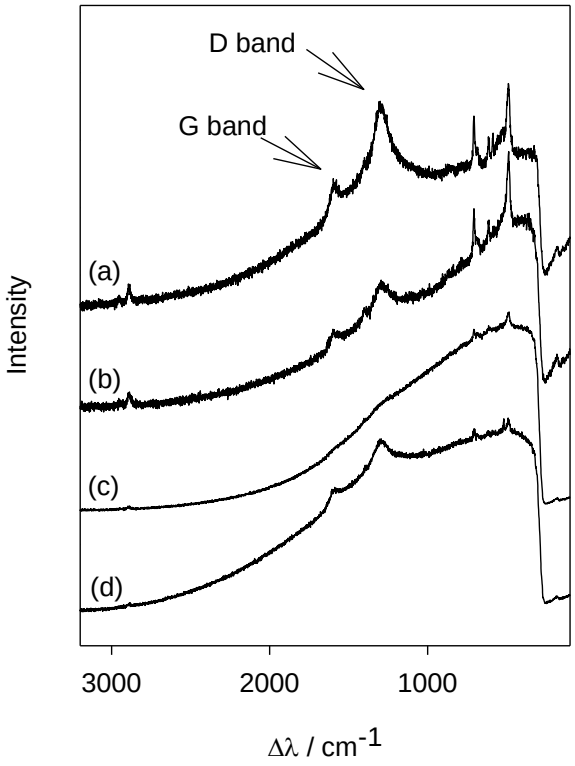

Figure 5.7: Raman spectra of random positions of breakdown channel in PDMS(E) as indicated in figure 5.6

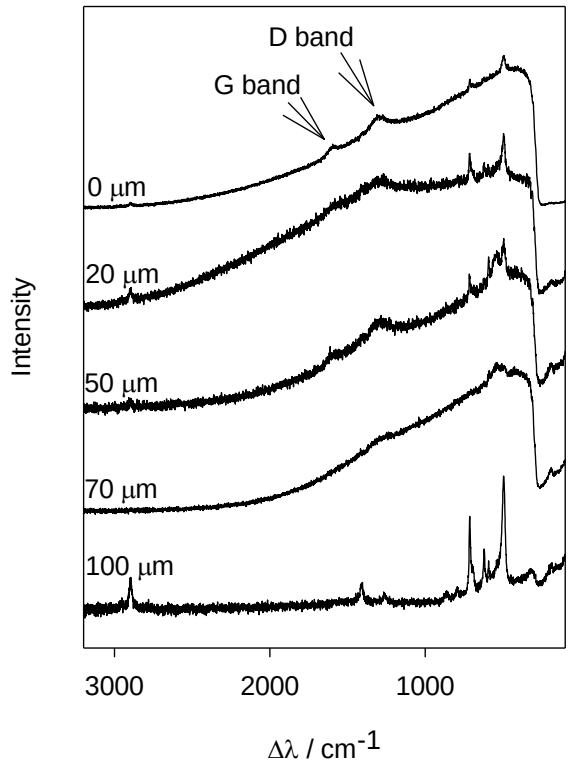

Figure 5.8: Raman spectra acquired as a function of distance from central axis of breakdown channel in PDMS(E)

surrounding polymer, 100 μm away from the central channel. This suggests that in the case where breakdown occurs in PDMS(E), material degradation is localised and restricted to the region close to the breakdown channel.

The presence of PAHs in the breakdown channel suggests that the process of breakdown in PDMS involves the breakdown of the bonds between both the siloxane, and the side groups of the polymer chain that contain CH_3. The presence of carbon found in aged PE samples in Vaughan *et al's* work [32] suggests chain scission of the polymer backbone itself. If this was the case in PDMS however, it would be expected that SiO_2, which is the most common and stable by product of PDMS, would be formed and results would show a large peak at 465 cm^{-1} [166] as indicated by figure 5.9 which is the spectra of crystallised SiO_2 (quartz) [167]. The results given here, surprisingly, show little or no evidence of this.

5.3.3 The Chemistry of Treeing in PDMS(E)

Figure 5.10 shows an optical micrograph of an electrical tree found in a sample of PDMS(E) grown at 15 kV. Once again, the surface shown has been exposed via microtomy to reveal segments of the tree channel. The areas marked in figure 5.10 were sampled via CRMS and the corresponding spectra can be found in figures 5.11 and 5.12. Figure 5.11 shows spectra from various points around the tree channel. From this we can see that there are similar features to those found in figure 5.7 but they are by no means as dominant as with the breakdown sample. Peaks relating to

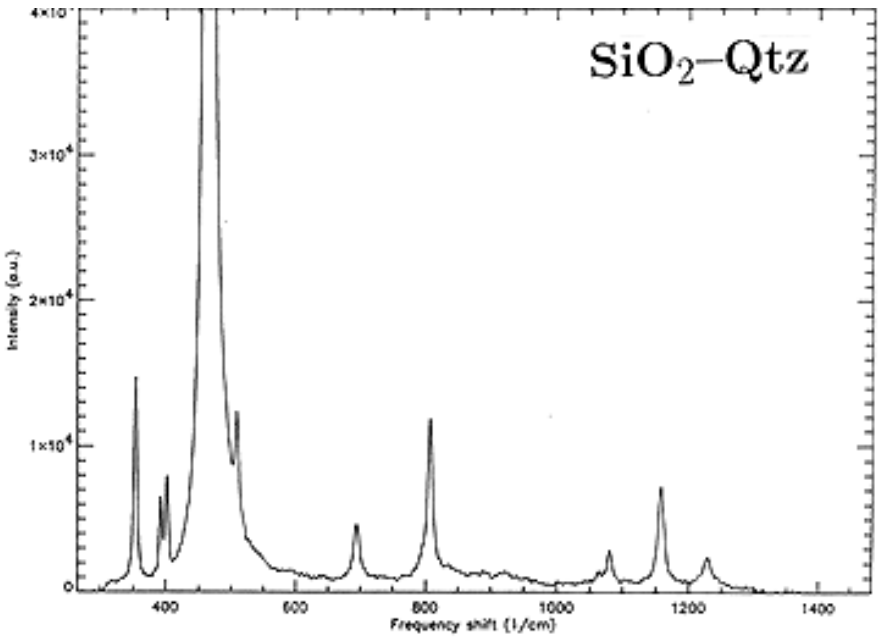

Figure 5.9: Image showing the Raman spectral peaks of SiO_2 in the form of Quartz [167]

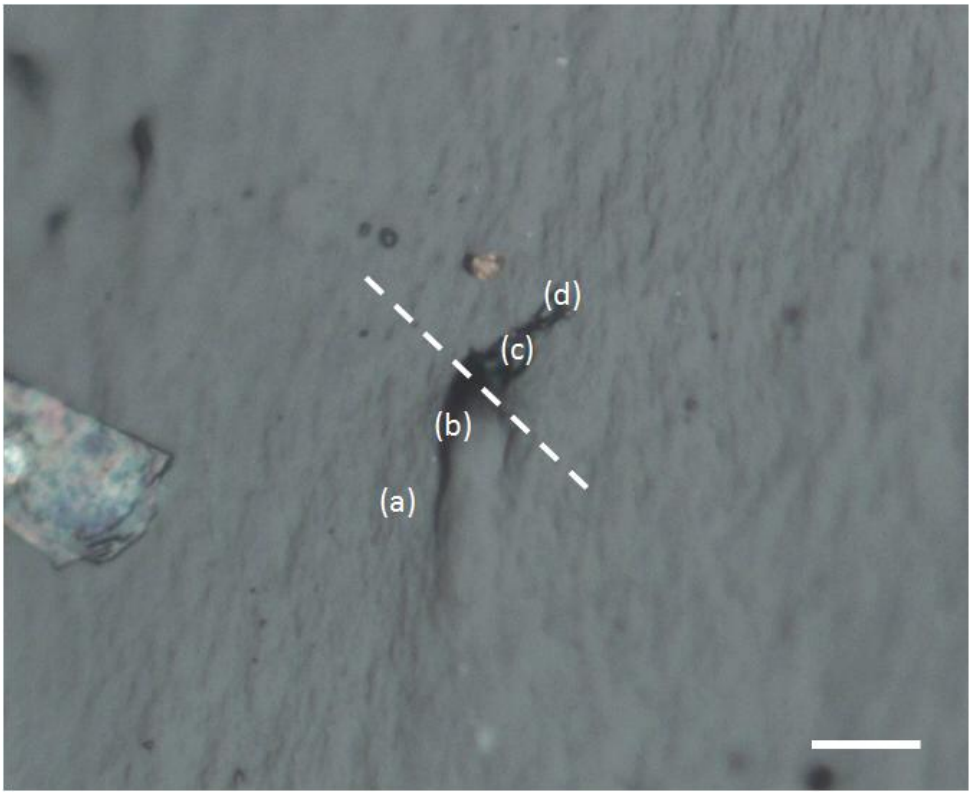

Figure 5.10: Optical micrograph showing the relative positions analysed on a small portion of an electrical tree grown in PDMS(E) (scale bar equivalent to 25 μm)

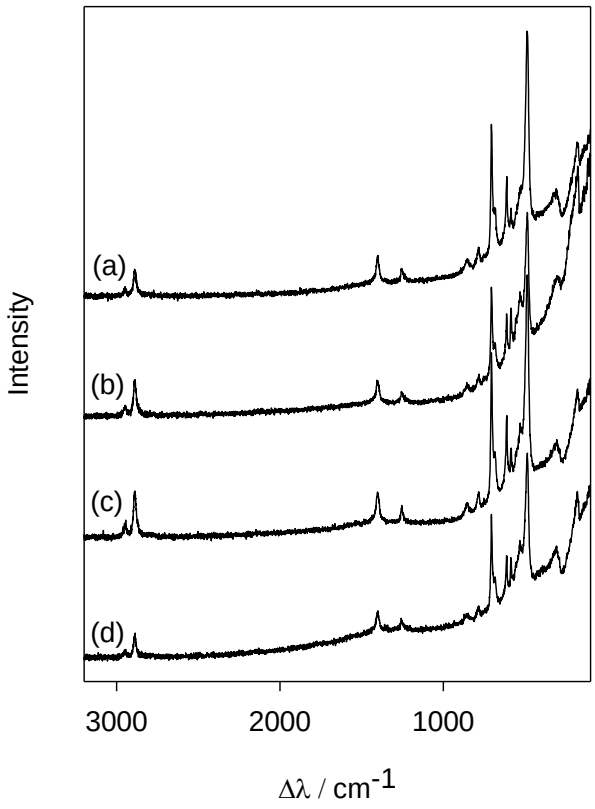

Figure 5.11: Raman spectra of various positions in an electrical tree channel in PDMS(E)

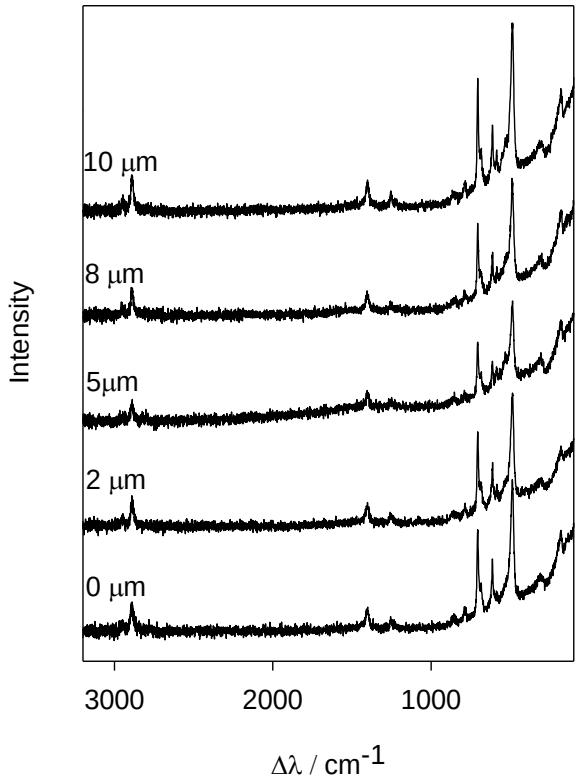

Figure 5.12: Raman spectra acquired as a function of distance from central axis of electrical tree channel in PDMS(E)

PDMS can be seen in all spectra and are now the dominant feature in the spectra. In all spectra in this figure, at the lower wave numbers, there is an increase in the slope of the spectra. Its intensity and contribution to the spectrum however, is not as large as in the spectra obtained from the breakdown channel and does not mask the peaks originating from the polymer matrix. Unlike previously mentioned it is believed that the origin of this slope, is related to the performance of the spectrometer and not a result of chemical changes within the polymer matrix. Inside the tree channel there is little or no evidence of the presence of PAHs, and the chemical matrix is largely unchanged from the unaged bulk of the material whereas in figure 5.7 the D and G bands dominated the relevant spectra. Figure 5.12 shows scans from points at various distances from the central axis (indicated by the dashed line in figure 5.10) all of which show spectra very similar to the original matrix.

It has been widely reported that the breakdown of PDMS leads to volatile cyclic silicates and other by-products [168-170]. More specifically, cyclic oligomers are formed and polymer chains are shortened following the formation of energetically favourable transition states of the 3d orbital's in the silicon atoms in PDMS [171]. TGA and FTIR analysis has also suggested that the formation of these cyclic oligomers, leads to by-products such as water, carbon dioxide and volatiles [172]. Despite the low oxygen

environment in the treeing samples used in this chapter it would be expected that similar by products would be found, namely SiO_2 and volatile organics. It is also possible that these volatiles diffuse away throughout the sample following ageing leaving no trace in the sample.

It is also worth noting that in all the spectra seen in figures 5.7, 5.8, 5.11 and 5.12, there is little or no evidence of the peaks relating to oxidisation products identified in the previous chapter. Although there are still some peaks in the region between 300 and 600 cm^{-1}, these peaks are synonymous with those of PDMS itself. Due to the medium in which the trees and breakdown channels are grown being largely of free air, there is little or no 'free' oxygen molecules within the system from which the oxygenated by-products can be made. As the PDMS backbone contains oxygen it is possible that there would be some oxygenated by-products but the quantities of which would be small compared to any by-product produced if there were air within the system. The absence of peaks relating to oxidised by products reinforces the work of Tomer *et al* who recently performed a thermal ageing study of various PDMS samples and concluded that with a variety of spectroscopic techniques, no significant oxidation products, formed as a result of ageing, were detected [172].

The results from these two samples, as with the results obtained by Vaughan *et al*, show 3 key elements even if the relative proportions are different in silicone rubber [25, 32]. The presence of the original polymer matrix is clear in all spectra and this (as with the PE) is superimposed on a background of fluorescence when focused upon the tree/breakdown channels. In both the tree and the breakdown channels there also appears to be varying degrees of PAHs, which is consistent with that of conducting trees in PE. One difference is that there appears to be little or no fluorescence in the surrounding matrix as was shown by Vaughan *et al* [32]. The reasons for this is that the tree examined contained few branches and hence, there are fewer sub surface channels giving out of focus photons from the localised degraded polymer. The fluorescence contributions to sub surface phenomenon is in line with the earlier work discussed in chapters 3 and 4.

5.3.4 A Breakdown channel in an epoxy resin

As with the PDMS(E) samples, an electrical tree grown at 24 kV, was allowed to evolve until failure such that a conductive path between the high voltage needle electrode and the earthed planer electrode was formed. This sample was then cut open, such that the internal walls of the breakdown channel were exposed. This breakdown channel (as can be seen in figure 5.13) was analysed using CRMS at various positions along its

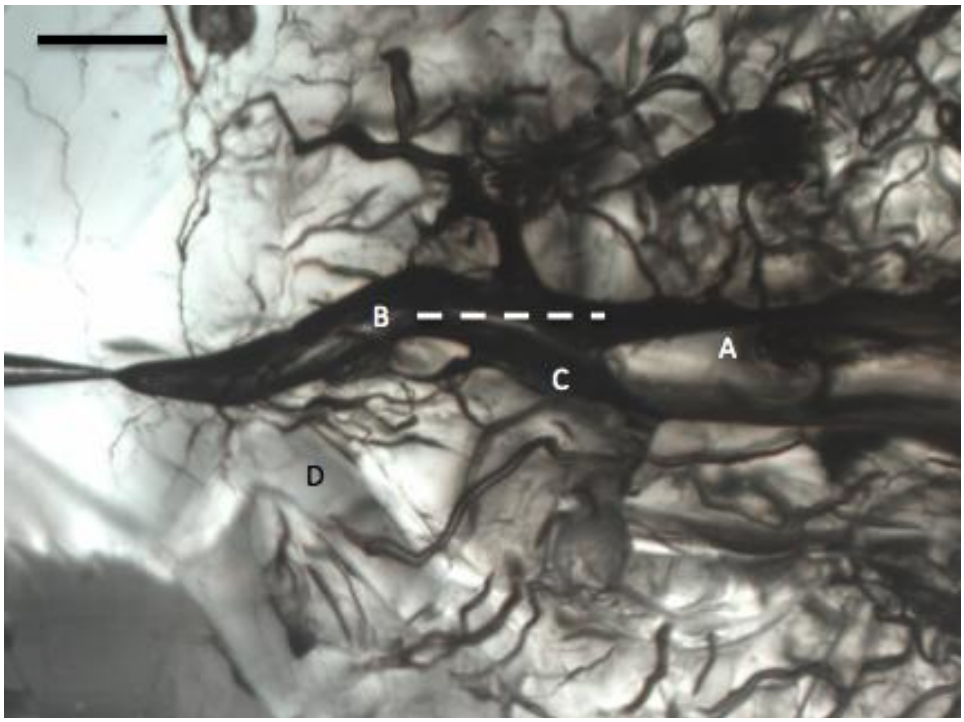

Figure 5.13: Optical micrograph showing the relative positions analysed on an electrical breakdown channel in epoxy resin (scale bar equivalent to 500 μm)

length, as can be seen in figure 5.14. Spectrum (d) in this figure, shows peaks similar to those we would expect to see in epoxy resin (as identified in the previous chapter) superimposed on a fluorescent background. This fluorescent background is likely to be due to out of focus sub surface photons from a highly fluorescent area below the surface thus contributing, but not dominating, the spectrum. Spectrum (d) shows that there are some localized areas that remain chemically unchanged near the breakdown channel but on average, the spectra obtained contain evidence of the wide spectral D and G bands of Carbon and large amounts of fluorescence as shown in specra (a), (b) and (c). This presence of the D and G bands superimposed onto a fluorescent background masks the spectral peaks of the original polymer matrix.

Figure 5.15 shows spectra acquired at various distances from the central axis of the breakdown channel, as indicated by the dashed line in figure 5.13. As expected, in the central portion of the breakdown channel the spectra are dominated by the D and G bands of carbon and fluorescence. These elements decline in significance as the distance from the breakdown channel increases, although fluorescence remains a large factor in all the spectra. This leads to the conclusion that the tree channels surrounding the breakdown channel are highly fluorescent perhaps as a result of the high energy dissipation in this region due to the breakdown events.

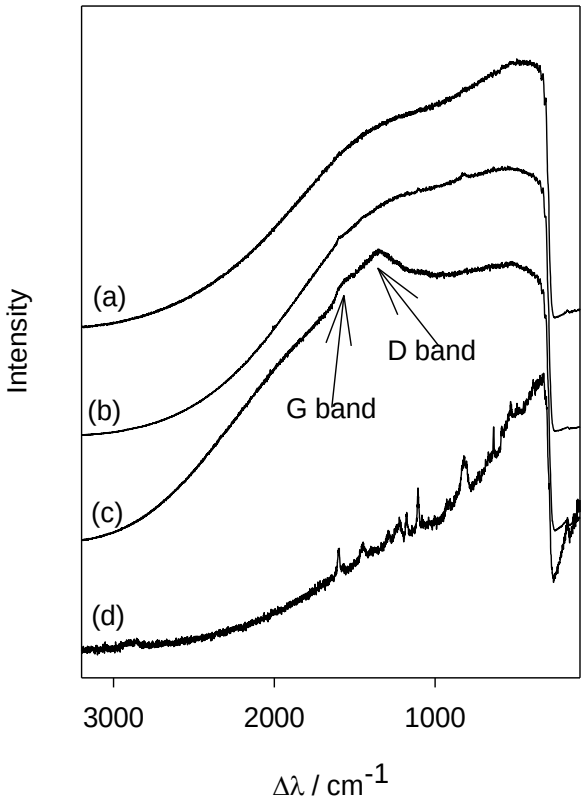

Figure 5.14: Raman spectra acquired at various positions in a breakdown channel in epoxy resin

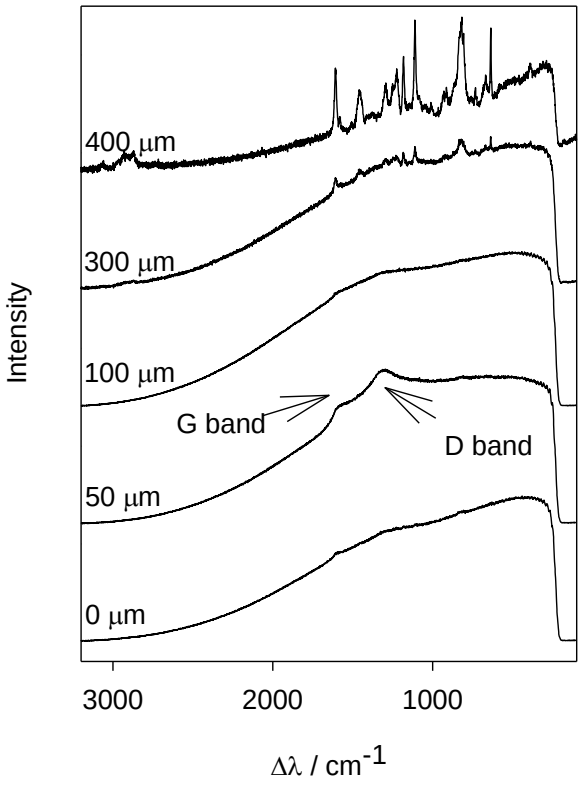

Figure 5.15: Raman spectra acquired as a function of distance from central axis of breakdown channel in epoxy resin

As shown in Chapter 2, the repeating unit in epoxy resins contains benzene rings and, as such, epoxy resins contain a large number of carbon atoms. Studies have shown that the degredation of amine cured epoxies (such as the one used in this study) degrade via a number of mechanisms. Chain scission between the bonds in the polymer matrix is one such reported method [173] and is the likely cause of the breaking of many carbon bonds in the samples in this chapter. This results in a strong presence of PAHs in the Raman spectra of electrically aged epoxy resin as shown in figures 5.14 and 5.15. This method of degradation and the resulting spectra are consistent with previous results presented in this chapter concerning PDMS(E) and the results obtained from electrically aged voids in chapter 4. Other methods of degradation in epoxy resin have been reported to be the formation of double bonds following the production of water molecules from the $-CH_2$-CH(OH)- group [174]. This method of degradation leads to mass loss of the polymer due to dehydration. Finally epoxy resins have been reported to degrade via a number of reactions including isomerisation, intramolecular cyclisation and chain transfer [175]. These reactions involve radicals formed in the previous methods of degradation [173].

5.3.5 The Chemistry of Treeing in an Epoxy Resin

A highly branched tree spanning two thirds of the bulk material between the electrodes was grown at 19 kV in the epoxy resin. The resulting tree can be seen in figure 5.16. Channels in this tree were then exposed and analysed via CRMS at positions indicated in figure 5.17. In contrast to the electrical breakdown channel in epoxy resin, peaks relating to the original polymer matrix dominate the resulting spectra, as can be seen in figure 5.18. There is a small amount of fluorescence in all the spectra and only a small indication of the broad D and G bands of carbon present in spectrum (b) and spectrum (c). This indicates that during the treeing process, although large amounts of physical damage occurred in the formation of many tree channels, few chemical changes occurred as in the case of the trees grown in PDMS(E).

This assumption is supported by the spectra shown in figure 5.19 which shows data obtained at various distances from the central axis. These spectra contain similar features to those shown in figure 5.18, with the exception that, when focused on the edge of the tree channel, evidence of a small amount of PAHs can be seen. The presence of PAHs on the surface of the tree channels is localized and is thought to be a precursor to the chemistry seen in the sample containing the electrical breakdown channel. From this it can be concluded that the PD activity during tree propagation is sufficient to break the bonds within the polymer. Only when breakdown occurs however, does this cause the amount of carbon in the sample to be formed in

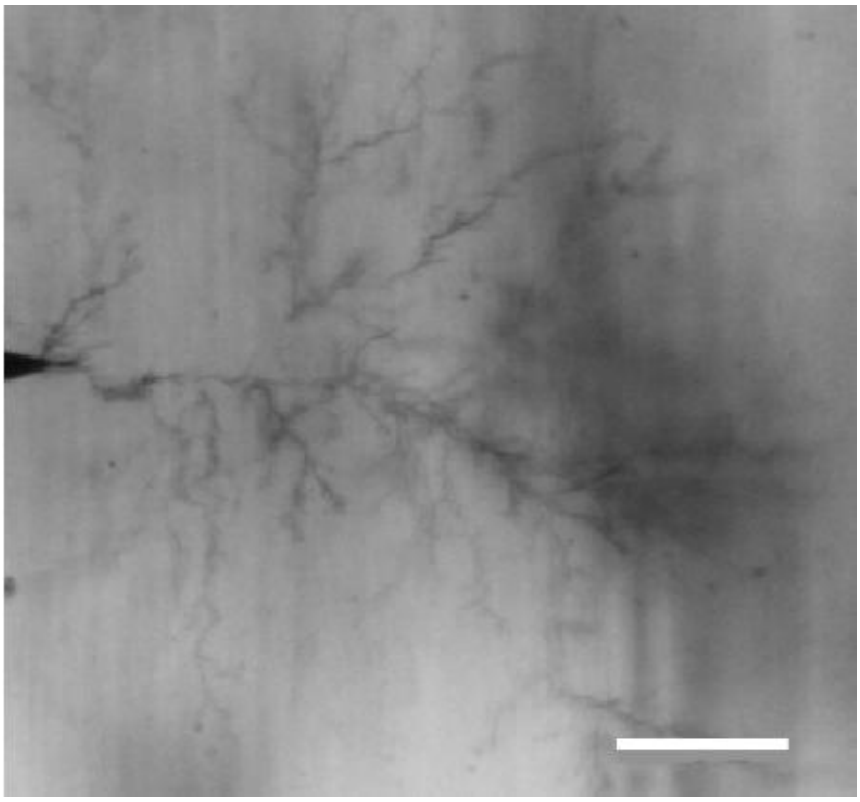

Figure 5.16: Optical micrograph of tree grown at 19 kV in the epoxy resin (scale bar equivalent to 500 μm)

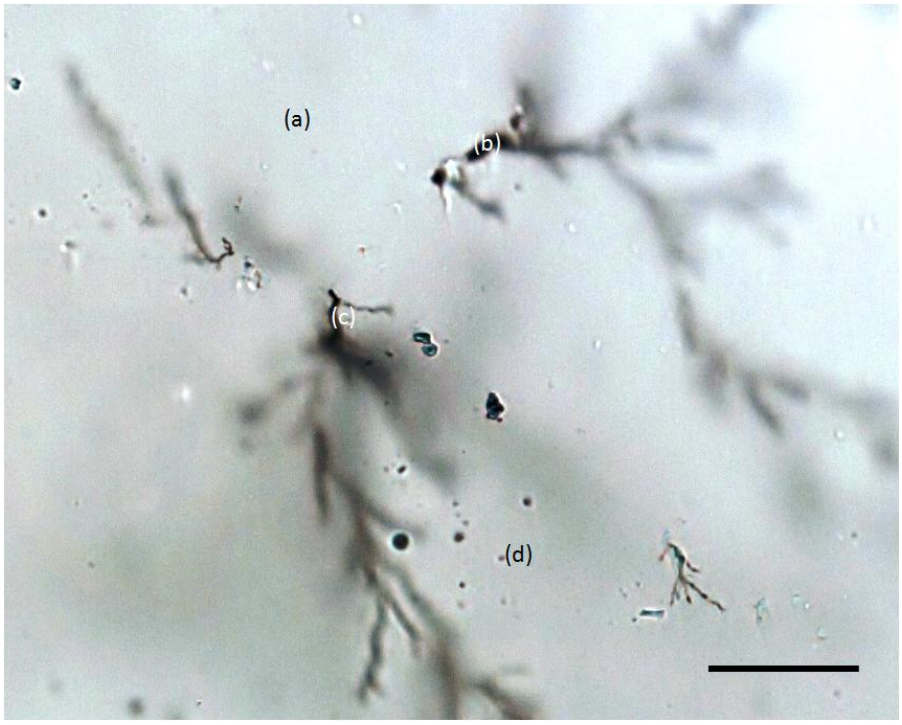

Figure 5.17: Optical micrograph showing exposed tree channels in the epoxy resin and the relative positions analyised with CRMS (scale bar equivalent to 50 μm)

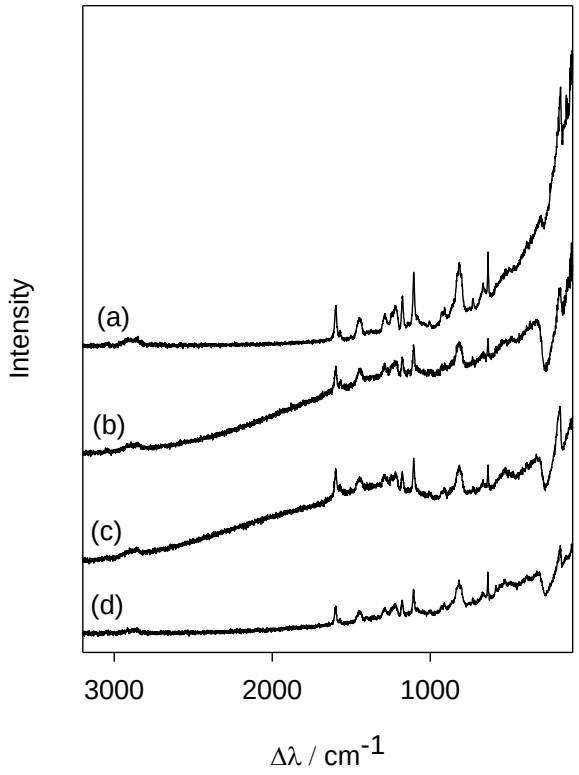

Figure 5.18: Raman spectra of various positions in an electrical tree channel in the epoxy resin

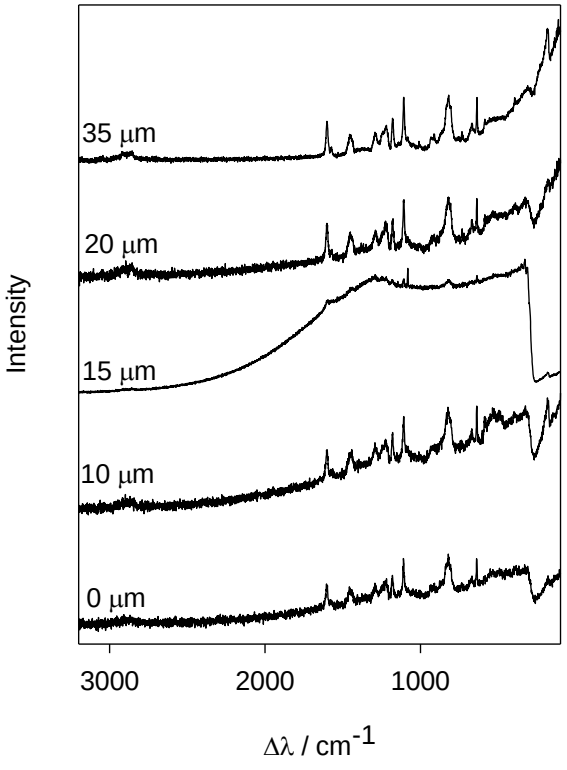

Figure 5.19: Raman spectra acquired as a function of distance from central axis of electrical tree channel in the epoxy resin

sufficient quantities to dominate the Raman spectra. As before this is in line with previous research and results.

5.3.6 FTIR Analysis

As with the void samples in the previous chapter, both the tree channel and breakdown channel analysed above in figures 5.6 and 5.10 were also subjected to FTIR analysis such that comparative and complimentary data to CRMS can be obtained. This FTIR analyis results in the spectra shown in figures 5.20 and 5.21 respectively. In both cases raw data was obtained from several positions within the sample and an average of this data was taken. The data has been normalized such that the peak located at 2500 cm^{-1} is comparable and then displaced vertically by an arbitrary amount to aid interpretation of the data. Figure 5.20 shows a comparison between un-aged PDMS(E) and a tree channel within the sample. In these spectra, peaks located between 1950 cm^{-1} and 2780 cm^{-1} can be seen, which are indicative of PDMS(E) [172]. From these spectra it is evident that there is no detectable chemical difference between the PDMS(E) and the tree channels. Although this supports the Raman data for the same channels a possible reason for no change in the detected signal could be due to the resolution of the FTIR. The FTIR set up in this study samples an area of 100 μm^2 whereas the channels themselves are only a few microns in diameter. In contrast, the spectra in figure 5.21, which shows a comparison between PDMS(E) and a breakdown channel in PDMS, shows a number of chemical changes. Peaks located at approximately 793, 1018, 1085, and 1257 cm^{-1} are present in the breakdown channel

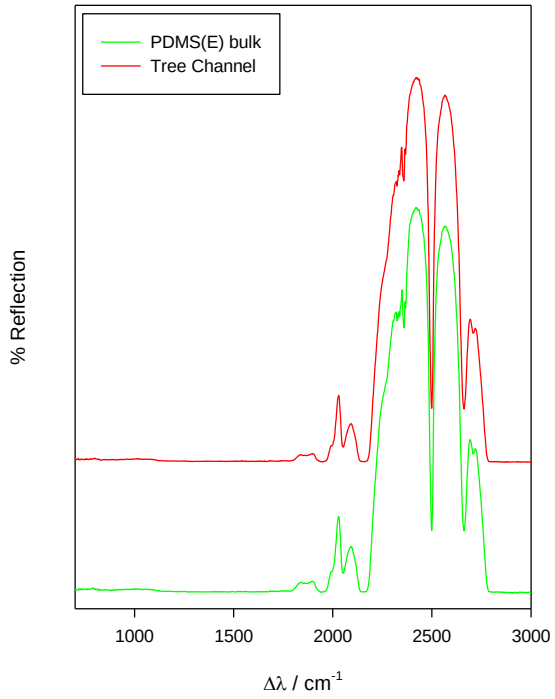

Figure 5.20: A comparison between the FTIR spectra of unaged PDMS(E) and a tree channel grown in PDMS(E)

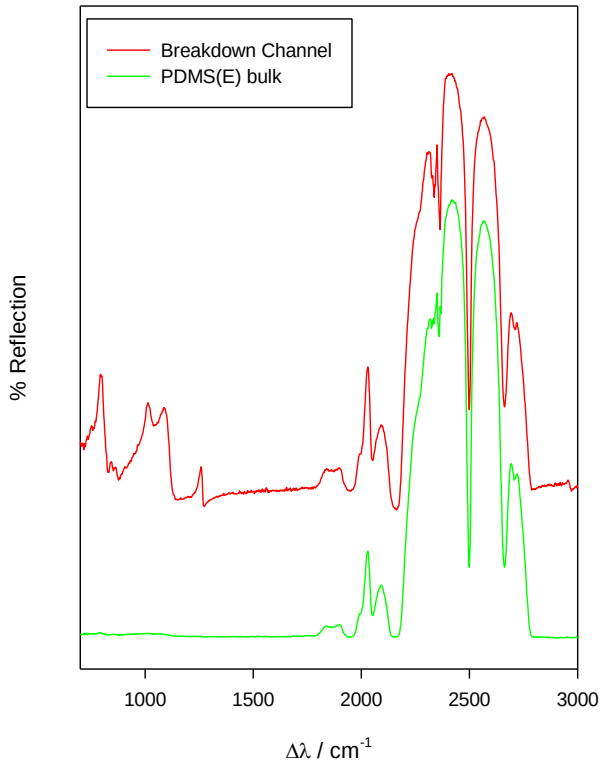

Figure 5.21: A comparison between the FTIR spectra of unaged PDMS(E) and a breakdown channel grown in PDMS(E)

but not the bulk material. As well as this, the peaks located between 1797 and 2150 cm^{-1} have an increased intensity. These peaks have all been reported to be related to carbon [133] and their presence reinforces the Raman data and shows that within the breakdown channel, there is an increase in carbonised species relating to PAHs originating from the side groups of the PDMS(E) bulk. With regards to the fluorescence that was identified in some of the previous CRMS scans, there were no features within the FTIR scans which could be attributed to this fluorescence. This is to be expected however as the incident bean has a different wavelength to the exciting beam used in CRMS.

FTIR data were not obtained from the tree and breakdown channels in the epoxy resin due to the difficulty of sample production. Samples thin enough to allow transmission of the FTIR source proved to be unobtainable.

5.3.7 SEM analysis

Figures 5.22 to 5.25 show a number of typical SEM images showing the internal structure of breakdown and tree channels grown in PDMS(E) and the epoxy resin. Figure 5.22a shows a SEM micrograph of the breakdown channel analysed in figures 5.6. Unsurprisingly it shows that, unlike PE, there is little or no morphology or

structure in the PDMS and consequently there is no visible evidence of material damage outside of the breakdown channel. A SEM micrograph of higher magnification at the position marked by an arrow in figure 5.22a can be seen in Figure 5.22b. This image shows that the walls of the breakdown channel exhibit a nodular structure with features approximately 1 μm in size. This nodular material is reminiscent of Vaughan *et al*'s results on PE [32]. In Vaughan *et al's* paper the SEM images of the tree channels were of etched surfaces and, as carbon isn't affected by the PE etch, it was deduced that the nodular structure seen on the channel walls in the SEM images is composed of carbon. The structural similarity when viewed by SEM to Vaughan *et al's* samples and the relevant Raman data for this channel, suggest that this nodular structure also contains a PAH residue.

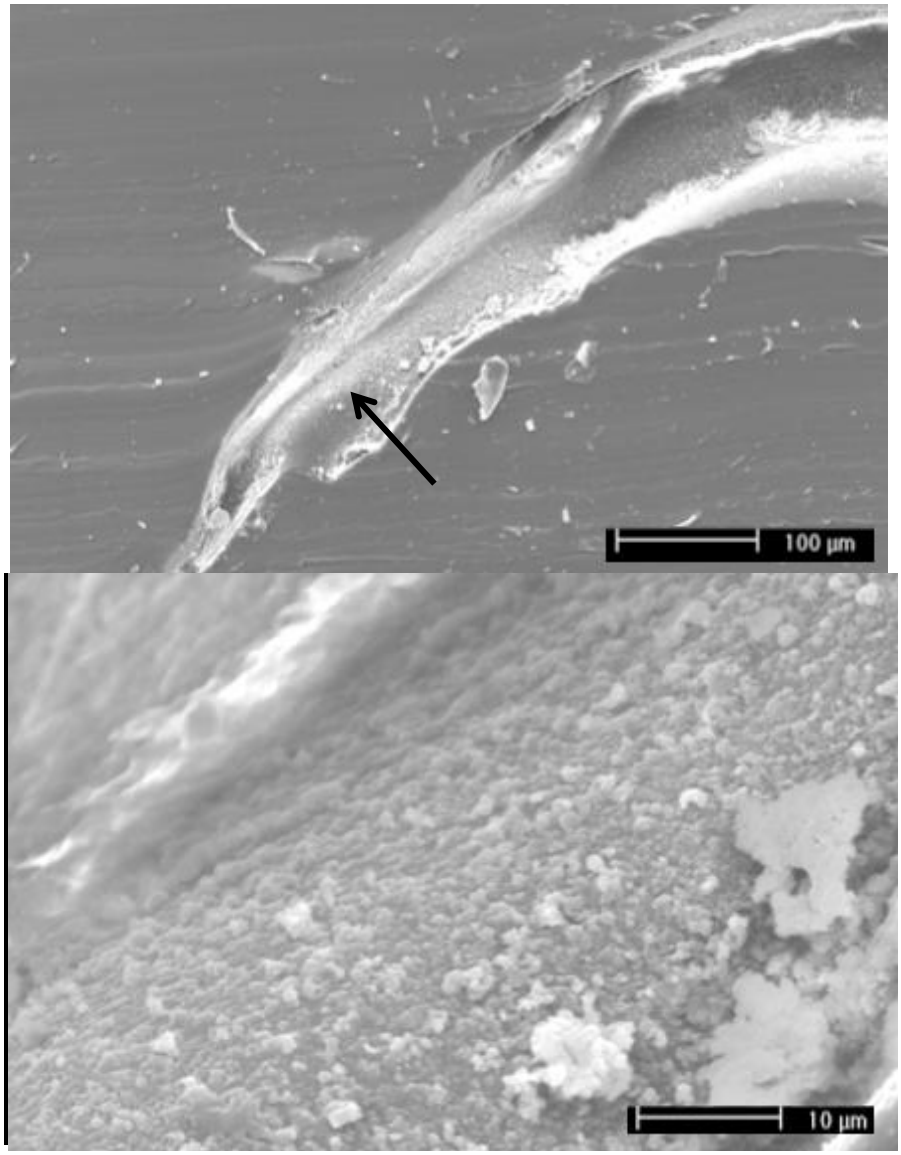

Figure 5.22: SEM images showing (a) section of breakdown channel in PDMS(E) analysed via Raman microscopy and (b) a high magnification of the arrowed area in (a)

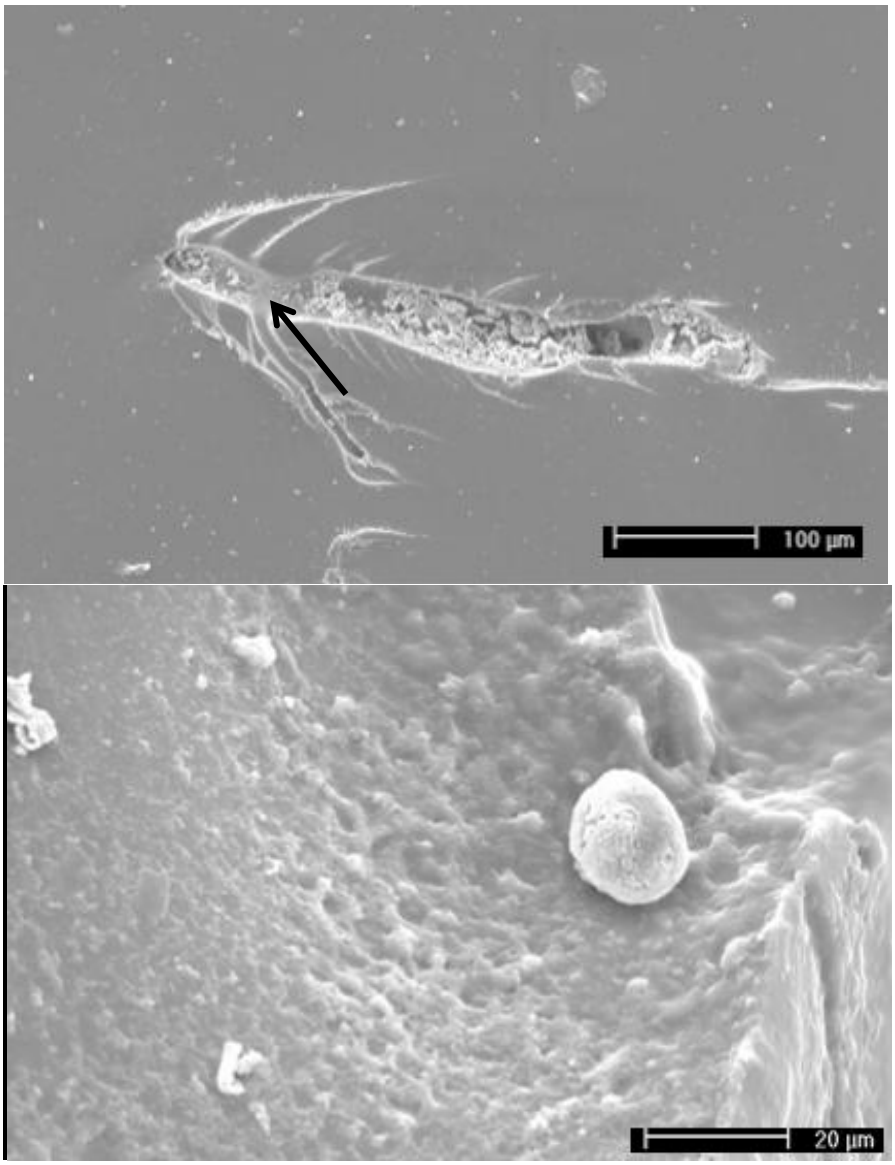

Figure 5.23: SEM images showing (a) section of breakdown channel in the epoxy resin analysed via Raman microscopy, (b) a high magnification detail of the arrowed region in (a)

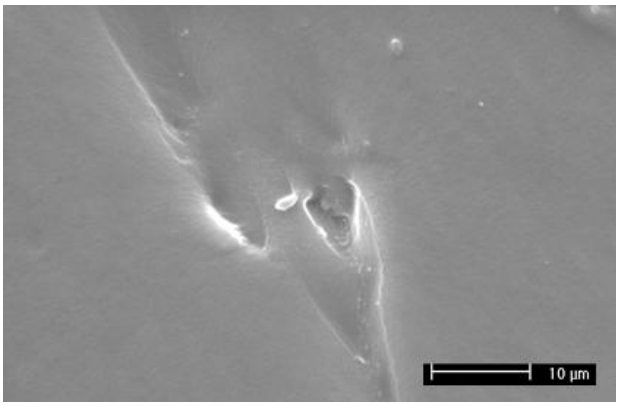

Figure 5.24: Area of tree channel in PDMS(E) analysed via Raman microscopy

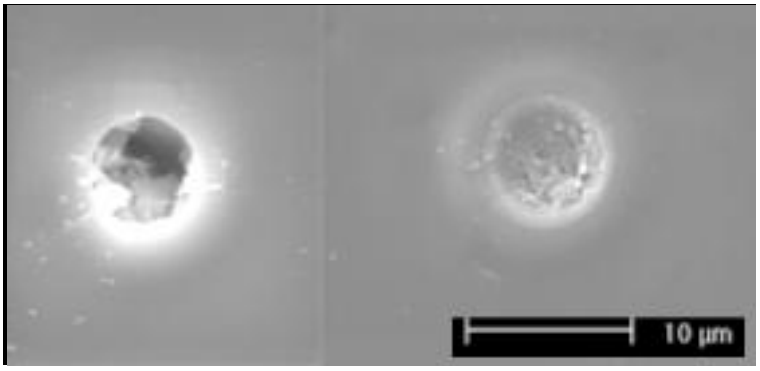

Figure 5.25: SEM images showing two different tree channels in the epoxy resin

As with the PDMS(E), the bulk of the epoxy resin, shown in figure 5.23a, appears to have no structured morphology reflecting its amorphous nature. The breakdown channel in the same image (which was the same channel as analysed in figures 5.14 and 5.15) also contains a material structure on the walls of the tree channel with a different morphology to that of the bulk of the material. Figures 5.23b shows this structure which can be located at the area marked in figure 5.23a by an arrow. Figure 5.23b reveals a comparable nodular structure to that shown above in figure 5.21b. As before, this structure coincides with a Raman spectrum that indicates the presence of PAHs and so it can be concluded that it is carbonaceous in nature. In contrast to the SEM images of PDMS(E) and PE, these nodular structures range in size from approximately 1 to 10 µm. This difference in size is likely to be related to the molecular structure of epoxy resin and its precise decomposition chemistry.

Individual tree channels grown in PDMS(E) and epoxy resin can be seen in figures 5.24 and 5.25 respectively. Figure 5.24 shows a typical SEM micrograph of the tree channel analysed in figures 5.11 and 5.12. As with the breakdown channel, there is little evidence of any morphology within the sample. Contrary to the breakdown channel in figure 5.22 however, the walls of this tree channel are smooth and have the same appearance as the surrounding polymer. There is no material with a nodular structure lining the walls. This reinforces the Raman data in figure 5.10 and indicates that there are no solid residues forming in PDMS(E) tree channels during the process of treeing. In contrast to this, the tree channels shown in figure 5.25 (which were analysed in figures 5.16 and 5.17), do contain debris of a nodular structure similar to that discussed above. This again reinforces the spectral results and it can be concluded that the energy involved in treeing is sufficient to initiate degradation via the chain scission of carbon bonds within the bulk of the epoxy resin.

The quantity of the residue formed in the breakdown channels (and, in the case of epoxy resin, tree channels) however, is not equal to the total loss of material within the channels. In several samples, a volume of material greater than 50 μm^3 has been 'lost'. The reasons for this mass loss is likely to be due to the production of water molecules (and hence dehydration of the samples) and the production of volatiles which diffuse away through the samples as reported by [174] and discussed in previous sections.

5.4 Conclusions

An optical and chemical study of electrical treeing has been provided in this chapter. A number of trees were grown in PDMS(E) and an epoxy resin and their shape/growth characteristics as a function of applied voltage and electrode separation were discussed. Following this, tree and breakdown channels in both systems were exposed by microtomy and analysed using CRMS, FTIR and SEM. Results were discussed in relation to previously published studies on electrical treeing.

From the results obtained we can draw the following conclusions:

- The growth rate and shape of electrical trees is dependent on many factors such as voltage, electrode separation, and not least temperature. When grown at room temperature the majority of trees grown in PDMS(E) are branched in structure with their fractal dimension increasing little with voltage.

- As proposed in previous chapters, CRMS is indeed an effective tool in the analysis of electrical trees that facilitates the chemical characterisation of the internal structure of tree channels grown in transparent polymers when the channel surfaces have been exposed via microtomy. This method however is still not without its flaws and care is needed not to create physical damage to the electrical trees caused by the localised heating effect of the laser.

- Previous work using CRMS to analyse electrical trees in PE showed that there were 3 key features (polymer, fluorescence and the D and G bands of carbon) within the spectra obtained in conducting electrical trees, whereas non conducting trees exhibit increased fluorescence but no evidence of carbon [25, 32]. Raman analysis of an electrical tree and a breakdown channel in an epoxy resin showed the same 3 key features, but with an increased presence of carbon due to the higher carbon content of the original polymer matrix. The results obtained from the breakdown channel in PDMS(E) also showed the same 3 features as those found in conducting trees in PE. The results obtained from

the tree channels in PDMS(E) however, showed some evidence of fluorescence and carbon, but not to the same extent as the breakdown channel or trees in PE and the epoxy resin. When the polymer contains a carbon based backbone, the energies involved in both treeing and breakdown are sufficient to initiate chain scission of the polymer backbone. When the polymer has a siloxane backbone however, no evidence of chain scissioning of the backbone can be seen and only in the case of breakdown is the energy sufficient to break the bonds of the carbon based side groups to form PAHs on the channel walls. Results also suggest that, unlike in the oxygen rich atmosphere of the relatively large voids in the previous chapter, in an oxygen limited environment such as treeing, any by-products related to oxidisation that may form are small when compared to the surrounding chemical matrix and in some cases appear to be non-existent.

- FTIR data obtained from the PDMS(E) trees and breakdown channels, was largely inconclusive. In the case of breakdown in PDMS(E) however, carbonaceous species can be seen reinforcing the Raman data.

- SEM imaging of the breakdown channels in PDMS(E) and epoxy resin is also in agreement with previously published work on conducing trees in PE. The nodular shell which lines the walls of the breakdown channels and the tree channels in epoxy resin is likely to be related to PAHs. Results from the tree channel in PDMS(E) were inconclusive as no difference in structure between the lining of the channels and bulk material could be seen and no evidence of SiO_2 could be identified. SEM imaging also indicated that varing amounts of mass loss occurs during treeing and breakdown. Previous research has indicated that this is likely to be due to the formation of water molecules and volatiles which diffuse away throughout the sample after ageing.

In summary, the results obtained provide an important step in being able to understand the process of electrical treeing in polymers of varying chemical makeup. Results for epoxy resin show similar features to those found in work previously published and there is evidence to suggest that, in the case of breakdown, the bonds between the atoms in the original polymer matrix are broken and the resulting debris contains large amounts of PAHs. Results for PDMS however did not yield the expected results of a SiO_2 debris but in the case of breakdown, large quantities of PAH originating from the sidegroups of PDMS can be found. In the case of treeing, carbon based polymers, as with breakdown, form by-products that are carbonaceous in nature, whereas siloxane based polymers do not appear to generate any residual by-products within the tree channels.

6 : Corona Ageing and Chemical Reproduction

This chapter takes a novel approach to the problem of characterising electrical ageing in solid dielectrics through ex-situ experiments that seek to reproduce the chemistry associated with aspects of electrical ageing in the bulk. Plaque specimens of a range of polymers were subjected to surface ageing via corona discharge in air and in a closed cell where the atmosphere can be controlled and adjusted. The residual products on both the sample surface and the high voltage electrode were characterised by CRMS, and the resulting fingerprints compared with, previously identified by-products. Following this, a number of liquid systems were aged via corona discharge and spark generation in order to try and reproduce the above chemistry from simpler systems in bulk. For comparison to the Raman data, FTIR and SEM analysis was also applied to the samples in order to give a more in depth understanding of them.

6.1 Background

At an ambient pressure and temperature and in the presence of a uniform field, air has a breakdown strength of 3×10^6 Vm^{-1} [176]. If the electric field exceeds this value, the molecules within the gas become ionised such that the air breaks down, resulting in a high energy discharge arc between the electrodes from which the field originates [27].

As reported by Howatson [27], when an electric field is applied between two electrodes any free electrons present in the surrounding gas are accelerated toward the positive electrode. Corona discharge involves a barrier of some sort being present between the two electrodes but the principle is the same. Collisions occur between the accelerated electrons and the gas molecules. The energy of these impacts can excite the electrons in the molecules into higher energy states, so creating excited molecules. These excited molecules relax into radicals, ions and photons and the resulting charged particles are accelerated towards the relevant electrodes. Subsequent ionisation events generate further charged particles such that gas between the two electrodes quickly becomes laden with electrons, positive ions and excited molecules and releases heat and light. It is at this point, when a diffuse glow arises between the two electrodes, and a corona is said to have formed [29].

Corona is often used to treat polymers in order to decrease their hydrophobic qualities and increase their adhesion properties [29, 177]. If the gas between the electrodes contains oxygen (i.e. air) then the free electrons excite the diatomic oxygen molecule (O_2) into vibrational and electrical excited states (as shown in figure 6.1). These

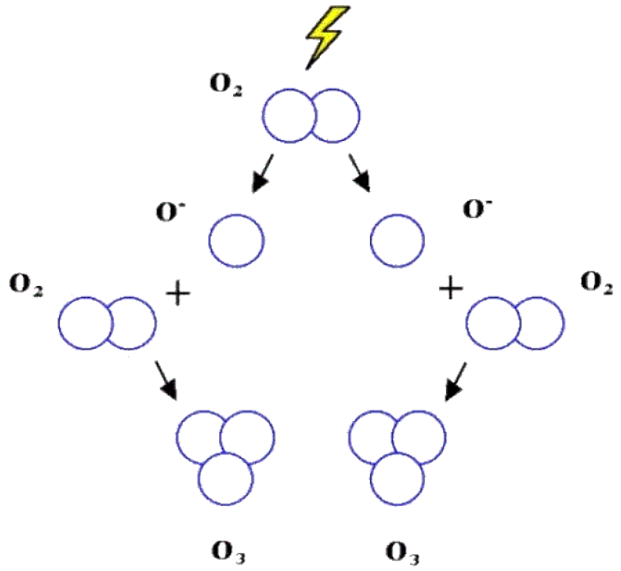

Figure 6.1: Ozone formation due to free electrons in corona discharge [104].

excited molecules can then split into oxygen ions and radicals. These unstable atoms can then bond with other oxygen molecules in order to form O_3 (ozone) [29]

These species molecules are highly reactive and react with other molecules, introducing functional groups containing oxygen into the surface of a polymer situated near the electrodes. These polar functional groups are one factor that increases the adhesive qualities of the treated polymer [178].

In addition to this, corona treatment of polymers causes a change in surface structure of the polymer, altering its external appearance [31, 179, 180]. Molecules in the surface have also been reported to become cross linked [181], leading to an increase in molecular weight of the polymer [182]. It has been reported that the high energy particles in the corona bombard the surface of the polymer creating micropits on the surface [118]. This is similar to the process of ion and electron bombardment in gas filled voids as discussed in chapter 4. It has been shown that these micropits increase in size, depth, and number with an increase in the electrical field (and hence energy of the corona), time of exposure, and temperature [116]. These micropits are thought to lead to an increase in adhesion due to a greater potential bond surface but are largely reliant on the surface energy, viscosity of the adhesive liquid, the size of the micropits and finally the shape of the micropits [29]. Other theories proposed for the increased adhesion of polymer surfaces, post treatment via corona, include the elimination of weak boundary layers [183] and electret formation [184].

By treating a polymer with corona discharge, adhesion is increased by the introduction of polar groups into the polymer surface and thus increasing the surface energy and

the hydrophilic nature of the polymer [29]. In the case of polymers used as outdoor high voltage insulation, it is desired that this effect is reduced due to hydrophilic polymers attracting water onto the surface and allowing a conductive path to form between electrodes, thus causing an electrical discharge in the form of a hot localised destructive arc. If electrical discharge does occur across the surface of the sample, then the heat of the arc channel can initiate thermal oxidation of the polymer in question, leading to further erosion [177].

Much work and research has been undertaken to study the effects of corona discharge on polymers [23, 178, 185] with much of it being focused on the surface effects [185] and the reduced hydrophobic qualities of the surface as a result of the corona discharge [23]. The mechanism thought to have an impact on corona discharge treatment is oxidation, and thus polar groups such as O=C-O, C=O and C-O are present [29, 178].

Many analytical techniques have been applied to the study the chemical reactions that take place on the surface of polymers [4, 23, 30, 186, 187] including FTIR [177], XPS [188] and RMS [31]. For example, in 2006 Zhu et al [177] used a combination of FTIR and SEM imaging in order to study the surface degradation of a PDMS(E) and an ethylene vinyl acetate (EVA). In this study a point to plane electrode system was used and it was discovered that there was obvious physical damage to the surface of the samples and this surface damage decreases with distance from the HV electrode. It was also found (using FTIR) that during the ageing process the hydrophobic C-H bonds were replaced by hydrophilic O-H bonds thus resulting in a reduction in the hydrophobic nature of the polymers, an effect disadvantageous when used as high voltage insulator materials.

The treatment of polymeric samples by corona discharge has been reported to be affected by factors such as humidity [189]. An increase in relative humidity means the discharge energy is increased, leading to proportionally higher concentrations of the hydrophilic C-O groups on the surface of the polymer. As well as this, impurities in the gas can lead to dramatic chemical changes in the polymer that has been subjected to corona discharge [184, 190, 191]. Zhang *et al* [29] aged films of a polyolefin using corona discharge in air, O_2, N_2, He and Ar and discovered that it was possible to 'corona-treat' polymers in all these gasses to the same level of surface energy. Despite the inert gasses used, following XPS analysis, the polymer surface still contained evidence of oxygen.

In 2003 Liu *et al* [7] used Raman microscopy in a study of surface ageing on low density polyethylene (LDPE) via corona discharge. They discovered that although there appears to be little chemical change in the surface composition of the aged samples, the deposits left on the HV electrode after the ageing process appear to contain traces of sp^2 hybridized carbon, a product previously identified and linked to conducting electrical trees in LDPE [31, 32]. This leads to a possible novel approach to the problem of characterising electrical ageing in solid dielectrics through ex-situ experiments that seek to reproduce the chemistry of electrical treeing in bulk. By reproducing the chemical changes formed in electrical trees, a deeper understanding of the processes involved can be formed. As well as this, the application of RMS to the corona treated surfaces can help us to confirm earlier theories about the degradation of polymers via corona discharge.

This study aims to extend the work of Liu *et al* [7] to include a similar analysis involving a wider range of polymers as a function of electrode separation and applied DC voltage in a closed chamber containing air. Subsequently, the samples were aged in the same chamber containing controlled nitrogen and argon atmospheres. The high voltage electrodes were then characterised using Raman microscopy in order to see how similar corona ageing is to electrical treeing in solid dielectrics. Following this initial survey, the results were compared to various liquid systems aged via corona discharge and spark aging such that the possibility of reproducing the internal chemistry of electrical trees can be assessed. Samples were also subjected to FTIR and SEM analysis for comparison.

It is noted that the energies involved in all the techniques used in this chapter cover a very wide range and are often much larger than those involved in PD activity and electrical treeing (typically 10^{-7} J). It is probable that this difference in energy can affect the ageing phenomena and hence chemistry of the by-products formed. In the previous chapter however it was shown that the difference in energy between electrical treeing and breakdown in PDMS and Epoxy resin yielded no evidence of the change in chemistry of the by-products formed only their quantity. Similarly, in chapter 4 it was shown that ageing time did not appear to affect the chemistry of the by-products formed in voids. If it can be shown that a similar trend can be found when using higher discharge energies then the bulk generation of the chemical by-products of electrical ageing becomes ever more probable as a higher quantity of debris can be formed with shorter ageing times.

6.2 Experimental

6.2.1 Materials

In this study, plaque samples of five different polymers were aged in order to see how surface ageing varies between different polymers. General information on the polymers used in this chapter (i.e. source) is described in Chapter 2. Information specific to the samples in this chapter such as their method of production and their approximate size are given below:-

Polyethylene: large sheet of additive free LDPE was cut into samples of approximate dimensions 30 x 30 x 1 mm.

Polystyrene: Samples were made by heating moulds filled with pellets of polystyrene at a temperature of 200 °C and adding a pressure of 4 tons. Samples were formed against a glass like surface, quenched from the melt and were approximately 35 x 35 x 5 mm in size.

Polyether ether ketone: Samples of approximate dimensions 30 x 30 x 4 mm were cut from a larger sheet.

PDMS(E): Samples in this project were all made from the Dow Corning Sylgard 184 Silicone Elastomer kit and were made in the same way as in chapter 5. Samples were then cut to size 5 x 30 x 30 mm

Epoxy Resin: Sheets of epoxy resin made by curing a mixture of the resin D.E.R 332 and hardener Jeffamine D230 in a mould at 100 °C. These sheets were then cut to form samples of dimensions 30 x 30 x 1 mm.

Following this, 4 liquid systems were subjected to corona ageing. The liquids used were hexane, dodecane (DD), dodecylbenzene (DDB) and PDMS(L). In each case 5 ml of the fluid was placed in a metal dish 20 mm in diameter and 10 mm in depth. With the exception of Hexane, these liquid systems were also subjected to spark ageing.

6.2.2 Method

6.2.2.1 Corona ageing

In order to achieve ageing the samples were placed upon a grounded aluminium base plate of diameter 25 mm inside a corona discharge test cell (as shown in figures 6.2 – 6.4) within a Perspex chamber beneath a high voltage electrode formed from a hypodermic needle (of tip radius approximately 3 μm) which was attached to a DC high voltage supply. In this experiment (and the preceeding one) a DC voltage was chosen as that is what is used in Liu *et al's* paper [31] and enabled the needle to become

charged such that it attracted the debris formed. The voltage and the electrode separation from the sample were varied such that a corona discharge was formed above the sample. Polymeric samples were subjected to ageing in air and atmospheres rich in nitrogen / argon which were formed by first purging the system of air and then establishing a flow of the desired gas until the desired atmosphere was achieved. The liquid systems analysed were aged in a nitrogen atmosphere to minimise oxidation effects and to ensure the safety of the system due to the volatile and combustible nature of some of the liquids.

Following ageing both the sample surfaces and the electrodes were characterised with CRMS. For the characterisation of the sample surfaces the laser was initially set to 100% but investigation showed that a laser power of 25% for the aged electrodes was more appropriate to minimise sample damage.

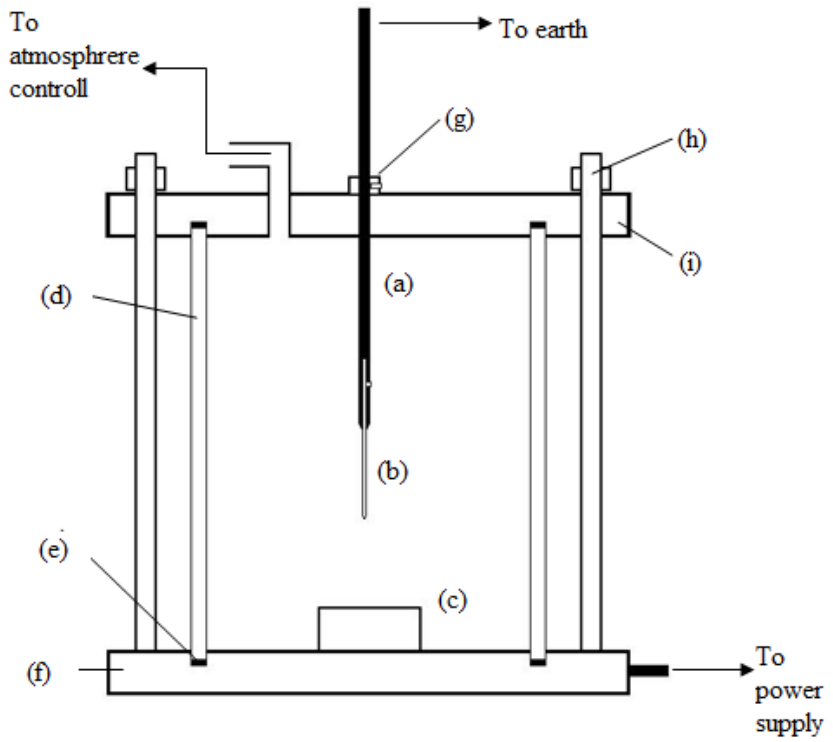

Figure 6.2: Diagram of corona discharge test cell with the following components: (a) Aluminium needle holder, (b) stainless steel hypodermic needle (tip radius approximately 3 μm) (c) Aluminium sample plate, (d) Perspex cylinder, (e) Rubber seals, (f) Aluminium base plate, (g) Washer and grub screw to allow height adjustment of (a), (h) Wooden bolt and nut for securing cell

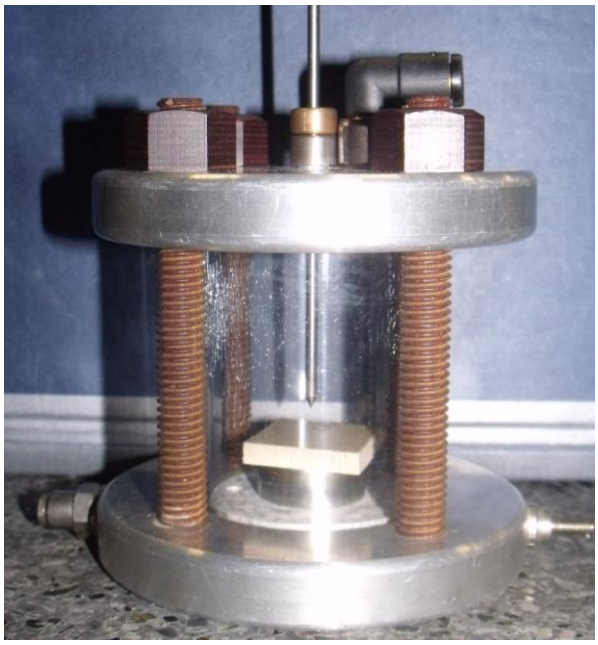

Figure 6.3: Photograph showing corona discharge test cell

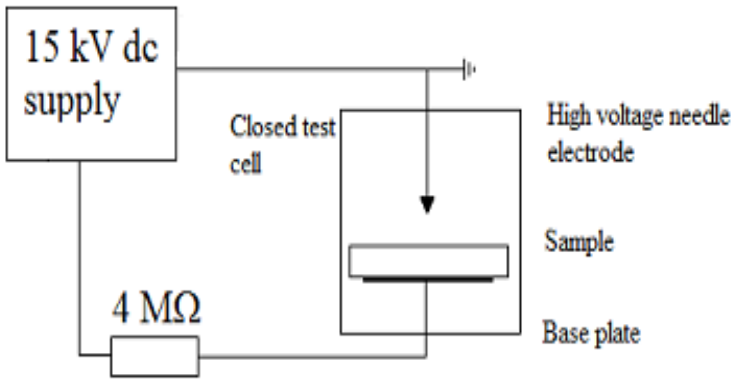

Figure 6.4: schematic showing circuit for corona discharge test cell

6.2.2.2 Spark ageing

In addition to corona ageing, all of the liquid systems were subjected to electrical ageing via a spark generator (with the exception of hexane due to its volatile nature). In each case the spark generator (with a spark gap of 0.3 mm) was immersed into 20 ml of the fluids and was set to a spark rate of approximately 1 spark per second for 16 hours. The energy and discharge duration of the sparks was controlled by the values of the capacitor and resistor marked in figure 6.5 which shows a schematic of the electrical ageing rig. The energies of the sparks ranged from 450 to 28 mJ and had durations ranging from 50 to 10 ms.

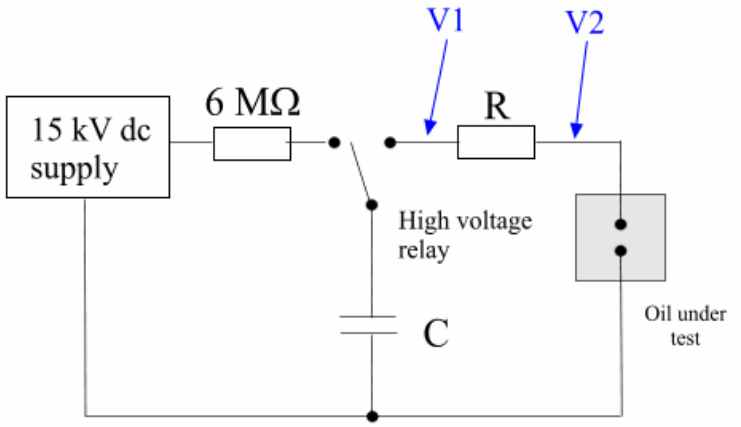

Figure 6.5: Schematic showing circuit for spark generator

Following ageing the debris was separated from the remaining liquid using a centrifuge and acetone (in the case of DD, hexane was used to clean the debris due to its similar chemical nature to DD). This debris was then analysed using CRMS with a laser power of 25% to prevent sample damage.

6.3 Results and discussion

6.3.1 Initial testing and ageing parameters

Before Raman analysis can be performed on the samples the optimum operating parameters including electrode type, electrode separation and ageing time were determined. In order to achieve this, samples of PDMS(E) were aged in air at room temperature with a voltage of 20 kV whilst each of the parameters were altered. Prior to and preceding aging, the mass of the samples and electrodes was measured. Due to the small magnitudes of the masses involved, however, it proved impractical to assess the effectiveness of the various ageing parameters in this way. Subsequently, the deposits on the electrodes were imaged after ageing such that the deposit size and form could be seen and the optimum parameters for the production of deposits on the needle determined. Below is a list of all of the possible ageing parameters.

- Electrode type – A stainless steel hypodermic needle with a tip radius of 5 μm or a tungsten needle that has been etched to give a tip radius of 2 μm.
- Separation between needle tip and sample surface– 1, 2, 3 mm
- Ageing time – 3, 6, 9 and 12 hours. Note, ageing time must be determined to give sufficient debris whilst still being time efficient.

Once the optimum value for each parameter was determined it was kept constant so that the other parameters could be efficiently determined. Figure 6.6 shows optical

micrographs of the deposits found of the subsequent needles. From these images it can be seen that despite having a smaller tip radius and hence a higher field at the electrode tip, there is less debris found on the etched needles than a hypodermic needle aged under the same conditions (although more uniform). As well as this, although not clear from the figure, it was found that the size of the deposits formed increases with ageing time but decreases with electrode separation. It was discovered, however, that once the ageing time exceeds approximately 5 hours, the rate of growth of the deposit decreases.

For the remainder of this chapter all samples that were subjected to corona ageing were done so for 6 hours with a hypodermic needle as the electrode positioned 1mm from the surface of the sample. As the corona is dependent on conditions such as sample size and atmosphere, the applied voltage was varied such that a stable corona was formed above the sample without exceeding the breakdown voltage of the surrounding atmosphere.

It is also worth noting the overall shapes of the deposits formed on the needles; when PDMS(E) is aged, it forms tree like structures. If we look at the trees in figures 6.6 a, c and f, it would appear that the formation of these structures, unsurprisingly, follow the electric field lines of the electrode. Figure 6.6 b) also shows this to some extent but part of the structure has collapsed, possibly due to coming into contact with an external body. Figures 6.6 e and g, however, don't appear to follow the field lines and form non uniform structures at random points along the needle tip. This suggests that, for these samples, the field surrounding the tip of the electrode was not uniform, hence causing the unexpected form of the structures for these needles. What is also interesting to note is that for PDMS(E) these structures are transparent, leading to the hypothesis that they are largely silicone and not carbon based. As well as this the size of the deposits for PDMS(E) is much greater than those formed from the carbon based polymers for which the reasons are as yet unclear.

6.3.2 Surfaces

Following the ageing process the aged surfaces of all the samples were analysed using CRMS. Although the aged surfaces appear visually damaged and pitted/cracked (as shown in figure 6.7), an effect which decreases with distance from the high voltage electrode, no chemical changes could be found using CRMS. Figures 6.8 to 6.12 show typical spectra from various positions on the sample surfaces that were aged in air. The bottom traces are from an unaged part of the surface and hence a typical representation of the matrix response and so can be used as a comparison. We can see from these spectra that there is little or no chemical change occurring on the

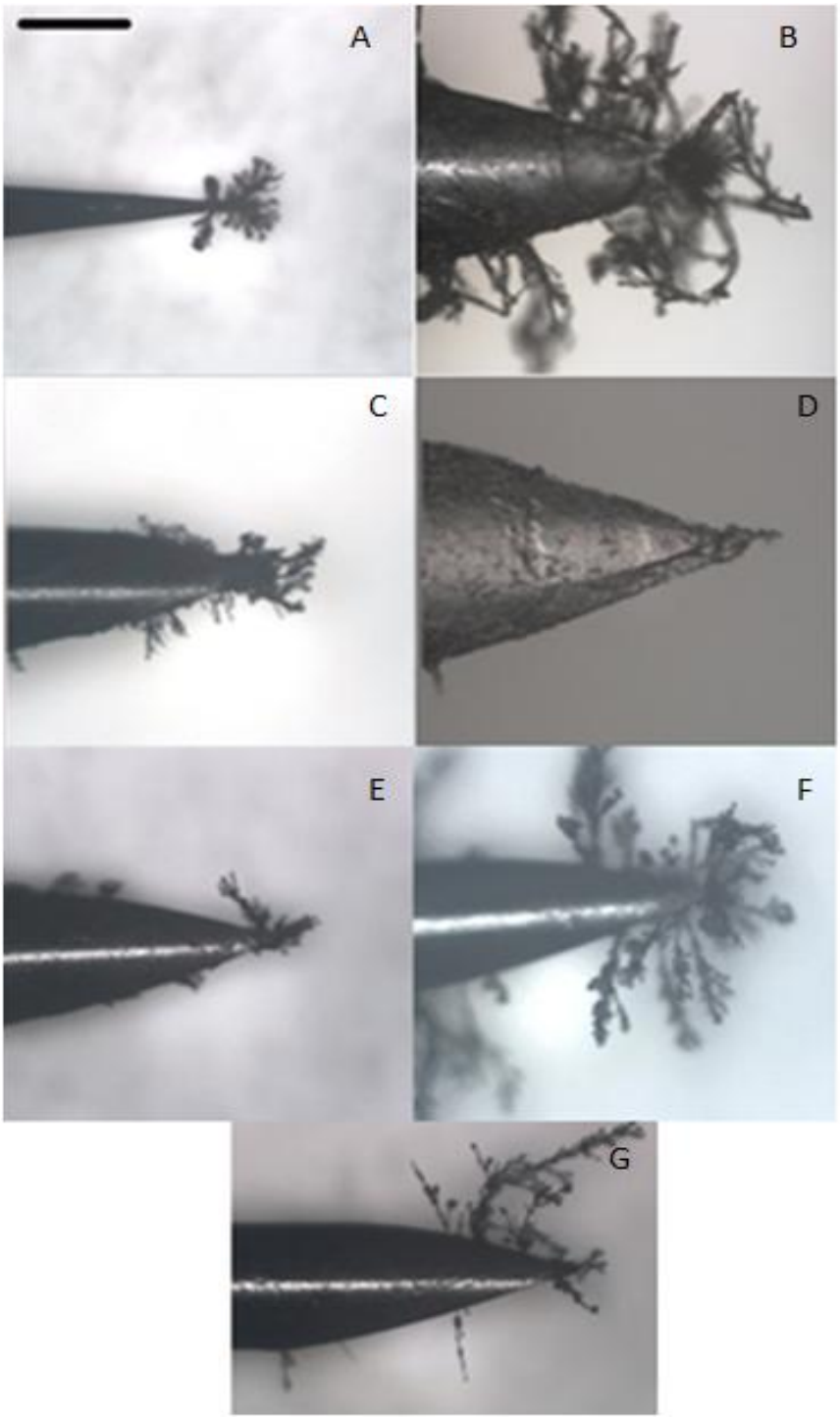

Figure 6.6: Optical micrographs of the deposits formed on high voltage needle electrodes following the corona ageing of PDMS(E) under different conditions, a) etched needle aged for 6 hours with a 1 mm electrode separation, b) hypodermic needle aged for 6 hours with a 1 mm electrode separation, c) hypodermic needle aged for 6 hours with a 2 mm electrode separation, d) hypodermic needle aged for 6 hours with a 3 mm electrode separation, e) hypodermic needle aged for 3 hours with a 1 mm electrode separation, f) hypodermic needle aged for 9 hours with a 1 mm electrode separation, and g) hypodermic needle aged for 15 hours with a 1 mm electrode separation.

sample surface after corona treatment, and with the exception of the occasional presence of a small amount of fluorescence, the spectra are identical to the non aged samples. This, however, does not mean that no chemical changes have taken place, only that in this case the predicted oxygen functional groups were not detected by Raman microscopy. This is perhaps another limitation to the method, in addition to those mentioned in previous chapters.

6.3.3 Electrode deposits

6.3.3.1 Air

After analysis of the sample surfaces, CRMS was then applied to the deposits left on the HV electrodes as shown in figure 6.6. The quantities of deposits varied from sample to sample but in all cases enough material was generated to be analysed with CRMS. Figures 6.13 to 6.17 show typical Raman spectra gained from various positions on the needle deposit of all of the electrodes aged in air. The Raman response of the matrix of the un-aged material is also included in each figure for comparison. (Note all spectra have been multiplied and displaced by arbitrary amounts along the y axis to improve clarity). In all cases we can see that the material found on the needle has little or no evidence of the original material and the peaks synonymous with LDPE, PS, PEEK,

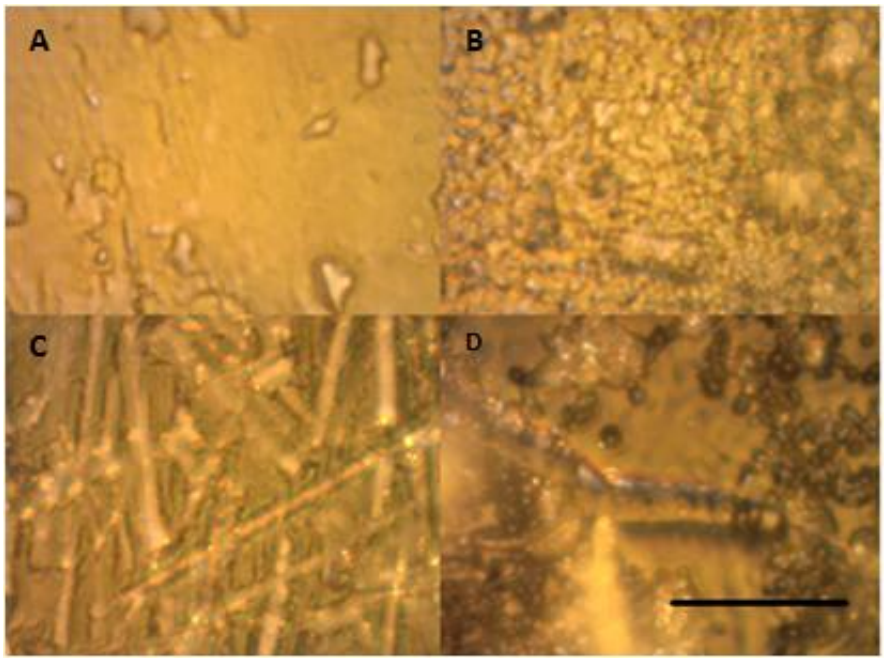

Figure 6.7: Optical micrographs showing a) un aged LDPE, b) corona aged LDPE, c) un aged PDMS(E), d) corona aged PDMS(E). Scale bar equivalent to 10 μm

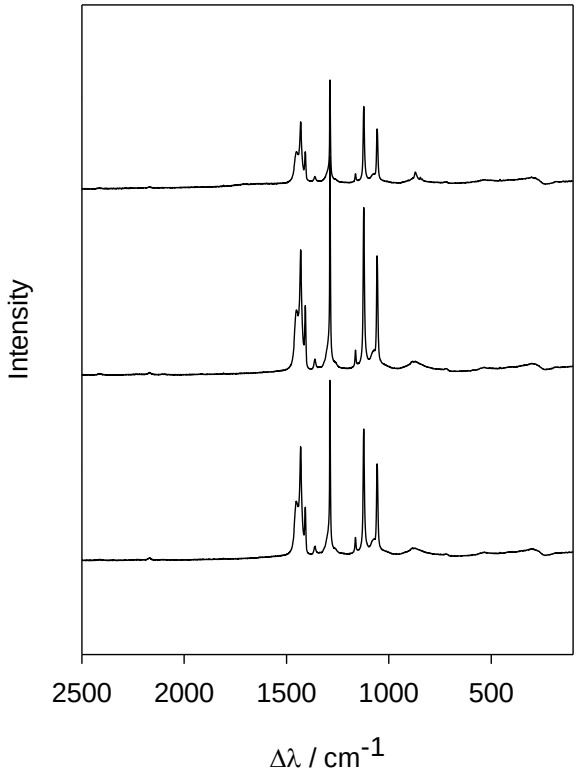

Figure 6.8: Raman spectra for various positions on LDPE surface aged by corona discharge.

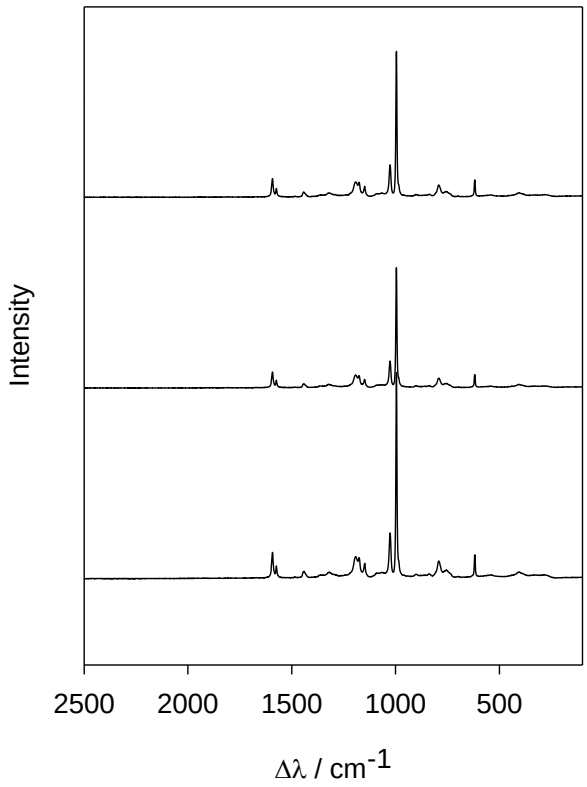

Figure 6.9: Raman spectra for various positions on PS surface aged by corona discharge

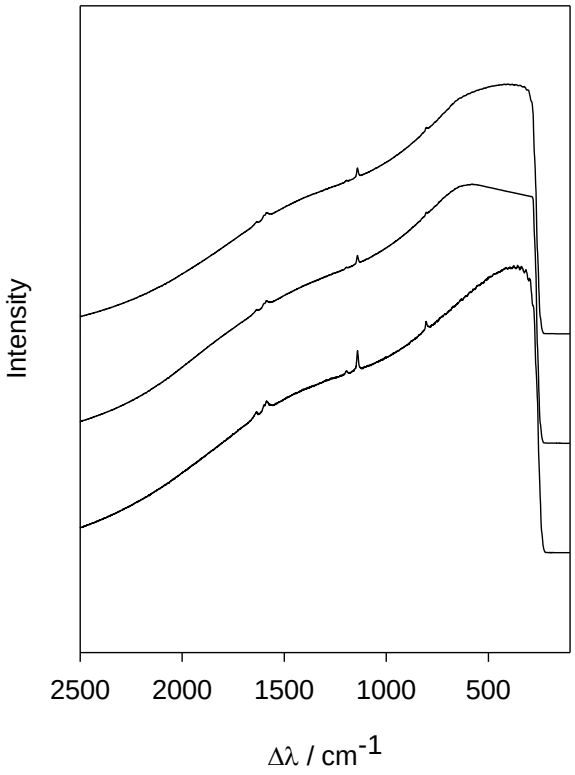

Figure 6.10: Raman spectra for various positions on PEEK surface aged by corona discharge.

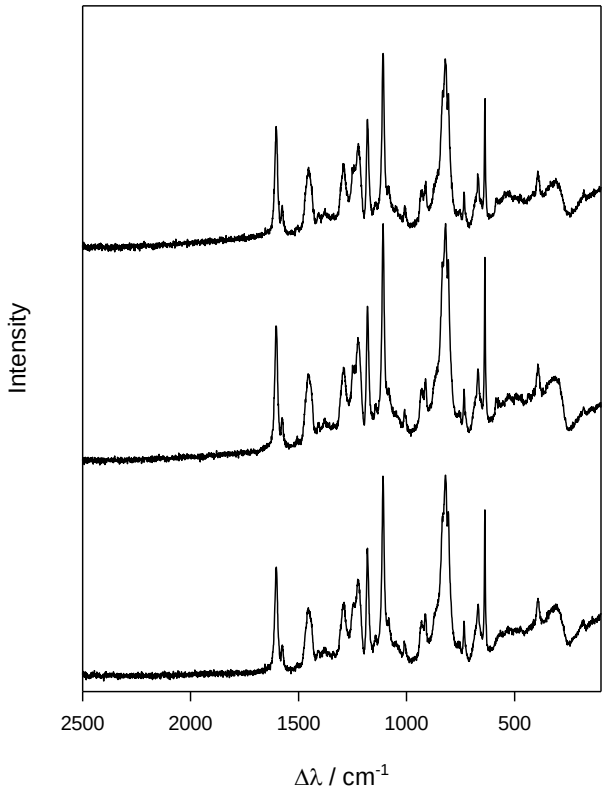

Figure 6.11: Raman spectra for various positions on epoxy resin surface aged by corona discharge

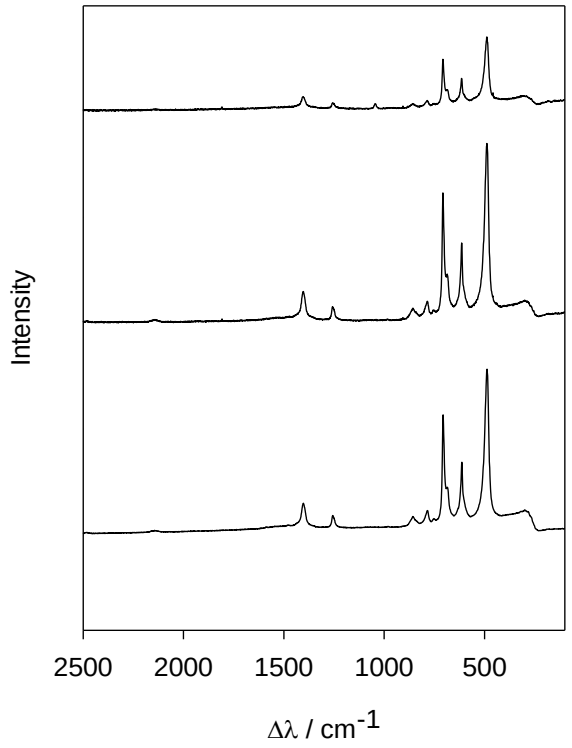

Figure 6.12: Raman spectra for various positions on PDMS(E) surface aged by corona discharge

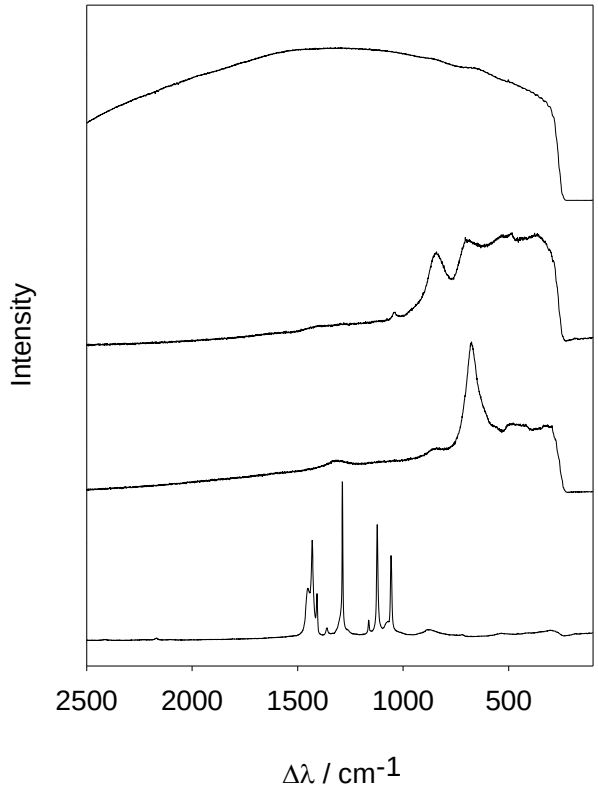

Figure 6.13: Raman spectra of corona aged LDPE

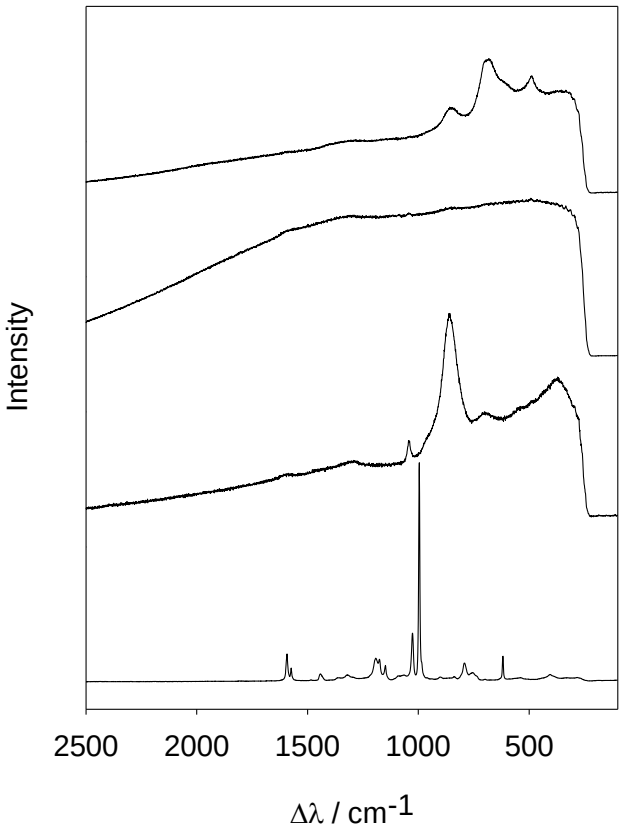

Figure 6.14: Raman spectra of corona aged PS

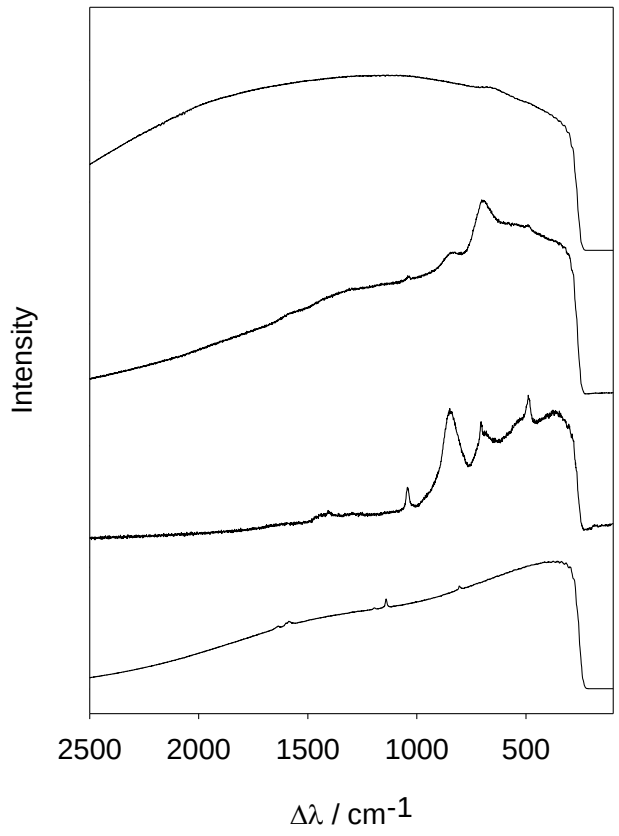

Figure 6.15: Raman spectra of corona aged PEEK

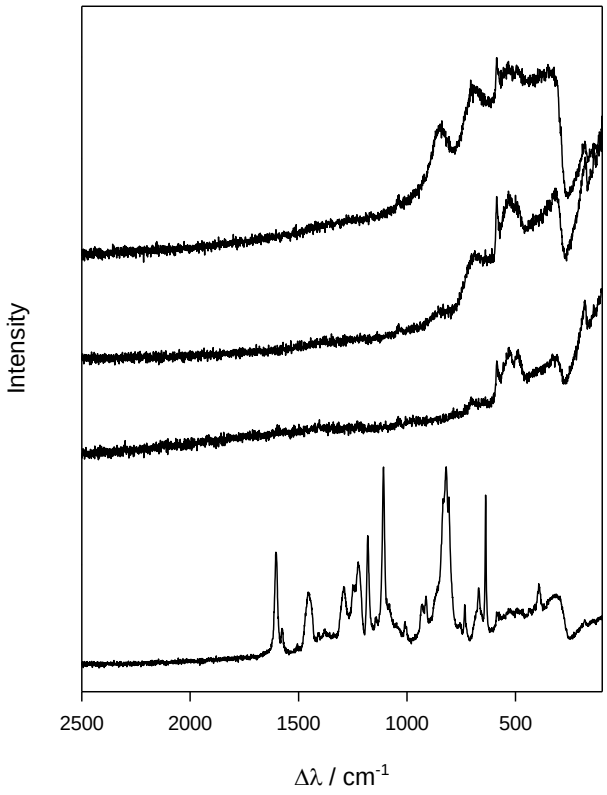

Figure 6.16: Raman spectra of corona aged epoxy resin

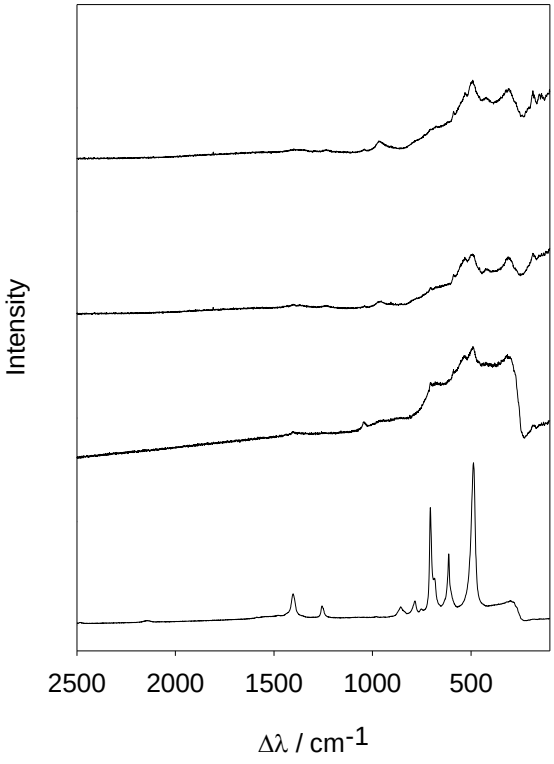

Figure 6.17: Raman spectra of corona aged PDMS(E)

epoxy resin or PDMS(E) are not present, suggesting that major chemical changes have indeed taken place during the ageing process.

Figures 6.13 to 6.16 all show similar behaviour and there is evidence of peaks at approximately 697 and 848 cm^{-1} on all electrodes. In some of the spectra for PEEK and PS there is also evidence of the D and G bands of sp^2 hybridized carbon at 1320 and 1580 cm^{-1} respectively although these peaks are small in comparison to the surrounding fluorescence. These peaks are similar to those predicted by Liu et al [31] and indicate that the presence of carbon on the needle which previous studies have linked to chain scission in polymers [25, 32] and electrical ageing processes such as PD activity in voids and electrical trees (as discussed in chapters 4 and 5).

Figure 6.17 shows the response from the needle used to age the PDMS(E) and from these data we can see several differences to Figures 6.13 to 6.16. Firstly, although there is a slight presence of fluorescence, it is on a much smaller scale to those of LDPE, PS and PEEK. There is also no evidence of the D and G bands of carbon. The peaks that are present in the Si traces appear at 318, 508, 687, 968, 1262 and 1412 cm^{-1}, and arise from a combination of the bonds in the original matrix (as identified in chapter 2) and oxygenated by-products (as identified in chapter 4). The peaks relating to the original polymer matrix appear broader than in a spectrum of an unaged sample, which is an indication of disorder within the molecules.

From these spectra, we can conclude that when aged via corona discharge, the polymers LDPE, PS and PEEK, all exhibit similar behaviour and deposits which show large amounts of fluorescence, traces of carbon and other polymeric materials. When you dramatically change the material, however, and use a polymer with a siloxane backbone rather than a carbon one, the fluorescence is reduced and the spectral peaks largely resemble those of the original matrix. The samples all exhibit evidence of the same oxygenated by-products identified in previous chapters. It is evident that in order to accurately reproduce the chemistry of treeing in bulk an oxygen free environment is needed.

6.3.3.2 Nitrogen

Figures 6.18 to 6.22 show the traces from the HV electrodes of the samples which were aged in an atmosphere of 100% nitrogen. As before, the lower trace is the typical Raman response of the original matrix. From these spectra we can immediately see some clear differences to the figures from the samples aged in air, especially with the spectra from PE and PDMS(E) as seen in figures 6.18 and 6.22. Firstly the fluorescence in these traces is increased and there are no visible peaks related to the original polymer. There are in figure 6.18, however, strong Raman bands corresponding to the

D and G bands of carbon, hence indicating the presence of PAHs. In the traces from PDMS(E) there are no traces of carbon, but there does appear to be a similar pattern in all of the spectra and again there is a large amount of fluorescence. It is clear that ageing the samples in nitrogen affects the composition of the deposit but the processes involved and its relation to electrical treeing remains unclear.

Published results on the Raman analysis of electrical trees in LDPE have suggested that, in conductive electrical trees, PAHs are present [25, 32]. As well as this, the same publications concluded that fluorescence is common in aged/impure samples and as a result of this; electrical trees are highly fluorescent structures. The chemistry of electrical treeing is unclear, but it is generally thought to involve chain scission reactions which result in the formation of volatile by-products [32].

With the results gained from the samples aged in air, there is evidence of similar behaviour between corona ageing in air and electrical treeing. There is, within the spectra, the presence of fluorescence and carbon even though the proportions of these factors vary. It is logical to assume that due to the similarities in spectra for PE, PS, PEEK and epoxy, polymers of a similar base structure respond to this ageing protocol in similar ways (although some of the by-products may vary). When the electrode deposits for PS, PEEK and epoxy resin that had been aged in nitrogen were analysed however, the resulting spectra do not show the same features to those of PE and PDMS(E). With these spectra (as seen in figures 6.19 to 6.21) there appears to be little difference to the spectra obtained from the samples aged in air and they contain similar features to the spectra obtained in the electrically aged voids in chapter 4. As before, there is a small amount of fluorescence, no evidence of the peaks relating to the original polymer matrix, and a range of peaks at the lower wave numbers previously thought to be associated with oxidation. There is some evidence of the presence of the D and G bands of carbon in the deposit from PS, but this is by no means conclusive.

When these samples are aged in nitrogen, the results from PE and PDMS(E) are more decisive and clearly show the same compounds found within electrical trees. Data collected from PDMS(E), although rather different to those obtained from the carbon based polymers, produces similar results to those obtained from electrical treeing of this system. This leads us to believe that the process of surface ageing is affected by the surrounding atmosphere and is best performed in an inert gas so that the decomposition products do not react with the surrounding air. It is possible that this is the reason why spectra from the samples aged in nitrogen much more closely

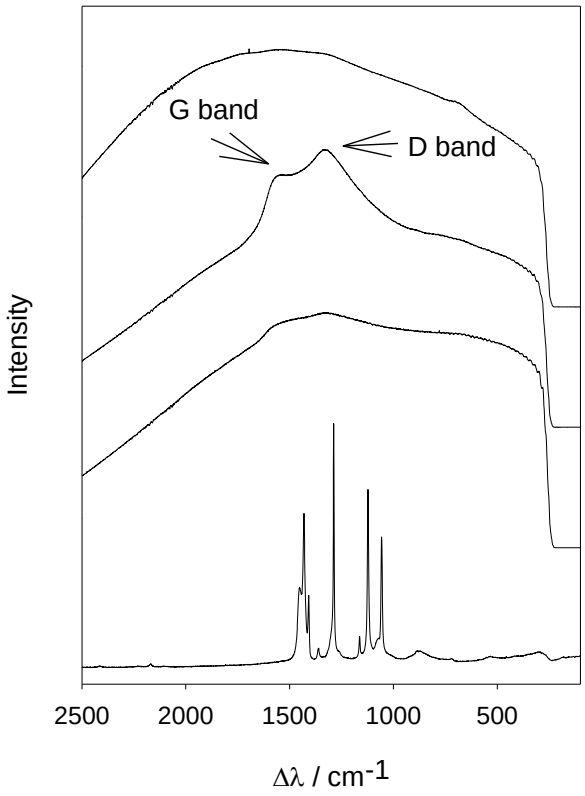

Figure 6.18: Raman spectra of corona aged LDPE in nitrogen

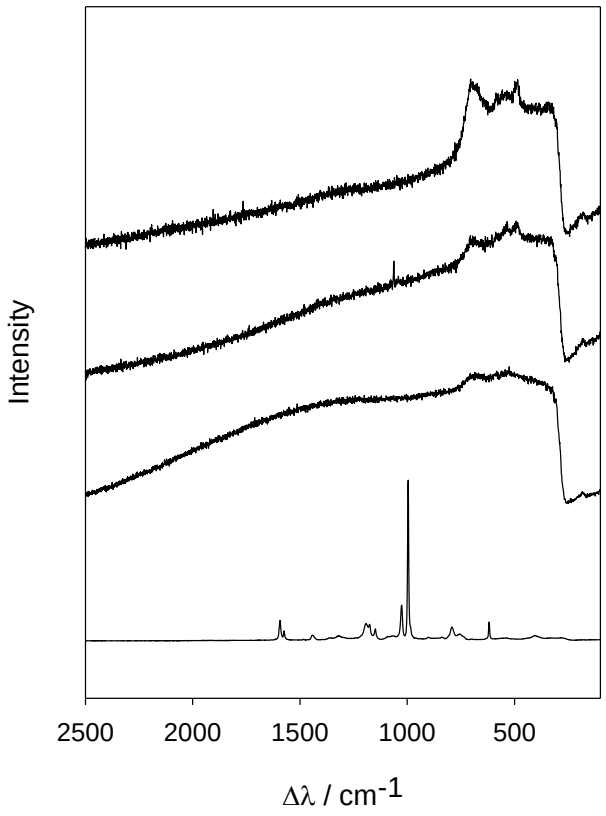

Figure 6.19: Raman spectra for aged PS in nitrogen

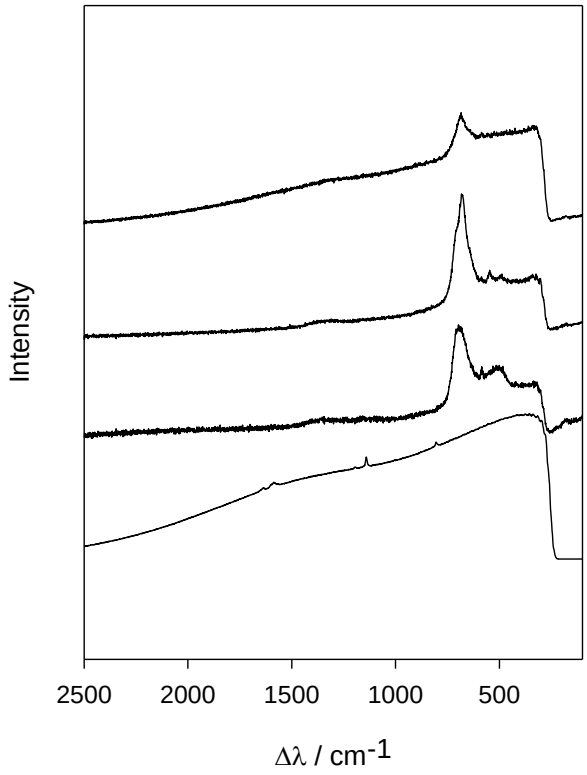

Figure 6.20: Raman spectra for aged PEEK in nitrogen

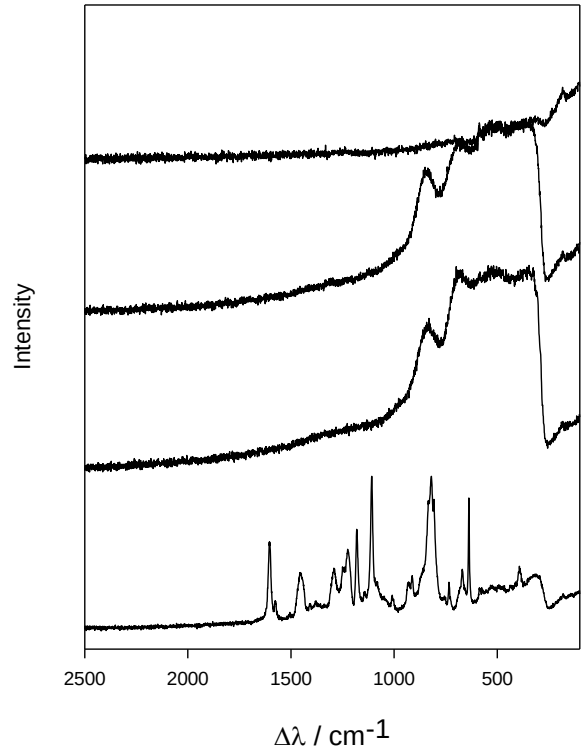

Figure 6.21: Raman spectra for aged epoxy resin in nitrogen

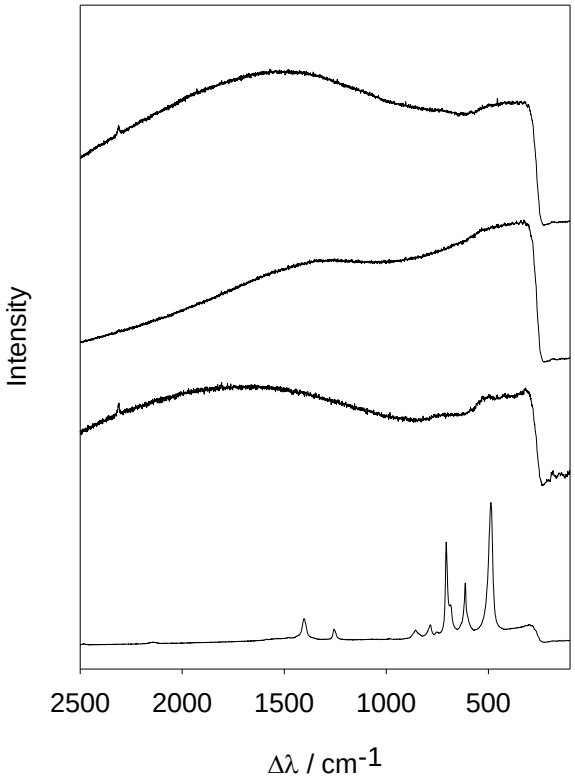

Figure 6.22: Raman spectra of corona aged PDMS(E) in nitrogen

resemble those obtained from electrical trees, where oxygen is likely to be limited. The spectra formed from the more complex carbon based polymers, however, cast doubt upon these conclusions due to containing peaks thought to be related to oxygenated by-products. It is possible that despite purging the system of air and replacing it with an atmosphere rich in nitrogen, the test cell is not completely air tight and some oxygen remained in the atmosphere resulting in some oxidisation occurring during ageing. An alternative theory is that the deposits on the needles react with oxygen once removed from the nitrogen filled test cell and exposed to air or that prior to ageing the surfaces of the polymers contain an amount of oxygen due to absorption from the surrounding air.

6.3.3.3 Argon

In order to provide a comparison with nitrogen, samples of the 5 selected polymers were also aged in argon, which was chosen for its inert properties and low cost. It is worth noting however, that the electrical breakdown strength of argon is much lower than that of air or nitrogen thus making it a poor insulator in comparison. For this reason much lower voltages were used to corona age the samples in argon such that a corona was formed but no arcs occured between the two electrodes. As with the samples aged in air and nitrogen, the voltage required to form a stable corona is dependent on factors such as sample size and composition, for this reason, the

applied voltage varied for each sample. In order to create a stable corona for each sample the following voltages were used: PE – 8.5 kV, PS – 11 kV, PEEK – 8.5 kV, Epoxy resin – 8.5 kV and PDMS(E) – 5 kV. Due to the lower voltages the energy of the system is reduced and hence less debris is formed on the needle electrodes. In all cases, however, using the same ageing conditions of previous chapters (6 hours ageing with a 1 mm separation between the surface of the sample and the tip of the high voltage electrode) sufficient deposits for the application of CRMS were formed.

Figures 6.23 to 6.27 show the Raman spectra from the deposits that had formed on the electrodes. In these figures the features associated previously with electrical treeing (namely fluorescence and the D and G bands of carbon) can be clearly seen. The intensity of the D and G bands of sp^2 carbon indicates the quantity of carbon and PAHs within the system. It is interesting to note that in the polymers where carbon atoms are abundant in the side groups of the polymer, such as in PDMS and the benzene rings of PS and PEEK, the intensity of the D and G bands is increased. For polymers where all of the carbon atoms within the polymer are constrained to the backbone, such as in PE, the intensity of the same peaks is reduced and only faint traces of carbon and PAHs can be seen. This indicates that the energy of the free electrons and ions moving in the corona is sufficient to break the bonds of the side groups of the polymers, but the probability of the same electrons and ions having a sufficient energy to break the bonds of the polymer backbone are reduced.

As well as evidence of PAHs the spectra in figures 6.23 to 6.27 show evidence of the peaks thought to be related to oxidisation at the lower energy levels but they no longer dominate the spectra as before. This supports the hypothesis that during the ageing process, the polymer that the polymer fragments that are eroded from the polymer surface are volatile and reactive. Therefore the by-products formed within various methods of electrical ageing are highly dependent on the surrounding atmosphere and if the chemistry of treeing is to be reproduced, then an inert atmosphere is needed in order to reproduce the oxygen limited environment of the polymers within which electrical trees form. Despite these observations, the results obtained in argon do not fit entirely with established theory and show evidence of oxygenated by-products previously identified in electrically aged voids. This could possibly be due to experimental error resulting in the desired atmosphere not in in fact being established for these samples, as wit nitrogen. For this reason more testing is required to confirm the above theory and to ascertain the reasons why not all the spectra conform to it.

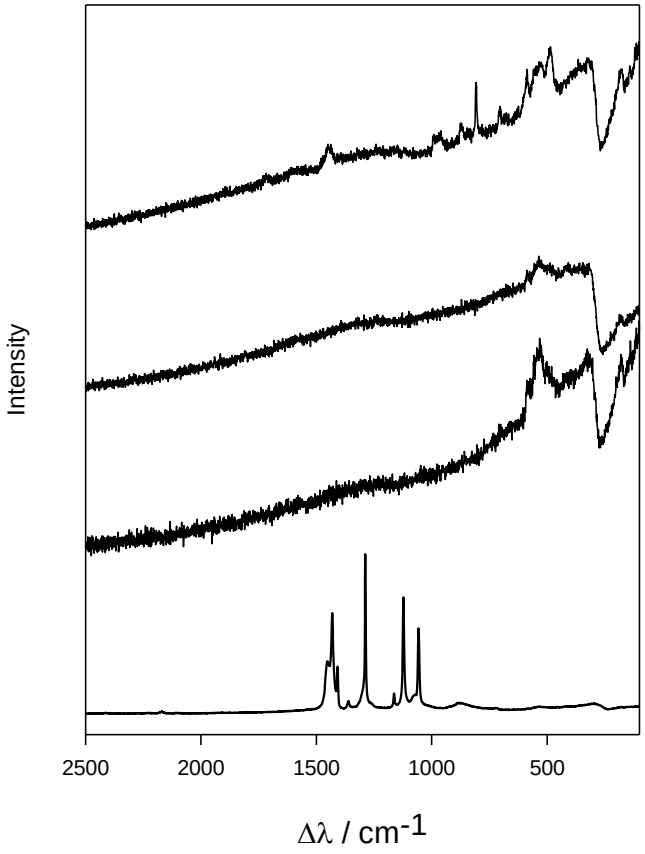

Figure 6.23: Raman spectra for LDPE aged in argon

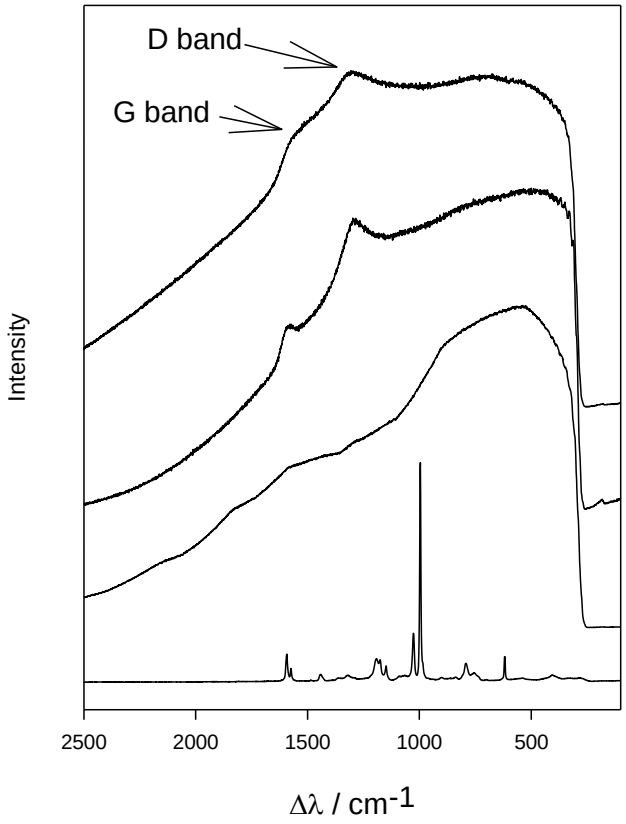

Figure 6.24: Raman spectra of PS aged in argon

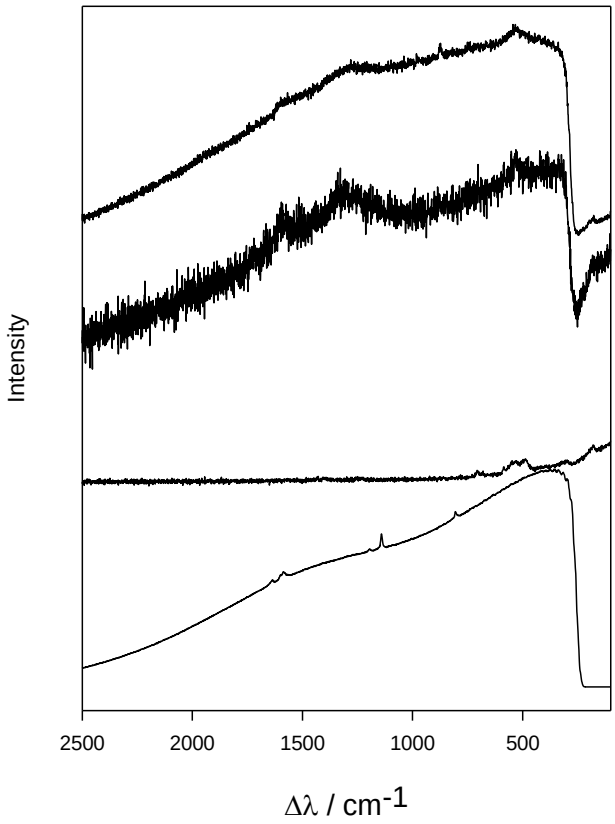

Figure 6.25: Raman spectra of PEEK aged in argon

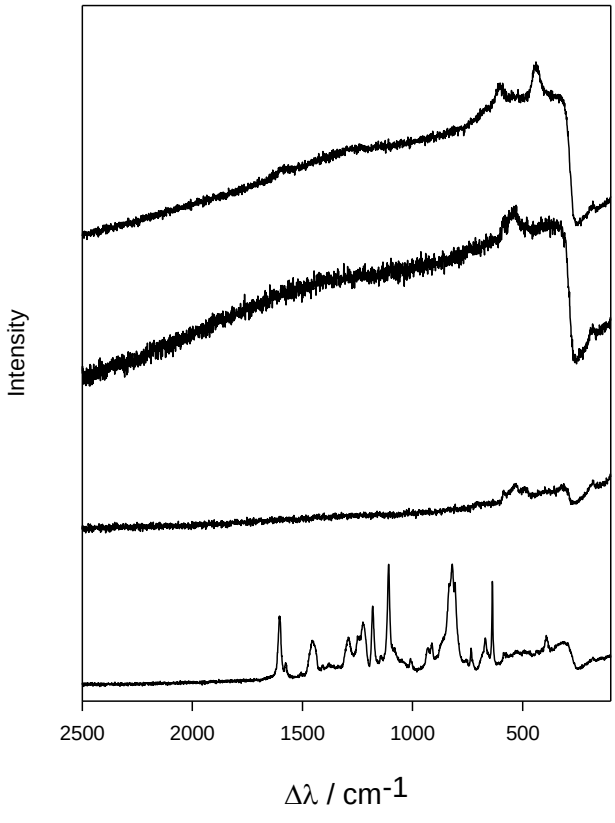

Figure 6.26: Raman spectra for Epoxy resin aged in argon

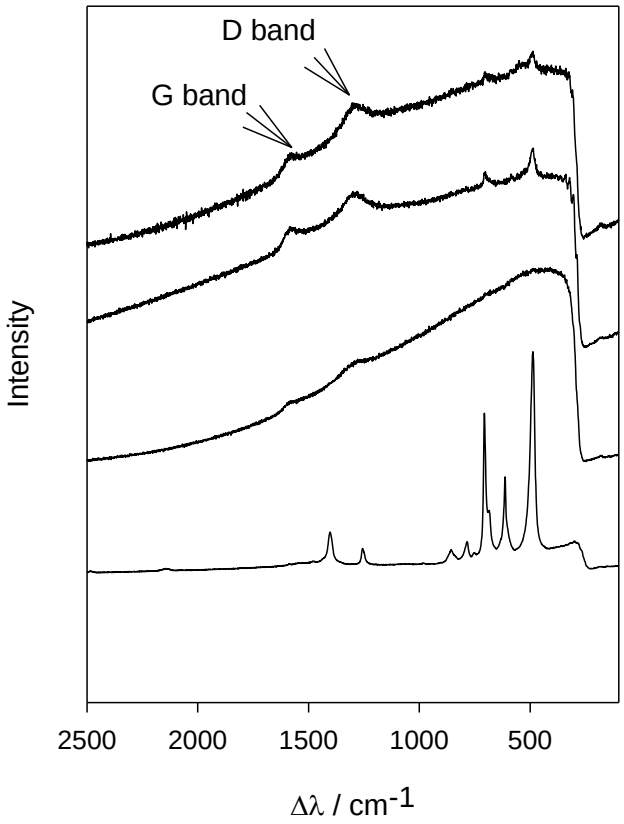

Figure 6.27: Raman spectra for PDMS(E) aged in argon

6.3.4 Electrode deposits of fluids

By repeating the corona discharge experiment on a liquid system containing a similar chemistry to those of the polymers analysed it is hoped that a deeper understanding of the mechanisms involved in electrical ageing can be obtained. To do this the liquid systems of hexane, DD and DDB were chosen due to their comparable chemistry to the polymers in the previous section. Hexane is comparable to LDPE, dodecane was chosen in order to provide a more complex chemical system to hexane in the same way PS, PEEK and epoxy resin were chosen due to their higher chemical complexity to LDPE. Finally, DDB was chosen in order to provide another complex chemical system containing large amounts of carbon and for its use in paper based cable insulation. In order to simplify the chemistry involved, all the liquid systems were aged in a nitrogen atmosphere, which also provided an atmosphere without oxygen, which enables us to safely age the highly volatile system of hexane. The liquid systems were all aged for 6 hours with the electrode approximately 1 mm from the surface of the liquid although this is difficult to be exact about due to the meniscus of the fluid and evaporation.

Figures 6.28 to 6.30 show the spectra obtained from the deposits formed upon the high voltage electrodes after ageing. From some of the traces in these spectra we can see the same features as those previously seen, namely, little evidence of the original

chemical matrix of the fluid, an increase in fluorescence, evidence of the presence of the D and G bands of carbon and in all cases the peaks at around 500 cm^{-1} indicated in the previous sections. In the case of hexane, strong carbon peaks can be seen, however, in the systems that are more complex and contain more carbon there is only an indication of their presence, if any at all. As well as this, it is worth noting that although deposits were formed on the needles, a larger quantity of deposit was formed on the electrodes when ageing the polymers. Due to the self healing nature of the liquids this is unsurprising. The small deposits leads to the conclusion that although ageing the liquid systems can reproduce the chemistry of the electrically aged polymers and hence electrical treeing, the small quantity of deposits and therefore ambiguous data means that it is not a viable method for reproducing in bulk the internal chemistry of electrical trees.

6.3.5 Spark ageing

The corona ageing of the liquid systems showed that it is possible to reproduce the desired chemistry by the ageing of these systems, but the energies involved in corona ageing is not sufficient to reproduce them in bulk. A novel method enabling us to control the energy involved in the ageing processes whilst ageing the liquid systems in an oxygen free environment is therefore needed. The proposed method and solution to this problem is to immerse a spark generator (as can be seen in the schematic shown in figure 6.5) into the liquid system of choice. With the exception of hexane (with which, due to its highly volatile nature, it is not possible to safely perform this experiment), all the liquid systems of the previous section were analysed. Samples were aged at a rate of 1 discharge per second for 16 hours. By varying the resistor and capacitor within the system the energy of the sparks generated can be altered. The energy of each spark E_s is given by the following equation:

$$E_s = ½ CV^2$$

Whereas the discharge duration T_d is approximately given by:

$$T_d = 5 RC$$

Therefore, with a voltage of 15 kV, a 4 nf capacitor and a 1.25 MΩ resistor, the resulting spark would have energy 450 mJ and duration 20 ms. These ageing times and energies are considerably larger when compared to PD in voids and gasses (usually in the order of 10^{-7}not 10^{-3}) and it is possible that the higher energies and longer ageing times could affect the chemistry formed. This experiment is still in its infancy however and is only meant to test the basic premise that the by-products of ageing can

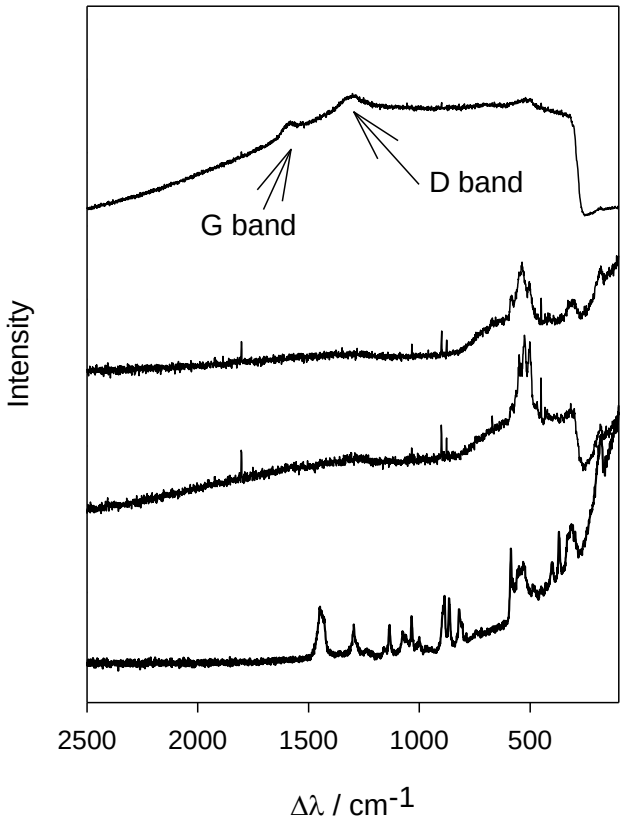

Figure 6.28: Raman spectra of hexane aged in nitrogen

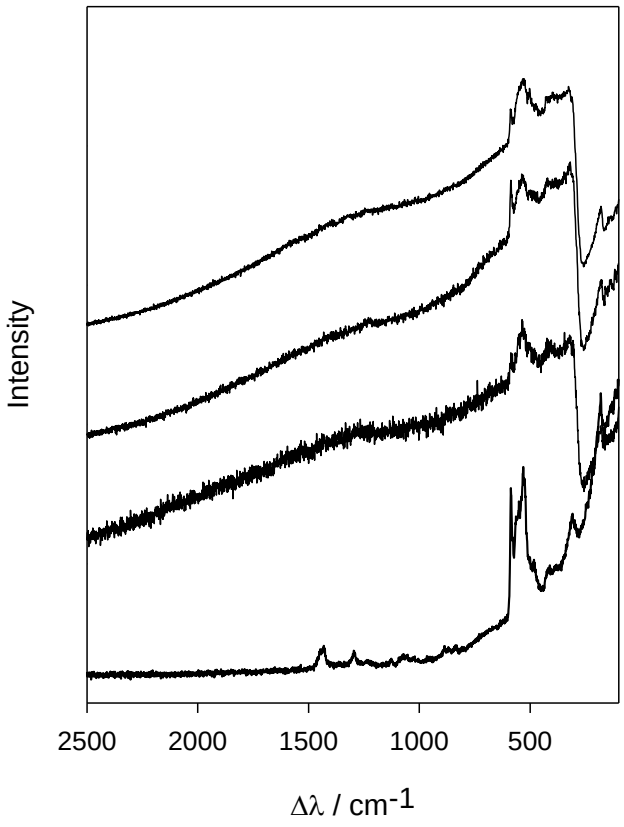

Figure 6.29: Raman spectra of Dodecane aged in nitrogen

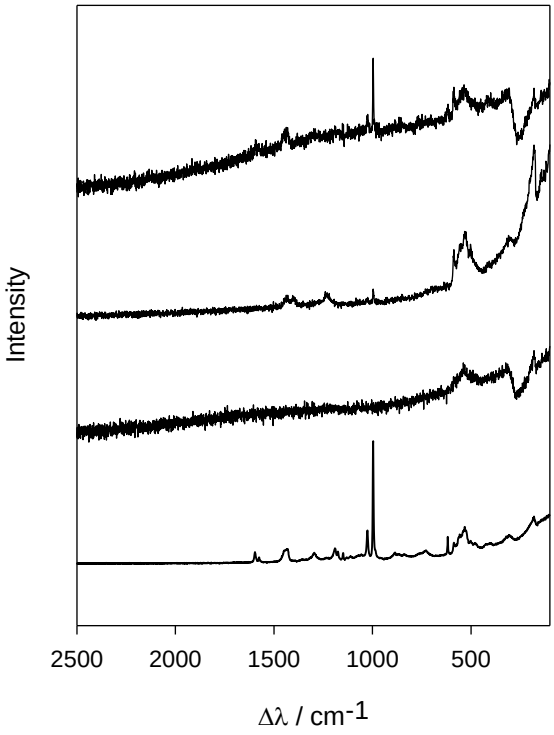

Figure 6.30: Raman spectra of DDB aged in nitrogen

be reproduced in bulk using this method. Future work could be to extend and alter this experiment so that it can simulate the energies and discharge energies of PD activity with a greater accuracy.

Following ageing the resulting debris was extracted and cleansed of any liquid residue. This provided a number of powders with mass in the order of magnitude of 1 μg, which could easily be analysed using CRMS. All spectra in this section are formed of the averages of a number of scans obtained from a number of points across the samples. As well as this the data was obtained using the x20 objective lens. This enables a larger focal volume and hence a more general overview of the chemistry of the samples.

Figure 6.31 shows the spectral data obtained from the resulting powders from PDMS(L) aged with a variety of different discharge energies and durations. From this figure we can clearly see the same spectral features as previously discussed. It can be concluded that this method of ageing PDMS(L) provides a large amount of debris that is comparable to the deposits formed on the needle via corona ageing PDMS(E) in an oxygen free atmosphere, and the internal surfaces of the electrical breakdown channel caused by treeing in PDMS(E). Figure 6.31 also shows that increasing the energy of the system does not greatly affect the spectral peaks or their intensity and so does not affect the chemistry of the resulting debris. It is possible that the method of using a

solvent to retrieve the debris from the liquid can affect the results, however no evidence of this can be seen possibly due to the large amount of fluorescence in the spectra.

When the above method was applied to the other liquid systems it was found that smaller discharge energies are not sufficient to produce enough analysable debris. As a result dodecane and DDB were aged using a capacitor value of 4 nf and a resistor of 1.25 MΩ, thus providing a discharge energy of 450 mJ per spark of duration 20 ms which is the maximum the equipment could provide. This tells us that although increasing discharge energy does not affect the chemistry involved, it does affect the quantity of debris formed and that different liquid systems require a different minimal discharge energy before debris can be formed. The resulting spectra from these liquid systems can be seen in figure 6.32, where they are compared to PDMS(L) that has been aged with the same energy. Once again it can clearly be seen that with all the liquid systems, when they are aged with a sufficient discharge energy, they provide debris of a comparable chemical structure to the carbon based polymers that have been aged via corona discharge and hence PD in voids and electrical trees. It can be concluded that

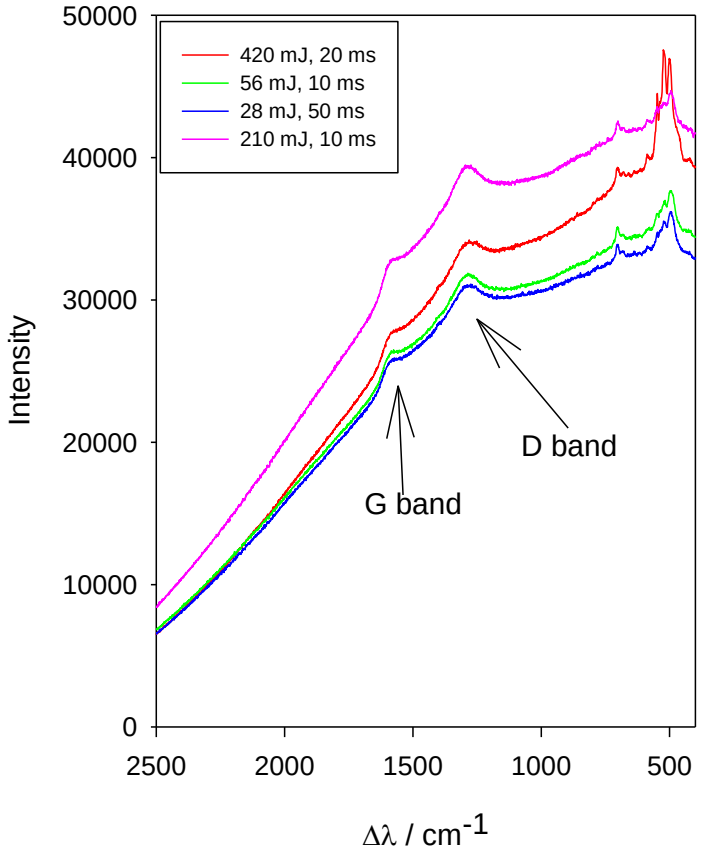

Figure 6.31: Raman spectra of debris from PDMS(L) aged at a range of energies

despite the fact that this method is still in its infancy, and much work needs to be done in order to perfect it and apply it to other systems to confirm the results presented here, spark ageing is an effective way of reproducing the chemistry involved in corona discharge, PD in voids and electrical treeing in polymeric insulators.

6.3.6 FTIR Analysis

Due to the non transparent nature of the samples and the small quantity of the deposits formed upon the needle electrodes that had been aged via corona discharge, an FTIR analysis of these samples was not performed. Figure 6.33 however shows the average FTIR spectra obtained from a selection of the debris obtained via spark ageing. All of the spectra in figure 6.33 have been normalised such that the peaks at 2200 cm^{-1} are comparable. From these spectra it can be seen that, although the relative intensities of the spectral peaks may differ slightly, the positions of the peaks are identical regardless of the liquid system used. Also, in this figure, the peaks located between 1950 cm^{-1} and 2780 cm^{-1} can be seen as in chapter 5. As well as this, a series of peaks can be seen in all the spectra which are similar to those identified in chapter 4 which were reported to be associated with carbonyl groups [133]. This reinforces the conclusion that by applying a spark generator to a liquid system of a chemical composition similar to polymeric insulators, debris is formed which reproduces, in bulk, the internal chemistry of electrical ageing in polymeric insulators.

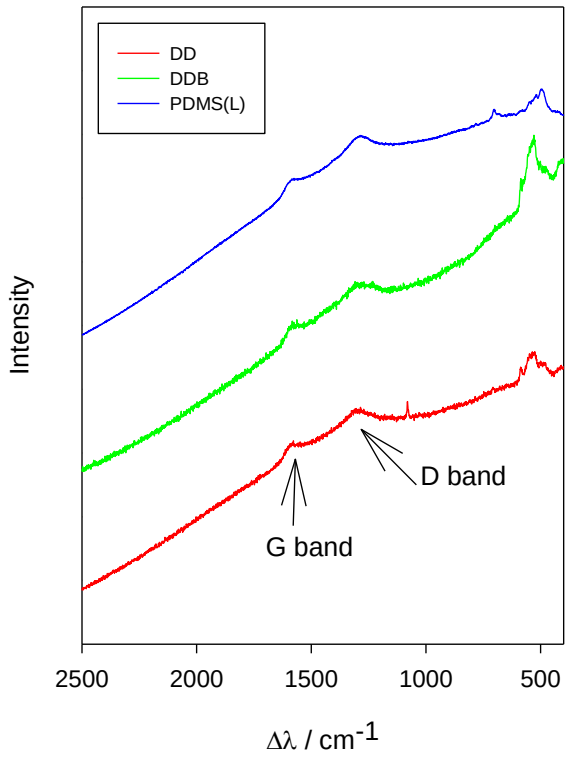

Figure 6.32: Raman spectra of Dodecane, DDB and PDMS(L) aged by spark ageing

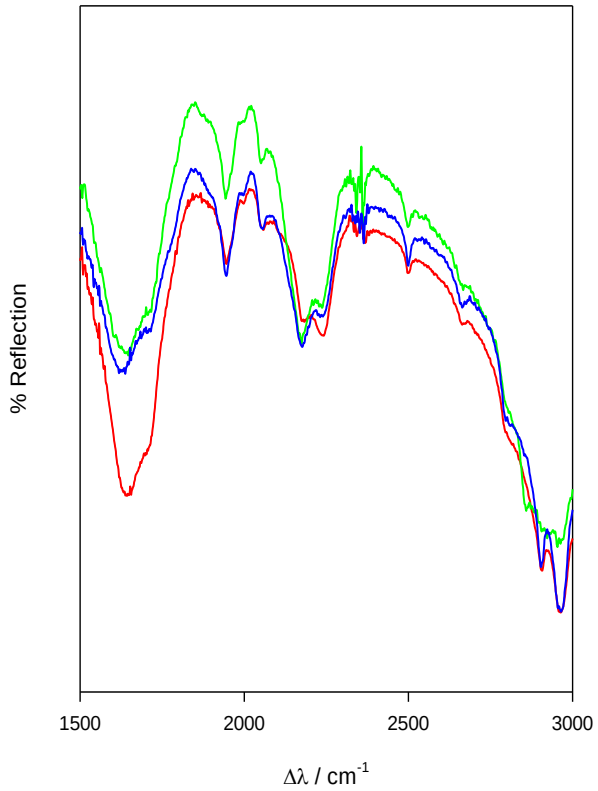

Figure 6.33: FTIR spectra of debris formed from spark ageing in PDMS(L), DD and DDB with a spark energy of 450 mJ

6.3.7 SEM Imaging

As with the FTIR analysis, SEM images were not obtained from the deposits formed on the needle electrodes subjected to corona discharge. This is because the deposits formed were incredibly fragile whilst still attached to the needle and so would have become damaged during the sample preparation needed for SEM imaging. It was also not possible to age for long periods of time to collect larger amounts of debris such that it could be collected as very large ageing times would be needed to generate enough material for collection and analysis via SEM. Figures 6.34 and 6.35 show SEM images of the debris obtained from PDMS(L) that had been aged at a relatively high spark energy (450 mJ) and a relatively low spark energy (28 mJ). In these images nodular structures reminiscent of those identified to be carbon based in previous chapters can be seen. In both figures, the structures seen range in size from approximately 2 to 20 μm. The debris formed in both images appear to be identical in structure, thus indicating that the energy of the discharges within the liquid are sufficient to initiate chain scission of the polymer to form PAHs. An increase in energy appears to not affect the chemistry or morphology of the debris formed only the quantity of the debris formed. It is therefore logical to suggest that in order to

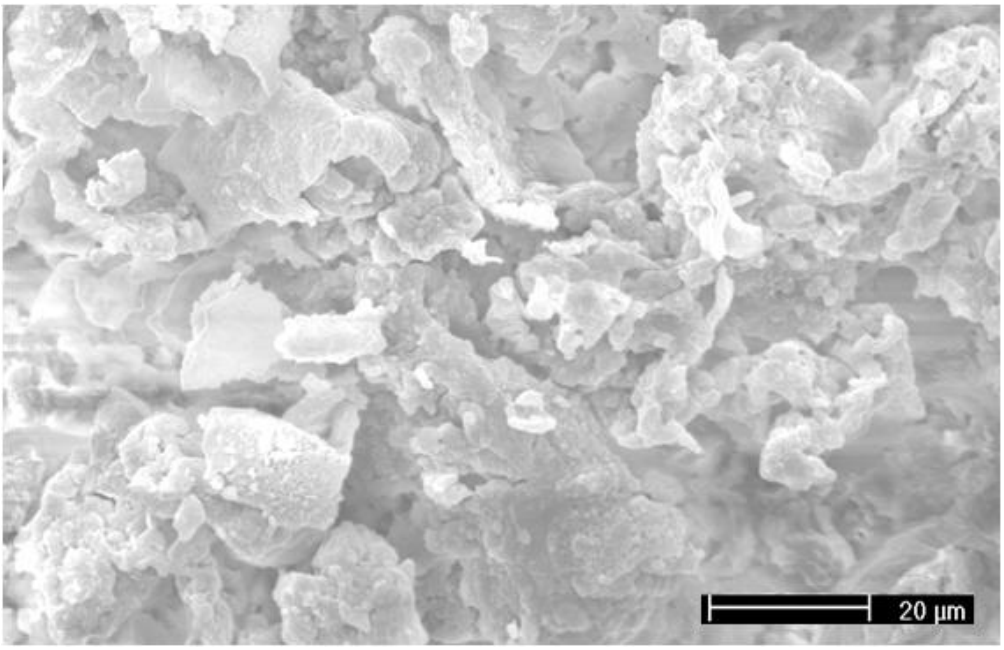

Figure 6.34: SEM image of PDMS debris obtained with a spark energy of 450 mJ

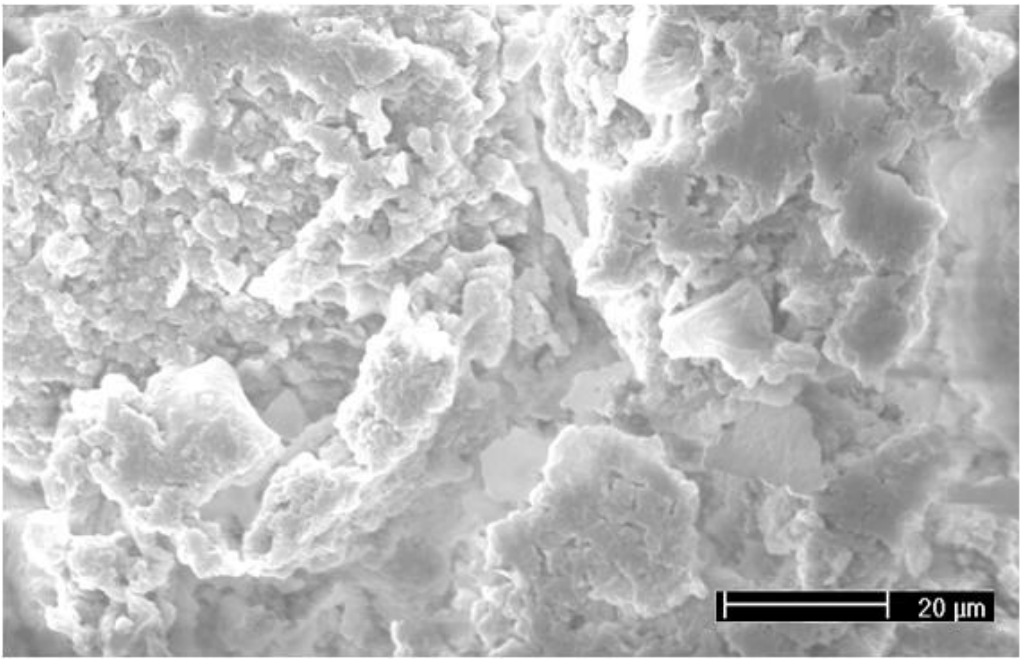

Figure 6.35: SEM image of PDMS debris obtained with a spark energy of 28 mJ

increase the reproduction of this debris, the capacitance of the system (and hence energy of the system) and the ageing time should also be increased.

Figure 6.36 shows a SEM image of debris obtained via spark ageing of DD such that a comparison between the debris formed in a liquid system with a carbon based backbone and the siloxane backbone of PDMS(L) can be made. In this figure several

similarities can be seen when compared to figures 3.34 and 3.35. The structure of the debris in figure 6.36 appears to be formed of nodular structures. The features are approximately 5 μm in size and as before are reminiscent of the carbonaceous structures identifies in chapters 4 and 5 and in the debris formed in the other liquid systems. The apparent plates of this material could be an indication of graphene sheets forming from the large quantity of carbon atoms within the liquid. It can be concluded, in conjunction with the Raman and FTIR data that this material has the same chemical composition as the debris formed within PDMS(L).

6.4 Conclusion

Plaque samples of LDPE, PS, PEEK, epoxy resin and PDMS(E) were subjected to a corona discharge in a variety of atmospheres and the subsequent deposits left on the high voltage electrode were analyzed using Raman microscopy. A similar analysis was then performed on deposits obtained from subjecting a number of liquid systems to corona discharge in an attempt to simplify the chemistry involved. Finally the same liquid systems were subjected to spark ageing in an attempt to a produce novel method to reproduce the chemistry of electrical ageing in bulk. Results were discussed in comparison to the results in previous chapters and previously published results on electrical ageing in voids and electrical trees.

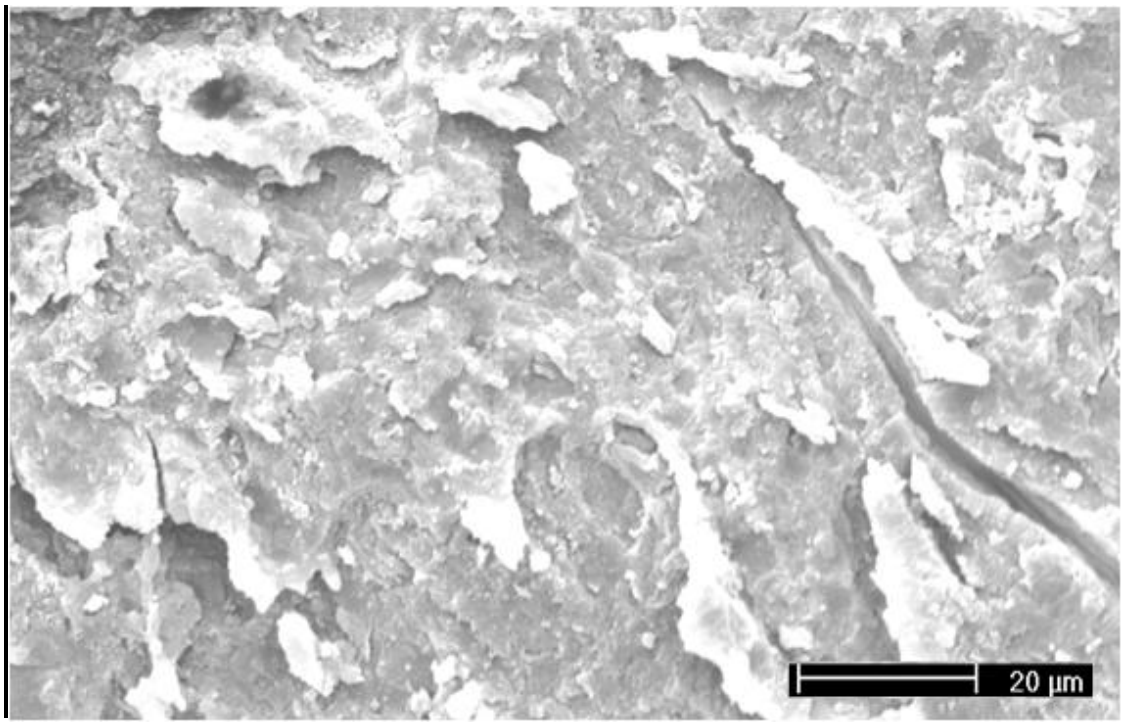

Figure 6.36: SEM image of DD debris obtained with a spark energy of 450 mJ

The work and results discussed in the previous section lead to the following conclusions:

- When the plaque samples were aged in air, it was found that all of the carbon based polymers exhibited similar results, and evidence of small amounts of fluorescence, PAHs and oxygenated by-products were found. This is similar to previous results from electrically aged voids and electrical trees and hence shows evidence of a link with the chemical processes that occur during electrical treeing. It was found that when the structure of the polymer was dramatically changed to PDMS(E), the deposits although apparently aged, have a similar chemical fingerprint to that of the original matrix. Analysis of the surfaces of the aged samples yielded no evidence of any chemical change in the polymer matrix.

- Following the initial experiments, samples of LDPE and PDMS(E) were corona aged in both nitrogen and argon filled atmospheres. Raman analysis of the resulting electrode deposits revealed a much closer resemblance to previous results on the Raman analysis of electrical trees and as well as large amounts of fluorescence. When aged in nitrogen the LDPE and PDMS samples showed strong evidence of the D and G bands and hence PAHs were found. Similar results were obtained when the samples were aged in an atmosphere rich in argon. It is clear that in order to recreate the by-products of electrical ageing in polymeric insulators an inert, oxygen free atmosphere is needed. The similarity in these results and previous published works suggest that there are common processes involved between corona surface ageing and electrical treeing especially when an inert atmosphere is used. It was not possible to create an environment completely devoid of oxygen, however, as peaks relating to oxidisation of the polymers can still be seen in some spectra.

- Liquid systems of similar chemistry to the plaque samples were also subjected to corona ageing in a nitrogen based atmosphere. Spectra of the deposits showed similar results to those from the plaques samples and evidence of fluorescence, PAHs and oxygenated by-products could be seen. The quantity of debris formed in corona ageing both the plaque and liquid systems however, was not sufficient for a more in depth analysis involving FTIR and SEM. It was realised that an alternative method for reproducing the chemical processes involved in electrical ageing in greater quantities is needed. Spark ageing was suggested as a way of achieving just that and as a result the same liquid systems were subjected to spark ageing using a capacitor discharge spark

generator. The debris formed following ageing was several mg in mass all exhibited similar Raman and FTIR spectra to previous results showed a clear link to the chemical by-products produced in electrically aged voids and electrical trees. SEM images also confirmed that the debris formed appeared to be of a similar morphology to the samples analysed in previous chapter.

The exact chemistry of electrical treeing still remains unclear but these observations suggest that it is possible to reproduce, ex situ, the processes involved and the by-products produced by using corona discharge. Where bulk quantities of the by-products are required spark ageing liquid systems of a similar chemical composition to the desired polymer is sufficient. It appears that performing these experiments within an inert and oxygen free atmosphere improves the quality of the products obtained, with them bearing a closer resemblance to those found in electrical trees. With further investigation into corona ageing in a controlled atmosphere and spark ageing of liquids, however, these processes will become clearer. Currently these results are consistent with observations made in previous chapters and established theory.

7 : Conclusions

This chapter details and summarises the conclusions formed in this project and suggests possible avenues of research form which this study can be expanded.

7.1 Conclusions

7.1.1 Optical Depth Profiling

Previous work based on CRMS have suggested and assumed that even when focused below the sample surface, the focal point is well defined and is accurate to 2 μm in the horizontal plane and 1 μm in the vertical optical plane. The work in this study has shown that this is not the case and in fact Raman photons originate from a large extended illuminated volume that extends both above and below the focal plane. This illuminated volume can be accurately modelled using revised version of a simple photon scattering approach proposed by Vaughan and Macdonald.

The depth profiling of polymers using CRMS enables the chemical analysis of areas that lie below the surface of the polymer but, due to refraction effects and surface scattering, results are greatly improved if analysis is performed using an oil immersion lens and a suitable immersion oil who's refractive index is similar to the sample. An exact match of refractive index between the sample and oil is not essential but when the sample surface is not optically flat, a close match greatly improves results. Care is needed in the use of immersion oils so that spectral peaks do not overlap and hence complicate the analysis but a simple numerical correction can be applied if this is the case.

Although CRMS has its limitations, it remains a useful tool when analysing the chemical changes which occur due to electrical ageing in sub surface features in polymeric materials. Despite this, CRMS is best used in order to gain an initial understanding and if a more accurate analysis is to be performed then exposing the area in question to the surface and applying RMS instead would prove to be prudent.

7.1.2 Raman Analysis of Electrical Ageing

In this study, it proved possible to identify the chemical traces previously identified with electrical treeing, such as PAHs and fluorescence, on the walls of subsurface voids aged by PD activity in PE. These chemical traces were apparent in samples containing voids regardless of if they have been formed chemically or by layering sheets of PE resulting in inclusion of known dimensions. As well as this, throughout the voids a series of peaks was observed at lower wavenumbers. These peaks appear to be related

to oxidation processes within the void. This suggests that the voids analysed contained an atmosphere containing oxygen. As well as this, with the exception of the intensity of the spectral features and fluorescence increasing, Raman spectra showed little or no relation between the chemical by-products formed, and ageing time. This tells us that there is no evidence that an increase in ageing time affects the chemistry and processes that occur within the voids and that an increase in aging time merely effects the quantity of debris formed.

It was also concluded that although oil immersion techniques enabled depth profiles of the voids to be obtained an imaged a far more effective way of analysing the void surfaces was to divide the sample via microtomy and expose the internal surfaces of the void for analysis.

Previous work in the analysis of electrical trees grown in PE showed that the Raman spectra aged samples contain various combinations of three key features, polymer matrix, fluorescence and the D and G bands of sp^2 hybridized carbon. In this study, samples containing electrical trees grown in PDMS(E) and epoxy resin were analysed using RMS. It was found that in samples where breakdown had occurred, the same 3 features can be seen. In samples where the polymer was merely aged and not broken down then spectra all showed evidence of fluorescence and the original polymer matrix but little or no evidence of carbon could be seen. As well as this, in all these samples there are a number of spectral features not present in the original polymer between 300 and 600 cm^{-1}. These peaks are thought to be related to oxidisation within the trees and not related to the bulk of the polymer. With the electrical trees grown in PDMS, little or no chemical changes were detected within the tree channels. This indicates that the energies involved are insufficient to break chemical bonds in the side groups of the silicone based polymer. In contrast to this, the tree channels of a tree grown in epoxy resin yielded spectra with strong D and G bands indicating chain scission of the polymer backbone and the formation of large quantities of PAHs.

The growth characteristics of electrical trees in PDMS(E) were also studied but it was discovered that due to the short ageing times, the bushed trees grown in PE by Vaughan *et al* were not possible with the setup used in this study. It is expected that a similar chemistry in bushed trees to branched trees grown in PDMS(E) will be seen using CRMS however it is expected that a higher concentration of PAH's will be found at the tips of the tree channels rather than the walls.

7.1.3 Chemical Reproduction

Analysis of a variety of polymers aged by corona discharge revealed that it is possible ex situ to reproduce, in bulk, the processes involved by applying a corona discharge to a plaque specimen of a polymer (or a comparable liquid system) and collecting the deposits formed on a needle electrode. A range of polymers was subjected to a corona discharge in a controlled atmosphere (including air, nitrogen, and argon). As well as this, a full investigation into the effects of electrode separation, needle tip size, length of ageing time, and applied voltage was achieved and the optimum parameters determined. When the samples were aged in air it was found that all of the carbon based polymers exhibited similar results to those obtained from voids and electrical trees. When the polymer is changed to silicone rubber, however, the spectral features of the deposits such as fluorescence and carbon are dramatically reduced. It appears that by performing these experiments within an inert gas the quality of the products obtained is improved and they bear an even closer resemblance to those found in electrical trees.

The formation of deposits via corona ageing of solid a liquid polymer, although does replicate the chemical by-products of PD activity in voids and electrical treeing, the quantity of debris formed is insufficient to perform many spectroscopic and microscopic analyses and in many cases the quantities produced were less than those formed in electrical treeing. As such, an alternative method of applying a spark generator to liquid systems resembling the desires polymeric insulator was proposed. This method proved to be successful in producing large quantities of 'debris' and Raman analysis of the resulting deposits showed that they were of the same chemical composition to the by-products previously identified in voids aged by PD activity and electrical trees. Not only was the chemical makeup reproduced and the quantity of the deposit increased using this method, due to an environment free of oxygen, the by-products related to oxidisation were eliminated.

7.1.4 Other Spectroscopic Techniques

In order to further the understanding of the chemical changes occurring in electrical ageing examples of all the samples aged by partial discharge, electrical treeing, corona discharge and spark ageing were analysed using FTIR and SEM. This allowed a comparison between FTIR and RMS to be made and hence the effectiveness of RMS in the analysis of electrical ageing in polymeric insulators can be evaluated. Results reinforced the Raman data and the spectral peaks related to carbonyl were seen in many of the samples. SEM analysis revealed that the deposits formed in all the ageing processes discussed, included a nodular structure previously identified to be carbonaceous in nature.

7.2 Future work

The model and work on using CRMS to depth profile transparent polymers can be extended and improved. Further revisions to the model can be made so that a more accurate fit to the data can be obtained and the contribution to the depth profile when focused above the sample more accurately calculated.
The work in this study on electrical ageing can be further developed to study a wider range of materials. The application of CRMS of the aged voids can be extended to include aged voids in a range of materials (such as epoxy resin), a range of sizes (from a few microns to a few mm) and of different quantities (such as foams) in order to see how these factors affect PD activity and hence chemical by-products. It would also prove to be useful to compare the by-products created with the PD signatures of the aged voids thus reinforcing the link between PD activity and ageing.

Electrical treeing experiments can also be extended to include a much wider range of polymeric materials and tree types. A full investigation between the growth characteristics of electrical trees in different polymers and their relation to the chemical by-products formed would also prove to be prudent. By extending research into this area it is possible that the electrical processes involved in electrical treeing and can be identified and understood. As well as this, in combination to the work in micro voids suggested earlier, the link between PD activity in voids and the consequential growth of electrical trees can be identified and understood.

The corona ageing test cell can also be improved such that it is air tight and a completely oxygen free experiment can be conducted. Experiments can then be repeated with longer ageing times to maximise the production of the deposits produced. The spark ageing experiment can be expanded and applied to a wider range of liquid systems, and an investigation into the quantity and quality of deposit production launched.

Finally all of the samples produced in the above suggested experiments could be subjected to a wider range of spectroscopic techniques such as XPS and XRD. This will enable the exact chemical compositions of the by-products to be determined and the link between the different methods of ageing to be reinforced.

References

1. A. Samee, Z. H. Li, C. H. Zhang, and Z. P. Huang, *Investigation on Electrical Treeing Characteristics of Thermally Aged XLPE Cable*. Proceedings of the 9th International Conference on Properties and Applications of Dielectric Materials, 2009, IEEE.

2. D. M. Hepburn, I. J. Kemp, A. J. Shields, and J. Cooper, *Degradation of epoxy resin by partial discharges.* IEE Proceedings-Science Measurement and Technology, 2000. **147**(3): p. 97-104.

3. T. Mito, Y. Muramoto, and N. Shimizu, *Electroluminescence properties and degradation of XLPE.* Annual Report Conference on Electrical Insulation and Dielectric Phenomena, 2007.

4. V. Griseri, L. A. Dissado, J. C. Fothergill, and G. Teyssedre, *Electroluminescence excitation mechanisms in an epoxy resin under divergent field.* Proceedings of the IEEE 7th International Conference on Solid Dielectrics, 2001.

5. P. W. Sayers, T. J. Lewis, J. P. Llewellyn, and C. L. Griffiths, *Investigation of the structural changes in LDPE and XLPE induced by high electrical stress*. Eighth International Conference on Dielectric Materials, Measurements and Applications. 2000. IEE.

6. N. J. Everall, *Confocal Raman microscopy: Why the depth resolution and spatial accuracy can be much worse than you think.* Applied Spectroscopy, 2000. **54**(10): p. 1515-1520.

7. K. Akutsu, A. Iwata, and Y. Iriyama, *Surface modification of polymeric films by atmospheric plasma treatment.* Journal of Photopolymer Science and Technology, 2000. **13**(1): p. 75-78.

8. A. Keller, *A Note on Single Crystals in Polymers: Evidence for a Folded Chain Configuration*, Philosophy Magazine. 1957. p. 1171-2275.

9. T. Blythe, and D. Bloor, *Electrical Properties of Polymers (2nd Ed)*. Cambrige University Press. 2005.

10. L. A. Dissado, and J. Fothergill., *Electrical Degredation and Breakdown in Polymers (2nd Ed).* London: Peter Perigrins. 1992.

11. D. J. Blundell, and A. Keller, *The concentration dependence of the linear growth rate of polyethylene crystals from solution.* Journal of Polymer Science Part B: Polymer Letters, 1968. **6**(6): p. 433-440.

12. H. I. Akamatsu, and Y. Matsunaga, *Electrical conductivity of the perylene–bromine complex.* Nature (London), 1954(173): p. 168-169.

13. H. I. Akamatsu, *On the electrical conductivity of violanthrone, iso-violanthrone, and pyranthrone.* Journal of Chemical Physics, 1950. **18**: p. 810-811.

14. C. K. Chiang, C. R. Fincher, Y. W. Park, A. J Heeger, H. Shirakawa, E. J. Louis, S. C. Gau, and A. G MacDiarmid, *Electrical Conductivity in Doped Polyacetylene.* Physical Review Letters, 1977. **39**(17): p. 1098-1101.

15. Y. W. Zhang, J. Lewiner, C Alquie, and N. Hampton, *Evidence of strong correlation between space-charge buildup and breakdown in cable insulation.*

IEEE Transactions on Dielectrics and Electrical Insulation, 1996. **3**(6): p. 778-783.

16. L. A. Dissado, G. Mazzanti, and G.C. Montanari, *The role of trapped space charges in the electrical aging of insulating materials.* IEEE Transactions on Dielectrics and Electrical Insulation, 1997. **4**(5): p. 496-506.

17. V. Adamec, and J.H. Calderwood, *Electrode Polarisation in Polymeric Dielectrics.* IEEE Transactions on Electrical Insulation, 1989. **24**(2): p. 205-214.

18. J. Kuffel , E. Kuffel, and W. S. Zaengl, *High voltage engineering fundamental*. 2nd ed. Newnes. 2000.

19. G. P. Mikhailov, *Dielectric losses and polarization of polymers.* Journal of Polymer Science, 1958. **30**(121): p. 605-614.

20. F. H. Kreuger, *Discharge detection in high-voltage equipment*. London: Heywood. 1964.

21. E. Kuffel, and W. S. Zaengl, *High Voltage Engineering Fundementals*. 1st ed. Pergamon Press. 1992.

22. L. A. Dissado, and P. J. J. Sweeney, *Physical Model for Breakdown Structures in Solid Dielectrics.* Physical Review B, 1993. **48**(22): p. 16261-16268.

23. N. Dumitrascu, T. Balau, M. Tasca, and G. Popa, *Corona discharge treatment of the plastified PVC films obtained by chemical grafting.* Materials Chemistry and Physics, 2000. **65**(3): p. 339-344.

24. X. R. Chen, Y. Xu, X. L. Cao, S. J. Dodd, and L. A. Dissaddo, *Effect of Tree Channel Conductivity on Electrical Tree Shape and Breakdown in XLPE Cable Insulation Samples.* IEEE Transactions on Dielectrics and Electrical Insulation, 2011. **18**(3): p. 847-860.

25. A. S. Vaughan, S. J. Dodd, and S.J. Sutton, *A Raman microprobe study of electrical treeing in polyethylene.* Journal of Materials Science, 2004. **39**(1): p. 181-191.

26. J. V. Champion, and S. J. Dodd, *Simulation of partial discharges in conducting and non-conducting electrical tree structures.* Journal of Physics D-Applied Physics, 2001. **34**(8): p. 1235-1242.

27. A. H. Howatson, *An Introduction to Gas Discharges*. Pergamom Press Oxford. 1965.

28. T. Tanaka, *Aging of polymeric and composite insulating materials - Aspects of interfacial performance in aging.* IEEE Transactions on Dielectrics and Electrical Insulation, 2002. **9**(5): p. 704-716.

29. Z. Dong, S. Qin, and L.C. Wadsworth, *Mechanism of corona treatment on polyolefin films.* Polymer Engineering and Science, 1998. **38**(6): p. 965-970.

30. R. M. Overney, R. Luthi, H. Haefke, J. Frommer, E. Meyer, H. J. Guntherodt, S. Hild, and J. Fuhrmann, *An Atomic Force Microscopy Study of Corona-Treated Polypropylene Films.* Applied Surface Science, 1993. **64**(3): p. 197-203.

31. X. S. Liu, A.S. Vaughan, and G. Chen, *A Raman spectroscopic study of bulk and surface ageing phenomena in polyethylene.* Annual Report Conference on Electrical Insulation and Dielectric Phenomena, 2003.

32. A. S. Vaughan, I. L. Hosier, S. J. Dodd, and S. J. Sutton, *On the structure and chemistry of electrical trees in polyethylene.* Journal of Physics D-Applied Physics, 2006. **39**(5): p. 962-978.

33. J. Laserna, *An Introduction to Raman Spectroscopy,* http://www.spectroscopynow.com/coi/cda/detail.cda?page=2&id=1882&type=EducationFeature&chId=6. [29/04/09].

34. R. Tabaksblat, R.J. Meier, and B.J. Kip, *Confocal Raman Microspectroscopy – Theory and Application to Thin Polymer Samples.* Applied Spectroscopy, 1992. **46**(1): p. 60-68.

35. T. Wilson, *Confocal Microscopy*. Academic Press: London. 1994.

36. Y. Gao, L. Y. Li, P. H. Tan, L. Q. Liu, and Z. Zhang, *Application of Raman spectroscopy in carbon nanotube-based polymer composites.* Chinese Science Bulletin, 2010. **55**(35): p. 3978-3988.

37. D. Garcia, *Confocal Raman spectroscopy and principal component analysis of multi-layer polymer films.* Abstracts of Papers of the American Chemical Society, 2007. **233**.

38. D. Garcia, and E. Rondele, *Confocal Raman spectroscopy analysis of multilayer polymer films.* Abstracts of Papers of the American Chemical Society, 2009. **237**.

39. J. P. Tomba, and J. A. Pastor, *Confocal Raman micro spectroscopy with dry objectives: A depth profiling study on polymer films.* Vibrational Spectroscopy, 2007. **44**(1): p. 62-68.

40. J. P. Tomba, and J. M. Pastor, *Confocal Raman Microspectroscopy: A Non-Invasive Approach for in-Depth Analyses of Polymer Substrates.* Macromolecular Chemistry and Physics, 2009. **210**(7): p. 549-554.

41. A. M. Macdonald, and A. S. Vaughan, *Numerical simulations of confocal Raman spectroscopic depth profiles of materials: a photon scattering approach.* Journal of Raman Spectroscopy, 2007. **38**(5): p. 584-592.

42. J. Kroschwitz, *Concise encyclopeidia of polymer science and engineering*, Wiley. p. 683.

43. A. M. MacDonald, A. S. Vaughan, and P. Wyeth, *On confocal Raman spectroscopy of semicrystalline polymers: The effect of optical scattering.* Applied Spectroscopy, 2003. **57**(12): p. 1475-1481.

44. Renishaw, *Renishaw Raman Imaging Microscope User Guide*.

45. J.M.Hollas, *High Resolution Spectroscopy*. Wiley. 1998.

46. A. M. Macdonald, *Raman Spectroscopy and the Conservation of Historic Painted Textiles (PhD Thesis),* University of Southampton, UK, 2004.

47. http://www.reading.ac.uk/cfam/facilities/raman.htm. 05/01/09].

48. J. L. Shi, *Unconventional physical mechanisms between stimulated Brillouin scattering and backward stimulated Raman scattering in liquid water.* Journal of Optics, 2011. **13**(7).

49. Z. Lazarevic, N. Romcevic, M. Vijatovic, N. Paunovic, M. Romcevic, B. Stojanovic, and Z. Dohcevic-Mitrovic, *Characterization of Barium Titanate Ceramic Powders by Raman Spectroscopy.* Acta Physica Polonica A, 2009. **115**(4): p. 808-810.

50. M. Todica, E. Dinte, C. V. Pop, C. Farcau, and S. Astilean, *Raman investigation of some polymeric gels of pharmaceutical interest.* Journal of Optoelectronics and Advanced Materials, 2008. **10**(4): p. 823-825.

51. A. Hernanz, M. Mas, B. Gavilan, and B. Hernandez, *Raman microscopy and IR spectroscopy of prehistoric paintings from Los Murciélagos cave (Zuheros, Córdoba, Spain).* Journal of Raman Spectroscopy, 2006. **37**(4): p. 492-497.

52. D. A. Skoog, F. J. Holler, S. R. Crouch, *Principles of Instrumental Analysis*. 6th ed. Brookes Cole. 2006.

53. D. V. Martyshkin, R.C. Ahuja, A. Kudriavtsev, and S. B. Mirov, *Effective suppression of fluorescence light in Raman measurements using ultrafast time gated charge coupled device camera.* Review of Scientific Instruments, 2004. **75**(3): p. 630-635.

54. A. M. Macdonald, and P. Wyeth, *On the use of photobleaching to reduce fluorescence background in Raman spectroscopy to improve the reliability of pigment identification on painted textiles.* Journal of Raman Spectroscopy, 2006. **37**(8): p. 830-835.

55. J. Kim, Y. Kim, and H. Chung, *Direct on-line Raman measurement of flying solid samples: Determination of polyethylene pellet density.* Talanta, 2011. **83**(3): p. 879-884.

56. S. C. Bae, H. Lee, Z. Q. Lin, and S. Granick, *Chemical imaging in a surface forces apparatus: Confocal Raman spectroscopy of confined poly(dimethylsiloxane).* Langmuir, 2005. **21**(13): p. 5685-5688.

57. W. M. Sears, J. L. Hunt, and J. R. Stevens, *Raman scattering from polymerizing styrene. I. Vibrational mode analysis.* The Journal of Chemical Physics, 1981. **75**(4): p. 1589-1598.

58. W. M. Sears, J. L. Hunt, and J. R. Stevens, *Raman spectra at low temperatures and depolarization ratios for styrene and polystyrene.* The Journal of Chemical Physics, 1982. **77**(4): p. 1639-1644.

59. J. K. Agbenyega, G. Ellis, P. J. Hendra, W. F. Maddams, C. Passingham, H. A. Willis, and J. Chalmers, *Applications of Fourier-Transform Raman-Spectroscopy in the Synthetic-Polymer Field.* Spectrochimica Acta Part a-Molecular and Biomolecular Spectroscopy, 1990. **46**(2): p. 197-216.

60. H. Vaskova, *Quasi real-time monitoring of epoxy resin crosslinking via Raman microsocpy.* International Journal of Mathematical Models and Methods in Applied Sciences, 2011. **5**(7): p. 1197 - 1204.

61. C. Minogianni, K. G. Gatos, and C. Galiotis, *Estimation of crystallinity in isotropic isotactic polypropylene with Raman spectroscopy.* Applied Spectroscopy, 2005. **59**(9): p. 1141-1147.

62. P. R. Griffiths, J. A. de Haseth, *Fourier Transform Infrared Spectrometry*. 2nd ed, New Jersey: John Wiley & Sons, Inc. 2007.

63. J. E. Stewart, *Infrared Spectroscopy*. New York: Marcel Dekker, Inc. 1970.

64. H. M. Ali, and V. H. Grassian, *FTIR study of the reactions of gaseous inorganic and organic acids on calcium carbonate.* Abstracts of Papers of the American Chemical Society, 2004. **227**: p. U1207-U1207.

65. C. Coury, and A. M. Dillner, *A method to quantify organic functional groups and inorganic compounds in ambient aerosols using attenuated total reflectance FTIR spectroscopy and multivariate chemometric techniques.* Atmospheric Environment, 2008. **42**(23): p. 5923-5932.

66. Y. Sanchez, C. Albano, R. Perera, A. Karam, and P. Silva, *Characterization of LDPE grafted with diethylmaleate by gamma radiation: Application of FTIR, GPC and SSA techniques.* Macromolecular Symposia, 2007. **257**: p. 139-146.

67. T. Zorba, E. Papadopoulu, A. Hatjiissaak, K. M. Paraskevopoulos, and K. Chrissafis, *Urea-formaldehyde resins characterized by thermal analysis and FTIR method.* Journal of Thermal Analysis and Calorimetry, 2008. **92**(1): p. 29-33.

68. Y. Hua-Zhong, Y. Shen, Z. Hao-Li, and L. Zhong-Fan, *Molecular orientation and electrochemical stability of azobenzene self-assembled monolayers on gold: an in-situ FTIR study.* Langmuir, 2000. **16**(17).

69. S. J. Martin, V. J. McBrierty, and D. C. Douglass, *Comparison of real-time monitoring of copolymer formation and composition by NMR, FTIR, and numerical simulation.* Macromolecules, 2001. **34**(26): p. 8934-8943.

70. R. N. Kumar, R. Mehnert, T. Scherzer, and F. Bauer,*Application of real time FTIR and MAS NMR spectroscopy to the characterization of UV/EB cured epoxidized natural rubber blends.* Macromolecular Materials and Engineering, 2001. **286**(10): p. 598-604.

71. E. A. Bruns, V. Perraud, A. Zelenyuk, M. J. Ezell, S. N. Johnson, Y. Yu, D. Imre, B. J. Finlayson-Pitts, and M. L. Alexander, *Comparison of FTIR and Particle Mass Spectrometry for the Measurement of Particulate Organic Nitrates.* Environmental Science & Technology, 2010. **44**(3): p. 1056-1061.

72. S. Lefrant, M. Baibarac, and I. Baltog, *Raman and FTIR spectroscopy as valuable tools for the characterization of polymer and carbon nanotube based composites.* Journal of Materials Chemistry, 2009. **19**(32): p. 5690-5704.

73. J. L. Goldstein, *Scanning Electron Micrscopy and X-Ray Microanalysis*. 3rd ed. New York: Springer. 2003.

74. L. Dolgov, O. Yaroshchuk, and L. Qiu, *SEM investigations of the polymer morphology in the liquid crystal-polymer composites with different polymer contents.* Molecular Crystals and Liquid Crystals, 2007. **468**: p. 687-696.

75. E. Suzuki, *High-resolution scanning electron microscopy of immunogold-labelled cells by the use of thin plasma coating of osmium.* Journal of Microscopy-Oxford, 2002. **208**: p. 153-157.

76. N. Erdman, N. Kikuchi, A. Laudate, V. Robertson, *Multispectral imaging in an FEG-SEM.* Advanced Materials & Processes, 2009. **167**(9).

77. J. E. McGregor, and A. M. Donald, *The application of ESEM to biological samples*, Electron Microscopy and Analysis Group Conference. 2009.

78. D. Bassi, F. Cappa, and P. S. Cocconcelli, *A combination of a SEM technique and X-ray microanalysis for studying the spore germination process of Clostridium tyrobutyricum.* Research in Microbiology, 2009. **160**(5): p. 322-329.

79. N. Grizzuti, *Evolution of the morphology in sheared polymer blends. An optical microscopy study*. 12th International Congress on Rheology, Proceedings. 1996. 125-126.

80. J. Sacristan, C. Mijangos, H. Reinecke, S. Spells, and J. Yarwood, *Depth profiling of modified PVC surfaces using confocal Raman microspectroscopy.* Macromolecular Rapid Communications, 2000. **21**(13): p. 894-896.

81. J. Sacristan, C. Mijangos, H. Reinecke, S. Spells, and J. Yarwood, *Selective surface modification of PVC films as revealed by confocal Raman microspectroscopy.* Macromolecules, 2000. **33**(16): p. 6134-6139.

82. J. Sacristan, H. Reinecke, and C. Mijangos, *Surface modification of PVC films in solvent-non-solvent mixtures.* Polymer, 2000. **41**(15): p. 5577-5582.

83. C. Sammon, S. Hajatdoost, P.Eaton, C. Mura, and J. Yarwood, *Materials analysis using confocal Raman microscopy.* Macromolecular Symposia, 1999. **141**: p. 247-262.

84. C. Sammon, C. Mura, P.Eaton, and J. Yarwood, *Raman microscopic studies of polymer surfaces and interfaces.* Analusis, 2000. **28**(1): p. 30-34.

85. C. Mura, J. Yarwood, R. Swart, and D. Hodge, *Raman microscopic studies of the distribution of the fungicide fluorfolpet in plasticised PVC films.* Polymer, 2000. **41**(24): p. 8659-8671.

86. P. Eaton, P. Holmes, and J. Yarwood, *ATR/FT-IR and Raman microscopic investigation of diffusion and distribution of silane coupling agents in PVC films.* Applied Spectroscopy, 2000. **54**(4): p. 508-516.

87. K. P. J. Williams, G. D. Pitt, D. N. Batchelder, and B. J. Kip, *Confocal Raman Microspectroscopy using a Stigmatic Specrtograph and CCD Detector.* Applied Spectroscopy, 1994. **48**(2): p. 232-235.

88. S. Hell, G. Reiner, C. Cremer, and E. H. K. Stelzer, *Abberations in Conforcal Flourescence Microscopy Induced by Mismatches in Refractive Index*. Journal of Microscopy-Oxford, 1993. **169**: p. 391-405.

89. S. Hajatdoost, and J. Yarwood, *Depth profiling of polg(methyl methacrylate), poly(vinyl alcohol) laminates by confocal Raman microspectroscopy.* Applied Spectroscopy, 1996. **50**(5): p. 558-564.

90. S. Hajatdoost, M. Olsthoorn, and J. Yarwood, *Depth profiling study of effect of annealing temperature on polymer/polymer interfaces in laminates using confocal Raman microspectroscopy.* Applied Spectroscopy, 1997. **51**(12): p. 1784-1790.

91. N. J. Everall, *Modeling and measuring the effect of refraction on the depth resolution of confocal Raman microscopy.* Applied Spectroscopy, 2000. **54**(6): p. 773-782.

92. H. Reinecke, S. J. Spells, J. Sacristan, J. Yarwood, and C. Mijangos, *Confocal Raman depth profiling of surface-modified polymer films: Effects of sample refractive index.* Applied Spectroscopy, 2001. **55**(12): p. 1660-1664.

93. N. J. Everall, T. Hahn, P. Matousek, A. W. Parker, and M. Towrie,*Photon migration in Raman spectroscopy.* Applied Spectroscopy, 2004. **58**(5): p. 591-597.

94. N. J. Everall, J. Lapham, F. Adar, A. Whitley, E. Lee, and S. Mamedov, *Optimizing depth resolution in confocal Raman microscopy: A comparison of metallurgical, dry corrected, and oil immersion objectives.* Applied Spectroscopy, 2007. **61**(3): p. 251-259.

95. N. J. Everall, *The influence of out-of-focus sample regions on the surface specificity of confocal Raman microscopy.* Applied Spectroscopy, 2008. **62**(6): p. 591-598.

96. K. J. Baldwin, and D. N. Batchelder, *Confocal Raman microspectroscopy through a planar interface.* Applied Spectroscopy, 2001. **55**(5): p. 517-524.

97. L. Baia, K. Gigant, U. Posset, G. Schottner, W. Kiefer, and J. Popp, *Confocal micro-Raman spectroscopy: Theory and application to a hybrid polymer coating.* Applied Spectroscopy, 2002. **56**(4): p. 536-540.

98. S. Michielsen, *Aberrations in confocal spectroscopy of polymeric materials: Erroneous thicknesses and intensities, and loss of resolution.* Journal of Applied Polymer Science, 2001. **81**(7): p. 1662-1669.

99. L. J. Bruneel, J. C. Lassegues, and C. Sourisseau, *In-depth analyses by confocal Raman microspectrometry: experimental features and modeling of the refraction effects.* Journal of Raman Spectroscopy, 2002. **33**(10): p. 815-828.

100. J. P. Tomba, L. M. Arzondo, and J. M. Pastor, *Depth profiling by confocal Raman microspectroscopy: Semi-empirical modeling of the Raman response.* Applied Spectroscopy, 2007. **61**(2): p. 177-185.

101. P. Torok, P. Varga, and G. Nemeth, *Analyitical Solution of the Diffraction Integrals and Interpretation of Wave-Front Distortion when Light is Focused Throught a Planar Interface between Materials of Mismatched Refractive-Indexes.* Journal of the Optical Society of America a-Optics Image Science and Vision, 1995. **12**(12): p. 2660-2671.

102. C. Sourisseau, and P. Maraval, *Confocal Raman microspectrometry: A vectorial electromagnetic treatment of the light focused and collected through a planar interface and its application to the study of a thin coating.* Applied Spectroscopy, 2003. **57**(11): p. 1324-1332.

103. C. A. Froud, I. P. Hayward, and J. Laven, *Advances in the Raman depth profiling of polymer laminates.* Applied Spectroscopy, 2003. **57**(12): p. 1468-1474.

104. J. Martín-Gil, A. I. De Andres-Santos, M. C. Ramos-Sanchez, M. T. Barrio-Arredondo, and N. Chebib-Abuchala, *Thermal behaviour of medical grade silicone oils.* Journal of Analytical and Applied Pyrolysis, 1997. **42**(2): p. 151-158.

105. K. H. Wong, S. A. Koopmans, T. Terwee, A. C. Kooijman, *Changes in spherical aberration after lens refilling with a silicone oil.* Investigative Ophthalmology & Visual Science, 2007. **48**(3): p. 1261-1267.

106. V. S. Gorelik, L. I. Zlobina, and O. N. Sharts. *Raman scattering in hydrocarbon and fluorocarbon zigzag structures*. in *6th Optics in Agriculture Conference on Biological Quality and Precision Agriculture II*. 2000. Boston, Ma: Spie-Int Soc Optical Engineering.

107. P. Matousek, I. P. Clark, E. R. C. Draper, M. D. Morris, A. E. Goodship, N. Everall, M. Towrie, W. F. Finney, and A. W. Parker, *Subsurface probing in diffusely scattering media using spatially offset Raman spectroscopy.* Applied Spectroscopy, 2005. **59**(4): p. 393-400.

108. C. A. Froud, I. P. Hayward, and J. Laven, *Advances in the Raman depth profiling of polymer laminates.* Applied Spectroscopy, 2005. **59**(1): p. 1468-1474.

109. R. Bruetsch, *High Voltage Insulation Failure Mechanisms.* Conference Record of the 2008 IEEE International Symposium on Electrical Insulation 2008.

110. L. Lamarre, and E. David, *Temperature Dependence of the Resistance of Modern Epoxy Mica Insulation of HV Rotating Machines.* IEEE Transactions on Dielectrics and Electrical Insulation, 2008. **15**(5): p. 1305-1312.

111. R. Vogelsang, R. Brutsch, T. Farr, and K. Frohlich, *Electrical tree propagation along barrier-interfaces in epoxy resin.* IEEE Annual Report Conference on Electrical Insulation and Dielectric Phenomena. 2002.

112. R. Jones, and H. Chandler, *Strength loss in E-glass fibres after exposure to organic acids.* Journal of Materials Science, 1985. **20**(9): p. 3325-3328.

113. L. A. Dissado, S. J. Dodd, J. V. Champion, P. I. Williams, and J. M. Alison, *Propagation of electrical tree structures in solid polymeric insulation.* IEEE Transactions on Dielectrics and Electrical Insulation, 1997. **4**(3): p. 259-279.

114. P. H. F. Morshuis, *Partial Discharge Mechanisms in Voids Related to Dielectric Degredation.* IEE Proceedings-Science Measurement and Technology, 1995. **142**(1): p. 62-68.

115. L. A. Dissado, and P.I. Williams, *Physical Origin for Differences in Electrical Tree Structures.* IEEE Annual Report - Conference on Electrical Insulation and Dielectric Phenomena, 1994.

116. C. Y. Kim, J. Evans, and D. A. I. Goring, *Corona-Induced Authoesion of Polyethelene.* Journal of Applied Polymer Science, 1971. **15**(6): p. 1365-&.

117. S. Serra, G. C. Montanari, and G. Mazzanti, *Theory of inception mechanism and growth of defect-induced damage in polyethylene cable insulation.* Journal of Applied Physics, 2005. **98**(3): p. 034102-15.

118. G. Mazzanti, and G. C. Montanari, *Electrical aging and life models: the role of space charge.* Dielectrics and Electrical Insulation, IEEE Transactions on, 2005. **12**(5): p. 876-890.

119. G. C. Montanari, A. Cavallini, L. Testa, and, L. A. Dissado, *Model of ageing inception and growth from microvoids in polyethylene-based materials under AC voltage.* Conference on Electrical Insulation and Dielectric Phenomena. 2008, IEEE.

120. S. Serra, G. C. Montanari, and G. Mazzanti, *Theoretical Study of inception mechanism and growth of defect-induced damages in XLPE cable.* Annual Report Conference on Electrical Insulation and Dielectric Phenomena. 2001.

121. F. Negri, E. di Donato, M. Tommasini, C. Castiglioni, G. Zerbi, and K. Mullen, *Resonance Raman contribution to the D band of carbon materials: Modeling defects with quantum chemistry.* The Journal of Chemical Physics, 2004. **120**(24): p. 11889-11900.

122. M. Frenklach, *Reaction mechanism of soot formation in flames.* Physical Chemistry Chemical Physics, 2002. **4**(11): p. 2028-2037.

123. H. Wang, and M. Frenklach, *A detailed kinetic modeling study of aromatics formation in laminar premixed acetylene and ethylene flames.* Combustion and Flame, 1997. **110**(1-2): p. 173-221.

124. M. Frenklach, D. W. Clary, T. Yuan, W. C. Gardiner, and S. E. Stein, *Mechanism of Soot Formation in Acetylene-Oxygen Mixtures.* Combustion Science and Technology, 1986. **50**(1-3): p. 79-115.

125. J. D. Bittner, and J. B. Howard, *Composition profiles and reaction mechanisms in a near-sooting premixed benzene/oxygen/argon flame.* Symposium (International) on Combustion, 1981. **18**(1): p. 1105-1116.

126. C. F. Melius, M. E. Colvin, N. M. Marinov, W. J. Pitz, and S. M. Senkan, *Reaction mechanisms in aromatic hydrocarbon formation involving the C5H5 cyclopentadienyl moiety*. Twenty-Sixth Symposium, ed. A.R.D.F.L. Burgess. 1996. 685-692.

127. S. Costa, E. Borowiak-Palen, M. Kruszynska, A. Bachmatiuk, and R. J. Kalenczuk, *Characterization of carbon nanotubes by Raman spectroscopy.* Materials Science-Poland, 2008. **26**(2): p. 433-441.

128. P. Puech, A. W. Anwar, E. Flahaut, D. J. Dunstan, A. Bassil, and W. Bacsa, *Raman G and D band in strongly photoexcited carbon nanotubes.* Physical Review B, 2009. **79**(8): p. 085418.

129. P. W. Sayers, T. J. Lewis, J. P. Llewellyn, and C. L. Griffiths, *Investigation of the structural changes in LDPE and XLPE induced by high electrical stress.* Eighth International Conference on Dielectric Materials, Measurements and Applications. IEE 2000.

130. *http://www.rubberworld.com/pdfs/detadd.pdf*. [14/08/2012].

131. I. F. Viblyi, N. A. Romanyuk, and V. V. Turkevich, *Infrared reflection spectra of Seignette-salt single crystals.* Optics and Spectroscopy, 1973. **34**(3): p. 298-301301.

132. J. T. Kloprogge, D. Visser, H. Ruan, and R. L. Frost, *Infrared and raman spectroscopy of holmquistite, Li-2(Mg,Fe2+)(3)(Al,Fe3+)(2)(Si,Al)(8)O-22(OH)(2).* Journal of Materials Science Letters, 2001. **20**(16): p. 1497-1499.

133. http://www2.ups.edu/faculty/hanson/Spectroscopy/IR/IRfrequencies.html [28/02/2012].

134. P. H. F. Morshuis, *Degradation of solid dielectrics due to internal partial discharge: Some thoughts on progress made and where to go now.* IEEE Transactions on Dielectrics and Electrical Insulation, 2005. **12**(5): p. 905-913.

135. J. C. Fothergill, L. A. Dissado, and P. J. J. Sweeney, *A Discharge-Avalanche Theory for the Propagation of Electrical Trees – a Physical Basis for their Voltage Dependance*. IEEE Transactions on Dielectrics and Electrical Insulation, 1994. **1**(3): p. 474-486.

136. L. A. Dissado, *Understanding electrical trees in solids: From experiment to theory.* IEEE Transactions on Dielectrics and Electrical Insulation, 2002. **9**(4): p. 483-497.

137. R. J. Densley, *Investigation into the Growth of Electrical Trees in XLPE Cable Insulation.* IEEE Transactions on Electrical Insulation, 1979. **14**(3): p. 148-158.

138. J. V. Champion, and S. J. Dodd, *Systematic and reproducible partial discharge patterns during electrical tree growth in an epoxy resin.* Journal of Physics D-Applied Physics, 1996. **29**(3): p. 862-868.

139. C. Laurent, and C. Mayoux, Analysis of the Propagation of Electrical Treeing using Optical and Electrical Methods. IEEE Transactions on Electrical Insulation, 1980. **15**(1): p. 33-42.

140. K. Wu, Y. Suzuoki, T. Mitutani, X. Hengkun, *Model for partial discharges associated with treeing breakdown: III. PD extinction and re-growth of tree.* Journal of Physics D-Applied Physics, 2000. **33**(10): p. 1209-1218.

141. O. P. Poznansky, *Bush region in the propagation of electrical degradation in polymers.* Computational and Theoretical Polymer Science, 2001. **11**(1): p. 81-82.

142. J. V. Champion, S. J. Dodd, Y. Zhao, A. S. Vaughan, M. Brown, A. E. davies, S. J. Sutton, and S. G. Swingler, *Morphology and the growth of electrical trees in a propylene/ethylene copolymer.* IEEE Transactions on Dielectrics and Electrical Insulation, 2001. **8**(2): p. 284-292.

143. J. H. Mason, *Assessing the Resistance of Polymers to Electrical Treeing.* IEE Proceedings-a-Science Measurement and Technology, 1981. **128**(3): p. 193-201.

144. R. Sarathi, and K. Sridhar, *Investigation in to growth of electrical trees in XLPE cables under transient voltages*. Proceedings of the IEEE 6th International Conference on Conduction and Breakdown in Solid Dielectrics. 1998.

145. M. H. Ahmad, H. Ahmad, N. Bashir, Z. A. Malek, Y. Z. Arief, and R. Kurnianto, *Statistical study on tree inception voltage of silicone rubber and epoxy resin.* International Conference on Electrical Engineering and Informatics. 2011.

146. P. Tiemblo, M. Hoyos, J. M. Gomez-Elvira, J. Guzman, N. Garcia, A. Dardando, and F. Guastavino, *The development of electrical treeing in LDPE and its nanocomposites with spherical silica and fibrous and laminar silicates.* Journal of Physics D-Applied Physics, 2008. **41**(12).

147. F. Guastavino, A. Dardano, G. C. Montanari, L. Testa, and F. Bellicci,*Electrical Treeing in EVA-Boehmite and EVA-Montmorillonite Nanocomposites*. IEEE Electrical Insulation Conference. 2009.

148. D. Pitsa, G. Vardakis, M. G. Danikas, and M. Kozako, *Electrical Treeing Propogation in Nanocomposites and the Role of Nanofillers: Simulation with the Aid of Cellular Automata*. Journal of Electrical Engineering-Elektrotechnicky Casopis, 2010. **61**(2): p. 125-128.

149. F. Guastavino, A. Dardano, G. C. Montanari, F. Deorsola, and M. Di Lorenzo del Casale, *A study about electrical treeing in different EVA-layered silicate nanostructured compounds*. Conference Record of the IEEE International Symposium on Electrical Insulation. 2006.

150. B. X. Du, Z. L. Ma, Y. Gao, and T. Han, *Effect of Ambient Temperature on Electrical Treeing Characteristics in Silicone Rubber.* IEEE Transactions on Dielectrics and Electrical Insulation, 2011. **18**(2): p. 401-407.

151. Q. Nie, Y. X. Zhou, Z. Z. Chen, and H. H. Chen, *Influence of frequency on tree initiation voltage and electrical tree shape in silicone rubber.* High Voltage Engineering, 2009. **35**(1).

152. Z. Z. Chen, Z. X. Cheng, Y. X. Zhou, Q. Nie, H. H. Chen, S. W. Guo, and R. Liu, *Influence of Gas Void and Gas Crack Defects on Electrical Tree Initiation in Silicone Rubber.* High Voltage Engineering, 2009. **35**(10).

153. O. S. Gefle, S. M. Lebedev, Y. P. Pokholkov, E. Gockenbach, and H. Borsi, *Tree-inception in PMMA with a barrier.* Journal of Physics D-Applied Physics, 2004. **37**(16): p. 2318-2322.

154. P. Basappa, and J. Kim, *Understanding of electrical treeing in PMMA by partial discharges and thermally stimulated discharges.* IEEE Conference on Electrical Insulation and Dielectric Phenomena, 2006.

155. J. Holto, and E. Ildstad, *Electrical tree growth in extruded s-polypropylene.* Proceedings of the 10th IEEE International Conference on Solid Dielectrics, 2010.

156. M. G. Danikas, I. Karafyllidis, A. Thanailakis, and A. M. Bruning, *Simulation of electrical tree growth in solid dielectrics containing voids of arbitrary shape.* Modelling and Simulation in Materials Science and Engineering, 1996. **4**(6): p. 535-552.

157. M. D. Noskov, A. S. Malinovski, M. Sack, and A. J. Schwab, *Self-consistent modeling of electrical tree propagation and PD activity.* IEEE Transactions on Dielectrics and Electrical Insulation, 2000. **7**(6): p. 725-733.

158. G. E. Vardakis, M. G. Danikas, and I. Karafyllidis, *Simulation of space-charge effects in electrical tree propagation using cellular automata.* Materials Letters, 2002. **56**(4): p. 404-409.

159. S. J. Dodd, *A deterministic model for the growth of non-conducting electrical tree structures.* Journal of Physics D-Applied Physics, 2003. **36**(2): p. 129-141.

160. S. J. Dodd, L. A. Dissado, J. V. Champion, and J. M. Alison, *Evidence for deterministic chaos as the origin of electrical tree breakdown structures in polymeric insulation.* Physical Review B, 1995. **52**(24): p. 16985-16988.

161. L. A. Dissado, J. C. Fothergill, N. Wise, A. Willby, and J. Cooper, *A deterministic model for branched structures in the electrical breakdown of solid polymeric dielectrics.* Journal of Physics D-Applied Physics, 2000. **33**(19): p. L109-L112.

162. L. A. Dissado, *Deterministic chaos in breakdown - Does it occur and what can it tell us?* IEEE Transactions on Dielectrics and Electrical Insulation, 2002. **9**(5): p. 752-762.

163. H. Mitsui, T. Yoshimitsu, Y. Mizutani, and K. Umemoto, *Electrical Failure Properties of Cast Epoxy-resins.* IEEE Transactions on Electrical Insulation, 1981. **16**(6): p. 533-542.

164. G. Chen, and C. H. Tham, *Electrical Treeing Characteristics in XLPE Power Cable Insulation in Frequency Range between 20 and 500 Hz.* IEEE Transactions on Dielectrics and Electrical Insulation, 2009. **16**(1): p. 179-188.

165. A. Xie, X. Zheng, S. Li, and G. Chen *Investigations of Electrical Trees in the Inner Layer of XLPE Cable Insulation Using Computer-aided Image Recording Monitoring.* IEEE Transactions on Dielectrics and Electrical Insulation, 2010. **17**(3): p. 685-693.

166. K. J. Kingma, and R. J. Hemley, *Raman-Spectroscopic Study of Microcrystaline Silica.* American Mineralogist, 1994. **79**(3-4): p. 269-273.

167. A. Wain, D. Waters, A. Jephcoat, and H. Olijynk, *The high-pressure to ultrahigh-pressure eclogite transition in the Western Gneiss Region, Norway.* European Journal of Mineralogy, 2000. **12**(3): p. 667-687.

168. Y. Israeli, J. L. Philippart, J. Cavezzan, J. Lacoste, and J. Lemaire, *Photooxidation of Polydimethylsiloxane Oils. 1. Effect of Silicon Hydride Groups.* Polymer Degradation and Stability, 1992. **36**(2): p. 179-185.

169. Y. Israeli, J. Cavezzan, and J. Lacoste, *Photooxidation of Polydimethylsiloxane Oils. 2. Effect of Vinyl Groups.* Polymer Degradation and Stability, 1992. **37**(3): p. 201-208.

170. Y. Israeli, J. Cavezzan, and J. Lacoste, *Photooxidation of Polydimethylsiloxane Oils. 3. Effect of Dimethlene Groups.* Polymer Degradation and Stability, 1993. **42**(3): p. 267-279.

171. S. J. Clarson, J. A. Semlyen, Siloxane Polymers. 1993, New Jersey: Prentice Hall.

172. N. S. Tomer, F. Delor-Jestin, L. Frezet, and J. Lacoste, *Oxidation, Chain Scission and Cross-Linking Studies of Polysiloxanes upon Ageings.* Open Journal of Organic Polymer Materials, 2012. **2**: p. 13-22.

173. J. Macan, I. Brnrdic, S. Orlic, H. Ivankovic, M. Ivankovic, *Thermal degradation of epoxy-silica organic-inorganic hybrid materials.* Polymer Degradation and Stability, 2006. **91**(1): p. 122-127.

174. N. Grassie, M. I. Guy, and N. H. Tennent, *Degredation of Epoxy Polymers . 4. Thermal Degredation of Bisphenol-A Diglycidyl Ether Cured with Ethylene Diamine.* Polymer Degradation and Stability, 1986. **14**(2): p. 125-137.

175. J. W. Graydon, S. J. Thorpe, and D. W. Kirk, *Interpretation of Activation-Energies Calculated from Nonisothermal Transformations of Amorphous Metals.* Acta Metallurgica Et Materialia, 1994. **42**(9): p. 3163-3166.

176. A. Bradwell, *Electrical Insulators*. IEE Electrical and Electronics Materials and Devices, ed. N. Parkman. Peter Peregrinus LTD. 1983.

177. Z. Yong, M. Otsubo, and C. Honda, *Degradation of polymeric materials exposed to corona discharges.* Polymer Testing, 2006. **25**(3): p. 313-317.

178. S. J. Park, and J. S. Jin, *Effect of corona discharge treatment on the dyeability of low-density polyethylene film.* Journal of Colloid and Interface Science, 2001. **236**(1): p. 155-160.

179. J. F. Carley, and P. T. Kitze, *Corona-Discharge Treatment of Polyethylene Films. 1. Experimental Work and Physical Effects.* Polymer Engineering and Science, 1978. **18**(4): p. 326-334.

180. X. Lihua, F Zhengping, S. Ping, and P. Mao, *Effects of corona discharge on the surface structure, morphology and properties of multi-walled carbon nanotubes.* Applied Surface Science: p. 6447-53.

181. J. M. Farley, and P. Meka, *Heat Sealing of Semicrystaline Polymer-Films . 3. Effect of Corona Discharge Treatment of LLDPE.* Journal of Applied Polymer Science, 1994. **51**(1): p. 121-131.

182. D. Briggs, and C. R. Kendall, *Chemical Basis of Adhesion to Electrical-Discharge Treated Polyethelyene.* Polymer, 1979. **20**(9): p. 1053-1054.

183. H. Schonhor and F. W. Ryan, *Surface Crosslinking of Polyethelyene and Adhesive Joint Strength.* Journal of Applied Polymer Science, 1974. **18**(1): p. 235-243.

184. M. Stradal and D. A. I. Goring, *Corona-Induced Autohesion of Polyethelyene – Dependance of Bonding on Frequency and Power-Consumption in Various Gasses.* Canadian Journal of Chemical Engineering, 1975. **53**(4): p. 427-430.

185. L. A. Rosenthal, and D. A. Davis, *Electrical Characterisation of a Corona Discharge for Surface Treatment.* IEEE Transactions on Industry Applications, 1975. **IA11**(3): p. 328-335.

186. M. Z. Huang, *Ambient Ionization Mass Spectrometry.* Annual Review of Analytical Chemistry, Vol 3. **3**: p. 43-65.

187. H. Suzuki, D. C. Zou, T. Izumi, H. Yamamoto, X. T. Tao, T. Watanabe, H. Usui, and S. Miyata. *Luminescence of dye-doped polymer films induced by corona discharge.* Journal of Applied Physics, 2000. **88**(10): p. 5791-5795.

188. G. C. Smith, *Quantitative Surface Analysis for Materials Science*. 1991: The Institute of Metals.

189. D. Briggs, *XPS Studies of Polymer Surface Modifications and Adhesion Mechanisms.* Journal of Adhesion, 1982. **13**(3-4): p. 287-301.

190. J. M. Evans, *Nitrogen Corona Activation of Polyethylene.* Journal of Adhesion, 1973. **5**(1): p. 1-7.

191. J. M. Evans, *Influence of Oxygen on Nitrogen Corona Treatment of Polyolefins.* Journal of Adhesion, 1973. **5**(1): p. 9-16.